

Genetic Design of Ultra High Strength Stainless Steels: Modelling and Experiments

Ph.D. thesis

September, 2009

Wei Xu



The work described in the thesis was carried out in the framework of the Materials Innovation Institute M2i (formerly Netherlands Institute for Metals Research) and in collaboration with and financially supported by Corus U.K.

Genetic Design of Ultra High Strength Stainless Steels: Modelling and Experiments

Proefschrift

ter verkrijging van de graad van doctor
aan de Technische Universiteit Delft,
op gezag van de Rector Magnificus prof.dr.ir. J.T. Fokkema,
voorzitter van het College voor Promoties,
in het openbaar te verdedigen op woensdag 30 september 2009 om 10:00 uur

door

Wei Xu

Master of Science in Solid Mechanics
University of Science and Technology of China
geboren te Dandong, Provincie Liaoning, China

Dit proefschrift is goedgekeurd door de promotor:

Prof.dr.ir. S. van der Zwaag

Copromotor:

Dr. P.E.J. Rivera Díaz del Castillo

Samenstelling promotiecommissie:

Rector Magnificus, voorzitter

Prof.dr.ir. S. van der Zwaag, Technische Universiteit Delft, promotor

Dr. P.E.J. Rivera Díaz del Castillo, Technische Universiteit Delft, copromotor

Prof.dr. K. Yang, Institute of Metal Research Chinese Academy of Sciences

Prof.dr. J. Ågren, Royal Institute of Technology, Sweden

Prof.dr. J.Th.M. de Hosson, University of Groningen, The Netherlands

Prof.dr. R. Boom, Technische Universiteit Delft

Prof.dr. E.H. Brück, Technische Universiteit Delft

Keywords: Alloy design, Ultra high strength, Stainless, Maraging, Precipitate strengthening steels, Genetic algorithm, Thermodynamics

Cover designed by Wei Xu

Copyright ©2009 by Wei Xu

ustcxuwei@hotmail.com

All rights reserved. No part of the material protected by this copyright notice may be reproduced or utilized in any form or by any means, electronic or mechanical, including photocopying, recording or by any information storage and retrieval system, without permission from the author.

Printed in The Netherlands by PrintPartners Ipskamp

ISBN: 978-90-77172-49-0

To Xi

Contents

1	Introduction	1
1.1	State of the Art of Ultra High Strength Steels	1
1.2	Alloy Design Approach	4
1.3	Scope and Outline of the Thesis	6
2	The Base Computational Alloy Design Model Combining Thermodynamics and Genetic Algorithms	9
2.1	Introduction	9
2.2	Desirable Microstructures	10
2.2.1	Matrix	10
2.2.2	Precipitation	10
2.2.3	Corrosion Resistance	14
2.2.4	Heat Treatment	14
2.3	Quantification of Microstructural Criteria	16
2.3.1	Ms Temperature	16
2.3.2	Precipitation	17
2.3.3	Cr Concentration in the Matrix	19
2.4	Desired Alloy System and Compositional Constraints	19
2.5	Calculation and Algorithms	20
2.5.1	General Algorithm	20
2.5.2	Optimisation Scheme: Genetic Algorithm	23
2.6	Results	25
2.7	Discussion	26

2.7.1	Effects of Individual Components in the Model Alloys . . .	26
2.7.2	Comparison of the Different Optimisation Methods	28
2.7.3	Comparison to Existing Alloys	31
2.8	Conclusion	32
3	Further Model Development: Precipitation Strengthening Contribution	35
3.1	Introduction	35
3.2	Precipitation Strengthening Factor: the New Optimisation Factor .	36
3.3	Alloy Design Exercises	39
3.4	Compositional Effect	42
3.5	Ageing Temperature Effect	46
3.6	Alloy Re-design by Incorporating the Ageing Temperature Gene .	48
3.7	Conclusion	50
4	Experimental Validation: the First Round of Prototype Alloys	51
4.1	Alloy Compositions	51
4.2	Experimental Procedures	54
4.3	Characterisation of As-rolled Materials	55
4.4	Solution Treatment Optimisation	57
4.5	Ageing treatment	60
4.6	Results	61
4.6.1	Mechanical Properties	61
4.6.2	Microstructures	65
4.6.3	Fractography	68
4.7	Discussion	69
4.7.1	The Presence of Undesirable Phases Prior to Ageing	69
4.7.2	Identification of Strengthening Precipitates in Alloy CarCo	72
4.8	Conclusion	73
5	An Integrated Model Incorporating both Composition and the Full Heat Treatment Cycle	77
5.1	Introduction	77
5.2	Integrated Model	78
5.2.1	Austenisation/Solution Treatment	78
5.2.2	Martensite Formation	79
5.2.3	Ageing Treatment: Precipitation in a Cr-rich Matrix	80
5.3	Model Application	80
5.4	Discussion	82
5.5	Conclusion	89
6	Experimental Validation: the Second Round of Prototype Alloys	91
6.1	Alloy Compositions	91
6.2	Experimental Procedures	94

6.3	Characterisation of As-hot-rolled Materials	95
6.4	Solution Treatment Optimisation	95
6.5	Cold Rolling	102
6.6	Ageing Treatment	104
6.7	Results	104
6.7.1	Mechanical Properties	104
6.7.2	Microstructures	108
6.7.3	Fractography	112
6.8	Discussion	113
6.8.1	The Effects of Composition and Heat Treatment Temperatures	113
6.8.2	Identification of Strengthening Precipitates	116
6.8.3	Corrosion Resistance	124
6.8.4	Comparison to Existing Counterparts	127
6.9	Conclusion	128
7	Summary	131
	Samenvatting	137
	Appendices	143
A	A KWN Based Precipitation Kinetics Model	143
	Bibliography	159
	Acknowledgements	175
	Curriculum Vitae	177
	List of Publications	179

1

Introduction

1.1 State of the Art of Ultra High Strength Steels

Steels combining properties of ultra high strength (UHS) and good ductility are of great importance in automotive, aerospace, nuclear, gear, bearing and other industries. They are the future key materials for lightweight engineering design strategies and corresponding CO₂ savings. Driven by the development of metallurgy and in response to commercial demands, both academia and industry have made great efforts to develop a large variety of steel grades and processing technology, and hence achieved continuous improvement for some decades.

Conventionally produced bulk high strength steels are known as high-strength low-alloy (HSLA) or microalloyed (MA) steels. This family of steels usually has a strength not exceeding 700-800 MPa and possesses a microstructure of fine grained ferrite that has been strengthened with carbon and/or nitrogen precipitates of titanium, vanadium, or niobium. These steels can be manufactured under relatively simple processing conditions and have widely been applied for weight reduction in automotive and general construction applications. In order to further enhance the combination of strength and ductility, more alloying elements have been added and more sophisticated alloy systems have been designed employing

various mechanisms including Dual Phase (DP) steels, Transformation Induced Plasticity (TRIP) steels, Twinning Induced Plasticity (TWIP) steels and maraging steels. Typical strength - ductility profiles of those steel families are shown in Figure 1.1. Dual phase steels have a microstructure of mainly soft ferrite, with islands of hard martensite dispersed throughout. The strength level of these grades is related to the amount of martensite in the microstructure along with its distribution and morphology [1][2][3][4][5][6][7][8]. TRIP steels are multiphase grades which involve special alloying and heat treatments to stabilise some amount of austenite at room temperature embedded in a primary ferritic matrix. During plastic deformation and straining, the retained austenite progressively transforms to martensite with increasing strain. This leads to a volume and shape change within the microstructure, which accommodates the strain and increases the ductility [9][10][11][12][13][14][15][16][17][18][19]. Unlike DP and TRIP steels, TWIP steels generally possess a fully austenitic microstructure at room temperatures. The formation of mechanical twins during deformation generates high strain hardening, preventing necking and thus maintaining a very high strain capacity and achieving a better combination of strength and ductility [20][21][22][23][24][25]. Another important category of UHS steels is maraging steels, in which martensite is formed upon quenching following solution treatment and consequently further strengthened by the formation of various strengthening precipitates such as carbides [26][27][28][29][30][31][32][33], Cu clusters [34][35][36][37][38][39][40][41][42] or $\text{Ni}_3\text{Ti}/\text{NiAl}$ [43][44][45][46][47][48][49][50] intermetallics at a moderate temperature of about 773 K. The superior properties of maraging steels, such as ultra high strength, high ductility, good hardenability, good weldability, simple heat treatment without deformation steps, sometimes in combination with a good corrosion resistance, have led to a widespread application of maraging steels for demanding applications. The composition and mechanical properties of some existing successful maraging steel grades are summarised in Table 1.1.

In applications of UHS steels, such as in automotive, aerospace and nuclear industries, the materials are usually subjected to extreme mechanical loads and harsh environmental conditions in which corrosion is an important issue. However, the most commonly used steels for these applications, such as maraging 300M for aircraft landing gear, and DP/TRIP in automotive industries, are non-stainless steel grades. Consequently, a specialised and costly coating/plating process has to be employed for corrosion protection. From manufacturing, environmental and reliability considerations, a stainless steel with equivalent mechanical properties but not requiring a corrosion protective coating would be an attractive alternative. Among existing stainless steels, the majority is austenitic, ferritic or duplex (austenite and ferrite) grades. However, because of the natures of ferrite and austenite, the strengths of those stainless steels are well below 1000 MPa and are hence not sufficient to replace non-stainless maraging counterparts. Therefore,

Alloy	C	Cr	Ni	Ti	Mo	Al	Cu	Co	Mn	Si	Others	YS	UTS	El	SS
300M	0.4	0.8	1.8		0.4				0.8	1.6	V(0.05)	1586	1995	0.10	N
Aermet 100	0.23	3.10	11.1		1.2			13.4				1724	1965	0.14	N
PH15-5	<0.07	14-15.5	3.5-5.5				2.5-4.5		<1.0			1228	1325	0.16	Y
PH17-4	<0.07	15.5-17.5	3.0-5.0				3.0-5.0		<1.0	<1.0		1275	1399	0.11	Y
PH13-8	<0.05	12.3-13.3	7.5-8.5		2.0-2.5	0.90-1.35			<0.1			1448	1551	0.12	Y
Custom450	<0.05	14.0-16.0	5.0-7.0		0.5-1.0		1.3-1.8		<1.0	<1.0		1296	1351	0.12	Y
Custom455	<0.05	11.0-12.5	7.5-9.5	0.8-1.4			1.5-2.5		<0.5	<0.5	Nb(0.1-0.5)	1689	1724	0.10	Y
Custom465	<0.02	11.0-12.5	10.8-11.3	1.5-1.8	0.75-1.25				<0.25			1707	1765	0.11	Y
Custom475	<0.01	10.5-11.5	7.5-8.5		4.5-5.5	1.0-1.5		8.0-9.0	<0.5			1972	2006	0.05	Y
Carpenter275	<0.02	11.0-12.5	10.8-11.3	1.55-1.80	0.75-1.25				<0.25		Nb(0.15-0.30)	1758	1896	0.06	Y
1RK91	0.01	12.2	9.0	0.87	4.0		1.95		0.32	0.15		1500	1700	0.08	Y
FerriumS53	0.20	10.0	5.5		2.0			14.0			W(1.0) V(0.3)	1517	1986	0.15	Y

TABLE 1.1. Compositions, yield strength (YS), ultimate tensile strength (UTS) and total elongation (El) of some successful grades of maraging stainless and non-stainless steels. The compositions are given in weight percent. The stainless grades are indicated by 'Y' in column 'SS'.

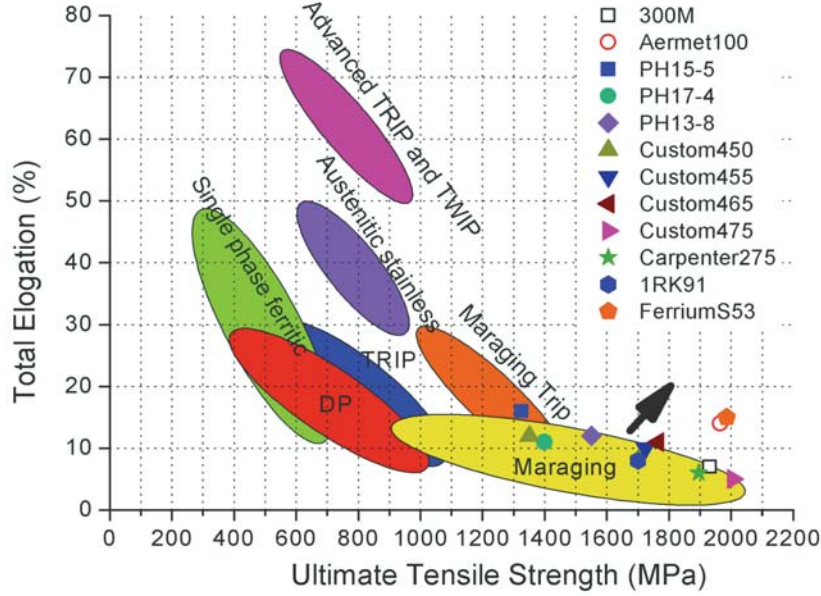


FIGURE 1.1. The strength-ductility profile of various steels. The symbols indicate the properties of existing high-end maraging steel grades [51][52][53].

many efforts for developing ultra-high strength stainless steels have been undertaken employing martensite as the matrix and further strengthening by various precipitates, while a high Cr content is imposed to ensure corrosion resistance. Some successful grades of those maraging stainless steels are shown in Table 1.1. Notwithstanding the efforts to develop high strength and high ductility stainless steels, Table 1.1 shows that none of the stainless steels meets the properties of their non-stainless counterparts in terms of strength and ductility.

1.2 Alloy Design Approach

Traditionally, new alloys have been developed through an empirical ‘trial-and-error’ approach, which is based on systematic experimental investigations. This semi-empirical approach is very dependent on intuition, experience and, to some extent, fortune. Depending on the matrix type and the strengthening system, modern high-end UHS steels possess intentionally, and with specified amounts, a range of elements such as C, Cr, Ni, Al, Ti, Mo, V, Mn, Nb, Co, Cu, W, Si, B and N in wide ranges of concentrations. The interactions of alloying elements display complex cross effects, obscuring the effects of individual elements. To understand the competition, conflict and synergy among various alloying elements experimentally, it would be necessary to systematically produce a large number of alloys with dif-

ferent compositions. Apart from the alloy composition, the heat treatment plays a paramount role on determining mechanical properties as well. After producing trial alloys, processing parameters need to be optimised via a tremendous amount of experimental work so as to achieve the best mechanical properties. Therefore, the conventional trial-and-error approach has been recognised as low success rate, very costly and time consuming.

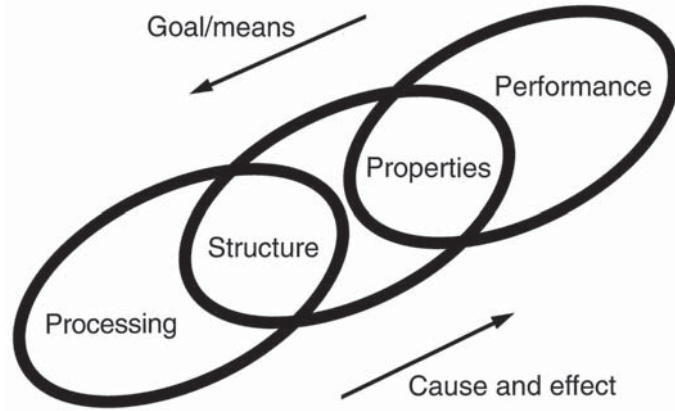


FIGURE 1.2. Chain model of the materials design methodology

With the improved understanding of processing / structure / property / performance relationships, and with the advent of more powerful and reliable computer hard- and software, alloy design philosophies are now increasingly oriented in the goal/means direction as demonstrated by the chain design model in Figure 1.2 [54]. The goal/means oriented alloy design approach starts with defining the target properties required by the applications. This first link shown in Figure 1.2 is mainly based on mechanical engineering. In the second step, the target microstructures are subsequently designed to obtain the desired properties, according to metallurgical and mechanical principles. The last link, attaining the tailored microstructures, is the key and most sophisticated process in the goal/means alloy design strategy. The alloy composition and/or heat treatment parameters are designed and optimised, employing various approaches, so as to obtain the desired microstructures.

Following fully or partially the goal/means oriented alloy design methodology, computational methods of different types have become a more efficient and powerful tool in providing guidance for designing new alloys as well as for process development [55][56][57]. Thermodynamics aided design approaches have been applied, in different degrees, to various systems such as Fe-Ni-Co [58], Al-Ti-V-Zr [59], Sn-Bi-In-Zn [60], Mg-Li-Al-Zn [61], Mg-Ce-Mn-Y [62], multicomponent powder metallurgy high speed steels [63], austenitic stainless steels [64] and UHS steels [65]. Another popular computational approach is artificial neural networks (ANN)

which extracts empirical trends from exploring large databases [66][67][68][69]. The neural networks are often coupled with genetic algorithms for alloy design [70][71][72] so as to fulfill the multi-objective optimisation goals. More recently, atomic level *ab initio* calculations are also applied to provide theoretical guidance in selecting and optimising composition of Ti-based alloys [73], stainless steels [74] and UHS steels [75]. With respect to the process development, the experimental approach can also be better guided by extracting information from computational thermodynamics [57][76][77] and artificial neural networks [78][64][79][80][81].

1.3 Scope and Outline of the Thesis

Inspired by the development of goal/means oriented alloy design approaches and considering the persistent demand to enhance the properties of ultra high strength stainless steels, this thesis pursues not only a general theory-guided computational alloy design methodology based on fundamental thermodynamic, mechanical and physical metallurgy principles, but also to provides prototype alloys of novel grades of ultra high strength stainless steels. It is attempted to develop the model in an integrated manner so that the alloy composition as well as the key heat treatment temperatures can be designed simultaneously. The model will be applied to design and optimise novel ultra high strength maraging stainless steel grades utilising different strengthening precipitate scenarios. Prototype alloys will be fabricated and characterised in order to validate the alloy design approach. The designed alloy will be compared to existing counterparts throughout the thesis, both computationally and experimentally. The general nature of the model enables its application in designing other alloy systems, provided the corresponding criteria are properly defined according to the target microstructures.

This thesis continues in Chapter 2 with the development of the basic alloy design approach following the goal/means oriented methodology. The desired microstructures are defined and translated into quantifiable criteria based on thermodynamic principles. The multiple criteria stemming from different aspects of desired microstructures are embedded in a genetic algorithm so as to compromise the conflicting criteria and to find the optimal alloy composition in a huge compositional domain. Four alloy design exercises of ultra high strength stainless steels utilising different strengthening precipitates are presented and the results are computationally compared to existing high end alloys. Applying physical metallurgy principles, the model is further developed in Chapter 3 to optimise the precipitation strengthening contribution, rather than the number density of precipitate particles as in Chapter 2. The exercise alloys are redesigned and compared to previous results and existing counterparts. The effects and sensitivities of variations of both alloy composition and ageing temperature are also discussed in Chapter 3.

The properties and microstructure of the first round of prototype alloys are presented in Chapter 4. Four alloy scenarios utilising different strengthening precipitates are followed. The microstructures and mechanical properties are characterised at different heat treatment stages. The shortcomings observed in the prototype alloys clearly suggest that the model focused only on the ageing treatment by assuming a fully martensitic matrix prior to ageing is not sufficient. Therefore, the entire heat treatment including homogenisation and ageing treatment are taken into account in Chapter 5. The integrated model allows the simultaneous optimisation of alloy compositions as well as heat treatment temperatures so as to achieve the desired microstructures while avoiding undesirable phases throughout the entire heat treatment. The model is used to redesign the second round of prototype alloys in Chapter 6. The prototype alloys are fabricated, heat treated and characterised by their microstructures, mechanical properties and corrosion resistance. Finally, the summary of the thesis is presented in Chapter 7.

2

The Base Computational Alloy Design Model Combining Thermodynamics and Genetic Algorithms

2.1 Introduction

In order to improve the properties of advanced ultra high strength (UHS) stainless steels used in aerospace and other demanding applications beyond their current high levels, the classical trial and error method does no longer suffice, and computational methods of different types are being increasingly used. The goal/means oriented computational alloy design approach starts with defining the target microstructures aimed at property tailoring as required by the application. Attaining the desired microstructures has to be translated into quantifiable design criteria. These are often competing and/or conflicting in the systematic optimisation process. Considering the extremely large number of compositional and thermomechanical scenarios to attain the target microstructures, the computational alloy design represents a significant challenge for developing efficient optimisation schemes. In this chapter, the basic alloy design framework will be developed following the goal/means direction step by step. The alloy composition is designed applying multiple criteria incorporating both physical principles and empirical rules. The optimal composition compromising different criteria is found by applying a genetic algorithm as the optimisation scheme. The model is as simple as possible, but still describes the physical phenomena it is aimed for.

2.2 Desirable Microstructures

2.2.1 *Matrix*

Austenitic and semi-austenitic precipitation hardening steels possess a primary austenitic microstructure at room temperature, which is retained or reversed from martensite during aging treatment. Although such alloys are strengthened by precipitation reactions taking place during aging, the crystallographic nature of the austenite intrinsically affects the flow behavior of the material [82][83]. While precipitation hardened austenite steels may achieve very high UTS values, they have quite low yield strength and therefore, are not ideal for new UHS steel design.

Alternatively, a lath martensitic microstructure can be created within the prior austenite grains by a suitable solution treatment followed by water or oil quenching. Such steels contain parallel arrays or stacks of lath-shaped crystals which provide an essential microstructural element for obtaining both high strength and toughness. The substructure of lath martensite includes a very high density of dislocations, which provide a direct strengthening contribution, as well as potential nucleation sites for a fine-scale precipitate dispersion [84][85]. A typical lath martensite structure is shown in Figure 2.1a [44]. Lath martensite has been widely accepted to be a very efficient matrix for precipitate strengthened UHS steels, and is employed and investigated in various commercial grades such as PH17-4[86][87][33][88][89][37], PH13-8 [90][91][92][47][93][94] and PH15-5 [35][34][95][96].

2.2.2 *Precipitation*

Precipitate species may potentially display the desired strengthening effect depending on the nature of precipitates and the distribution of their population in terms of size, density and spatial distribution. Obtaining the most desirable combination of these parameters strongly depends on the precipitation thermokinetics and can be tailored through alloy composition and heat treatment.

Carbon is an interstitial solute in iron and hence has a much higher mobility than substitutional solutes or iron. It is natural, therefore, that iron carbides are the first to form when the martensite matrix is tempered. M_2C is a typically a desired carbide precipitate in steels. It has a hexagonal structure and commonly precipitates as fine needles parallel to $\langle 100 \rangle_\alpha$. The orientation relationship is that of Pitsch and Schrader [97]: $\{0001\}_{M_2C} // \{011\}_\alpha$ and $\langle 11\bar{2}0 \rangle_{M_2C} // \langle 100 \rangle_\alpha$. M_2C is generally considered to nucleate on matrix dislocations and martensite lath boundaries. Its composition can vary widely and contains Mo, Cr and V in significant quantities. The characterisation of M_2C carbide and its influence on mechanical properties in various steel grades have been extensively studied

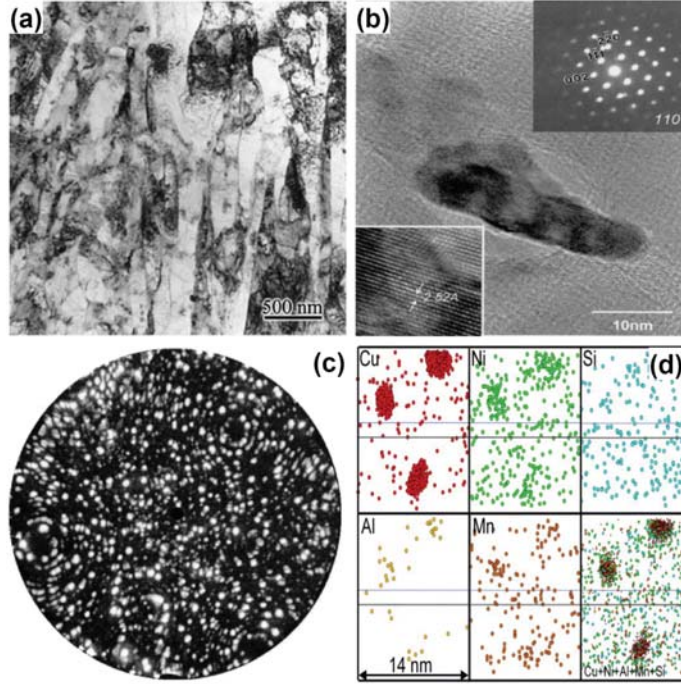


FIGURE 2.1. Examples of desirable microstructures in UHS steels: (a) high resolution TEM image of lath martensite in PH13-8 maraging steel [44], (b) TEM image of NbC carbides in HSLA steel [31], (c) FIM image of NiAl precipitates in PH13-8 maraging steel [47] and (d) APT reconstructions of Cu-rich precipitates in HSLA steel [36].

[98][99][100][101][102][103][33]. Servant *et al.* [33] studied the PH 17-4 (17Cr-4Ni-1Mo) stainless steel and found that various carbides (TiC , Mo_2C , M_{23}C_6 and M_7C_3) form at different aging temperatures while a hardening peak was observed for aging close to 400 °C which is related to the Mo_2C carbide precipitation. However, the presence of Mo is also frequently accompanied by the precipitation of undesirable intermetallic compounds such as Fe_2Mo (Laves phase). Dawood *et al.* [100][101] studied a similar system 16Cr-5Ni-1Mo, and concluded that aging at 475 °C results in Mo_2C precipitation, aging at 625 °C leads to Fe_2Mo while annealing at 750 °C results in Cr_{23}C_6 and TiC . The steel shows secondary hardening and a decrease in impact toughness after aging at 475 °C due to the precipitation of Mo_2C carbide. However, a good combination of strength, ductility and toughness could be achieved by aging at 550-625 °C for 4 hours. Campbell and Olson *et al.* [65][102] recently designed the UHS steel Ferrium S53 with a UTS above 1.9 GPa, in which the strength is significantly increased by the formation of coherent nano size M_2C precipitates.

MC is usually composed by Ti, V, Nb and/or W and is stable and expected even in low C grades. It has a NaCl type FCC structure displaying a Baker Nutting

orientation relationship with the martensitic matrix [104]: $\{100\}_{MC} // \{100\}_{\alpha}$ and $\langle 001 \rangle_{MC} // \langle 011 \rangle_{\alpha}$. MC particles form in a fine dispersion within the martensite laths, and it is therefore believed that they contribute significantly to the strength. They basically show two types of distribution [105][106]: (i) a coarse dispersion (1–10 μm) primary particles formed during solidification and (ii) a fine dispersion (5–500 nm) of secondary precipitates (Figure 2.1b). Under some conditions, part of the primary MC carbides can be dissolved during the solution heat treatment, and they reprecipitate as fine secondary precipitates during the aging treatment or when these materials are subjected to high-temperature applications. The MC carbide precipitation is predominantly intragranular, on dislocations and stacking faults. However, MC precipitation at grain boundaries can also occur [106]. The nucleation and growth of NbC particles at grain boundaries is favoured at extrinsic grain boundary dislocations and at grain boundary topographical defects [107][108]. Many steel grades containing MC carbides have been investigated [26][27][28][29][30][31][32][33]. For example, Klueh *et al.* [28] has studied various 9Cr-MoVNiNbN and 12Cr-MoVNiNbN steels after different thermomechanical treatments. The mechanical properties are significantly improved in some conditions due to the formation of a dense dispersion of nano-scale MC precipitates. Gavriljuk *et al.* [26] investigated the effect of C and N content on the precipitate kinetics and concluded that the partial substitution of C by N in 15Cr-1Mo steel leads to delayed MX precipitation during aging and an increase of impact toughness. Miyata *et al.* [30][31] studied the effect of composition on the coarsening kinetics of MC carbide and concluded that, at the early stages of aging, the finer MC carbide retains coherency at the interface between precipitate and matrix. The addition of V and Nb stabilise MC instead of M_2C carbide. Partitioning of V, Nb, and Mo continuously changes the MC carbide compositions and also affects the coherency and the growth rate of MC carbides.

Steel grades based on intermetallic precipitates, only contain a small amount of C in order to avoid the formation of carbides or carbonitrides. A well known example of a high strength steel based on intermetallic precipitates, PH13-8 martensitic stainless steel, contains a large amount of Ni and Al (Table 1.1); the alloy is significantly hardened by the formation of ordered β -NiAl precipitation (Figure 2.1c), having a B2 (CsCl) superlattice structure. Ping *et al.* [44] investigated the 13Cr-8Ni-2.5Mo-2Al steel system for different aging temperatures. A high number density (10^{23} to 10^{25} m^{-3}) of ultra-fine (1-6 nm) β -NiAl precipitates are formed during aging at 450-620 $^{\circ}\text{C}$, which are spherical in shape and are uniformly dispersed with full coherency with the matrix. The decrease in strength at higher temperature (above 550 $^{\circ}\text{C}$) was attributed to the decrease in the number density of the β -NiAl precipitates and the reversion of austenite, and also to the formation of larger $(\text{Cr},\text{Mo})_{23}\text{C}_6$ carbides. Erlach *et al.* [45][46] studied the precipitation in a medium carbon system 0.14C-2.6Cr-1.4Mo-6.0Ni-5.0Al, and found the alloy is strengthened by both M_2C and NiAl precipitates. The chemical evolution of the NiAl particles towards equilibrium conditions simultaneously takes place with

particle coarsening. Guo *et al.* also reported the strengthening effect from precipitates rich in Ni and Al [47]. Another very similar intermetallic strengthening precipitate is Ni_3Ti . He *et al.* recently designed a 19Ni-4Mo-2Ti maraging steel [48][49] and found that, at the peak-aged condition of 480 °C, moderately sized Ni_3Ti precipitates distribute uniformly in the martensite matrix, leading to an optimal combination of yield strength of 2000 MPa and a good fracture toughness. The orientation relationship between Ni_3Ti and martensite was observed as $\{0001\}_{\text{Ni}_3\text{Ti}}//\{011\}_{\alpha}$ and $\langle 11\bar{2}0 \rangle_{\text{Ni}_3\text{Ti}}//\langle 111 \rangle_{\alpha}$. In a similar system, 18Ni-4Mo-2.5Ti [50], it was observed that the yield strength even reaches 2.3-2.4 GPa after aging at 440-540 °C, owing to the strengthening contribution of Ni_3Ti precipitates. Van der Walker *et al.* [43] also reported Ni_3Ti precipitate may form and contribute to strength in the the reversed austenite matrix in a 18.5Ni-3Mo-1.5Ti system.

The microstructure development in commercial PH15-5 stainless steel (Table 1.1) after different heat treatments has been studied by Habibi-Bajguirani *et al.* [34][35]. Two stages of hardening have been identified which are associated to the formation of two types of Cu precipitates. Age hardening of PH15-5 initially undergoes the formation of Cu clusters displaying a BCC structure at 450 °C, which further transforms to 9R (at 4 nm), 3R (at 15 nm) and then to FCC precipitates upon further aging. The second stage of hardening at higher ageing temperature (650-700 °C) is associated with the formation of another type of Cu precipitates with spherical shapes. Experimental data shows them to be coherent with the matrix initially, and later becoming semi-coherent on further aging. Isheim *et al.* [36] also reported that a high number density (10^{24} m^{-3}) of Cu rich precipitates are found after aging at 490 °C for 100 minutes in a metastable α -Fe matrix instead of martensite and this leads to near-peak hardness (Figure 2.1d). Yoo *et al.* [37] report that in a PH17-4 steel, FCC Cu-rich particles may precipitate in the δ -ferrite during long-term aging at 400 °C. The hardness and yield strength increase while elongation decreases dramatically caused partially by the nucleation and growth of Cu precipitates in δ -ferrite. Stiller *et al.* [38][39][40][41][42] studied the precipitation sequence in Nanoflex 1RK91 (12Cr-9Ni-4Mo-2Cu) maraging stainless steel. The investigation showed that, on aging at 475 °C, Cu is the element which precipitates only after a few minutes, the fine Cu particles act as nuclei for $\text{Ni}_3(\text{Ti},\text{Al})$ precipitates. After 2 hours of aging, Cu and Ni rich phases are well separated, coarsening of Ni_3Ti precipitates are observed and large Ni/Ti rich and Cu rich particles are found in the lath boundaries. The Ni and Cu rich precipitates play the most important role for the strength increment up to about 4 hours. The Mo rich precipitate and R' phase appear and become more important in prolonged aging. Apart from high alloy steels, Cu enriched precipitate is also reported in different High Strength Low Alloy (HSLA) steels [109][110].

In addition to the homogenous intragranular strengthening precipitates forming within the lath martensite matrix, the formation of intergranular precipitates such

as MX carbides (Ti,Nb,V)(C,N) along prior austenitic grain boundaries during the solution treatment is also desired. Their pinning effect will retard the growth of austenite grains and therefore increase the toughness and decrease the ductile brittle transition temperature.

While fostering the formation of desirable precipitates (carbides or intermetallics) as described above, the formation of phases limiting strength or toughness (e.g. $M_{23}C_6$, M_6C and M_7C_3 , cementite, μ phases, χ phases) should be prevented. Once it is thermodynamically ensured that only the desired precipitates can form and undesirable precipitates are thermodynamically unstable, it is necessary to control microstructural aspects of the desired precipitates such as their size, size distribution, location, morphology and coherency. For a given total fraction of precipitates, fine-scale precipitates result in a low interparticle spacing, which displays an increase in strengthening effects [111]. Therefore, the desired ultra high strength is promoted by the refinement of precipitate dispersions down to the nanometre level, usually in the range of 10 nm in size [112]. For this reason, precipitate nucleation, rather than precipitate growth, plays dominant role in attaining the desired nanostructures.

2.2.3 Corrosion Resistance

Corrosion resistance in stainless steels is due to the formation of a Cr-rich oxide passive film on the external surface. Such a film is primarily composed of M_2O_3 and M_3O_4 ($M = Cr, Fe, Ni$) oxides; the formation and stability of the film are governed by the amount of Cr partitioning to the film. Kirchhem and co-workers [113] have experimentally studied the formation of this film on Fe-Cr alloys and shown that the Cr concentration in the oxide film is logarithmically dependent on the matrix Cr concentration. Various experimental studies have shown that the retained Cr concentration in the matrix needs to be larger than 12% in weight for obtaining corrosion resistance at room temperature and non-extreme conditions [114].

It is worth noting that the formation of precipitates in the range of a few nanometres does not jeopardise corrosion resistance: at such length scale, the passive oxide film size approaches that of the strengthening particles, so the precipitates do not significantly limit the film formation.

2.2.4 Heat Treatment

The microstructures of the UHS stainless steels described above can be obtained by a sequence of heat treatments consisting of solution treatment (austenisation), quenching and ageing. The heat treatment is schematically shown in Figure 2.2:

1. The as-rolled materials is firstly solution treated at austenisation temperature typically in the range of 1273-1473 K. This process is aimed at austenising the matrix, dissolving the precipitates formed in previous treatments and homogenising the solute atoms in the matrix.
2. The austenitic matrix transforms to martensite upon quenching and its morphology depends on the quench media and, more importantly, the Martensite Start (M_s) temperature.
3. In order to further increase the strength, the material is subjected to the ageing treatment around 773 K for stimulating the formation of various desirable precipitates depending on the alloy composition. The ageing treatment time may vary from seconds to days and finally it is cooled down to room temperature.

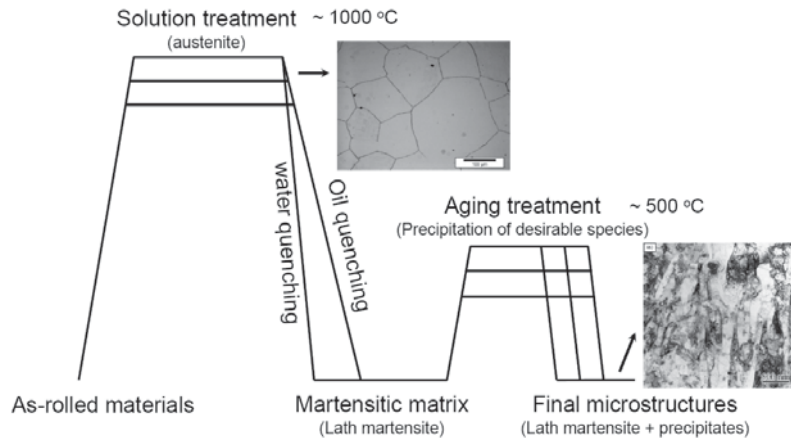


FIGURE 2.2. A schematic diagram of heat treatment for maraging steels

In practice the proper austenisation conditions define both the austenisation temperature and time. In order to obtain a fully austenitic matrix, the austenisation temperature should be above A_3 temperature and above the dissolution temperature of any prior precipitate phases presented, but as low as possible to prevent significant grain growth and oxidation. The austenisation time should be kept as short as possible for commercial reasons. In the model, it is assumed that there are always austenisation conditions to be found which yield the ideal homogeneous starting state. With respect to the martensitic transformation, the quenching condition and hardenability determine whether a full martensitic structure is obtained, as will be explained in more detail in section 2.3. The optimal ageing conditions (temperature and time) are determined by the nature of strengthening precipitates and they are mostly optimised by systematic experiments. In modelling the formation of desirable precipitates, a fixed aging temperature of 773 K

was imposed. This temperature is chosen because, for commercial alloys containing the same precipitate species, maximum strength is attained for aging temperatures within the range of 755-797 K [51].

2.3 Quantification of Microstructural Criteria

In this paragraph we will explain the quantification of the desired microstructural parameters in detail.

2.3.1 *Ms Temperature*

The ability to form a fine scale lath martensite upon quenching to room temperature depends on the Martensitic start temperature (M_s), which itself is primarily composition dependent. Experimental observations on regular engineering steels have shown that an M_s temperature above 150 °C is required to obtain a lath microstructure when quenching to room temperature from the solution treatment temperature [115][65]. As C concentration increases, the fraction of retained austenite increases and the lath microstructure coarsens to a plate-like morphology.

Since the 1940's, many empirical relationships to estimate the martensite start temperature (M_s) from composition have been produced [116][117][118][119][120]. Most of them were, however, limited to narrow ranges of alloying elements and compositions. Later, thermodynamics based models have been developed [121][122][123] in which the driving force for martensite transformation is calculated accounting for magnetic contributions to the Gibbs free energy, covering a wide range of alloying elements and temperatures. More recently, Ishida [124] extended the model to predict the effects of alloying elements on the M_s temperature due to both chemical and mechanical contributions. In his model, magnetic and non-magnetic contributions to the Gibbs energy constitute the chemical part, while the mechanical effect stems from the frictional forces required for moving the dislocations accompanying the transformation. A composition dependent equation was postulated for estimating the M_s temperature, and applied to alloy steel systems of up to 11 components, showing good agreement with experimental observations:

$$\begin{aligned}
 M_s(^{\circ}C) = & 545 - 33000 \times C_c + 200 \times C_{Al} + 700 \times C_{Co} - 1400 \times C_{Cr} \\
 & - 1300 \times C_{Cu} - 2300 \times C_{Mn} - 500 \times C_{Mo} - 400 \times C_{Nb} \\
 & - 1300 \times C_{Ni} - 700 \times C_{Si} + 300 \times C_{Ti} + 400 \times C_V
 \end{aligned} \tag{2.1}$$

where all the concentrations are given in weight fraction.

Ghosh and Olson [125] developed a physically-based model for martensite formation which contains the critical driving force for heterogeneous martensitic nucleation in multicomponent alloys in terms of the competition between the lattice strain energy, the nucleation defect size dependent interfacial energy term, the frictional forces required for dislocation motion and a composition dependent chemical free energy contribution. The M_s temperature was predicted in combination with a well known and validated thermodynamic calculation via ThermoCalc [126]. Martensite is supposed to form at the temperature at which the thermodynamic driving force equals the critical driving force obtained from the model.

Despite the simplicity of equation 2.1, it accounts for a wide range of components and has been successfully applied to various systems. Comparing it to the computationally expensive Ghosh and Olson's model, Ishida's equation was chosen to be used in this work for calculating the M_s temperature. A go/no-go criterion of $M_s \geq 200$ °C was imposed in the alloy optimisation procedure, and the alloy composition was taken as input to equation 2.1.

2.3.2 Precipitation

Alloy strengthening is achieved by ensuring a homogenous finely dispersed distribution of precipitates of MC carbides, NiAl/Ni₃Ti intermetallics and/or Cu-rich particles. Precipitate growth and coarsening should be prevented and the nucleation conditions should be chosen such that fine precipitates close to their nucleation stage become quickly stable. Furthermore, the system should reach equilibrium before the precipitates grow significantly by rapidly consuming most of the solute available from the matrix.

The classical nucleation rate is expressed as [127]

$$I = \frac{dN}{dt} = N_0 \frac{kT}{h} \exp\left[\frac{-(G^* + Q^*)}{kT}\right] \quad (2.2)$$

where N_0 is the initial density of nucleation sites, Q^* is the activation energy for the transfer of atoms across the interface, k is the Boltzmann constant, h is the Planck's constant and G^* is the free energy required to overcome the barrier for nucleation.

The activation energy G^* for a spherical nucleus is given by

$$G^* = \frac{16\pi}{3} \frac{\sigma^3}{\Delta G_v^2} \quad (2.3)$$

where σ is the precipitate/matrix interfacial energy per unit area and ΔG_v is the precipitation driving force per unit volume.

From equation 2.2, it is clear that the nucleation rate can be increased either by raising the number of potential nucleation sites N_0 or the driving force ΔG_v . Given that the lath martensite matrix provides already a high density of dislocations capable of promoting nucleation, the optimisation effort is focused on maximising the driving force for precipitation.

The critical radius for nucleation of a spherical particle can be estimated as:

$$r^* = -\frac{2\sigma}{\Delta G_v} \quad (2.4)$$

Similar equations apply to precipitates of other geometries. Equation 2.4 indicates that the size of the stable nucleus, *i.e.* the initial size of the precipitate, decreases with increasing the driving force ΔG_v .

In addition to the nucleation rate and the particle size, the number density of particles also controls the strengthening contribution [128]. Given the precipitate size is in the range of a few nanometres, the particles nearly stay at their nucleation size as the volume fraction approaches equilibrium. Following this assumption, the total number of precipitate particles can be as approximated by

$$NPP = \frac{VF}{\frac{4}{3}\pi(r^*)^3} \quad (2.5)$$

where VF is the equilibrium volume fraction of the precipitate. The interfacial energy σ is always taken as 1 J/m² for different precipitates. The molar volumes of different precipitate species are difficult to estimate and therefore, the precipitate volume fraction VF , instead of real precipitate volume is used to calculate the precipitate particle number NPP . NPP should be taken as an adimensional relative value.

The thermodynamic calculations were performed with ThermoCalc software coupled to a modified version of the TCFE3 [129] steel database. From this database and software, the volume fraction and composition of the equilibrium phases, as well as the driving force for the formation of the precipitate phases (assuming a BCC matrix for the martensite) were extracted. The number of precipitate particles (NPP) (equation 2.5) was used as one of the optimisation indices. In performing the calculation, the NPP of the desirable species was maximised, whereas those of undesired precipitates were suppressed by making sure that their driving force for formation was positive. For undesirable phases which could not be completely avoided, a total maximum volume fraction of 1% was allowed.

2.3.3 Cr Concentration in the Matrix

The formation of a Cr-rich passive oxide film at the surface requires a reservoir of at least 12 wt% Cr in the matrix. This was enforced by requiring such a minimum Cr level in the matrix upon completion of the precipitation reactions.

2.4 Desired Alloy System and Compositional Constraints

Throughout the years, a large number of elements have been added into various steel families so as to change, often dramatically, the properties and characteristics of the alloys such as strength, ductility, toughness, corrosion resistance and others. Various binary and ternary systems have been intensively studied over centuries and this led to a comprehensive understanding of not only their alloying effects but also of the various mechanisms behind them. However, in multicomponent systems, the overall alloying effects are no longer straightforward because they display very complicated cross effects, often conflictive. Nevertheless, the generic alloying effects may remain efficient in very complex systems depending on other component species, concentrations and their interactions. In this section, the expected effects of alloying elements involved in the calculations are briefly discussed. The composition ranges of various elements are also given considering the thermodynamic database availability and practical constraints on alloy fabrication.

C is a key element to be incorporated in the alloy. Its versatile and cheap carbide forming capabilities may be exploited for strengthening purposes. MC is a desirable phase due to its hardening and grain refining (pinning) effects. Nevertheless, an excess of C strongly lowers the Ms temperature and may foster the formation of various undesirable carbides. In the present case, a C concentration range of 0.05-0.2 wt% was imposed. Cr is of paramount importance for obtaining corrosion resistance by forming the oxide film. It may also take part in the precipitation process. To ensure enough Cr content to be present in the matrix, the Cr range is set to 12.0-20.0 wt%.

Ti, Mo, Nb and V act as carbide formers. They stabilise MC carbides and therefore suppress other undesirable precipitates such as $M_{23}C_6$, M_7C_3 and cementite [130][131][132][133]. However, while they increase the driving force for the formation of MC carbides, they may promote microsegregation during solidification and also stimulate formation of undesirable phases such as Fe_2Mo . Ti and V increase the Ms temperature while Mo and Nb decrease it. Considering industrial constraints and price, the ranges considered for these components are 0.01-1.5 wt% Ti, 0.5-10.0 wt% Mo, 0.01-0.1 wt% Nb and 0.01-0.2 wt% V, respectively.

Ni and Al are essential for the formation of NiAl and Ni_3Ti desired intermetallics. Al increases the Ms temperature but Ni decreases it significantly. Cu nanoprecipitates strengthen the alloy and also stimulate the formation of NiAl and Ni_3Ti intermetallic precipitates. Cobalt is also an important element in martensitic stainless steels because it catalyses carbide precipitation during aging by increasing the thermodynamic driving force for the formation of precipitates [134], and by retarding dislocation recovery which promotes heterogeneous nucleation of carbides on dislocations [131]. On the downside, Cobalt is a very expensive alloying element and its content should be minimised. For these reasons, element concentration ranges of 1.0-15.0 wt% Ni, 0.01-1.0 wt% Al, 0.5-10 wt% Cu and 0.01-2.0 wt% Co were imposed.

N, Si and Mn are components whose presence cannot be neglected in steels. N forms carbonitrides. while Si and Mn also partition in various precipitates and solid solution. The concentrations of N and Mn are set at 0.01 wt% and 0.5 wt%, respectively; Si was allowed to vary from 0.3-1.0 wt%.

In summary, the alloy system considered in the calculations is based on 13 alloying elements: C-Cr-Ni-Ti-Mo-Al-Cu-Co-Nb-N-V-Mn-Si. The concentration ranges employed for each element in the optimisation procedure are summarised in Table 2.1. It is very important to notice that the several alloying elements may have conflicting interactions as to the desired microstructures. For example, Ti is a major carbide former while it is also required for forming Ni_3Ti . Similarly, Al pairs with Ni to form NiAl, which conflicts with the formation of Ni_3Ti . Higher Cr concentration is preferred for corrosion resistance, but Cr decreases the martensite Ms temperature significantly and, in turn, limits the solubility of other desired alloying elements such as Ni, Mo and Nb. In general, the alloy composition optimisation has to systematically balance the amount of different alloying elements, find a compromise between the positive and negative effects of each component, and evaluate their influences on forming the desirable microstructures while suppressing those known to be undesirable. The model employed here scans the full composition ranges of Table 2.1, employing the searching criteria to be presented next.

2.5 Calculation and Algorithms

2.5.1 General Algorithm

Except for alloying elements N and Mn, the concentrations of all other components are varied within a certain range (Table 2.1). The candidate solutions are obtained by analysing all potential compositions sampling the concentration range of each of the 11 remaining alloying elements. If the components are allowed to take 32

	C	Cr	Ni	Ti	Mo	Al	Cu	Co	Nb	N	V	Mn	Si
Min	0.05	12.00	1.00	0.01	0.50	0.01	0.50	0.01	0.01	0.01	0.01	0.50	0.30
Max	0.20	20.00	15.00	1.50	10.0	1.00	10.00	2.00	0.10	0.01	0.20	0.50	1.00

TABLE 2.1. Concentration ranges of all components employed in the optimisation (wt%).

	C	Cr	Ni	Ti	Mo	Al	Cu	Co	Nb	N	V	Mn	Si	NPP	MS (K)	VF	CCr
Alloy1	0.20	12.00	4.16	1.50	0.50	0.01	3.87	2.00	0.10	0.01	0.01	0.50	1.00	15.26	201.64	0.0000	13.00
Alloy2	0.07	12.00	1.00	0.15	0.50	0.01	10.00	1.04	0.01	0.01	0.20	0.50	1.00	4.16	200.20	0.0082	12.94
Alloy3	0.05	15.61	7.77	1.50	0.50	1.00	0.50	2.00	0.10	0.01	0.20	0.50	1.00	0.37	202.25	0.0057	15.65
Alloy4	0.20	12.00	2.36	1.45	0.50	0.01	5.10	2.00	0.10	0.01	0.01	0.50	1.00	16.80	211.14	0.0088	13.08

TABLE 2.2. Composition, number of precipitate particles (NPP), Ms temperature (Ms), total volume fraction of undesirable phases (VF) and Cr concentration in the matrix (C_{Cr}) of designed Alloy 1-4. Concentrations are in wt%.

potential concentration levels by equally dividing their composition range (Table 2.1), the solution space contains 32^{11} or 4×10^{16} options. For those candidate solutions, the following algorithm (Figure 2.3) is applied for evaluating the criteria described in previous section:

1. The system is defined in ThermoCalc and the relevant thermodynamic information is retrieved from a modified version of the steel database TCFE3. The tempering temperature is set at a fixed value of 500 °C.
2. Using the concentration of a candidate alloy, the Ms temperature is calculated from equation 2.1.
3. A thermodynamic equilibrium calculation at the precipitation temperature is performed. All equilibrium phases are identified; their volume fractions and compositions are recorded. The total volume fraction of undesirable phases is summed up and the Cr concentration in the matrix (Fe-rich BCC phase) is recorded. The candidate alloy is discarded if the total volume fraction of the undesired phases exceeds 0.01 or if the Cr matrix concentration is lower than 12 wt%.
4. The Fe-rich BCC phase is set as matrix and the precipitate driving forces are calculated through a second equilibrium calculation by changing their status as dormant.
5. The number of precipitate particles (NPP) is calculated from equation 2.5 based on the volume fractions obtained in step 3 and the driving forces from step 4.

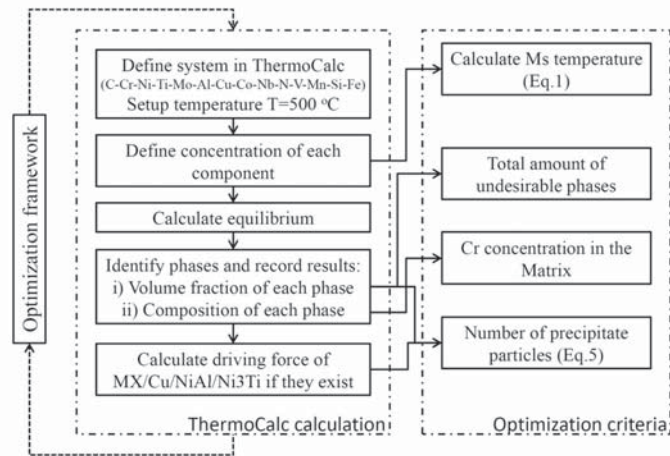


FIGURE 2.3. General algorithm of the thermodynamic calculation and criteria evaluation

2.5.2 Optimisation Scheme: Genetic Algorithm

To scan the enormous solution space of $\sim 10^{16}$ candidate alloys, a suitable optimisation algorithm is essential. Genetic Algorithms (GAs) [135] are recognised as a powerful strategy for multi-parameter multi-objective optimisation, especially for those having very complex expression or implicit criteria. GAs are different from traditional search methods in several ways: 1) GAs are inspired by evolutionary processes in natural systems by following the survival of the fittest principle. Individuals producing potential solutions evolve towards a better solution. GAs employ populations of solutions rather than a single solution so as to avoid a local (other than a global) optimum. 2) The initial population is randomly generated and therefore an initial input in the proximity of the optimum is not required. The optimisation result is not determined by the initial input. 3) GAs work with discontinuous or implicit objective functions. Derivatives are not computed. 4) The heuristic evolution is controlled by probabilistic operators such as selection, crossover, and mutation rather than deterministic functions. 5) They work with representations of candidate solutions such as binary strings of 0s and 1s (called chromosomes) rather than the parameter set (alloy composition). 6) They deal with multi-objective optimisation problems in a natural way through a fitness function which reflects their necessity and priority. These especial features of the GAs make them the favorite optimisation technique for the composition optimisation problem addressed here.

To this aim a master-slave FORTRAN program where the master role is taken by the genetic algorithm, and the slave routine performs the calculation of the thermodynamic parameters and assesses the evolution criteria (Figure 2.3) was developed. Each candidate solution is coded as a binary string (chromosome) by concatenating the concentration of each element expressed in base-2 (genes), as demonstrated in Figure 2.4. In order to get the desirable accuracy in the alloy composition, 5 binary bits are linked to each component wherein 00000 stands for the minimum concentration and 11111 refers to the upper boundary as given in Table 2.1. In this way, there are $2^5=32$ candidate concentrations for each component distributed equally between the concentration limits of each element and represented by 5 bits. Thus, each potential composition set is represented by a binary string of $11 \times 5 = 55$ bits.

The evolution algorithm is shown in Figure 2.5. The computations start with a randomly generated population of individuals and the iteration proceeds in generations. An initial population of ten individuals was generated to represent the diversity following the Micro-GA technique [136]. This method significantly reduces the number of individuals required to be evaluated in each generation. The fitness is evaluated after transforming back to base-10 composition sets which are employed as input for the thermodynamic calculations. For each generation, a fraction of the existing population with a higher fitness score is likely to be selected to

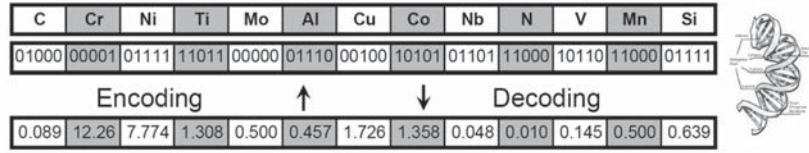


FIGURE 2.4. Schematic representation of compositional chromosome concatenated by 11 concentration genes

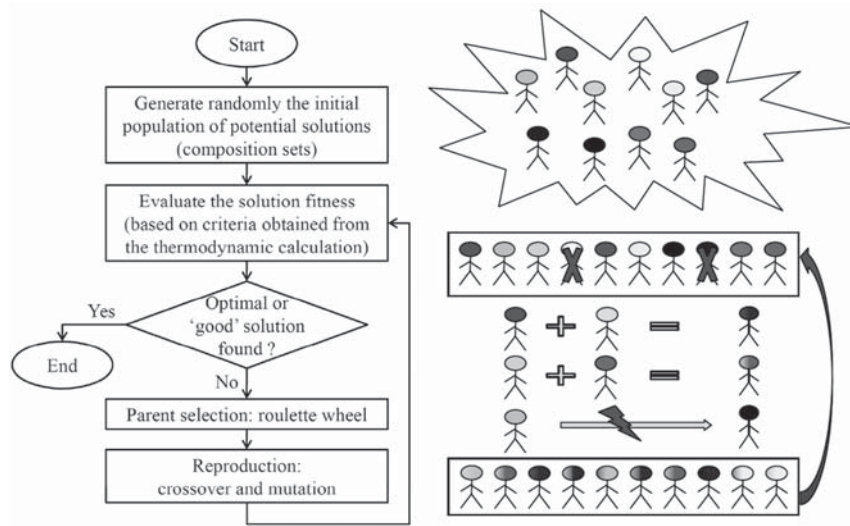


FIGURE 2.5. Flowchart of genetic algorithm

contribute to the next generation. The roulette wheel selection process is applied wherein each chromosome is assigned with a probability of reproduction so that its likelihood of being selected is proportional to its fitness relative to other chromosomes in the population. Afterwards, chromosomes selected for reproduction are copied and entered into the mating pool for performing crossover and mutation. The crossover operation is a procedure in which the selected parents create offsprings by breaking their chromosomes at certain points and exchanging genetic code, as demonstrated in Figure 2.6. This is an operation of inheriting information from previous generations and meanwhile keeping diversity. The uniform crossover method [137] is used in this work. Mutation originates from natural evolution. This operation simply changes one or more bits in the binary expression of the chromosome, from 0 to 1 or vice versa. The mechanisms of crossover and mutation are schematically shown in Figure 2.6. Although reproduction and crossover operations effectively select the fittest populations, mutation provides a mechanism for introducing new features into subsequent generations, and thus avoids local optimisation by preventing the subsequent populations from becoming too similar

to each other, which may slow or even stop evolution. The new population is then used in the next iteration of the algorithm and the generational cycle continues until a desired termination criterion is reached.

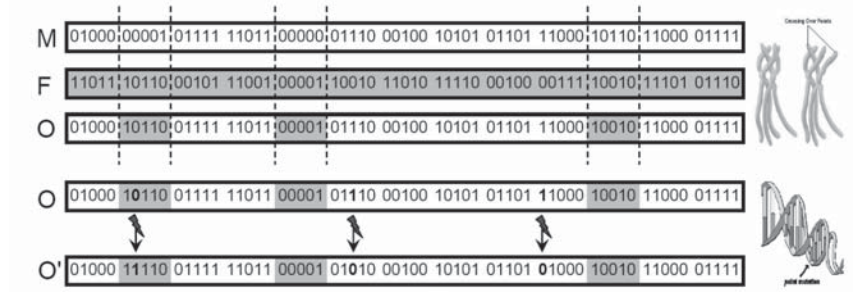


FIGURE 2.6. Representation of mechanism of crossover and mutation. M stands for male parent, F stands for female parent, O stands for offspring, O' stands for offspring with mutation.

2.6 Results

The computations were performed on a Dell precision 380 dual-core workstation. Four alloy scenarios for four different strengthening systems were considered. The number of precipitate particles (*NPP*) was maximised employing equation 2.5 for alloys containing: 1) MC carbides, 2) Cu particles, 3) Ni-rich particles (NiAl and Ni₃Ti) and 4) all previous precipitates added together. The results are summarised in Table 2.2. The *NPP* for each alloy is plotted in Figure 2.7a. The corresponding driving forces and volume fractions are shown in Figure 2.7b and 2.7c, respectively. Calculations of the type presented here typically took 48 to 72 hours on the specified hardware.

The effects of each alloying element on precipitation are studied for Alloy 1 (see Table 2.2) by varying its optimised composition over an extended range. The results are shown in Figure 2.8. The unslashed area in each plot shows the concentration ranges within which the optimisation is preformed for each element; in each of these plots, the optimum concentration for the other elements remains constant. For the calculations presented in Figure 2.8, the critical three initial conditions related to *Ms*, *VF* of undesirable precipitates and $C_{Cr}^{matrix} > 12 \text{ wt}\%$ are imposed. The value that maximises the *NPP* within the search range is marked by an arrow.

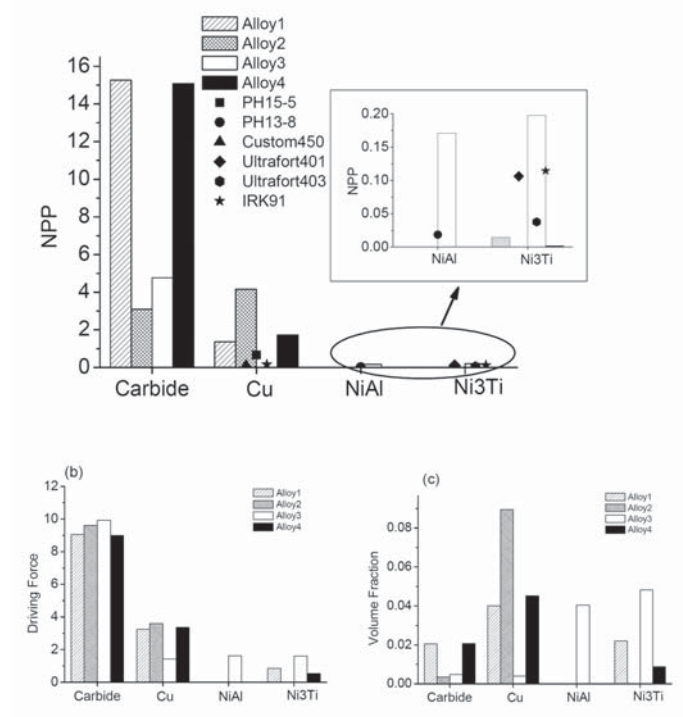


FIGURE 2.7. Comparison of designed Alloys: a) number of precipitate particles (NPP), b) driving force for precipitation, and c) volume fraction

2.7 Discussion

2.7.1 Effects of Individual Components in the Model Alloys

From Figure 2.7, it can be observed that in Alloy 1, the maximum *NPP* of MC carbide is achieved along with a significant amount of Cu precipitates and a very small amount of Ni₃Ti. C, Ti and Nb are carbide formers and take their allowed maximum concentrations. Another carbide former, Mo, takes its minimum value because it strongly decreases the *Ms* temperature. The MC carbide coexists with Cu particles, and therefore the Cu concentration takes a middle value within its permitted range. On the other hand, Al takes a minimum value to suppress the formation of NiAl. In spite of the fact that Ni decreases the *Ms* temperature, and combines with Ti to form Ni₃Ti, preventing the formation of TiC, it takes a value higher than its minimum allowance so as to prevent the formation of undesirable phases as indicated in Figure 2.8. The elemental analysis of concentration levels just presented demonstrates the complex interactions occurring between the 11 varying components of this system.

In Alloy 2, Cu particles were selected as the most important contribution to precipitate strengthening. Similar to Alloy 1, Alloy 2 has a significant *NPP* of MC

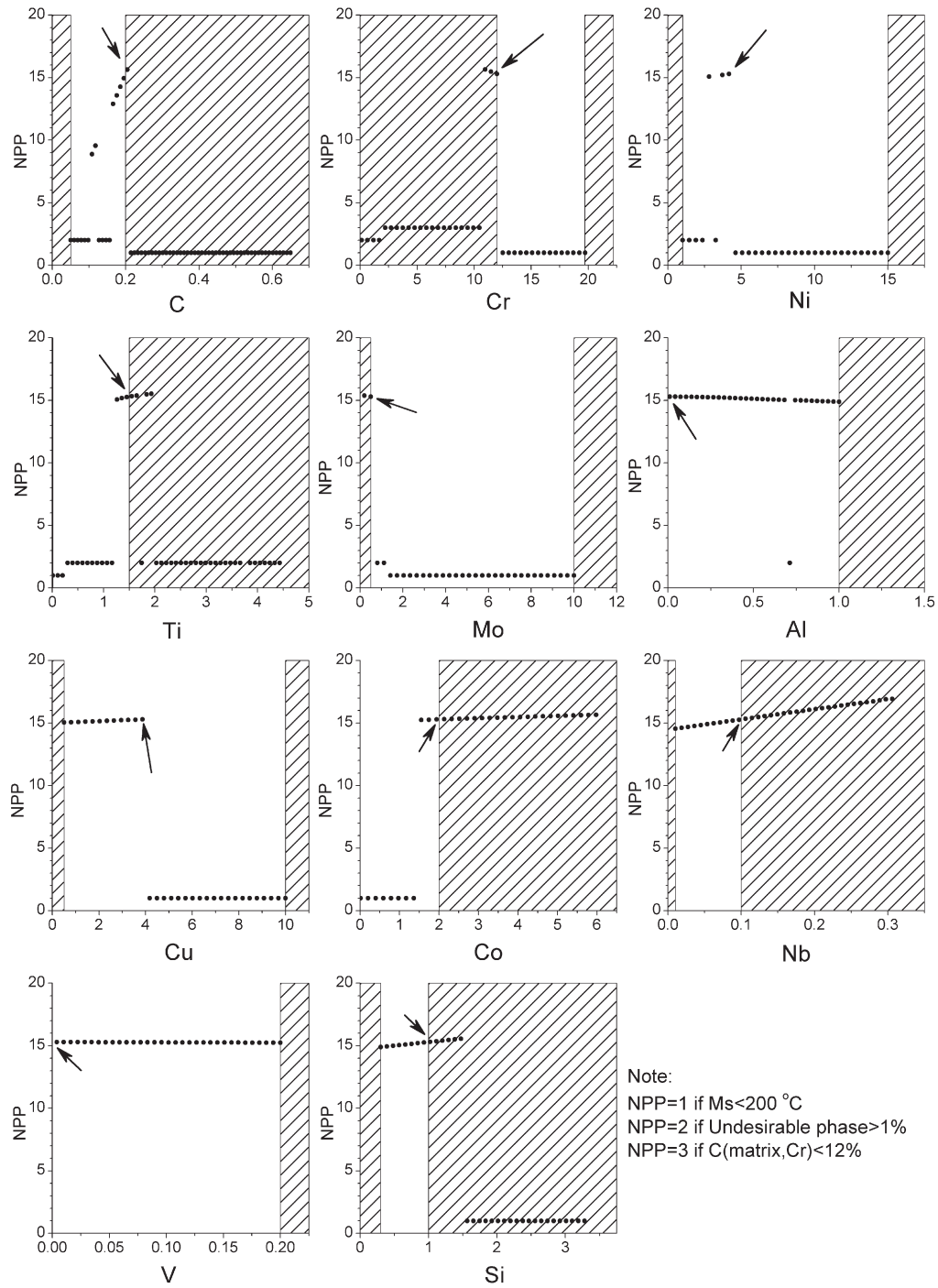


FIGURE 2.8. Effects of each component concentration on number of precipitate particles for Alloy 1. The concentrations are in weight percent.

carbide. The presence of Ni_3Ti or NiAl precipitates is not predicted. The Cu level is at its maximum value and C, Ni, Al and Ti levels are at minimum values.

In Alloy 3, which maximises the *NPP* of Ni rich, or intermetallic strengthening particles, similar values for *NPP* of NiAl and Ni_3Ti are obtained. A significant amount of additional MC carbides is found. The fact that similar population values for Ni_3Ti and NiAl (Figure 2.7a) are obtained stems from the fact that their thermodynamic stabilities (Figure 2.7b) and equilibrium volume fractions (Figure 2.74c) are comparable. From a thermodynamic perspective, the formation of Ni-based precipitates is in conflict with that of Cu particles, so the amount of the latter element is at its minimum level. Ti and Al take their maximum level to promote the formation of NiAl and Ni_3Ti ; C takes a minimum value to suppress MC carbide precipitation which consumes Ti. Ni takes a medium value for balancing other criteria.

The *NPP* of MC carbides and Cu particles can reach a much higher level compared to the Ni family precipitates. Therefore, when optimising for the total number of precipitate particles for all species, the resulting alloy is dominated by MC and partially by Cu. Therefore, Alloy 4 appears to be quite similar to Alloy 1 in terms of composition and precipitate configuration. The reason why the absolute value of the *NPP* of MC and Cu is largest is because it is proportional to the volume fraction and the cube of the driving force (equation 2.3-2.5). Figure 2.7b reveals a much better thermostability of MC as compared to Cu particles, and especially to the Ni family of precipitates.

2.7.2 Comparison of the Different Optimisation Methods

In addition to the described genetic algorithm, two additional optimisation schemes were explored, herewith referred to as the Combinatorial Algorithm (CA) and the Periodic Iterative Algorithm (PIA). The CA tries all the candidate alloys through their composition space and finds the best one according to the same criteria followed by the genetic algorithm. Its computational cost is very sensitive to the resolution of each elemental composition variable, because it increases exponentially with the number of potential values of each variable dimension. Therefore in this comparison only three possible concentrations were considered for each component: the minimum and maximum value given in Table 2.1 for each component and their average. Hence, the total number of potential compositions is only 3^{11} (1.7×10^6). The thermodynamic calculations described in Figure 2.3 were performed for each composition. The computation takes about 1 week, and its results are compared to the genetic algorithm in Figure 2.9.

The periodic iterative algorithm (PIA) was explored in order to have a finer concentration resolution. In this approach, the calculation starts with a given reference composition. A linear search is successively performed for each additional

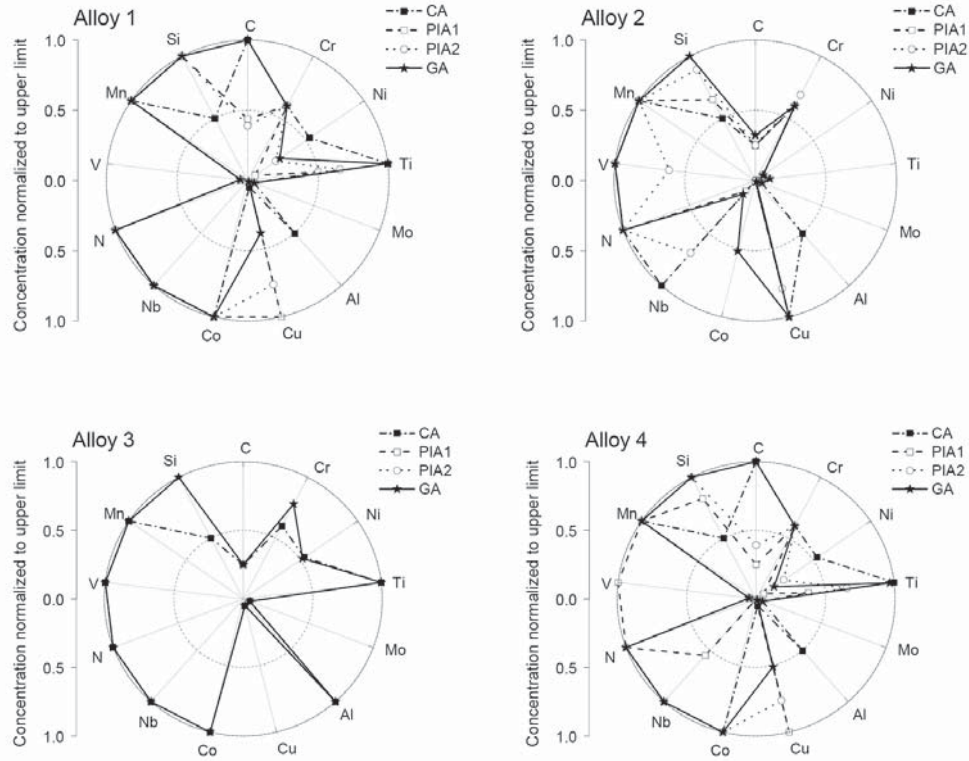


FIGURE 2.9. Optimal compositions of Alloy 1-4 via different optimisation algorithms: combinatorial approach (CA), periodic iterative algorithm (PIA) and genetic algorithm (GA)

element and the best concentration is obtained; the transient optimal composition is updated component by component until there is no change for all elements and the solution converges. The same resolution employed in the genetic algorithm was followed (32 potential values per component).

Because the PIA requires an initial composition, the computations were started from the minimum concentration values of the search range, following the order of C-Cr-Ni-Ti-Mo-Al-Cu-Co-Nb-N-V-Mn-Si (PIA1). Results for alloys optimised to MC carbides, Cu precipitates and the total precipitate densities were obtained and are shown in Figure 2.9; no result could be obtained for alloys based on the Ni intermetallic precipitates family. In order to check the consistency of the solution, optimisations starting from the upper boundary and middle value for all components are performed, but no results were found because the M_s temperature remained above 200 °C. A final calculation (PIA2) was performed starting with the lower boundaries as previously, but following an opposite sequence in the elements:

starting from Si and ending up with C. Again no results were found again for alloys based on Ni family intermetallic precipitate strengthening. The results for the other alloy optimisation criteria are shown in Figure 2.9. The computation time was approximately one day.

The combinatorial algorithm is the most straightforward method, but it is also very inefficient. For a further increase in resolution, for instance by computing 5 possible concentration values per component, the total number of calculations will be 5^{11} . This is not computationally achievable with a conventional workstation. If the resolution employed in the genetic algorithm is applied (32^{11}), the calculation becomes impossible. The application of the combinatorial approach to the present problem results in a quite good approximation; this is due to the optimum concentrations of most of the elements being at the limits of their range. However, for systems containing 11 variables, the combinatorial approach does not present a practical way to find the optimum result. A comparison of the *NPP* values by the CA and other approaches is shown in the histogram of Figure 2.10.

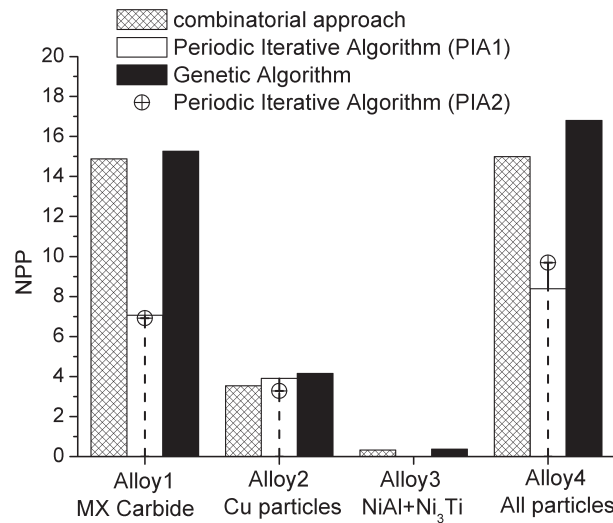


FIGURE 2.10. Number of precipitate particles (NPP) of designed Alloy 1-4 obtained from different optimisation algorithms: Combinatorial Approach (CA), Periodic Iterative Algorithm (PIA) and Genetic Algorithm (GA)

In the PIA, the results are dependent on the starting reference composition, and also the sequence of elements followed in the optimisation. In some cases, the

results are better than the low resolution combinatorial algorithm (alloys optimised on Cu precipitates), but for other optimisation criteria no results are obtained.

Finally, the optimisation through the genetic algorithm takes 2-3 days; it is the most efficient algorithm among those explored in this work. The optimisation result does not depend on the initial conditions or the nature of the fitness function: explicit or implicit, continuous or discontinuous. The principle of elitism ensures a good solution while diversity is enforced via mutation. This framework can be easily extended by coupling it to other criteria by modifying the fitness function.

The convergence of the genetic algorithm was also assessed. All GA optimisations start from a randomly generated population of potential solutions. In order to study the relevance of the initial solutions, different random numbers were given for generating the initial candidate pool. The same optimum results were obtained although they were achieved after a different number of generations, and also a totally different optimising history. Moreover, Figure 2.8 shows that the concentrations optimised through the genetic algorithm are the best values in the searching domain for each component. This strongly suggests that the optimisation via the genetic algorithm has encountered and evaluated a sufficient number of generations and therefore the global optimum is likely to have been reached.

2.7.3 Comparison to Existing Alloys

For validation purposes, the model was also applied to the commercial precipitate strengthening steels listed in Table 1.1. For each commercial alloy, the compositions are given as an input for the algorithm shown in Figure 2.3; the *NPP* is estimated from equation 2.5 and the results are shown in Figure 2.7a. The thermodynamic calculation successfully predicts the presence of the strengthening precipitates experimentally observed except for the alloy possessing MC/M₂C carbides strengthening systems, in which the calculation shows better thermostability of M₂₃C₆ and M₆C carbides. For systems utilising Cu strengthening particles, the computationally designed alloy (Alloy 2) can achieve up to ten times the *NPP*, which reveals a very promising strengthening increase. The alloy scenarios of promoting Ni₃Ti and NiAl precipitation (Alloy 3) also show at least two times as many precipitate particles compared to the existing steels.

The composition of the designed novel alloys are also compared to the commercial grades listed in Table 1.1. By denoting as C_i^N , C_i^E and C_i^{Max} and as the concentration of element $i = \text{C, Cr, Ni} \dots$ in the new alloy, the existing alloy and the upper limit of the searching range Table 2.1, respectively, if $|(C_i^N - C_i^E)/C_i^{Max}| < 0.1$, then the boxes under i in Table 2.3 are filled with the number of the designed alloy satisfying this condition. It can be observed that the boxes corresponding to some

Grades	C	Cr	Ni	Ti	Mo	Al	Cu	Co	Nb	N	V	Mn	Si
PH15-5	3	3	1		1 2	1 2	1			1 2	1		1 2
					3 4	4				3 4	4		3 4
PH13-8		1 2				3	3			1 2	1		
		4 3								3 4	4		
Custom 450		1 2			1 2	1 2				1 2	1		
	3	4 3			3 4	4				3 4	4		
IRK91		1 2								1 2	1	1 2	
		4 3								3 4	4	3 4	
Ferrium S53	1		1	2		1 2				1 2	1		
		4					4 3			3 4	4		
Aermet100	1				1 2	1 2				1 2	1		
		4			3 4	4 3				3 4	4		
300M			2		1 2	1 2				1 2	1		
			4		3 4	4 3				3 4	4		

TABLE 2.3. Comparison of the designed alloys to some commercial steels.

components are filled for most commercial grades, suggesting that the designed new alloys resemble their existing counterparts. However, new composition levels for elements such as Ti, Co, Nb and Si are present (and their boxes poorly populated), showing that further improvement of the properties of corrosive resistance high strength alloys are possible.

2.8 Conclusion

The basic computational alloy design approach coupling thermodynamic calculations with a genetic optimisation framework has been developed. Four scenarios of UHS stainless steels employing different strengthening precipitates and consisting of 13 alloying elements are considered. The comparison of new alloys with the existing commercial counterparts shows that the designed alloys possess significant increases of total number of precipitate particles (NPP) assuming they keep the critical nuclei size. The new alloy compositions partially resemble the success of existing alloys while other components explored better concentrations. Other optimisation algorithms, including combinatorial and periodic iterative algorithms are assessed and their results are compared to those obtained from the genetic algorithm. It is demonstrated that the genetic approach is the most efficient and reliable optimisation scheme.

The design approach is of a general nature, and it can be easily extended to design alloy implement other quantifiable criteria, or for the optimisation of heat treatment by incorporating heat treatment parameters. In this chapter, the potential strength increase of newly designed alloys is revealed by the increase of precipitate particles number, but not in form of strength. A quantification of desirable precipitate formation representing its contribution to strength will be more

explicit and will provide solid validation in comparison with existing counterparts. It would also be better to incorporate the effect of aging temperature as it plays a very important role in maraging steels.

3

Further Model Development: Precipitation Strengthening Contribution

3.1 Introduction

The formation of precipitate particles generally increases the yield and tensile strength of alloys because the particles represent effective obstacles to dislocation movement. The contribution of precipitation strengthening is determined by more factors than just the precipitate species and the number of precipitate particles. The precipitate particle size, distribution, inter-particle spacing and to further extent, their shape, coherency with the matrix and orientation relationship are also of great importance. To quantify the precipitation strengthening effect, different strengthening mechanisms have been postulated based on the manner in which dislocations interact with precipitate particles, either to cut through them [112] or go around [111] the precipitates.

In chapter 2, a base alloy design model rooted on thermodynamics has been proposed. It optimises the alloy composition so as to achieve the maximum number of precipitate particles of the desired species. Such precipitates are generated by tempering a quenched homogenous system at a fixed temperature while fulfilling other criteria. This chapter is to further develop the model to optimise the precipitation strengthening contribution, estimated according to metallurgical and mechanical principles. Moreover, the ageing temperature plays a paramount role in determining the precipitate species and their population, and hence their properties. Therefore, a new gene representing aging temperature is implemented in the optimisation model which allows the variation of ageing temperature so as

to simultaneously find the best alloy composition and aging temperature. This chapter also presents a systematic analysis of the compositional and temperature effects on the precipitate strengthening contribution.

3.2 Precipitation Strengthening Factor: the New Optimisation Factor

In the early stages of precipitation, precipitate particles are likely to be coherent with the matrix and deformable as dislocations cut through them, as illustrated in Figure 3.1. When a dislocation passes through a coherent precipitate, the particle will be sheared by one Burgers vector across the glide plane by breaking favourable bonds within the particle creating disorder, for example, an antiphase boundary (APB) on the slip plane. At the same time, it also creates a new lunar-shaped precipitate/matrix interface area. Both interactions require additional work and oppose the motion of dislocations.

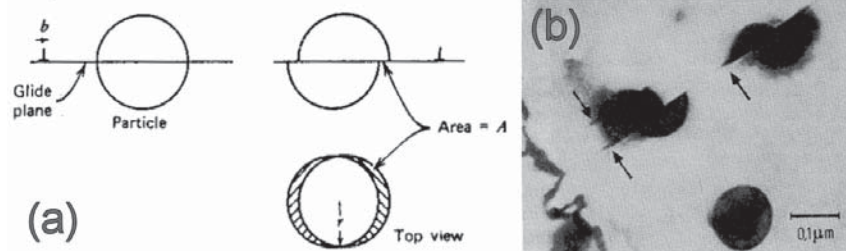


FIGURE 3.1. (a) Schematic demonstration of shearing of a coherent and soft particle by dislocation across the glide plane and (b) TEM image of sheared Ni_3Al particle in a 19Cr-6Al-Ni alloy [112].

As the number of precipitates and their size increase, it becomes increasingly difficult for a dislocation to shear the precipitate. When a gliding dislocation moves under the influence of applied stress and encounters a row of strong and uncuttable obstacles, it bows around them. As the applied stress is sufficiently increased, semicircular dislocation loops between particles are formed; subsequently, the two dislocation arms meet and thus annihilate each other and the main dislocation moves on, as demonstrated in Figure 3.2. Every time the dislocation by-passes the precipitate particles, it leaves one dislocation loop around the particle and the dislocation density increases with increasing plastic strain. This strengthening mechanism was first suggested by Orowan [111] and thereon called Orowan strengthening mechanism.

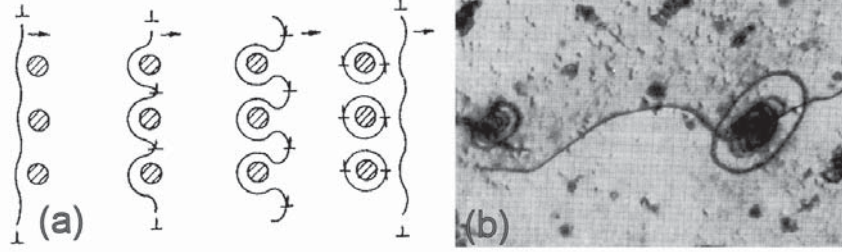


FIGURE 3.2. (a) Schematic illustration of different stages of a moving dislocation in bypassing a row of precipitate particles and (b) Image of dislocation loops round Al_2O_3 particles in a 30Zn-Cu single crystal. The dislocation loop is about 100 nm in diameter [112].

A critical parameter in the precipitate strengthening contribution is the inter-particle spacing. One successful model for estimating the inter-particle spacing was proposed by Friedel, which relies on the assumption of steady-state for the number of precipitates along the dislocation line in motion. Then the spacing is given by the calculation of the dislocation curvature under the applied resolved shear stress on the slip plane [138]. For such a situation, the obstacle strength can be estimated as [139]:

$$\sigma_p^{\text{sheared}} = \left(\frac{3}{4\pi}\right)^{1/2} \beta^{-1/2} k^{3/2} M \mu b^{-1/2} (f_v \cdot r)^{1/2} = c_1 f_v^{1/2} r^{1/2} \quad (3.1)$$

and

$$\sigma_p^{\text{by-passed}} = \left(\frac{6}{\pi}\right)^{1/2} M \mu b f_v^{1/2} r^{-1} = c_2 f_v^{1/2} r^{-1} \quad (3.2)$$

for sheared and by-passed particles respectively, where M is the Taylor factor, b is the length of the Burgers vector, μ is the precipitate shear modulus, k and β are constants, f_v is the precipitate volume fraction and r is the average particle radius. In spite of the fact that the precipitation strengthening contribution is straightforward from such formulae, absolute values are difficult to estimate, as in addition to the volume fraction (f_v) and the precipitate radius (r), several other factors play a role. These are incorporated in constants c_1 and c_2 , which are in turn dependent on factors difficult to measure or compute, such as the precipitate interfacial energy and the precipitate shear modulus. These factors, however, are reasonably constant for a given precipitate system.

According to equations 3.1 and 3.2, in the small particle regime where particles are shearable, the precipitation strengthening effect increases as volume fraction increases or particle size increases. In the larger particle regime where precipitates become non-deformable, the obstacle strength is proportional to $f_v^{1/2}$ but strongly decreases with the dispersion of coarser precipitates. As shown in Figure 3.3, there

is a critical size at which the strengthening is a maximum, where the radius for obstacle strengths is identical for the two mechanisms. The transitional critical size bridging the two mechanisms is usually in the range of 5-30 nanometres, independent of the present volume fraction:

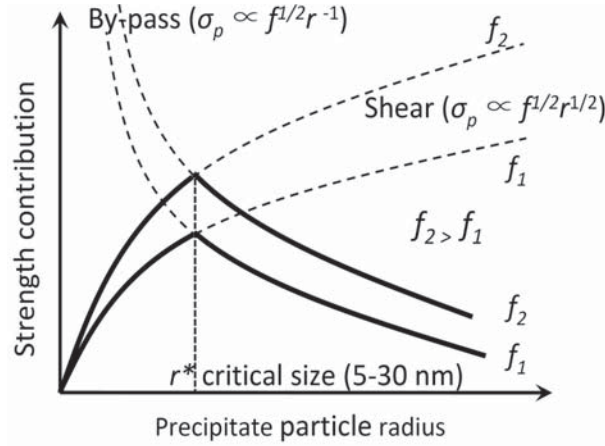


FIGURE 3.3. Evolution of the strengthening contribution with precipitate size

In maraging steels, the size of the nuclei of strengthening carbides and inter-metallic precipitates is generally a few nanometres in radius, their exact values depend on the precipitate nature, the interfacial energy and the driving force. Whether the precipitate dimensions reach the levels belonging to the by-pass mechanism depends on the precipitation growth kinetics. Based on Equation 2.4, the refinement of precipitates can be realised by increasing their driving force for precipitation. Moreover, in order to avoid significant growth and coarsening, fast nucleation is required such that very fine precipitates become quickly stable by rapidly consuming most of the solute available from the matrix. The nucleation process can be stimulated by a large number density of dislocations supplied by the lath martensite matrix and a homogenous distribution of supersaturated solute atoms, and further accelerated by increasing the precipitation driving force according to Equation 2.2. This automatically leads to a refinement of the precipitate particle size (Equation 2.4). Given all these conditions, the precipitates are very likely to form in a very fast and homogeneously, and stay approximately at the transition zone between both mechanisms (5-30nm). Assuming that the shearing mechanism (Equation 3.1) dominates in the newly designed alloy, the strengthening contribution becomes proportional to $f_v^{1/2} r^{1/2}$. However, this criterion is not consistent with the principle of particle refinement as bigger particle sizes will lead to larger strengthening effects according to Equation 3.1. If the particle size grows beyond the transition radius, a different strengthening mechanism takes place and Equation 3.2 should be used.

In order to reach a compromise between the conflicting objectives, an optimisation factor of $\sigma_p^{sheared}/r$ is applied so as to balance the requirement of strengthening contribution maximisation and particle size minimisation.

$$\sigma_p = \sigma_p^{sheared}/r \propto f_v^{1/2} r^{-1/2} \quad (3.3)$$

such index can be considered as mixed shear ($f_v^{1/2} r^{1/2}$) and by-pass ($f_v^{1/2} r^{-1}$) mechanisms, it also reflects the fact that the precipitate particles are likely to be in the transition zone between the two mechanisms. Due to the precipitate size is aimed at values approaching their nucleation dimensions, r is taken as the critical nucleation size according to Equation 2.4, and the driving force is calculated by ThermoCalc.

The precipitation strengthening contribution is implemented in the genetic algorithm as the new optimisation factor. The entire algorithm is shown schematically in Figure 3.4.

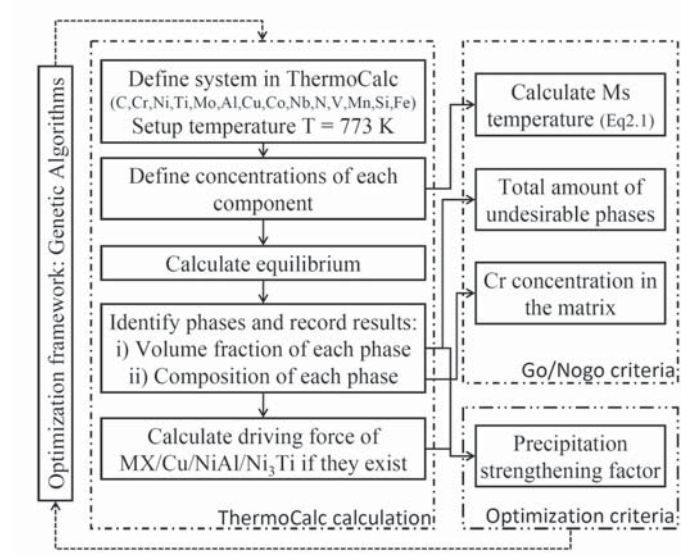


FIGURE 3.4. Algorithm of the thermodynamic calculation and criteria evaluation.

3.3 Alloy Design Exercises

As in Chapter 2, three alloy design scenarios utilising different strengthening systems are considered: 1) MC carbides, 2) Cu particles and 3) Ni-rich particles (NiAl and Ni₃Ti); the alloys resulting from these systems will be hereon termed alloy 1A,

2A and 3A, respectively. The strengthening factor $f_v^{1/2}r^{-1/2}$ of the corresponding strengthening system is maximised while the other go/nogo criteria, as described in Chapter 2, are enforced. Initially, the thermodynamic calculations are preformed at a fixed precipitation temperature of 773 K for all alloys. The alloy compositions are optimised within the ranges shown in Table 2.1.

The normalised compositions with respect to the upper searching limit are shown in Figure 3.5. A comparison to existing commercial grades is also shown in this figure. The volume fractions and precipitation driving forces for each alloy are plotted in Figure 3.6a and 3.6b. The precipitation strengthening factor according to shear (Equation 3.1) and by-pass (Equation 3.2) mechanisms are shown in Figures 3.6c and 3.6d, respectively.

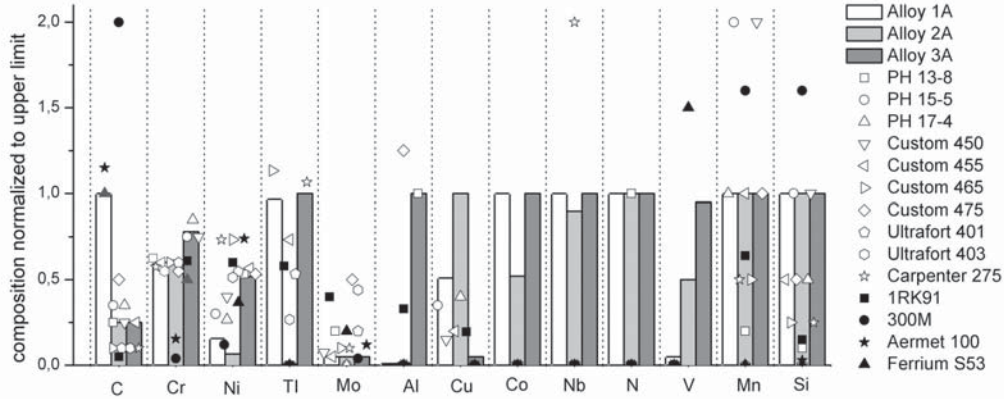


FIGURE 3.5. Normalized compositions of 3 designed alloys and existing successful precipitation strengthening steel grades.

From Figures 3.5 and 3.6, it can be observed that in alloy 1A, C, Ti and Nb take their maximum allowed concentrations as they are strong carbide formers, even though Nb decreases the M_s temperature. It is important to notice that the maximum carbide strengthening contribution is achieved along with a significant amount of Cu precipitates and a relative small amount of NiAl/Ni₃Ti particles, which will further contribute to the strength of alloy 1A. In alloys 2A and 3A, C takes a lower concentration but Cu and Ni/Al/Ti take very high levels in order to promote the formation of Cu and NiAl/Ni₃Ti precipitates, respectively. Unlike the case of carbides, Cu and NiAl/Ni₃Ti precipitates are expected to be more dominant; however, due to the relatively high driving force for carbides precipitation, there are still notable strengthening effects from these as shown in Figure 3.6c and 3.6d.

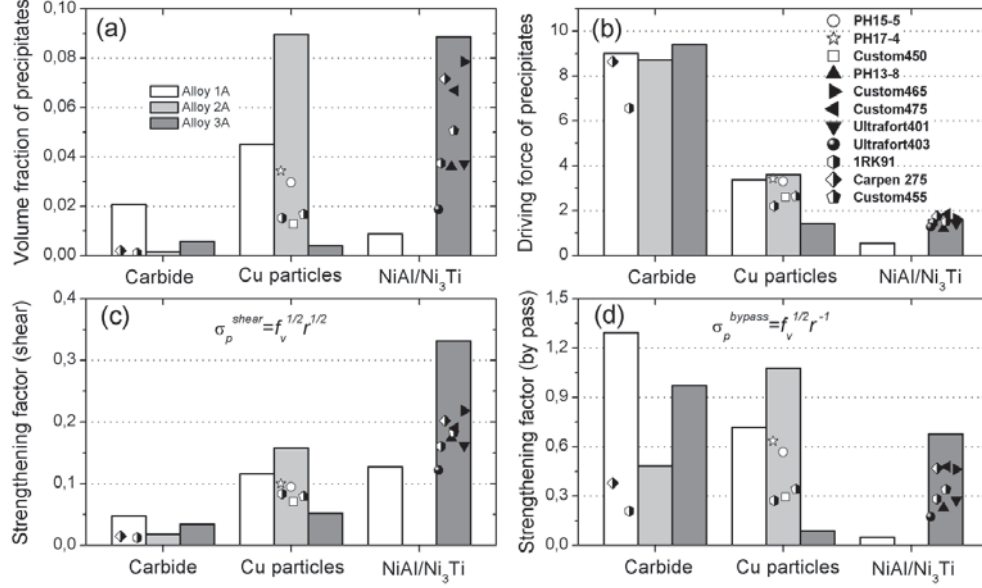


FIGURE 3.6. Comparison of designed and existing grades: (a) volume fraction of precipitate, (b) normalized driving force for precipitation and normalized precipitation strengthening factor calculated by shear mechanism (c) and by-pass mechanism (d). Symbols indicate values for commercial steels.

For validation purposes, the model was applied to 11 commercial precipitate strengthening steels and the results are shown in Figure 3.6. The comparison of designed and existing commercial alloys clearly indicates that the strengthening factors of the designed alloys are higher than their existing counterparts both considering shear and by-pass mechanisms. Moreover, by comparing the compositions of those alloys to commercial grades (Figure 3.5), it is seen that, for some components, the designed alloys do share the same concentrations with certain existing grades. This suggests that the designed new alloys partially resemble their existing counterparts. However, new composition levels for elements such as Ti, Co, Nb and V are present. The calculations postulate partially new compositions which inherit some of the elemental values of successful existing grades, while incorporating new values for other elements.

The strengthening factor computations presented here are based on the assumption that the particle radius equals the critical nucleation radius. This has been assumed to be the case as the initial fast nucleation regime tends to limit precipitate growth by rapidly consuming the available solutes. Employing the critical nucleation radius, the experimental yield strength increase by aging treatment of the existing alloys versus the strengthening factor calculated by shear (Equation 3.1) and by-pass (Equation 3.2) mechanisms are plotted in Figure 3.7. Since precipitation is the dominant strengthening mechanism in our alloys, the yield strength

increase is therefore a good indicator to compare to the calculated strengthening factor. Nevertheless, the net strengthening effect of multiple precipitates is very difficult to evaluate because different precipitates have different physical parameters. Thus, the strengthening factors of those steel grades containing several types of precipitates are calculated by adding their contributions assuming the same critical parameters. In Figure 3.7, the yield strength increase either due to shear or by-pass mechanisms versus the calculated strengthening factor are shown. The fact that the commercial grades lie on an approximately straight line adds confidence to the design philosophy presented here. Furthermore, alloys 1A-3A are indicated in Figure 3.7 and their position indicates that the designed alloys have a clear potential for improving the *net alloy* strength via their precipitation contribution.

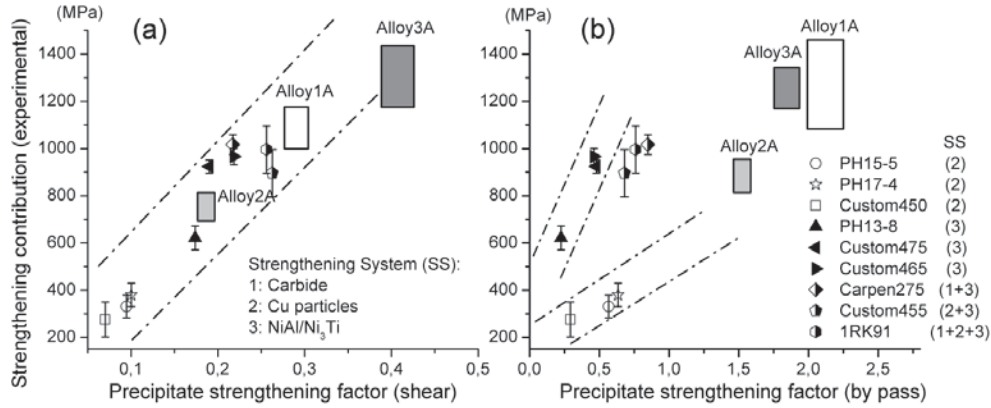
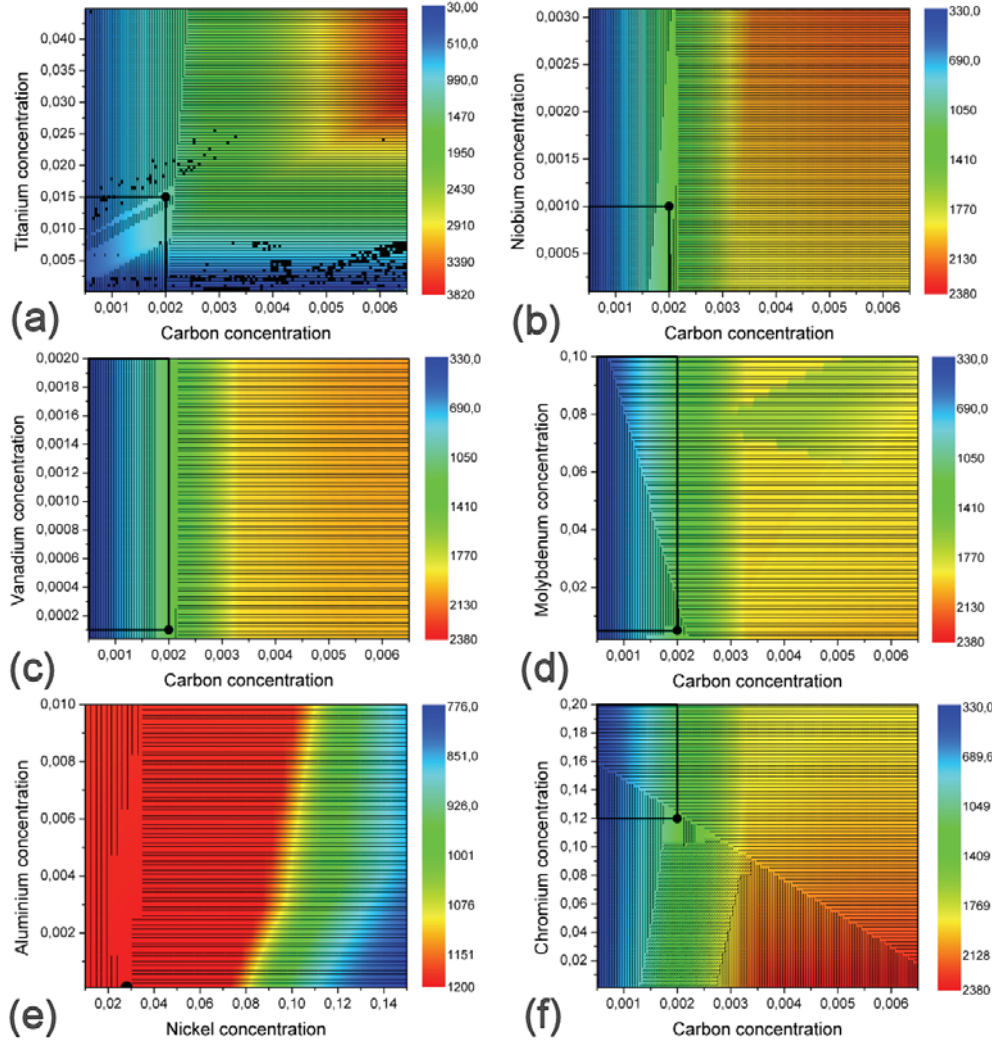


FIGURE 3.7. Calculated strengthening factors for alloys 1A-3A as well as commercial UHS steel grades assuming (a) shear and (b) bypass strengthening mechanisms.

3.4 Compositional Effect

Alloy 1A is taken as a baseline to demonstrate the effects of composition in relation to strengthening, as well as those emerging from the Ms constraint, the volume fraction of unwanted precipitates and the minimum allowed chromium concentration. To this aim, selected elements are paired up on the basis of the strengthening mechanism they might contribute to: carbide formers (C-Ti, C-Nb, C-V, C-Mo); Ni rich precipitates (Ni-Al) and the rest of the elements C-Cr, C-Cu, C-Co and C-Si. The compositional domains studied are extended beyond the ranges shown in Table 2.1: for those components in which alloy 1A takes the minimal values from Table 2.1, the new minimal studied concentrations are extended to zero while following the same concentration intervals as applied in the optimisation of the same

component; for those alloy 1A has the maximum of the searching range, the ranges are extended to 3 times the previous maximum with the corresponding concentration intervals, the rest of the elements keep the same range as in Table 2.1. The results for a fixed aging temperature of 773 K are shown in figures 3.8 a-i. The colour code of the background in these figures indicates the degree of precipitation strengthening $f_v^{1/2}r^{-1/2}$ obtained due to the aging treatment (blue is a low strength increase, red is a high strength increase). It is interesting to note that in some cases (figures 3.8 a and b) the strength increases when the concentrations of both alloying elements increases, in some others (figures 3.8 e and f) the higher strength increase is obtained for one alloying element being low, while the other is relatively high, and finally that in some instances (figures 3.8 c, d and g-i) the effects of elements other than carbon are rather small anyway.



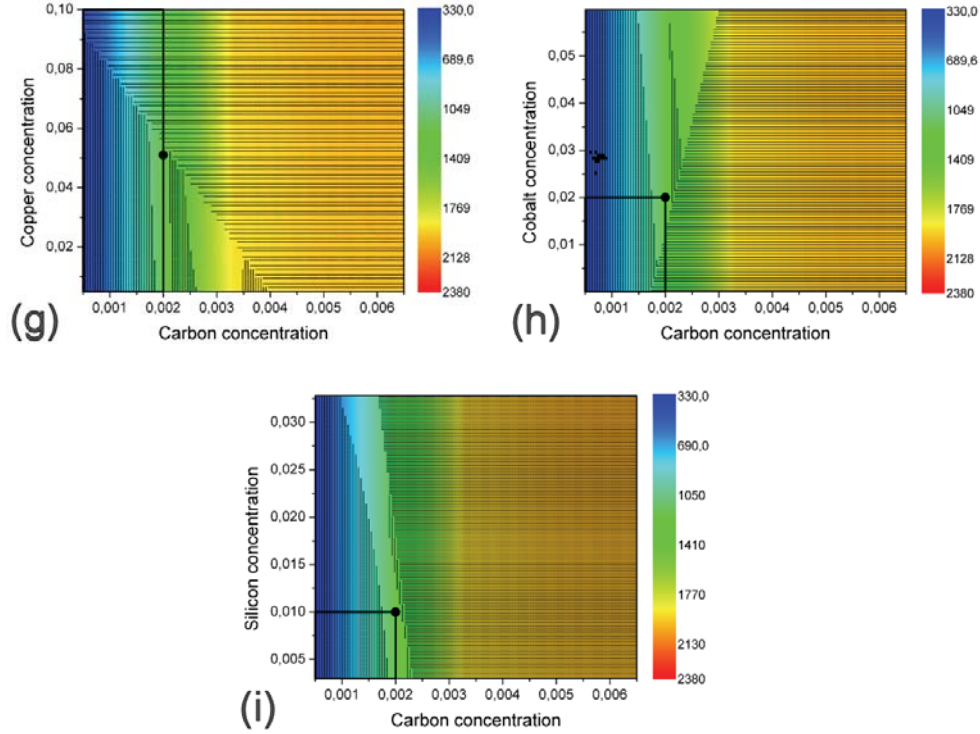


FIGURE 3.8. Binary compositional effects of (a) C-Ti, (b) C-Nb, (c) C-V, (d) C-Mo, (e) Ni-Al, (f) C-Cr, (g) C-Cu, (h) C-Co and (i) C-Si. The background contour shows the carbide precipitation strengthening factor. The horizontal, vertical and forward slash patterns demonstrate the area not fulfilled the go/nogo criteria of Ms temperature, total amount of undesirable phases and Cr concentration in the matrix, respectively. The scattered black spots show compositions where ThermoCalc equilibrium calculation can not be successfully performed. All concentrations are given in weight fraction.

The horizontal patterns in figures 3.8 superimposed on the colour coded background display the (forbidden) composition domains where Ms temperature is below 473 K; the vertical patterns mask the (forbidden) area in which the total amount of undesirable phases is over 1% in volume and the forward slash region shows the (forbidden) domain where Cr concentration is below 12 wt% after the completion of precipitation. The unhashed areas unveil the composition domains in which precipitation strengthening factor is maximised, while meeting the other constraints.

In figures 3.8 b-d and f-i, the background contours show that carbon displays the most important contribution to the strengthening factor, although the concentration of some components changes one order of magnitude more than that of carbon. Figure 3.8 a shows that Ti, provided that it varies 10 times as much as carbon, will produce equivalent changes in the strengthening factor. A comparison among

carbide formers (figures 3.8 a-c) shows that the carbide precipitation strengthening capability with same alloying additions follows the order of Ti, Nb and V. Other elements which do not directly participate in carbide precipitate still show considerable effects as they vary the thermostability of the strengthening phases.

Concerning the line patterns plotted in the composition domains in figures 3.8 a-i, it is interesting to note that the right hand side sections of the figures are mostly masked by horizontal lines, which correspond to composition domains of $M_s < 473$ K. This is due to the fact that carbon strongly decreases M_s temperature (2.1). The lower left hand corner in the Figures 3.8 is often covered by the line pattern connected to the presence of more than 1% undesirable phases. This is because the shortage of carbon frees the solutes to form other undesirable phases. As displayed by the forward slash zone (Figure 3.8 f), only Cr changes the matrix Cr concentration significantly.

In figures 3.8 f-h, the open areas are split into two sections by a narrow vertical zone, which indicates the formation of undesirable phases. The unexpected phases forming over narrow regions in this composition domain are due to σ and laves phases, capable of creating a few volume percents of phases. Although the forbidden regions are rather narrow and are somewhat unexpected from a metal physical point of view, the thermodynamic database of σ and laves phases are well enough defined to take the forbidden regions seriously.

The bold squares within figures 3.8 a-i are the regions within which alloy 1A composition was optimised (Table 2.1). The black circle shows the optimised composition value. As expected, the black circles are always located at the maximum strengthening level in the uncovered area of the searching domain, implying that the genetic algorithm indeed found the best alloy composition. Looking at the horizontal line passing through the circle, the carbon concentration window (0.17-0.21 wt%) is narrow but well within the industrially controllable level. The vertical direction through the circle is less restricted and thus inhomogeneities of those alloying elements become acceptable to different levels according to the appropriate gap width.

It can be observed in figures 3.8 b and f-i that concentrations of Nb, Cr, Cu, Co and Si in alloy 1A can be lowered without significantly decreasing the precipitate strengthening factor. This is favorable because it reduces the complexity of the alloy and its cost as it sets less restrictive demands on the scrap alloys used as starting materials. On the other hand, an increase in the content of these elements or other elements such as V, Mo, Al and Ni (figures 3.8 c-e, respectively) will not extensively increase the carbide precipitate strengthening contribution. However, it is possible to achieve further improvements in alloy 1A via increasing C searching upper limit while either keeping Cu searching range (Figure 3.8 g), or decreasing Cr lower limit (Figure 3.8 f) or increasing Co upper limit (Figure 3.8 h).

3.5 Ageing Temperature Effect

Aging temperature effects are studied within the 573-973 K range, which covers the typical aging temperatures for existing UHS stainless steel grades. The calculations are performed with a temperature step of 1 K for all alloys. The total volume fraction of undesirable phases, Cr concentration in the matrix, the molar fractions, driving force and precipitation strengthening factor of each strengthening precipitates are shown in figures 3.9, for alloys 1A, 2A and 3A respectively. It is important to note that, despite of the fact that alloys 1A-3A are designed to utilise carbide, Cu and Ni-rich precipitates respectively, multiple strengthening precipitate systems appear in each system.

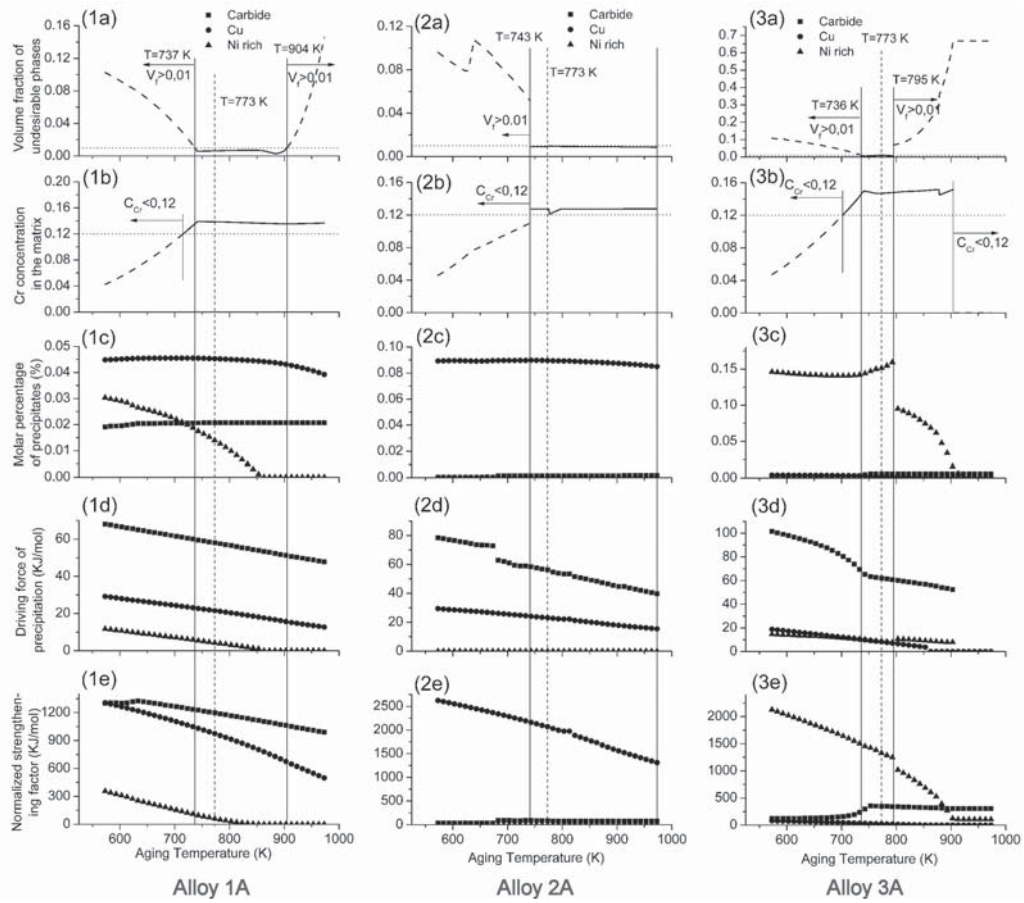


FIGURE 3.9. Temperature effects in alloy 1A, 2A and 3A on the total volume fraction of undesirable phases (a), weight fraction of Cr in the matrix (b), the molar fractions (c), driving force (d) and normalized precipitation strengthening factor (e) of each strengthening precipitate.

In figures 3.9 1e, 2e and 3e, it is shown that a lower temperature will generally result in a better strengthening contribution; however, a relatively high temperature may be favourable from a manufacturing point of view as this reduces the cycle time of the ageing treatment. The go/nogo criteria shown in figures 3.9 1a-1b, 2a-2b and 3a-3b considerably limit the available aging temperature window around 773 K at which those alloys were designed. In alloys 1A and 3A, the undesirable phase fraction sets up lower and upper temperature boundaries while the Cr criterion constitute a second limit. In alloy 2A, they together build the lower border while no upper constraints stem from the go/nogo criteria. It is worth noticing that the 1% volume of undesirable phases is quite a strict criterion. If this constraint is relaxed and higher fractions of undesirable precipitates are allowed, a considerable improvement of strengthening effect in alloy 1A and 3A may be achieved by a lower aging temperature, although the kinetics will be even slower. Nevertheless, with the current criteria, the aging temperature window is wide enough to find an optimum which compromises the thermodynamics favoured low temperature and kinetics preferred high temperature limits.

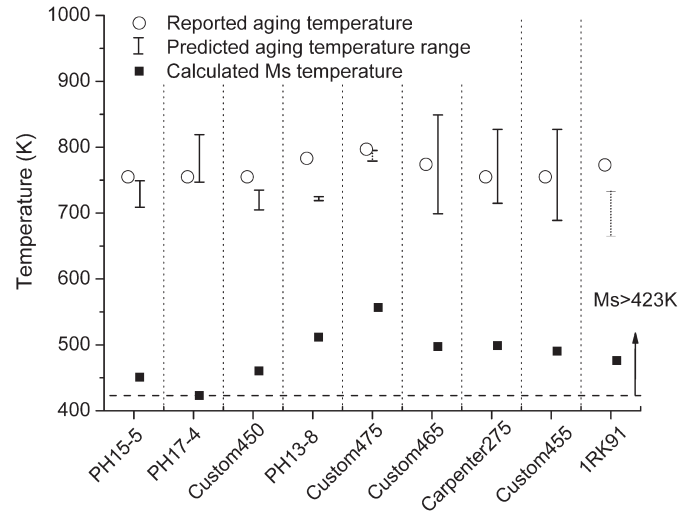


FIGURE 3.10. Predicted aging temperature windows (bar), experimental optimal aging temperatures and prediction Ms temperature of various existing alloys. The dot bar of Custom 475 and 1RK91 are obtained by allowed maximal undesirable phase as 11% instead of 10%, and Cr concentration in matrix as 10 wt% instead of 12 wt%. The dot line at 423 K indicates the experimental Ms temperature threshold of lath martensite formation.

In order to assess the capability and reliability of the model, identical calculations were performed for a range of existing commercial precipitation strengthening stainless steels in the same aging temperature window from 573 to 973 K. The tolerance of undesirable phases amount was increased to 10%. The predicted effective

aging temperatures are indicated by vertical bars in Figure 3.10. The empty circles show the industrially employed aging temperatures which were optimised experimentally. It shows that the predicted optimal aging temperature is either located within the predicted windows or slightly above it. The reason that some real aging temperatures are above the predicted value could be that, although from a thermodynamic point of view the strengthening contribution is optimised at the lowest allowed temperature, the kinetics is very slow and does not constitute the best practical choice. It should be pointed out that such a quantitative justification of optimal ageing temperatures of precipitation hardenable stainless steels has not been reported in the literature yet.

Finally, the Ms temperatures of the existing UHS stainless steel grades are calculated according to Equation 2.1 and shown in Figure 3.10. All grades show an Ms temperature above 423 K which is consistent with the Ms temperature constraint considered in the alloy optimisation (section 2.3.1).

3.6 Alloy Re-design by Incorporating the Ageing Temperature Gene

To investigate the combined effects of composition and aging treatment temperature, the genetic algorithm is modified by adding an extra 5-bits gene representing the aging temperature. This allows the aging temperature to vary from 698 K to 853 K in 32 (2^5) intervals of 5 K. The concentrations are concurrently optimised in the same range as Table 2.1. The same three scenarios are designed and termed alloy 1B, 2B and 3B. The compositions are shown in Figure 3.11. The precipitation strengthening factors are compared to previous alloys (1A-3A) in Figure 3.12.

The new composition optimisations incorporating a gene for ageing temperature variation show quite similar composition results to alloy series “A”, as shown in figure 3.11. Alloy 1B has exactly the same composition as alloy 1A. The optimal aging temperature of alloy 1B is found to be 738 K which is very close to the temperature showing the highest strengthening contribution in figure 3.9 1e. The composition of alloy 2B only slightly decreases V and it results in an optimal aging temperature of 738 K. Alloy 3B has a new composition with 5 new concentrations as compared to alloy 3A. The best aging temperature is found to be 733K.

For alloys 1A-3A, the strengthening contribution can be further increased by changing its aging temperature as discussed in the previous section with figures 3.9. The optimal results are shown in Figure 3.12 as dot bars on the top of alloys 1A-3A. Alloy 1A achieves the same potential strengthening level as alloy 1B because the compositions are the same and the aging temperature is almost the same. Alloy

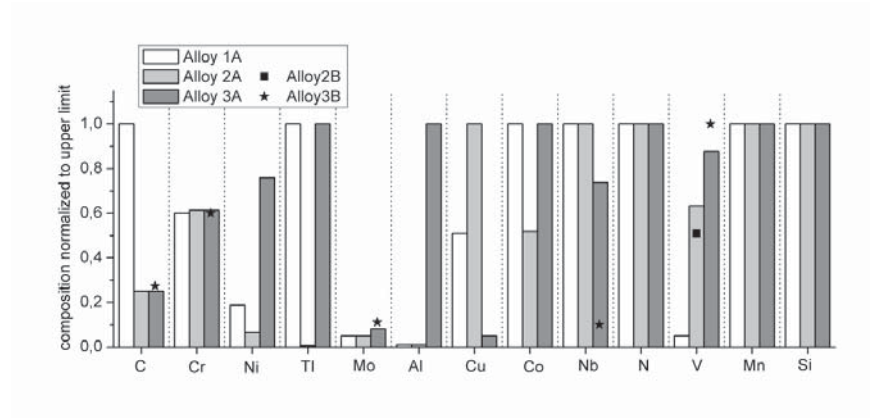


FIGURE 3.11. Compositions of designed alloys 1A-3A and alloy 1B-3B. For alloy 1B-3B, only the components which have new concentrations are displayed

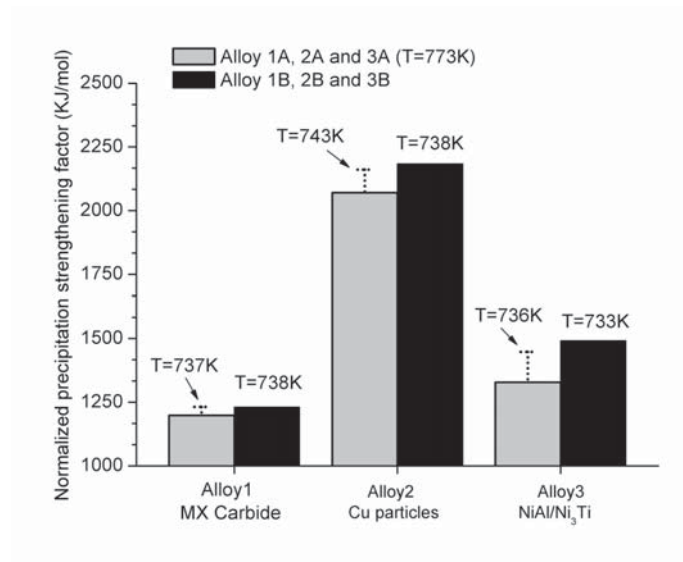


FIGURE 3.12. Comparison of precipitation strengthening factors of alloys 1-3 at 773 K (grey bars), the optimal temperature in the range of 573-973 K (dot bar) and alloy 1'-3' with corresponding aging temperature (black bars).

2B shows an extra strengthening contribution by varying V concentration given optimal aging temperature of 738K, compared to alloy 2A at best temperature 743 K. Because of the relative big composition deviation of alloy 3B, it has a considerable better strengthening effect than alloy 3A.

Instead of the fixed aging temperature at 773 K, the new optimisations show lower optimal aging temperatures which are very close to the optimal temperatures as shown in figures 3.9. However, the alloy compositions in alloys 1B and 2B do not change significantly. Even for the relative new composition of alloy 3B, the strengthening contribution does not increase remarkably. For the three alloy scenarios considered, taking into account the extra computational cost generated by introducing the new gene, the composition could have been optimised using a fixed temperature and an aging temperature to be optimised afterwards separately, but this statement may not hold true for more complex systems.

3.7 Conclusion

The genetic computational alloy design approach presented in Chapter 2 is further developed by: (1) incorporating the precipitation strengthening contribution as the optimisation factor, (2) adding a new ageing temperature gene to optimise such processing parameter. Stemming from the precipitation strengthening factor, three new alloy compositions have been postulated. The new alloys possess significant precipitation strengthening improvements with respect to commercial alloys when the model is applied to them. Moreover, the contributions of various alloying elements combined in pairs are disentangled. The model shows the ability to find optimal compositions among the conflicting criteria, some of which have been outlined. Furthermore, the binary elements contour plots may be an aid for the alloy manufacturer to identify elements on which compositional variations are allowed, without compromising aimed properties such as strength.

The effect of ageing temperature has been studied and it presents a quantitative justification of the precipitation temperature of existing commercial UHS stainless steels. The predicted ageing temperature windows show good agreement with the experimental optima. The implementation of new ageing temperature gene in the model allows the alloy composition and ageing temperature to be optimised simultaneously in an integrated manner. The results show that further strength improvements are possible by slight variations in both composition and ageing temperature. However, for the UHS stainless steel systems considered, the integrated optimisation of composition and ageing temperature did not lead to a significantly improvement compared to the sequential optimisation of composition and ageing temperature.

4

Experimental Validation: the First Round of Prototype Alloys

4.1 Alloy Compositions

In order to validate the computational alloy design approach described in the previous chapters, a series of prototype alloys strengthened by different precipitate families have been designed. The strengthening precipitate scenarios are slightly different to the alloy design exercises shown in earlier chapters: alloys have been designed to be strengthened by precipitation of MC carbides, and Ni_3Ti intermetallics, respectively. A third alloy pursues a balance between precipitates of Cu and Ni rich (NiAl and Ni_3Ti) intermetallics because the fast formation of Cu clusters may work as preferable nucleation sites for further precipitation of Ni rich intermetallics. The alloys are hereon termed Car, NiTi and CuNi, respectively, which reflects the precipitate species in each alloy. The compositions of these three alloys are optimised applying the model developed in Chapter 2 in which the total number of precipitate particles is maximised while other go/nogo criteria are fulfilled. The concentration ranges applied in the optimisation are also slightly modified in order to further enhance the precipitation strengthening effect of the selected species, for instance, the upper limit of Nb increases from 0.2 to 0.3 wt% for alloy Car, upper limits of Ni and Ti increase to 1.5 times their standard values in the design of alloy NiTi. The composition searching ranges are summarised in Table 4.1 and the design results are shown in Table 4.2.

Another alloy utilising MC carbides for strengthening but with higher allowed Co concentration was designed to maximise the MC precipitation strengthening

contribution employing the model presented in Chapter 3, and is hereon termed alloy CarCo. The new extended searching ranges for this alloy are indicated by superscript 4 in Table 4.1. The optimal alloy composition and corresponding Ms temperature are also shown in Table 4.2.

The strengthening precipitate configurations of alloys Car, NiTi and CuNi are compared by the total Number of Precipitate Particles (*NPP*) in Figure 4.1(a)¹. As described in Chapter 2, the MC carbide strengthened alloy Car precipitates a significant amount of Cu particles, although it is optimised to achieve a maximum number of MC carbide only. In alloy NiTi, there is also a significant amount of NiAl coexisting with a maximum of Ni₃Ti, and hence it provides extra strengthening effect. A balance of Cu and Ni rich precipitates is achieved in alloy CuNi which also contains some MC carbide as well. The precipitation strengthening contribution (Section 3.2) of desired species in all four alloys is compared in Figure 4.1(b) for alloys Car, NiTi and CuNi, which are designed employing the earlier model. It can be seen from 4.1(b) that the MC carbide strengthening contribution in CarCo increases remarkably due to the application of new optimisation criteria, and also because of the extension of the searching ranges, particularly the increases of C, Co and Nb.

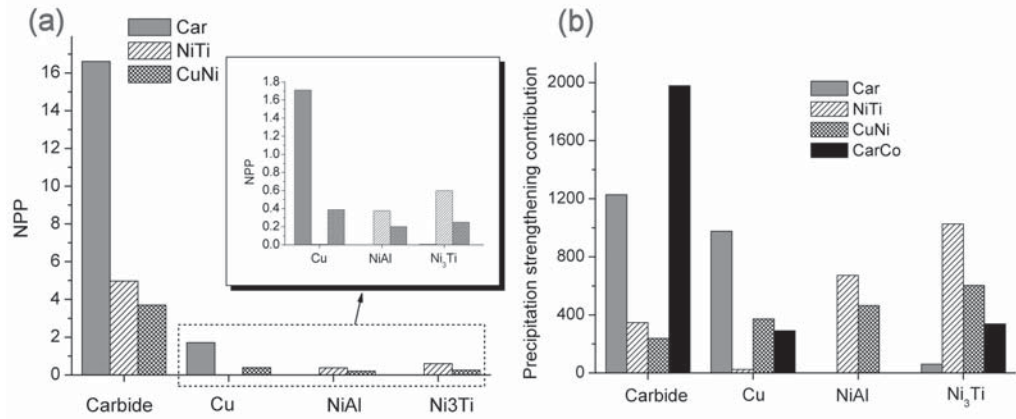


FIGURE 4.1. The strengthening precipitate configurations of (a) alloys Car, NiTi and CuNi in terms of the total number of precipitate particles and (b) precipitation strengthening contributions of all four alloys.

¹It is important to highlight that, as introduced by equations 2.4 and 2.5, *NPP* should be taken as an adimensional value. It stems from a critical nucleation radius assuming an interfacial energy per unit area of 1 J/m².

	C	Cr	Ni	Ti	Mo	Al	Cu	Co	Nb	N	V	Mn	Si
Min	0.05 (0.03 ²)	12.00	1.00	0.01	0.50	0.01	0.50 (2.50 ²)	0.01	0.01	0.01	0.01	0.50	0.30
Max	0.20 (0.30 ⁴)	20.00	15.00	1.50 (2.25 ² , 2.00 ⁴)	10.0 (1.50 ³ , 2.00 ⁴)	1.00	10.00 (2.50 ² , 2.00 ⁴)	2.00 (15.00 ⁴)	0.10 (1.00 ⁴)	0.01	0.20 (0.30 ¹ , 1.00 ⁴)	0.50	1.00

TABLE 4.1. Concentration ranges of all components employed in the prototype alloys design (wt%). The extended composition ranges are indicated by superscripts for the corresponding alloy systems: 1, 2, 3 and 4 refer to alloys Car, NiTi, CuNi and CarCo, respectively.

Alloys		C	Cr	Ni	Ti	Mo	Al	Cu	Co	Nb	N	V	Mn	Si	P	S	Ms(K)
NiTi	Design	0.05	12.26	11.39	2.25	0.50	1.50	0.50	0.52	0.08	0.010	0.20	0.50	0.30			473.09
	Actual	0.06	12.24	11.22	2.21	0.51	1.67	0.59	0.59	0.09	0.005	0.05	0.55	0.37	0.002	0.004	469.13
CuNi	Design	0.03	12.52	9.58	1.50	0.81	1.00	2.50	2.00	0.02	0.010	0.20	0.50	1.00			474.44
	Actual	0.05	12.42	9.27	1.51	0.80	0.95	2.45	2.00	0.04	0.007	0.12	0.54	1.05	0.001	0.003	472.25
Car	Design	0.20	12.00	2.81	1.45	0.50	0.01	5.10	2.00	0.30	0.010	0.01	0.50	1.00			477.48
	Actual	0.20	11.82	2.79	1.36	0.50	0.03	5.07	2.00	0.32	0.014	0.02	0.54	1.02	0.003	0.002	479.20
CarCo	Design	0.30	12.00	5.07	2.00	0.50	0.01	2.00	11.13	1.00	0.010	0.01	0.50	1.00			518.13
	Actual	0.30	11.93	5.43	1.97	0.50	0.01	2.08	11.10	1.01	0.003	0.02	0.60	1.26			508.88

TABLE 4.2. The designed and actual alloy compositions and Ms temperature of alloy NiTi, CuNi, Car and CarCo. Concentrations are in wt%.

4.2 Experimental Procedures

The first three alloys, NiTi, CuNi and Car, were prepared as laboratory casts of 60 Kg approximately. The ingots were vacuum melted, using high purity ingredients to achieve the best cleanness. Phosphorus, Sulphur, Arsenic, Boron and Tin were controlled to the lowest possible levels. The ingots were subsequently soaked at 1523K, rolled to plates of dimension 30x150x1200 mm approximately, and finally air cooled to room temperature. The other alloy, CarCo, was produced in a vacuum induction melting furnace as in ingot of 23 Kg in weight, under an argon protective atmosphere (0.01 Pa). The ingot was ground to smooth its surface, soaked at 1473 K for 2 hours and subsequently forged into a slab of 80x80x300 mm. The slab was reheated to 1473 K for a homogenisation treatment of 2 hours, and subsequently rolled into a plate of 15 mm thickness by 6 continuous passes in the temperature range of 1323-1073 K (Table 4.3), followed by air cooling.

Temperature	1323	1323	1313	1223	1123	1073
Thickness reduction	80-60	60-45	45-34	34-27	27-20	20-15
Reduction ratio %	25	25	24	21	26	25

TABLE 4.3. Hot rolling processing parameters of alloy CarCo.

The chemical analysis of the experimental alloys is given in Table 4.2. In general, the actual alloy compositions of all prototypes correspond rather well to desired ones for all the prototypes. However, notable deviations of Ni, Al and V in alloy NiTi, C, Ni and V in alloy CuNi, Ti in alloy Car, and Ni in alloy CarCo may produce significant differences in phase fractions and the final microstructures, and hence influence the material properties.

The as rolled materials were subjected to various solution treatment conditions and subsequently quenched to room temperature in order to achieve the lath martensite matrix before ageing. The details are discussed in the next section. The solution treated specimens at the best condition were aged at 723, 773 and 823 K from 6 minutes up to one day, followed by air cooling. The tensile specimens were prepared along the longitudinal direction following ASTM standards. The tensile tests were performed at room temperature at strain rate of 10^{-3} /s. The Vickers hardness was measured with load of 1 Kg.

The microstructures were investigated by optical microscopy, scanning electron microscopy (SEM), transmission electron microscopy (TEM) in combination with energy dispersive spectroscopy (EDS). X-ray Diffraction (XRD) was also applied to identify phases. Optical microscopy was carried out on specimens etched with Villela's reagent. Electron microscopy was conducted on samples of the selected

heat treatment conditions. SEM was used for microstructure characterisation with specimens electrochemically etched by 10% Oxalic acid at 15 V and also for the fractography. The TEM investigation was carried out with a Philips CM30T operated at 300 kV and Jeol JEM-2200 FS at 200 kV. The TEM thin foils were firstly mechanically polished to approximately 50 μm in thickness and punched to 1.8 mm in diameter in order to reduce the magnetic effect resulting from the martensitic matrix. Electro-polishing was performed with a universal solution (10% perchloric acid + 90% methanol) maintained at 233 K and 35 Volts, and then the specimens were embedded in copper rings of standard size of 3 mm diameter.

4.3 Characterisation of As-rolled Materials

The microstructures of the slabs after hot rolling were characterised using optical microscopy and SEM on the cross-section along the longitudinal (rolling) direction. Figure 4.2(a) shows the microstructure at the centre of the NiTi alloy slab where a continuous macro crack exceeding 100 μm in width was found. In the adjacent area to the central crack, big second phase particles and micro cracks can be observed, as indicated by the arrows. The big precipitates are identified as TiNbC carbides using SEM-EDX. The microstructure further away from the central cracks looks very different and more homogeneous as shown in Figure 4.2(b) which suggests severe chemical segregation at the centre of the slab. The phases presented at this stage (Figures 4.2(b)-(c)) are austenite matrix with second phases of δ -ferrite and big TiNbC carbides as confirmed by XRD analysis. In addition, smaller precipitates were found along and within the δ -ferrite grains as shown in Figure 4.2(d).

Cracks can also be observed in alloy CuNi at the centre and their sizes are smaller than those in alloy NiTi. The same as in alloy NiTi, the segregation at the centre leads to more precipitation of NbTiC carbides and less δ -ferrite compared to the bulk materials where the microstructures are mainly composed of an austenitic matrix, a small amount of TiNbC carbides and δ -ferrite with finer precipitates along and within their grains as shown in Figures 4.3. It is also important to note that although the segregation at the centre is less severe than in alloy NiTi, clear inhomogeneity along the thickness direction can be identified which led to some banded martensite structure close to the centre as indicated in Figures 4.3(a)-(c).

The alloys Car and CarCo are more homogeneous throughout the entire slabs and their microstructures are shown in Figures 4.5 and 4.6. In both alloys, the matrix was found to be martensitic as confirmed by XRD. Significant amounts of TiNbC carbides were also observed both intergranularly and intragranularly, with bigger amounts in alloy CarCo due to the higher C concentration. Results of EDX analysis on the carbides in alloy CarCo are shown in Figure 4.6(b) which suggests that the precipitates are rich of Ti and Nb. Moreover, in Figure 4.5 some small cracks and δ -ferrite along the prior austenite grain boundaries can be observed.

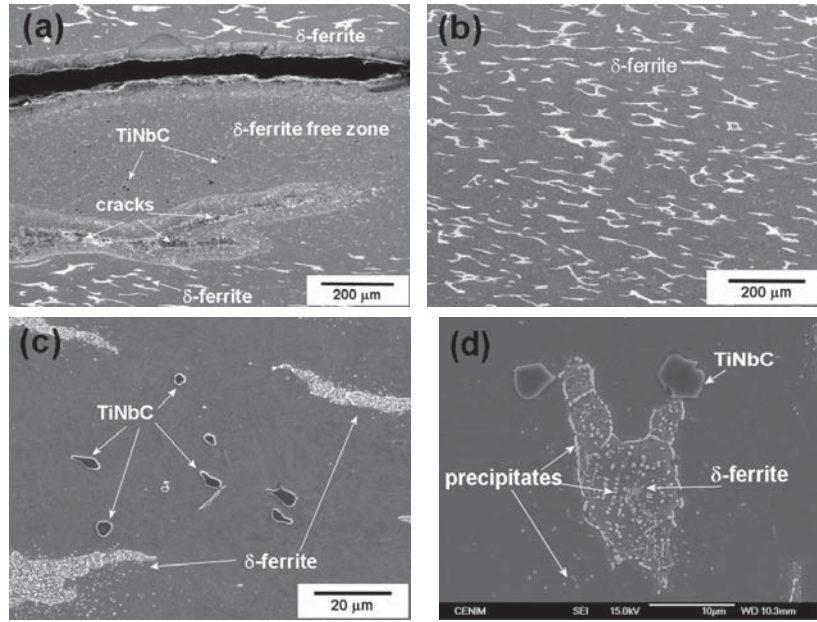


FIGURE 4.2. SEM Micrographs of alloy NiTi on the longitudinal cross section in the as hot rolled condition: (a) at the center, (b)-(d) in the bulk of the slab. The specimens were electrochemically etched by 10% oxalic acid at 15 Volts.

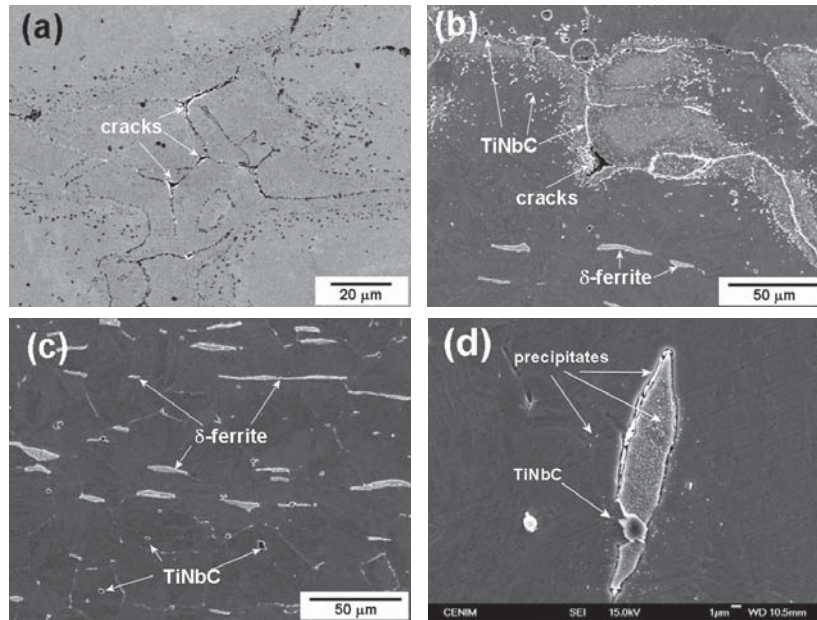


FIGURE 4.3. SEM Micrographs of alloy CuNi on the longitudinal cross section in the as hot rolled condition: (a) at the centre (non etched), (b) at the centre (etched) and (c)-(d) in the bulk of the slab (etched). The specimens were electrochemical etched by 10% Oxalic acid at 15 Volts.

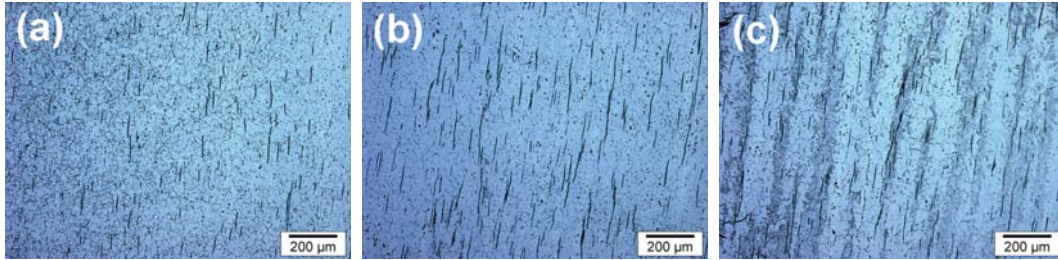


FIGURE 4.4. Optical micrographs of alloy CuNi on the longitudinal cross section in the as quenched condition from the surface (a) to the centre (c) of the slab. The specimens were electrochemical etched by 10% Oxalic acid at 15 Volts.

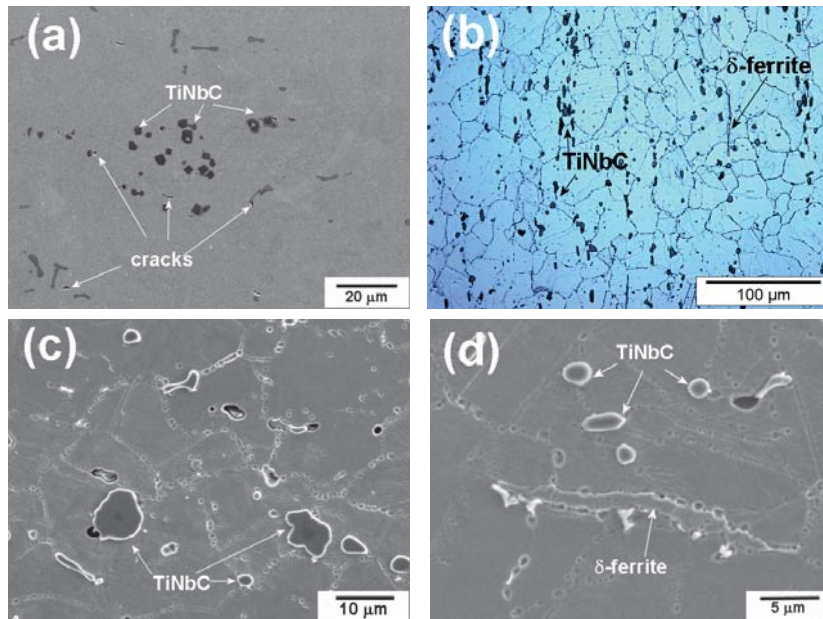


FIGURE 4.5. Micrographs of alloy Car on the longitudinal cross section in the as hot rolled condition: (a) SEM micrograph (non etched), (b) optical micrograph (etched) and (c-d) SEM micrograph (etched). The specimens were electrochemical etched by 10% Oxalic acid at 15 Volts.

4.4 Solution Treatment Optimisation

The hot rolled slabs were cut into small pieces for solution treatment in order to achieve better homogeneity, and aimed at dissolving the undesirable phases from the casting and rolling processes. The solution treatment condition should be selected so as to sufficiently homogenise the solute atoms in the austenite matrix

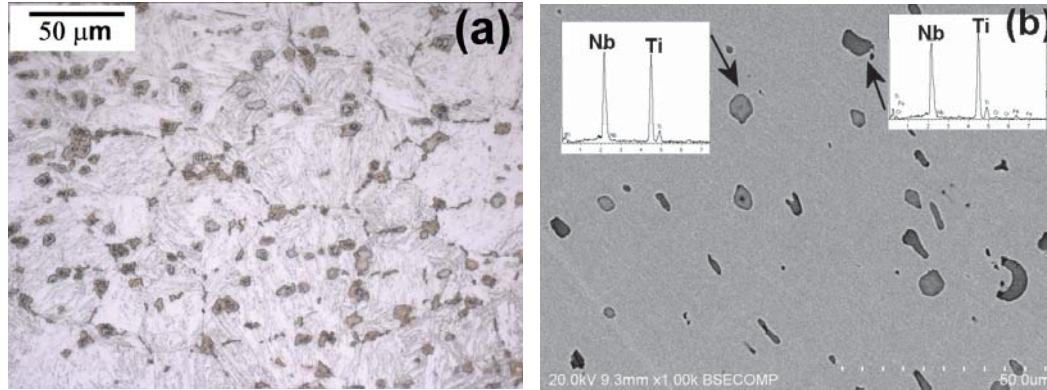


FIGURE 4.6. Micrographs of alloy CarCo on the longitudinal cross section in the as hot rolled condition: (a) optical micrograph (etched by villela's reagent) and (b) SEM micrograph (non etched) with EDX analysis on the selected particles.

while avoiding significant grain growth which may be deleterious for the mechanical properties. To avoid oxidation and decarbonisation, the materials were sealed by double folder Ti-rich stainless steel envelopes to achieve "semi-vacuum" condition, because the envelopes are heated first and the high content of Ti in the envelopes rapidly consumes the oxygen left inside. In addition, the furnace chamber was protected by Ar atmosphere. Different solution treatment conditions were carried out within a temperature range of 1123-1523 K, for the residence times from 5 minutes up to 24 hours. After solution treatment, the specimens were water quenched.

In alloys NiTi and CuNi which possess an austenite matrix with significant amounts of δ -ferrite and some primary carbides TiNbC, the main concern was to dissolve the δ -ferrite and possibly the primary carbides, and hence redistribute the solute and homogenise the matrix which will further transform to martensite upon quenching according to the design criterion of $M_s \geq 473$ K. However, in the temperature and time domains applied, both alloys showed no conditions in which δ -ferrite could be dissolved significantly. Further increase of the solution treatment temperature beyond 1523 K may lead to the formation of a liquid phase and also significant austenite grain growth. On the other hand, solution treatment at temperatures below 1123 K can not achieve solute homogenisation within an affordable time because of the very slow kinetics, and the existing primary carbides may coarsen and other undesirable phase can form as well. Therefore, the δ -ferrite and primary carbides from casting can not be dissolved just by the solution treatment. A better compromise was chosen for a solution treatment temperature of 1423 K and a time of 15 minutes. After water quenching, the matrix partially transformed to martensite and the rest remained as austenite. In order to promote the transformation into martensite, the specimens were cryogenically treated by submersion in liquid nitrogen for 3 minutes. Typical microstructures after solution

treatment and quenching are shown in Figures 4.7 and 4.8, for alloys NiTi and CuNi respectively. In Figures 4.7(b) and 4.8(b), the formation of lath martensite becomes visible.

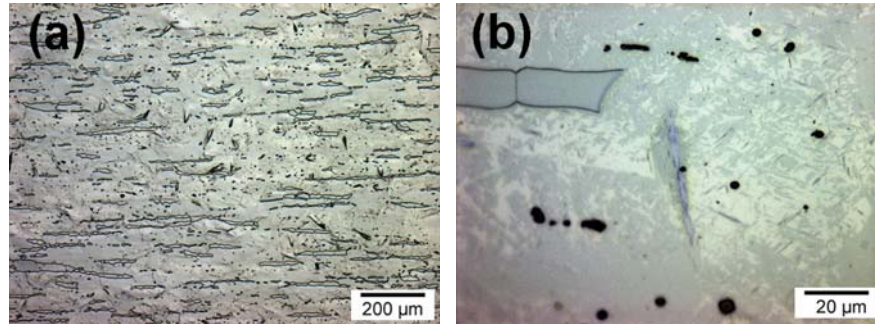


FIGURE 4.7. Optical micrographs of alloy NiTi after solution treatment at 1423 K for 15 minutes and quenching.

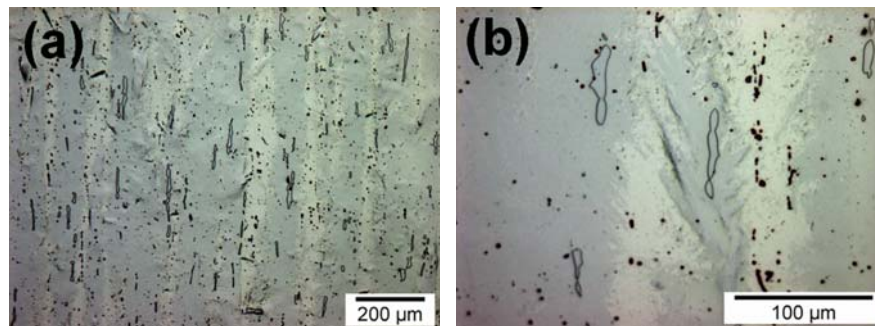


FIGURE 4.8. Optical micrographs of alloy CuNi after solution treatment at 1423 K for 15 minutes and quenching.

Unlike alloys NiTi and CuNi, alloys Car and CarCo utilising MC carbides for strengthening were in the martensitic state after hot rolling. The main purpose of the solution treatment on these two grades is to dissolve the primary carbide TiNbC and release the solutes of C, Ti and Nb so as to form fine precipitates during the following ageing treatment for further strengthening. In general, the primary carbides require very high temperature to be dissolved. Considering industrial practice, the solution treatment was conducted at temperatures from 1273 up to 1573 K. In light of the experimental results, it is claimed that, due to the high content of C in combination with those of Ti and Nb, the primary carbides are very stable and can not be dissolved into the austenite matrix even at 1573K. The amount of carbides almost remains at the same level at various conditions. Considering the fast grain growth at high temperature, the same optimal solution

treatment condition was selected as 1423 K for 15 minutes. Microstructures after solution treatment and subsequent oil quench are shown in Figures 4.9 and 4.10 for alloys Car and CarCo respectively.

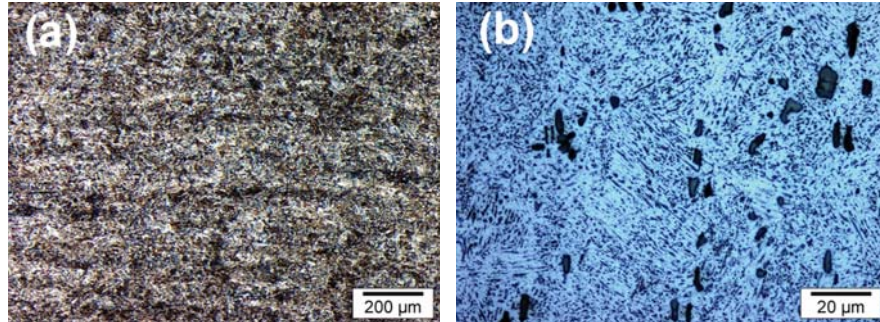


FIGURE 4.9. Optical micrographs of alloy Car after solution treatment at 1423 K for 15 minutes and quenching.



FIGURE 4.10. Optical micrographs of alloy CarCo after solution treatment at 1423 K for 15 minutes and quenching.

4.5 Ageing treatment

The solution treated specimens were subjected to ageing treatment in order to form fine precipitates for strengthening. As discussed in section 3.5, lower ageing temperature leads to more precipitates and slower kinetics while higher temperature results in smaller fraction but faster growth. The experimental optimisation on existing maraging alloys found the optimal ageing temperature to be around 773 K. Given that the prototype alloys were also designed applying ageing temperature of 773 K, the experimental ageing temperature was applied in the range of 723 - 823 K with intervals of 50 K, and times from 6 minutes up to 1 day at each

temperature. The ageing treatments were conducted in a salt bath with neutral salt and followed by natural cooling. The tensile tests were performed at room temperature. The microstructures and hardness were characterised on the cross section of the tensile specimen.

4.6 Results

4.6.1 Mechanical Properties

Variations of hardness, tensile strength and total elongation at fracture, as function of aging time and at different temperatures are shown in Figures 4.11-4.15, for alloys NiTi, CuNi, Car and CarCo respectively. The hardness of alloy NiTi after solution treatment was measured both before and after the tensile test. As shown in Figure 4.11(a), the hardness after tension increases significantly by more than 50%, while no clear ageing hardening can be observed at all ageing temperatures. Figure 4.11(b) shows that the UTS of alloy NiTi of all conditions are in the range of 850-1050 MPa and that the ageing treatment does not show distinct strengthening effects. The alloy NiTi is also found to possess very good ductility up to 55% of the total elongation as indicated in Figure 4.11(c). In most cases, the stress-strain curves of alloy NiTi show double yield feature as shown in Figure 4.12(a). The double yield phenomenon can be explained by the Transformation Induced Plasticity (TRIP) effect, which results from the martensitic transformation under deformation. This is in agreement with the observation that the hardness increases dramatically after the tensile test at the solution treated condition. Figure 4.12(a) also demonstrates a stress-strain curve with the same heat treatment but showing no double yield effect while the UTS achieve the same level. This maybe because, in that particular specimen, more martensite has already been transformed upon quenching prior to the ageing treatment and no further martensite can be formed upon deformation. The different types of stress-strain curves together with the big scatter in properties also reflect the microstructure inhomogeneity of alloy NiTi.

The mechanical properties of alloy CuNi shown in Figure 4.13 are very similar to those of alloy NiTi. Remarkable hardness increase is observed on the as solution treated specimen after the tensile test. The hardness levels for different ageing treatment conditions remain the same as that for the deformed specimen after solution treatment. The tensile strength is in general higher than that of alloy NiTi while the ductility is lower. The same TRIP effects have been observed in alloy CuNi as demonstrated in Figure 4.12(b). The results also clearly reveal the inhomogeneity as the deviations of properties are even bigger than the variation of mean values of properties at different heat treatment conditions.

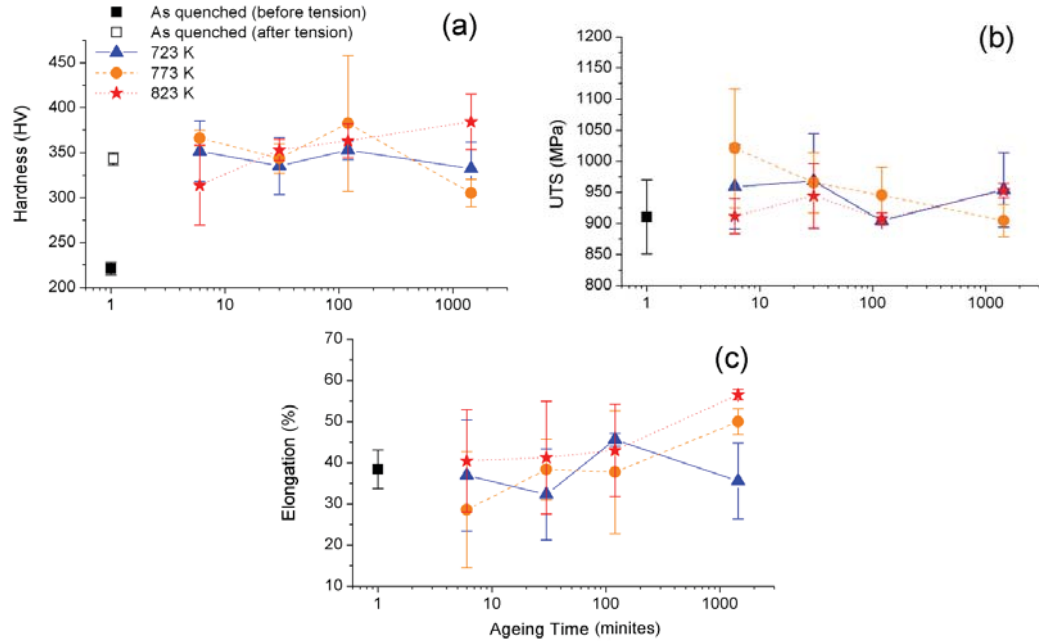


FIGURE 4.11. Variation of hardness, tensile strength and total elongation of alloy NiTi with ageing time. The ageing temperatures are 723, 773 and 823 K respectively.

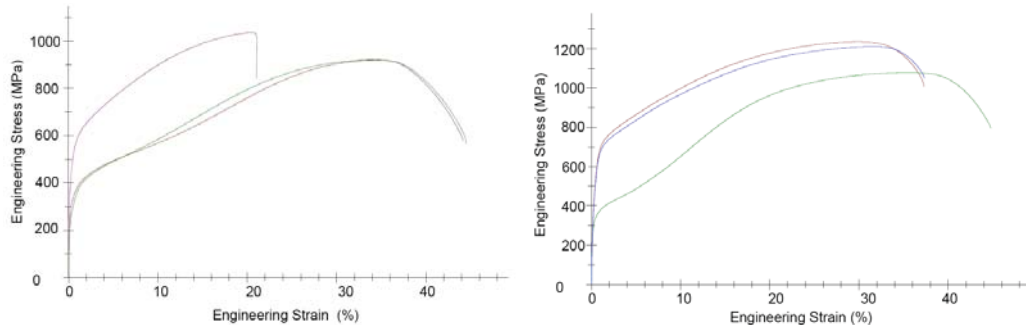


FIGURE 4.12. Typical stress-strain curves of (a) alloy NiTi after ageing treatment at 723 K for 6 minutes and (b) alloy CuNi after ageing treatment at 823 K for 24 hours.

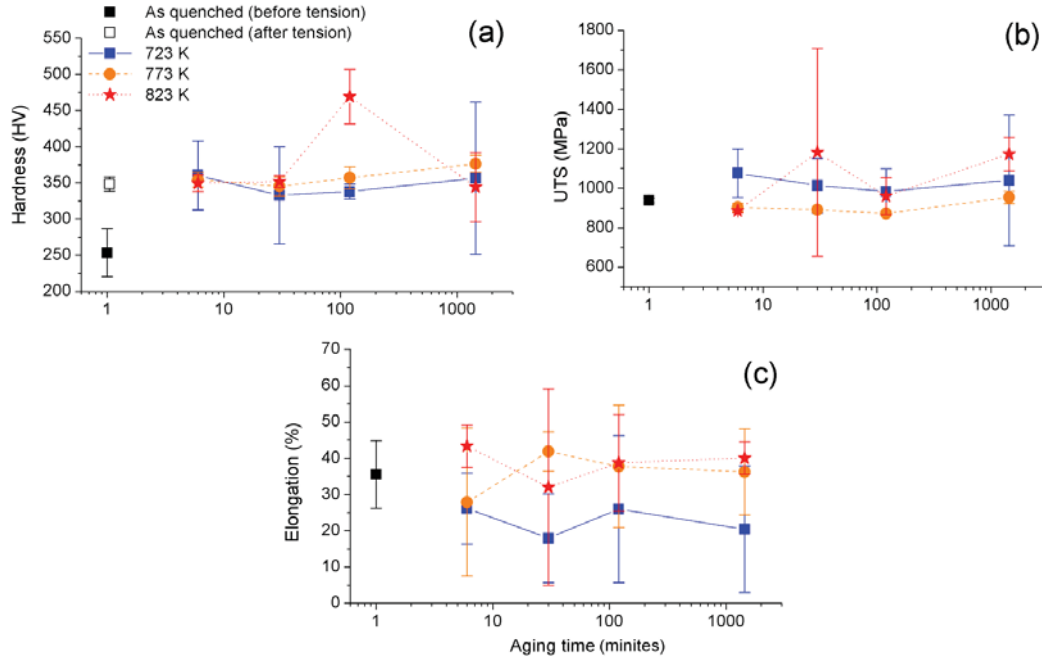


FIGURE 4.13. Variation of hardness, tensile strength and total elongation of alloy CuNi with ageing time. The ageing temperatures are 723, 773 and 823 K respectively.

The variation of hardness as a function of ageing time at different temperatures for alloy Car is shown in Figure 4.14(a). The deformation does not change the hardness on the solution treated specimen because the matrix was already found to be fully martensite as shown in Figure 4.9, therefore, no further hardness increase due to strain induced martensite formation is observed. It was found that the ageing response is fairly rapid at 773 and 823 K at which almost 80% of total increase of ageing hardening is attained within ageing treatment of 6 minutes. The precipitation strengthening kinetics at 723 K seems to be slow and the hardness keeps increasing till the longest ageing time investigated (24 hours). A monotonic hardness increase with respect to ageing time is also observed at the ageing temperature of 773 K and no evidence of overageing has been found up to 24 hours at which the hardness achieves the maximum of 642 Hv. However, at the ageing temperature of 823 K, the ageing hardening shows very different kinetics as the hardness begins to decline after the very short ageing time of 6 minutes. The strength evolution with ageing treatment as shown in Figure 4.14(b) does not display consistency with hardness results: strength decreases with ageing time at 723 K, fairly stays the same values at 773 K and reach peak hardness at 823 K after 2 hours. Nevertheless, because of the bigger deviation of strength in comparison with hardness, which partially results from the fact that tensile test is more sensitive to specimen preparation, the hardness results are considered to be more reliable and reflect the precipitation strengthening kinetics better. Furthermore, most of

the specimens underwent brittle fracture except those aged only for short times at 723 K and for longer time at 823 K, in which case the yield strengths are indicated by empty symbols in Figure 4.14(b) and notable total elongations at fracture can be observed in Figure 4.14(c).

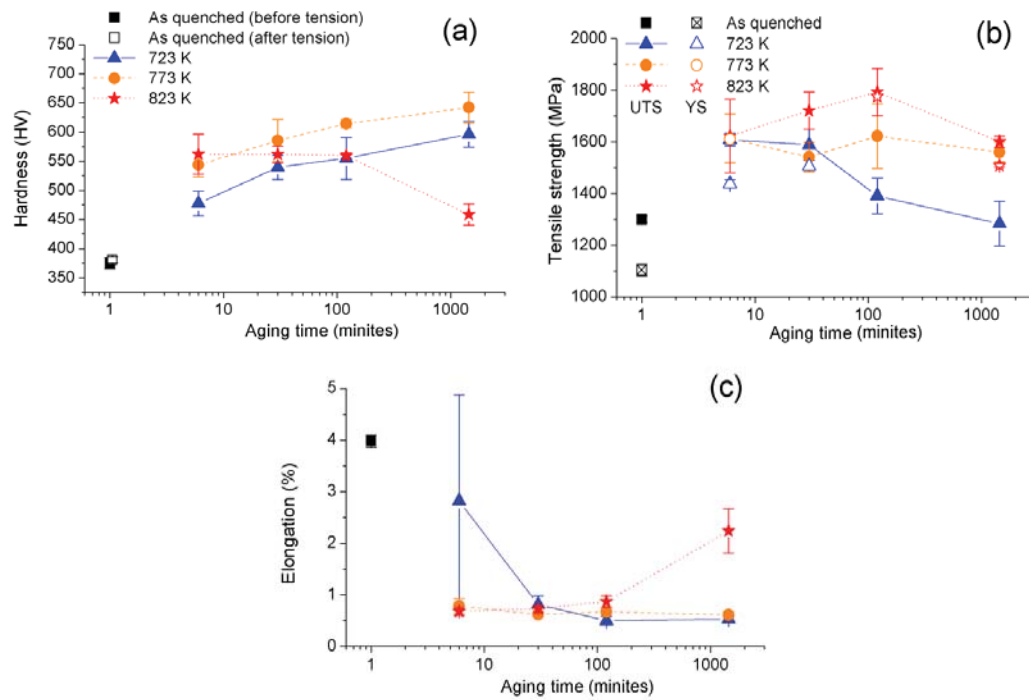


FIGURE 4.14. Variation of hardness, tensile strength and total elongation of alloy Car with aging time. The aging temperatures are 723, 773 and 823 K respectively.

The hardness, tensile strength and total elongation of alloy CarCo are plotted in Figure 4.15 as a function of ageing time. The results indicate very strong ageing strengthening effect, especially for ageing at 723 and 773 K for 24 hours in which the hardness increases from 350 to almost 700 Hv. The precipitation hardening displays slow kinetics for 723 and 773 K in which hardness almost remains the same after 6 minutes ageing, continuously increase with ageing time and at 24 hours, achieve hardness above 650 Hv at both temperature. Ageing at 823 K shows faster precipitation process and overageing occurs after 15 minutes according to the hardness. However, the tensile tests suggest ageing treatment at 823 K displays the best precipitation strengthening contribution, resulting in a UTS around 1700 MPa after 60 and 120 minutes and also some ductility as indicated in Figure 4.15(b) by the numbers adjacent to the strength. A good balance of strength and ductility can be achieved after ageing at 823 K for 24 hours in which the ultra high strength is obtained together with ductility of close to 10 %. Specimens aged

at 723 and 773 K do not show strength as high as that for the samples aged at 823 K though the hardness indicates the opposite.

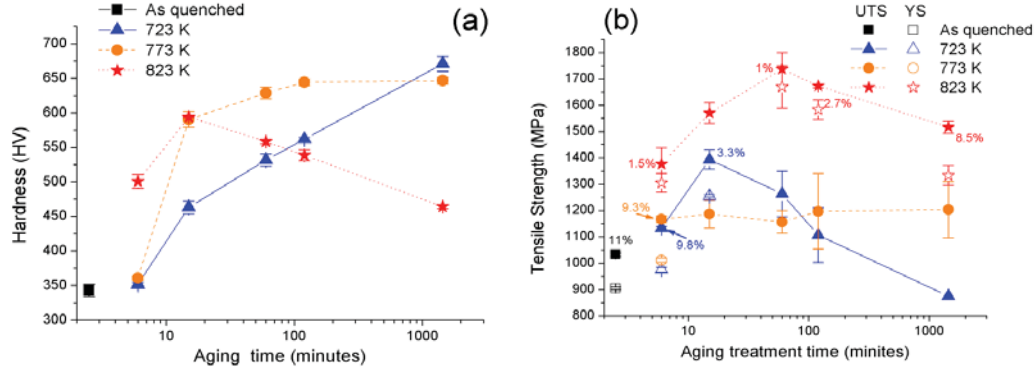


FIGURE 4.15. Variation of hardness, tensile strength and total elongation of alloy CarCo with ageing time. The aging temperatures are 723, 773 and 823 K respectively. The total elongations are only indicated by values in plot (b) on cases which the yield strength and UTS are clearly distinguished.

4.6.2 Microstructures

Representative optical micrographs of selected conditions of alloys NiTi, CuNi, Car and CarCo are shown in Figures 4.16-4.19, respectively. In comparison with Figure 4.7(a), Figure 4.16(a) clearly reveals that more martensite has been formed after the tensile test on the as solution treated condition of alloy NiTi. This corresponds to the TRIP effect as demonstrated in Figure 4.12 and the hardness increase as shown in Figure 4.11(a). For all different ageing treatment conditions of alloy NiTi, the matrix is found to be a mixture of lath martensite and retained austenite. The martensite distribution in Figure 4.16(a) is more homogenous while orientation preference can be observed in some areas as shown in Figure 4.16(b) which may relate to microsegregation and hot rolling. Beside the δ -ferrite and TiNbC primary carbides formed prior to ageing, some newly formed precipitates can be identified in some sections as shown in Figure 4.16(c). This kind of precipitate can only be found in some specific areas and particle size evolution cannot be justified. However, the mechanical properties are not strongly affected by the formation of this precipitate as both hardness and tensile test suggest no notable precipitation strengthening by ageing treatment.

The matrix of alloy CuNi after tensile test contains more of lath martensite than alloy NiTi while the retained austenite can also be clearly distinguished, as displayed in Figures 4.17(a) and (b). It is also found that the inhomogeneous

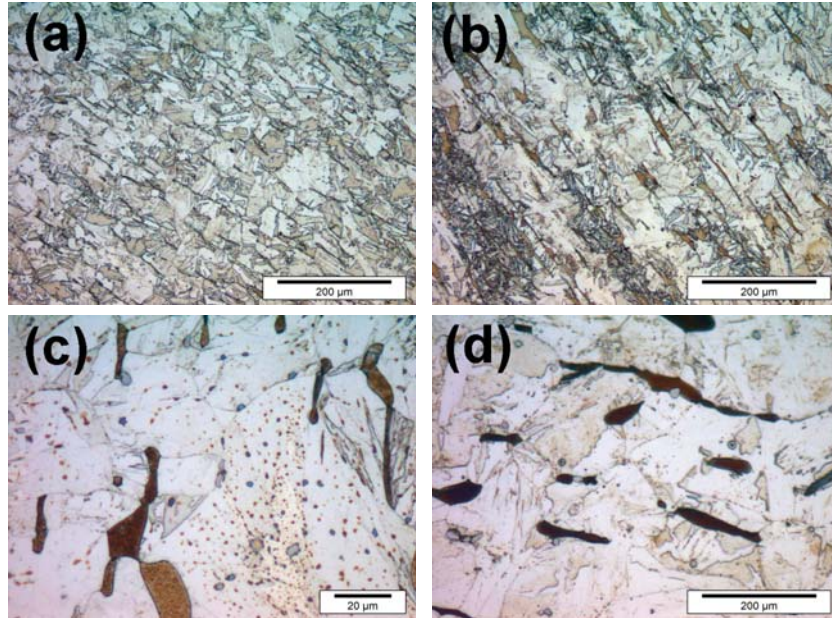


FIGURE 4.16. Optical micrographs of alloy NiTi on the cross section of specimens after tensile test from (a) solution treatment (ST), (b) ST+ageing at 723 K for 24 hours, (c) ST+ageing at 773 K for 30 minutes and (d) ST+ageing at 823 K for 24 hours.

martensitic transformation is very prominent so that even the magnetic character varies between different sections of the specimen due to the different amount of martensite. Severe inhomogeneities have been observed in the per-ageing condition as demonstrated in Figures 4.4, leading to significant deviations in mechanical properties as discussed in previous section. Chemical segregation also results in an inhomogeneous precipitate distribution, as demonstrated in Figure 4.17(c) with a very dense network of precipitates but much less precipitates in Figure 4.17(d). As displayed in Figures 4.13, no significant precipitation strengthening effect has been found but due to the prominent martensitic transformation, the hardness and strength are better than those of alloy NiTi.

In alloy Car, lath martensite matrix forms upon quenching prior to ageing treatment and therefore in all ageing conditions, only lath martensite can be clearly identified as shown in Figures 4.18(a) and (b). Due to the presence of TiNbC primary carbides formed before ageing treatment, the fast and significant precipitation strengthening as shown in Figure 4.14 can only be explained by the formation of another population of precipitates. At the early stages, no precipitates could be identified (as shown in Figure 4.18(b)), but they become distinct after long time ageing at 723 K (Figure 4.18(c)) and 823 K (Figure 4.18(d)) due to precipitate growth and coarsening.

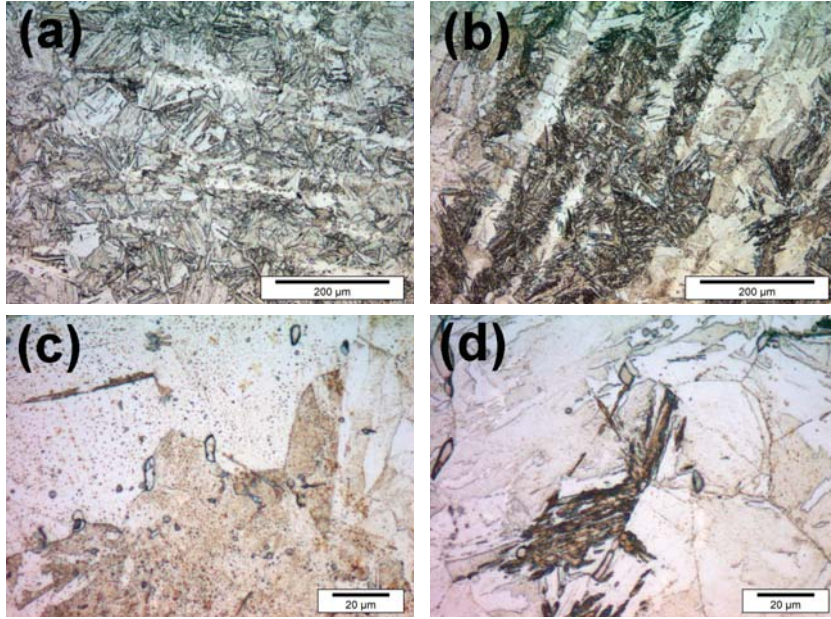


FIGURE 4.17. Optical micrographs of alloy CuNi on the cross section of specimens after tensile test from (a) solution treatment (ST), (b) ST+ageing at 723 K for 24 hours, (c) ST+ageing at 773 K for 24 hours and (d) ST+ageing at 823 K for 24 hours.

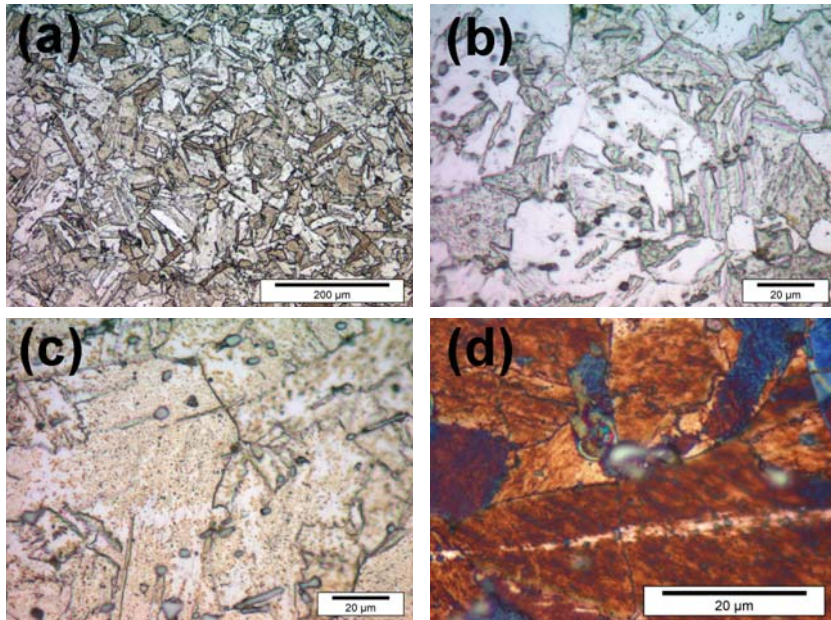


FIGURE 4.18. Optical micrographs of alloy Car on the cross section of specimens after tensile test from (a) solution treatment (ST), (b) ST+ageing at 723 K for 6 minutes, (c) ST+ageing at 723 K for 24 hours and (d) ST+ageing at 823 K for 24 hours.

After ageing treatment, alloy CarCo also shows a fully martensitic matrix with a significant amount of coarsened primary carbides homogeneously distributed in the matrix, the same as observed prior to ageing. However, other smaller precipitates can be found throughout the martensite matrix, as shown in Figure 4.19. The precipitate size and density evolution with time and temperature can not be determined from optical micrographs but obvious differences can be observed in Figure 4.19. Further investigation is required to characterise the precipitation and hence explain the strengthening effects.

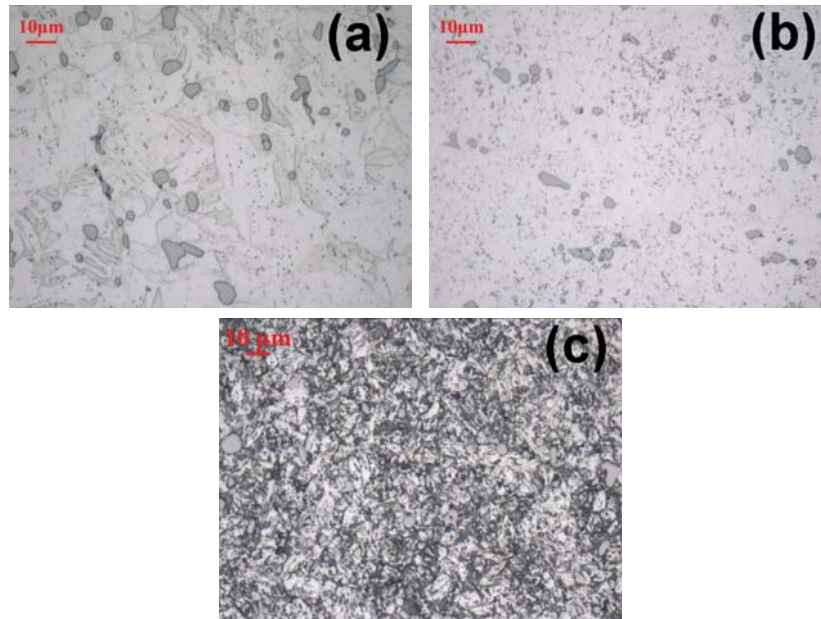


FIGURE 4.19. Optical micrographs of alloy CarCo on the cross section of specimens after tensile test from (a) ST+ageing at 723 K for 6 minutes, (b) ST+ageing at 723 K for 24 hours and (c) ST+ageing at 823 K for 1 hour.

4.6.3 Fractography

The fracture surfaces of alloy CarCo for different aging treatment conditions were investigated by SEM. Figure 4.20(a) shows a typical fracture surface for aging conditions in which no ductility was observed. The fractograph shows no clear dimples. Some ductile fracture regions can be found in the tensile specimen after aging treatment at 723 K for 15 minutes. In these regions, very small and shallow dimples are observed as shown in figure 4.20(b). Big TiNbC carbide particles are indicated by arrows. The dimple structures are easily noticeable for aging conditions of 723 K for 60 and 120 minutes and they become deeper and bigger in

Figures 4.20(c) and (d). The fractography results are consistent with tensile experiments. It can also be observed that the fracture progresses transgranularly for all aging conditions, which can be explained by the presence of intragranular large size TiNbC primary particles and smaller precipitates formed during aging. The limited ductility is due to both the nature of martensite matrix and large TiNbC precipitates throughout the matrix, both intergranularly and intragranularly. If a proper heat treatment could be found to (partially) dissolve the large carbides prior to aging, it will contribute to both ductility and strength via enhanced precipitation of finer carbides.

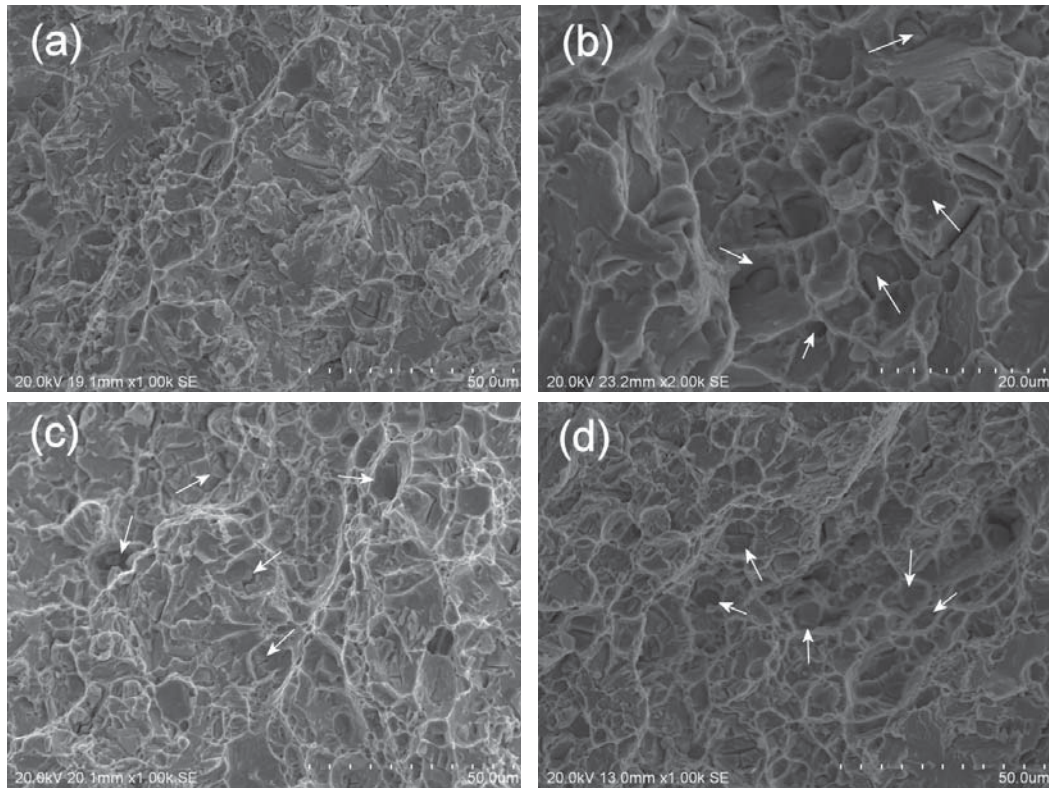


FIGURE 4.20. Fractographs of tensile specimens of alloy CarCo (a) aged at 723 K for 60 mins, (b) 723 K for 15 mins, (c) 823 K for 60 mins and (d) 823 K for 120 mins.

4.7 Discussion

4.7.1 The Presence of Undesirable Phases Prior to Ageing

The presence of primary carbides in the final microstructure of the alloys is very detrimental to mechanical properties such as fracture toughness and thermal-

fatigue life [140][141][142]. Microcracks initiate either at the primary carbide/matrix interfaces or at primary carbides themselves at relatively low stress-intensity factors, and then readily propagate through adjacent primary carbides. The fracture toughness and hardness of the maraging steels may depend mostly on the amount and distribution of the coarse primary carbides and depend partly on the characteristics of the matrix. The mechanical properties can be improved by reducing its volume fraction and/or obtaining a homogeneous distribution of finer primary carbides [143][144]. The presence of δ -ferrite in maraging steels can also lead to inferior mechanical properties (creep resistance, ductility and toughness) and corrosion resistant properties [145][146][147]. Moreover, the formation of primary carbide and δ -ferrite also influences the distribution of alloying elements and therefore affects the martensitic transformation present upon quenching, as well as the subsequent precipitation process during ageing [83].

Thermodynamic equilibrium calculations were performed with ThermoCalc on both designed and actual alloy compositions at solution treatment temperatures of 1123, 1423 and 1523 K. The phases predicted are shown in Table 4.4. The calculations correctly predict the presence of δ -ferrite and primary TiNbC carbides in alloys NiTi and CuNi in the temperature range of 1123-1523 K. The calculation results also suggest that the amount of δ -ferrite in alloy NiTi increases with higher temperature while in alloy CuNi, the amount of δ -ferrite is the lowest at a temperature of 1423 K. Despite of the significant changes of austenite and δ -ferrite fractions, the amount of primary carbides almost remains the same at different solution treatment temperatures. From a more quantitative point of view, the results are also in agreement with experimental observations: a significant amount of δ -ferrite in alloy NiTi, a noticeable amount of δ -ferrite in alloy CuNi and a small amount of TiNbC in both alloys. These calculations therefore provide a theoretical justification to the experimental optima of solution treatment temperature (1423 K) as discussed in section 6.4 at which the amount of δ -ferrite in alloy CuNi is minimal. The choice of 1423 K for alloy NiTi is also reasonable though 1123 K gives the least δ -ferrite amount which was not experimentally observed because of the very slow kinetics. With respect to alloys Car and CarCo, ThermoCalc indicates that TiNbC is the only precipitate presented at the solution treatment and can not be dissolved up to 1523 K. Moreover, the results show that the primary carbide amount at those temperatures is almost the same which is also in good agreement with experimental observations. Furthermore, a lower solution treatment temperature of 1123 will lead to the formation of some δ -ferrite in alloy Car according to the calculations and therefore, 1423 K is a good solution treatment temperature for the alloy Car and CarCo too. Relative to alloy Car, there are more carbides predicted in alloy CarCo because of the higher C concentration.

The presence of phases other than austenite at solution treatment temperature affects the matrix composition, and hence the subsequent martensitic transformation. ThermoCalc calculations suggest that the solubilities of C and Ni in δ -ferrite

		1123 K			1423 K			1523 K		
		Austenite	TiNbC	δ -ferrite	Austenite	TiNbC	δ -ferrite	Austenite	TiNbC	δ -ferrite
NiTi	Design	92.64	0.59	4.70	85.26	0.58	14.16	76.60	0.56	22.85
	Actual	89.30	0.66	8.42	84.44	0.64	14.91	75.90	0.62	23.44
CuNi	Design	88.43	0.39	11.19	94.66	0.28	4.96	90.64	0.36	8.90
	Actual	89.63	0.57	9.81	96.06	0.55	3.38	92.19	0.53	7.28
Car	Design	85.33	2.11	9.79	97.91	2.09	–	97.95	2.05	–
	Actual	90.93	2.14	4.17	97.89	2.11	–	97.93	2.07	–
CarCo	Design	96.23	3.13	–	96.89	3.11	–	96.91	3.09	–
	Actual	96.30	3.07	–	96.95	3.05	–	94.76	3.01	–

TABLE 4.4. Phase equilibrium predictions of prototype alloys by ThermoCalc at various solution treatment temperature. The amounts of phases are in molar percent.

are lower than those in austenite while Ti is higher. Therefore, the formation of δ -ferrite depletes the Ti content, while enriches the C and Ni in the matrix. According to Equation 2.1, C and Ni decrease the Ms temperature but Ti increases it. Consequently, the Ms temperature of the austenite in the prototype alloys becomes lower than those predicted by applying alloy composition without considering the δ -ferrite formation. This justifies that only part of the austenite matrix in alloys NiTi and CuNi can be transformed to martensite upon quenching, especially given that the predicted Ms values of those two alloys in Table 4.2 are exactly on the limit of 473 K. With the influence of δ -ferrite, the Ms temperature of austenite matrix becomes lower than 473 K and the austenite remains metastable after quench. During the tensile test, the martensitic transformation is triggered by the applied stress and therefore the alloys display TRIP effects. With respect to alloys Car and CarCo, the formation of unexpected primary carbides depletes the C in the matrix and hence increases its Ms temperature and further ensures the formation of lath martensite. However, the presence of TiNbC primary carbides also depletes the C, Ti and Nb in the matrix, consequently suppressing the formation of finer MC carbides, aimed at being the main strengthening precipitates.

4.7.2 Identification of Strengthening Precipitates in Alloy CarCo

Given the fact that no age hardening effects were observed in alloys NiTi and CuNi, and also due to the similarity of alloy Car and CarCo, only alloy CarCo was selected for further identification of the precipitates formed during the ageing treatment. Figure 4.21(a) shows a bright field TEM image of alloy CarCo after solution treatment and quenching. It can be seen that the matrix is lath martensite of a few hundred nanometres in width. Inside the lath martensite matrix, some precipitates other than primary carbides can be observed but with much smaller size around 100 nm, as indicated by arrows. It is also important to mention that the distribution of the small precipitate is not homogeneous throughout the matrix and even difficult to find in some area. The precipitates are identified as Laves phase by the diffraction patterns shown in Figure 4.21(a). After ageing treatment at 723 K for 24 hours, which is one of the optimal ageing conditions as indicated in Figures 4.15, there seems to be less precipitates of Laves phase as shown in Figure 4.21(b). Therefore, the Lave phase is taken not to be responsible for the significant ageing strengthening. Nevertheless, no other strengthening precipitates can be observed given the magnification of Figure 4.21(b). The bright field TEM image of specimen after ageing treatment at 773 K for 24 hours is very similar to Figure 4.21(b) and this condition was investigated by High Resolution TEM. It can be observed in Figure 4.21(c) that a very dense network of nano precipitates of size lower than 10 nm are homogeneously distributed in the lath martensite matrix. The finely dispersed precipitates are identified as Ni_3Ti by the diffraction pattern as shown in Figure 4.21(d) and are believed to be the reason of the significant strengthening increase during ageing. The highly dispersed nanosized Ni_3Ti precipitates, which

remain the very small size and do not coarsen even after long ageing, have also shown to lead to a significant strengthening effect in other maraging steels [148][53].

Thermodynamic equilibrium calculations were also performed with the actual alloy composition at the aging temperatures of 723, 773 and 823 K. The results are compared to predictions at solution treatment temperature and shown in Table 4.5. As discussed in previous section, the TiNbC carbide is stable at 1423 K and hence the formation of the primary carbides consume most of the solutes of carbide formers. Moreover, the equilibrium molar fractions of TiNbC at various ageing temperatures are also at similar levels as the solution treatments, indicating the TiNbC carbide population will not significantly change during aging except by coarsening of the existing primary carbides after long times. However, the thermodynamic calculations predict that the Ni₃Ti intermetallics are also stable at aging temperatures of 723-823 K, which can provide remarkable strengthening effects as shown in Figure 4.1. Therefore, the thermodynamic calculations further confirm that the Ni₃Ti intermetallic precipitates are the principal strengthening system in alloy CarCo. Furthermore, the laves phase is also predicted at 823 K although not at the solution treatment temperature. The formation of Laves phase in the as quenched condition may result from microsegregation and hence shows a inhomogeneity distribution as experimentally observed. During ageing, the Laves phase tend to be stable at 823 K and may be subjected to slow dissolution at lower temperature according to the calculations.

Temperature (K)	Austenite	TiNbC	δ -ferrite	Ni ₃ Ti	Laves phase
1473	96.95	3.05	–	–	–
823	–	3.01	–	2.82	0.51
773	–	2.99	–	2.93	–
723	–	2.97	–	3.33	–

TABLE 4.5. Phase equilibrium Predictions of alloy CarCo at solution treatment temperature 1423 K and ageing temperature 723, 773 and 823 K. The amounts of phases are in molar percent.

4.8 Conclusion

The first round of prototype alloys employing Ni₃Ti (alloy NiTi), Cu and NiAl/Ni₃Ti (alloy CuNi), MC carbides (alloy Car) and MC carbides with high Co content (alloy CarCo) were designed applying the models presented in Chapter 2 and 3. The prototype alloys have been fabricated and characterised employing various techniques. In all prototype alloys, undesirable phases of TiNbC primary carbides

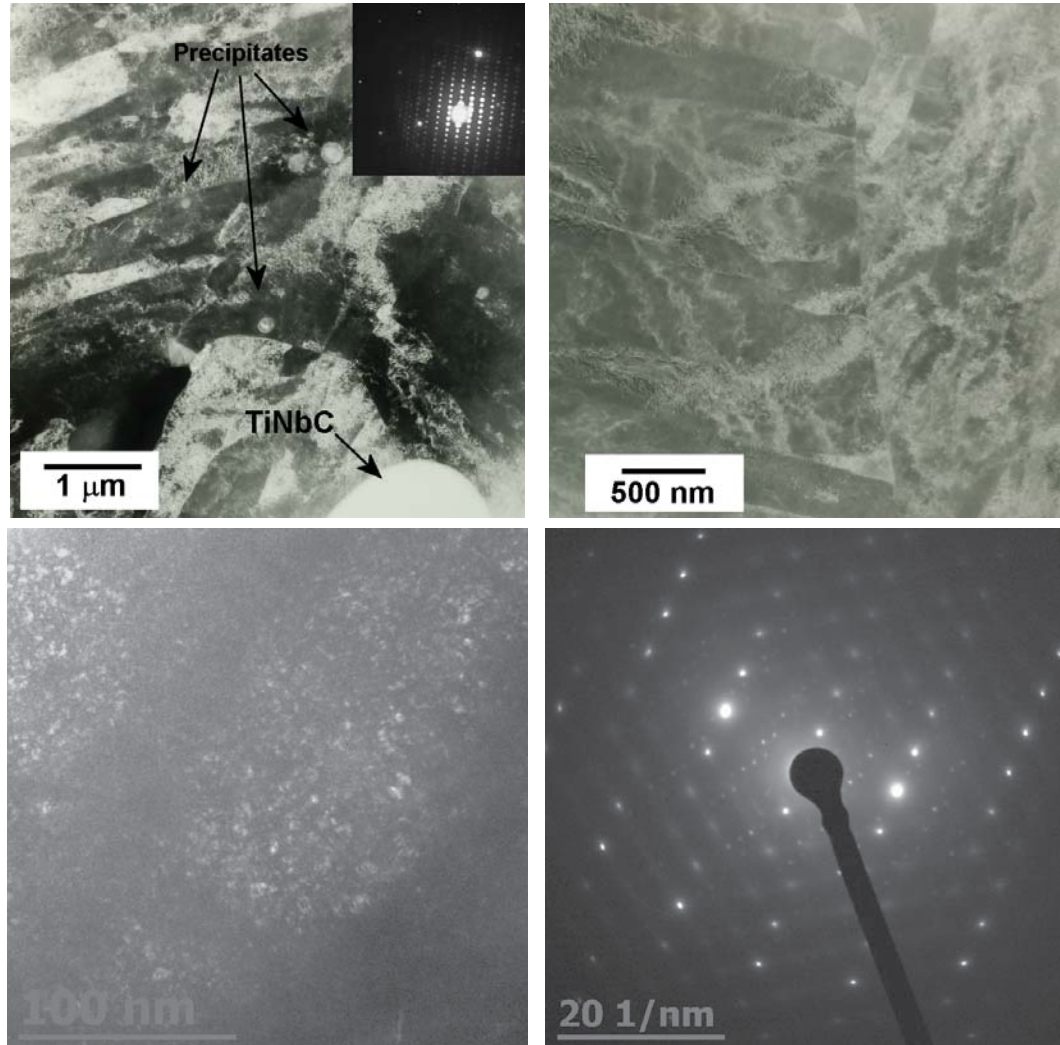


FIGURE 4.21. TEM investigations of alloy CarCo: (a) bright field TEM image and corresponding diffraction pattern of precipitates in the as quenched condition, (b) Bright field image after ageing at 723 K for 24 hours, (c) dark field HRTEM image after ageing at 773 K for 24 hours and (d) the corresponding diffraction patterns of both matrix and precipitates.

and/or δ -ferrite were observed in the pre-ageing condition and could not be dissolved by homogenisation treatment. The presence of these undesirable phases influences the austenite matrix composition, and hence the martensitic transformation upon quenching. Moreover, it also jeopardises the formation of desirable strengthening precipitates.

In the pre-ageing condition of alloy NiTi and CuNi, the microstructures were found to contain δ -ferrite and TiNbC primary carbides which could not be dissolved by solution treatment. The austenitic matrix was only partially transformed to martensite upon quenching. The results of mechanical tests did not show notable ageing precipitate strengthening, while a good combination of high strength and ductility was achieved because of the TRIP effect. The alloys Car and CarCo displayed fully lath martensite matrix as designed, but with a significant amount of primary carbides formed during casting. The primary carbides remain stable at solution treatment and therefore can not release solutes to form strengthening precipitates of finer TiNbC carbides during aging and limit fracture strength levels due to their crack initiating effect. Nevertheless, obvious ageing strengthening effects have been observed in alloys Car and CarCo leading to ultra high strength above 1.6 GPa as well as some ductility. The strengthening precipitate in alloy CarCo was found to be a finely dispersed population of nanosized Ni_3Ti .

The results clearly suggest that assuming that the matrix is fully in the austenitic state during solution treatment, and hence transforms to martensite upon quenching, does not hold true for all alloy compositions. However, the ThermoCalc calculations on prototype alloys can well predict the presences of δ -ferrite, TiNbC primary carbides, as well as the strengthening precipitates observed during ageing. These lead to the conclusion that, the current thermodynamic aided alloy design approach employing ThermoCalc is validated but demands further improvement which should be focused on the implementation of suitable criteria for the pre-ageing treatment so as to avoid the formation of undesirable phases.

5

An Integrated Model Incorporating both Composition and the Full Heat Treatment Cycle

5.1 Introduction

As discussed earlier in section 2.2.4, the desirable microstructures for UHS stainless steels can be obtained by a sequence of heat treatments: solutionising to achieve a homogenous fully austenitic state, followed by quenching to room temperature for generating the martensitic matrix, and further ageing at a modest temperature, to allow for precipitation in a finely grained matrix structure. However, the models developed in Chapter 2 and 3 are mainly focused on the ageing stage by assuming only austenite is present during the austenisation stage which is subsequently transformed to a fine lath martensitic matrix upon quench. Such matrix fosters the precipitation of the finely dispersed desired phases. Nevertheless, the first prototype alloys presented in Chapter 4 clearly show that there are undesirable phases present other than austenite at the end of the austenisation stage, which remain in the martensitic matrix after quenching, and therefore strongly affect the precipitation process in the ageing treatment and hence the mechanical properties of the alloy.

Undesirable phases left over from casting and high temperature homogenisation steps in the steels concerned include primary carbides (MC/M_2C), δ -ferrite and retained austenite. The primary carbides form during solidification both intergranularly and intragranularly, and they display a low number density per unit volume but a large size [106][132]. They frequently act as crack initiators and may also cause intergranular corrosion, although some intergranular carbides may display

a positive pinning effect on limiting the growth of prior austenite grains during austenisation/solution treatment. For some conditions, all or part of the primary carbides can be dissolved during the austenisation/solution heat treatment, and subsequently reprecipitate as a fine secondary strengthening phase during the ageing treatment, or when these materials are subjected to high-temperature applications [132]. Moreover, δ -ferrite normally appears in the as cast condition and its volume fraction decreases during austenisation and solution treatment [83]. The presence of δ -ferrite in maraging steels can lead to inferior mechanical and corrosion resistant properties [145]. More importantly, the content of δ -ferrite also influences the distribution of alloying elements and therefore affects the martensitic transformation present upon quenching, as well as the subsequent precipitation process during ageing [83]. The retained austenite in the pre-ageing condition may increase the ductility while decrease the strength. However, austenite which transforms into martensite upon quenching and its retained form are thermodynamically identical, and therefore cannot be tackled employing our computational framework without invoking kinetic or other stability criteria.

In this chapter, the pre-ageing heat treatment will be taken into account in the alloy optimisation scheme in order to avoid the presence of undesirable phases. The entire heat treatment (austenisation and ageing) will be accounted for in an integrated manner, where the chemical composition and temperature determine phase stability at the various stages. Employing the same precipitation scenarios as in earlier chapters, the new alloys composition, together with corresponding optimal ageing and austenisation temperatures will be designed simultaneously.

5.2 Integrated Model

While keeping the genetic optimisation framework unchanged, the optimisation algorithm is adjusted to account for new criteria related to the austenisation treatment. The entire process is explained in this section following the order in which the heat treatments are performed.

5.2.1 *Austenisation/Solution Treatment*

In practice, the austenisation and the solution treatment are two separate processes. However, they are given the same relevance in the calculation in terms of avoiding undesirable phases in the pre-ageing condition. Thermodynamic equilibrium is therefore calculated at only one pre-ageing temperature, denoted as T_{Aus} . It is desired to obtain a near pure austenitic matrix of similar composition to the alloy. Such matrix should fully transform into lath martensite upon quenching provided the M_s criterion is met. The criterion takes the form of a go/nogo condition requiring an equilibrium austenite volume fraction larger than 99% in volume at

T_{Aus} . Therefore, the maximum amount allowed for all undesirable phases including primary carbides and δ -ferrite is 1 % in volume. Due to the positive pinning effects of primary carbides, the amount of primary carbides itself is limited at a maximum level of 0.5 % in volume. The candidate solutions will only be further assessed given that these two criteria are fulfilled. The entire solution evaluation algorithm is shown in Figure 5.1.

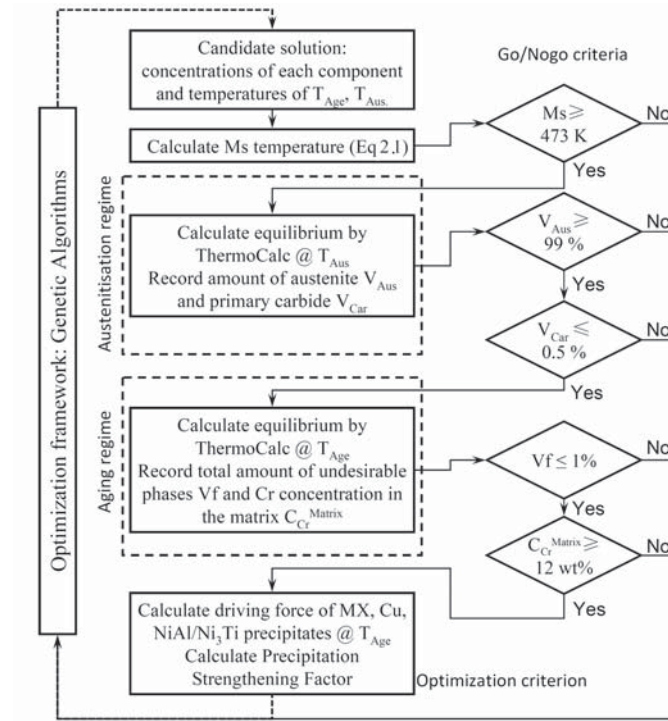


FIGURE 5.1. Algorithm of the thermodynamic calculation and criteria evaluation.

5.2.2 Martensite Formation

To ensure full lath martensitic structures upon quenching, the M_s temperature, as estimated by Equation 2.1, is enforced as before via a go/nogo criterion of $M_s \geq 473 \text{ K}$. Due to the explicit expression of M_s temperature as a function of the alloy composition, the M_s criterion is evaluated before the thermodynamic calculation at austenisation temperature so as to save computation time. The solutions not fulfilling the criterion are discarded as illustrated in Figure 5.1.

5.2.3 Ageing Treatment: Precipitation in a Cr-rich Matrix

Ageing is the key treatment for maraging steels as it determines the type of precipitates and populations to be formed in the lath martensite matrix. For candidate solutions fulfilling all previous criteria, the thermodynamic equilibrium is calculated at the ageing temperature, denoted as T_{Age} by ThermoCalc. The amounts of undesirable phases are summed up and a maximum allowed volume fraction of all those phases together is less than 1% is enforced as a go/nogo criterion. The critical Cr concentration in the matrix upon completion of precipitation is artificially set at $C_{Cr}^{matrix} \geq 12$ wt% in order to ensure the formation of a Cr-rich corrosion resistant film. Only solutions (composition and temperatures) fulfilling all criteria are taken as a valid candidate for the next appraisal: the precipitation strengthening contribution according to Equation 3.3. The calculation of strengthening factor (fitness function) completes the evaluation of the candidate solution and will be used to reproduce offspring solutions in the genetic algorithm framework.

5.3 Model Application

The same alloying components and their concentration ranges (Table 2.1) as used in the earlier chapters are employed in the application of the new model. In addition, the ageing temperature and austenisation/solution treatment temperature are allowed to vary within the range of 698-853 K and 1223-1533 K with intervals of 5 and 10 K, respectively.

Three alloy scenarios involving different strengthening precipitate systems are explored: 1) MC carbides, 2) Cu particles and 3) Ni-rich intermetallics (NiAl and Ni₃Ti). The alloys resulting from these systems will be hereon termed alloy families 1, 2 and 3, respectively. Two series of alloys are computationally designed: C series (1C, 2C and 3C) with fixed T_{Age} of 773 K and T_{Aus} of 1473 K, and D series (1D, 2D and 3D) in which T_{Age} and T_{Aus} are allowed to vary in the ranges mentioned above. The alloy compositions, T_{Age} and T_{Aus} are summarised in Table 5.1. For comparison purpose, the compositions found in Chapter 3 (not taking into account the austenisation/solution treatment effects) are also listed in Table 5.1. They are, termed alloys 1A-3A (for a fixed ageing temperature of 773K) and alloys 1B-3B (for a variable ageing temperature), respectively.

From Table 5.1 it can be concluded that the concentrations of C and Ti in alloys 1C and 1D have decreased significantly with respect to those for alloys 1A and 1B. This is because the high C and Ti contents in alloys 1A and 1B lead to the formation of a considerable amount of primary carbides as experimentally observed (Chapter 4). Moreover, the concentrations of V and Nb are higher in alloy 1D than in 1C by allowing the austenisation temperature increase from 1473 K to

	C	Cr	Ni	Ti	Mo	Al	Cu	Co	Nb	N	V	Mn	Si	T _{Age}	T _{Aus}
Alloy1A	0.20	12.00	2.81	1.50	0.50	0.01	5.10	2.00	0.10	0.01	0.01	0.50	1.00	773	NA
Alloy1B	0.20	12.00	2.81	1.50	0.50	0.01	5.10	2.00	0.10	0.01	0.01	0.50	1.00	738	NA
Alloy1C	0.08	12.00	3.26	0.39	0.50	0.01	0.50	1.04	0.05	0.01	0.03	0.50	0.32	773	1473
Alloy1D	0.08	12.00	4.61	0.35	0.50	0.01	5.10	0.27	0.10	0.01	0.20	0.50	0.64	743	1533
Alloy2A	0.05	12.26	1.00	0.01	0.50	0.01	10.00	1.04	0.10	0.01	0.13	0.50	1.00	773	NA
Alloy2B	0.05	12.26	1.00	0.01	0.50	0.01	10.00	1.04	0.10	0.01	0.10	0.50	1.00	738	NA
Alloy2C	0.05	12.00	3.26	0.44	0.50	0.01	8.16	1.65	0.10	0.01	0.03	0.50	0.64	773	1473
Alloy2D	0.05	12.00	2.81	0.20	0.50	0.01	8.77	1.55	0.10	0.01	0.03	0.50	1.00	718	1523
Alloy3A	0.05	12.26	11.39	1.50	0.81	1.00	0.50	2.00	0.07	0.01	0.18	0.50	1.00	773	NA
Alloy3B	0.05	12.00	11.39	1.50	1.11	1.00	0.50	2.00	0.01	0.01	0.10	0.50	1.00	733	NA
Alloy3C	0.05	12.00	11.39	0.73	0.81	1.00	0.50	2.00	0.05	0.01	0.01	0.50	0.91	773	1473
Alloy3D	0.05	12.00	11.39	1.12	0.81	1.00	0.50	2.00	0.01	0.01	0.20	0.50	0.95	728	1533

TABLE 5.1. Compositions and heat treatment temperatures of designed alloy systems 1 (Carbide based), 2 (Cu based) and 3 (Ni3Ti/NiAl based), considering only ageing treatment at fixed temperature of $T_{Age}=773$ K (A series) and varying T_{Age} (B series); considering both ageing and austenitisation/solution treatment at fixed $T_{Age}=773$ K and $T_{Aus}=1473$ K (C series) and varying T_{Age} and T_{Aus} (D series). Concentrations are in weight percent.

1553 K. The V concentration is even higher than alloys 1A and 1B. This is due to V having a higher solubility in austenite. Furthermore, because of the partial substitution of Ti by V, the ability to form secondary MC carbides during ageing remains maximised while avoiding the primary counterparts during austenisation. However, the amount of carbide strengthening precipitates is expected to decrease due to the lower C concentration. Ni, Co and Si also adjust their concentrations to follow other go/nogo criteria.

In alloys 2C and 2D, the concentration of Cr decreases slightly while that of Ni increases. This is expected as Ni is a strong austenite stabiliser and Cr is a ferrite stabiliser. The concentration of Ti increases while V decreases; Cu decreases but Co increases. This is all because of the solubility of alloying elements in austenite and their effects on the formation of other undesirable phases such as δ -ferrite and primary carbides. The new criteria based on austenisation seems to have insignificant effects on alloys 3C and 3D because of the high Ni and Al concentrations leading to NiAl/Ni₃Ti precipitation can be well dissolved in austenite.

For all alloys 1-3, the optimal austenisation temperatures in D series tend to be close to the upper limit in order to increase the solubility of alloying elements while avoiding the formation of δ -ferrite. The best ageing temperature to stimulate the formation of desirable strengthening precipitates is lower than the fixed value of 773 K, but the new temperature still falls within the range of the experimentally determined optima.

5.4 Discussion

In order to illustrate the effect of the new austenisation criteria on the precipitation strengthening capability, the overall strengthening contribution for the three systems and the four optimisation strategies employed so far are compared in Figure 5.2. The precipitation strengthening factor of alloy 1 is drastically decreased for alloys 1C and 1D because of the C decrease required for avoiding primary carbides during austenisation. In alloys 2C and 3C, the strengthening contributions of Cu and NiAl/Ni₃Ti precipitates also drop notably, while through increasing austenisation temperature and decreasing ageing temperature, they can be well compensated and become comparable to those in the A and B series. The volume fractions, precipitation driving forces and normalised precipitation strengthening contributions of each precipitate in alloys 1D-3D are plotted in Figure 5.3(a)-(c) respectively. For validation purposes, in Figure 5.3 the model was also applied to 11 commercial precipitate strengthening steels which are grouped according to their main strengthening systems. Although the precipitation strengthening factors are lower than those displayed by the A and B series (Figure 5.2), the new alloys 1D-3D still show improved strength levels over their existing counterparts. It is also

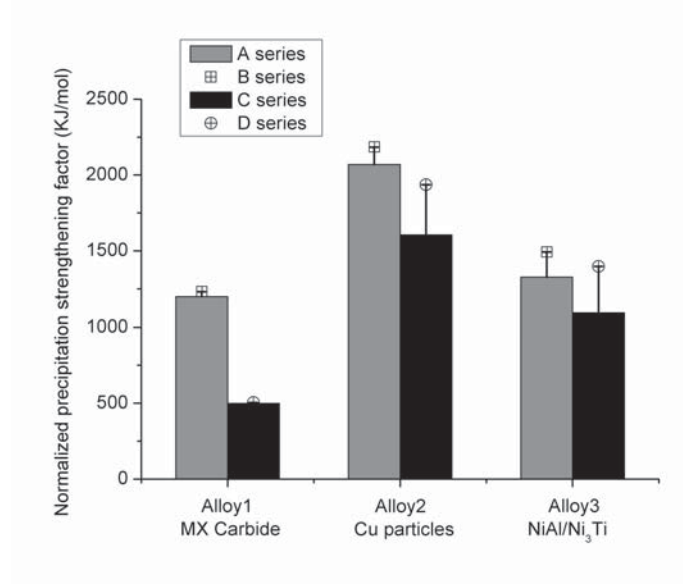


FIGURE 5.2. Comparison of normalized precipitation strengthening contributions of alloys 1-3, A-D series.

important to point out that all new alloys 1D-3D possess multiple strengthening precipitate systems despite the fact that they were designed to be strengthened by one kind of precipitate only. The formation of the additional desirable precipitate species will further contribute to the alloy strength.

To demonstrate the effects of all criteria on alloy composition optimisation, alloy 1A was taken as the baseline to explore the binary compositional effects of C-Ti and C-Cr, (keeping the levels of all other elements as found by the optimisation scheme) as shown in Figure 5.4 and Figure 5.5 respectively. For this purpose, the composition domains studied have been extended beyond the original search ranges in Table 2.1, marked by the two orthogonal solid lines in the bottom or top left corner. The colour contour of the background in these figures indicates the degree of strengthening contribution obtained due to precipitation at 773 K. The black vertical patterns in Figures 5.4(a) and 5.5(a) superimposed on the colour coded background display the (forbidden) composition domains where M_s temperature is below 473 K; the horizontal black pattern masks the (forbidden) area in which the total amount of undesirable phases is over 1% in volume and the forward slash region shows the (forbidden) domain where Cr concentration is below 12 wt% after the completion of precipitation. The scattered black spots show compositions where ThermoCalc equilibrium calculations were not successful. The unhashed areas in Figures 5.4(a) and 5.5(a) unveil the composition domains in which precipitation strengthening factor is maximised, while meeting the constraints mentioned above. The star symbols show the concentration value of alloy 1A, which is located exactly

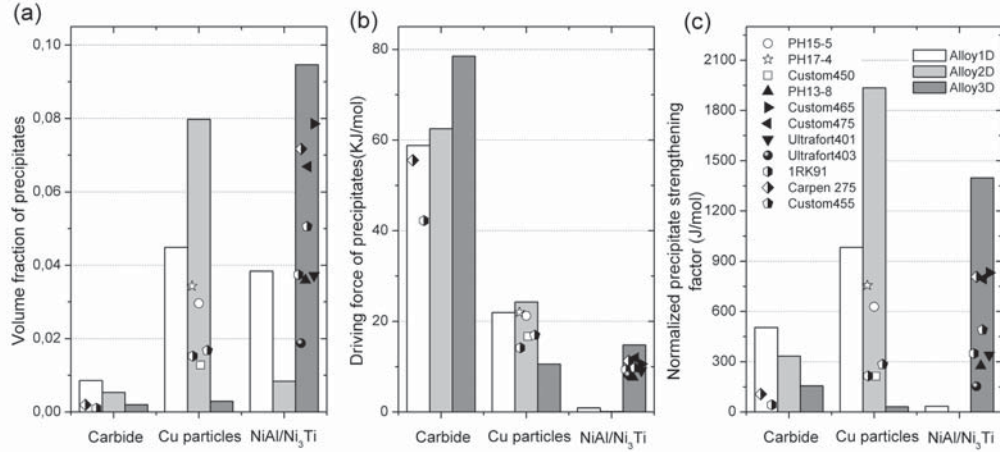


FIGURE 5.3. Comparison of designed (1D-3D) and existing grades: (a) volume fraction of precipitates, (b) driving force for precipitation and (c) normalized precipitation strengthening factor. The symbols indicate values for commercial steels.

at the maximum strengthening level in the uncovered area of the searching domain. Imposing the new criteria of austenisation treatment as discussed previously, the compositional domain where austenite volume fraction is less than 99% at 1473 K is masked by white horizontal lines and the area where the primary carbides volume fraction at 1473 K exceeds 0.005 is indicated by the vertical white line pattern. It can be seen in both Figures 5.4(b) and 5.5(b) that, the new criteria imposed covers all of the search area. In agreement with the experimental results shown in Chapter 4, if all criteria are applied simultaneously, Figures 5.4(c) and 5.5(c) suggest that there are no solutions for C, Ti and Cr concentrations, given the condition that concentrations of the remaining elements are the same as in alloy 1A. Therefore, the new optimal composition considering austenisation treatment has to be found somewhere else in the entire search domain.

The same type of plot is generated based on alloy 1D, which was optimised for the carbide system considering the entire heat treatment. The components and temperatures are paired as C-Ti, C-Cr, C-T_{Age} and C-T_{Aus}. The results are shown in Figures 5.6-5.9, respectively. In Figure 5.6(a), a large open area can be observed while most of it (the high C and high Ti region) is covered in Figure 5.6(b) because the formation of primary TiC carbide violates the criteria of austenite fraction and primary carbides itself. However, there is still a solution area meeting all criteria (Figure 5.6(c)) in which the black star shows the location of highest strength level which is exactly the composition of C and Ti of alloy 1D. Figure 5.7 shows the same trend that high carbon concentration tends to promote the formation of primary carbides as demonstrated by the vertical white lines in Figure 5.7(b) and high Cr content leads to formation of non-austenite phase due to the limited solubility of

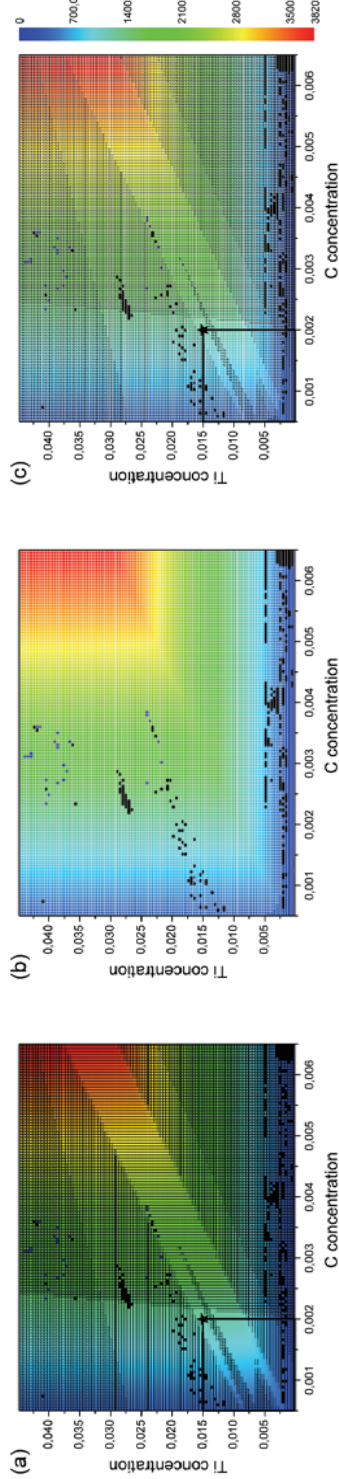


FIGURE 5.4. Binary compositional effects of C-Ti based on alloy 1A. The background contour shows the carbide precipitation strengthening factor as scaled in (c). The black vertical, horizontal and forward slash patterns demonstrate the area not fulfilling the go/nogo criteria of Ms temperature, total amount of undesirable phases and Cr concentration in the matrix, respectively (a). The white horizontal and vertical patterns indicate the new criteria for volume fractions of austenite and primary carbides initiating from austenitisation/solution treatment (b). The combination of both sets of criteria are shown in (c). The scattered black spots show compositions where ThermoCalc equilibrium calculation can not be successfully performed. The composition with a star indicates the optimal (alloy 1A) solution. All concentrations are given in weight fraction.

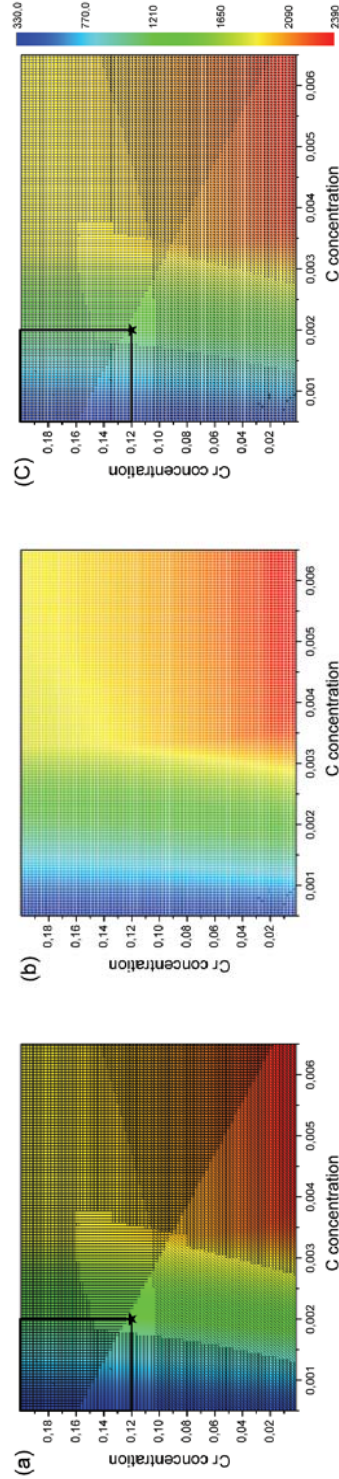


FIGURE 5.5. Binary compositional effects of C-Cr based on alloy 1A. The patterns are the same as described in the caption of Figure 5.4.

Cr in austenite as indicated by the horizontal white lines. There is a very small area which fulfils all conditions in the searching space and the solution is indicated by the star in Figure 5.7(c). The background colour in Figure 5.8(a) shows that there is a preferred ageing temperature range around 740 K depending on the carbon concentration. Again, Figure 5.8(b) shows the high carbon concentration results in primary carbides promotion while very low carbon leads to the formation of other phases, for instance, δ -ferrite. The strengthening level in Figure 5.9 only changes with carbon content because it is calculated for the ageing temperature of 743 K and is not directly related to the austenitisation temperature. Looking at the upper edge of the vertical white pattern in Figure 5.9(b), it is clear that a higher austenitisation temperature is required for higher carbon content in order to dissolve all carbon in the austenite without forming primary carbides. However, if the austenitisation temperature is too high, liquid may start to be present as shown by the white backslash in Figure 5.9(b). When all criteria are taken into account, the best C concentration and austenitisation temperature are found to be 0.08 wt% and 1533 K, respectively.

In order to visualise compositional and temperature effects on the strengthening factor, as well as on all other criteria in more detail, a simulation was performed in which the composition and temperature are varied taking alloy 1D as a reference. In Figure 5.10, the vertical axis is the normalised concentration or temperature where 1 stands for the minimum and 32 represents the maximum of the searching range. In each group, the first colour bar (STR) represents the strengthening contribution, calculated by fixing all the remaining composition and temperature parameter values as of alloy 1D. The second bar (TMS) stands for the Ms temperature criterion of which the white part is the window fulfilling $M_s \geq 473$ K and the gray scaled part indicates the unfavourableness regarding this criterion (the darker the worse). Following the same principle, the other bars referred to the go/nogo criteria of total volume amount of undesirable phases during ageing (VF), Cr concentration in the matrix (Cr), austenite percentage in the austenitisation treatment (Aus) and the amount of primary carbides (Car) are plotted next to each other. The best solution should be found with the highest strengthening factor in the first column, while all the go/nogo criteria are fulfilled (represented by white colour instead of gray scale). The black circles demonstrate such values in each group and all of them are found to be the same as in alloy 1D, which provides strong evidence that the alloy design and optimisation approach described above is applicable for such complex system accounting for the entire heat treatment. The results also show that there are very narrow solution windows for C, Cr, Ni, Ti, Mo, Al and T_{Aus} while for the other parameters, the windows are relatively big. For Nb, there is no unfulfilled criterion in the considered searching range. Focusing on strengthening precipitation, the STR bars show that C, Ni, Ti, Nb and T_{Age} have the strongest strengthening effects. On the hand, for go/nogo criteria, the most important parameters are: (1) C, Cr, Ni, Mo and Cu for Ms temperature criterion (TMS). (2) C, Cr, Ni, Ti, Mo, V and T_{Age} for the total amount of un-

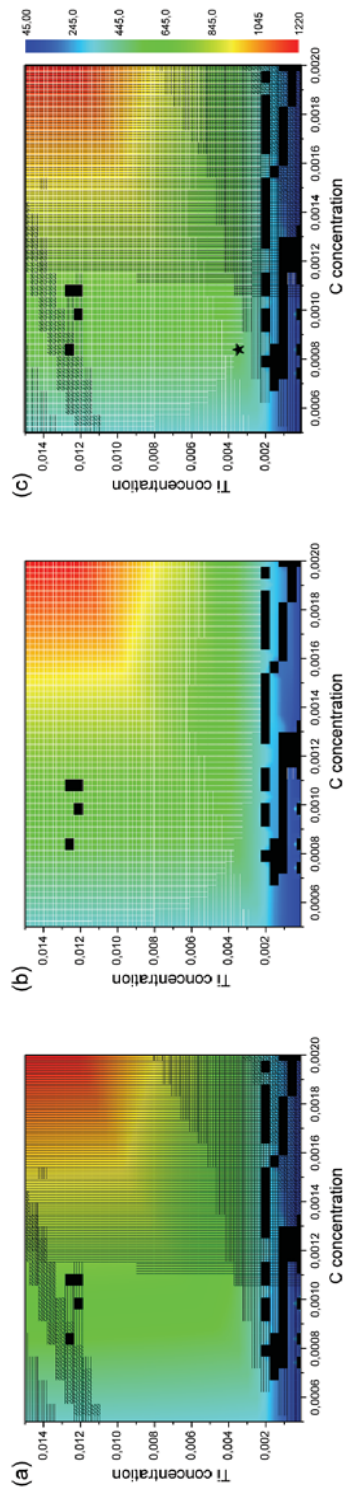


FIGURE 5.6. Binary compositional effects of C-Ti based on alloy 1D. The patterns are the same as described in the caption of Figure 5.4.

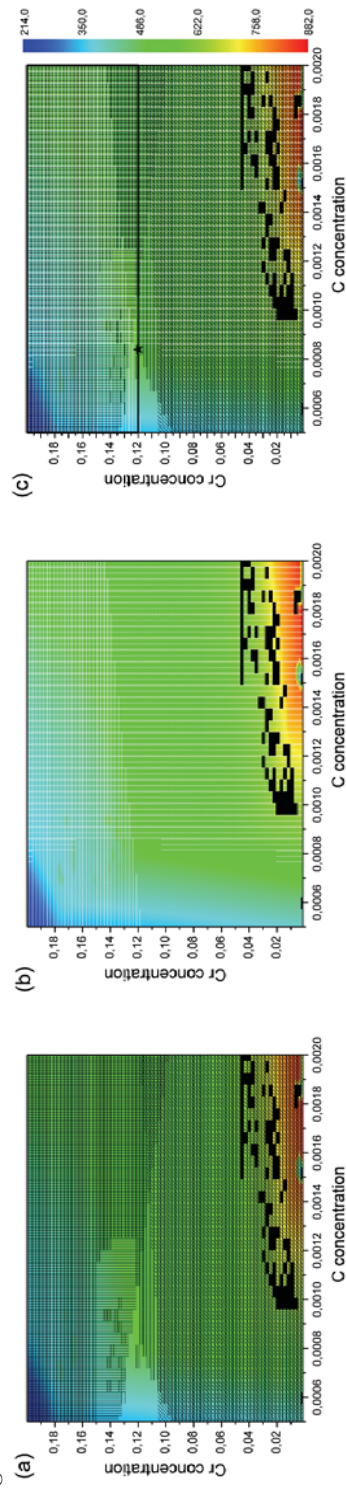


FIGURE 5.7. Binary compositional effects of C-Cr based on alloy 1D. The patterns are the same as described in the caption of Figure 5.4.

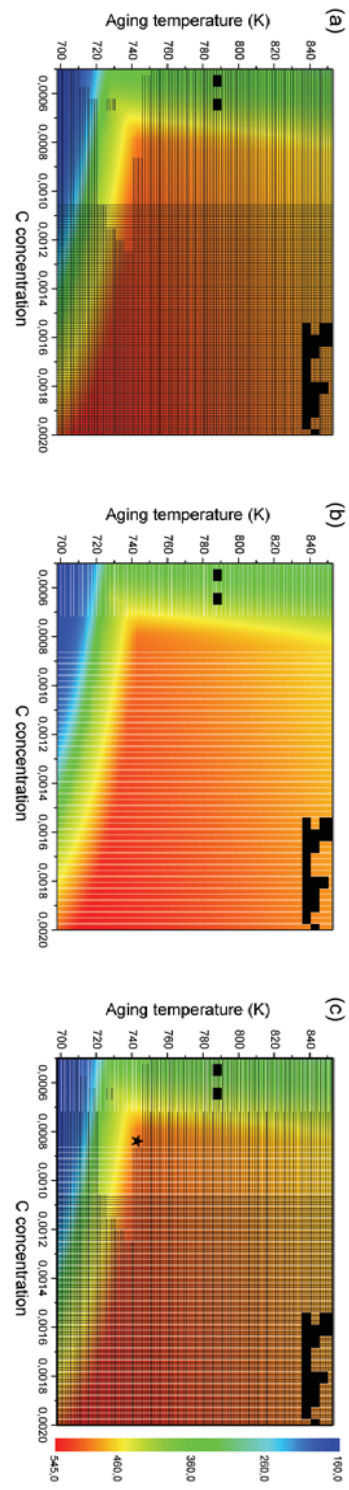


FIGURE 5.8. Binary effects of C-TAge based on alloy 1D. The patterns are the same as described in the caption of Figure 5.4.

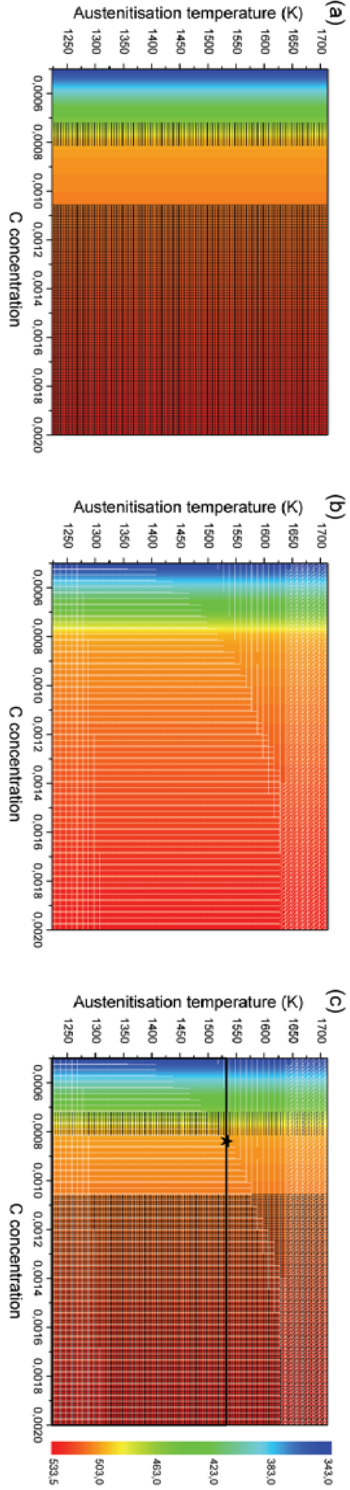


FIGURE 5.9. Binary effects of C-TAus based on alloy 1D. The patterns are the same as described in the caption of Figure 5.4.

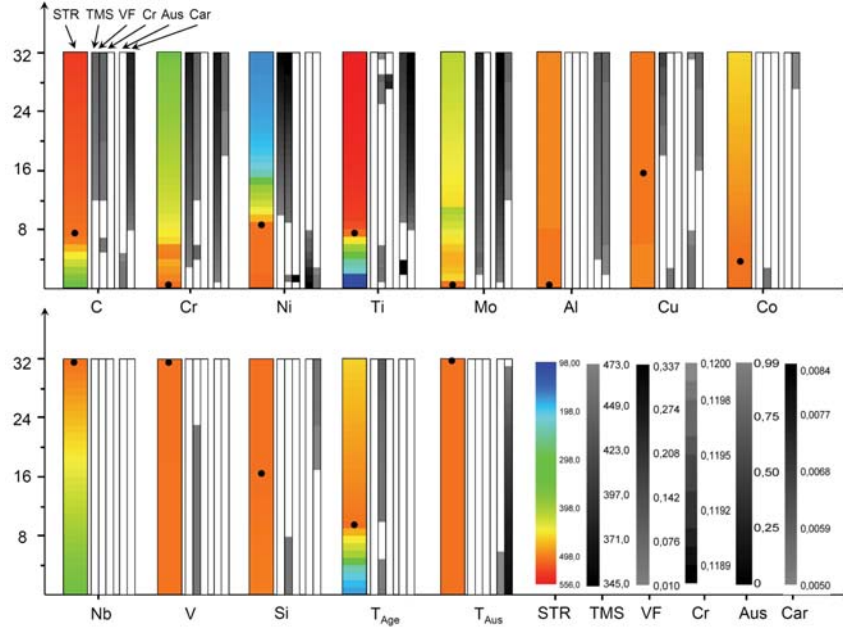


FIGURE 5.10. The effects of alloy composition and austenitisation/ageing temperatures on strengthening factor and all go/nogo criteria: precipitation strengthening factor (STR), Ms temperature (TMS), volume fraction of all desirable phases during ageing (VF), Cr concentration in the matrix (Cr), austenite volume fraction in the austenitisation treatment (Aus) and the volume fraction of primary carbides (Car). Red and white represent the desired values in the coloured and gray scales. Alloy 1D is taken as the base line for the analysis.

desirable phases (VF). (3) Ni and Ti for the Cr concentration in the matrix (Cr). (4) Cr, Ni, Ti, Mo, Al, Cu and T_{Aus} for the austenite fraction (Aus). (5) C, Cr, Ti, Mo, Al, Cu, Si and T_{Aus} for the primary carbides (Car). Given the alloy 1D as the baseline, the criteria of TMS, VF, Aus and Car blocked most of the windows and are therefore the most difficult ones to be fulfilled, but this statement may not hold true for other systems.

5.5 Conclusion

An integrated computational alloy design model is developed wherein the alloy composition as well as the key heat treatment parameters incorporating the entire heat treatment are designed and optimised simultaneously. Compared to the previous design models including only the aging stage, the consideration of undesirable phases present during the austenitisation treatment leads to significant compositional changes in the alloys strengthened by MC carbides and Cu particles, but minor changes in the system utilising NiAl/Ni₃Ti. The optimal strengthening con-

tribution in all three systems decreases notably by incorporating new criteria in alloy series C (fixed T_{Aus} of 1473 K). However, in alloys 2D and 3D (variable T_{Aus} and T_{Age}), through increasing austenisation temperature and decreasing ageing temperature, they can be well compensated and become comparable to those in the corresponding A and B series (without considering austenisation). The examples described in the text demonstrate the advantages of the integrated model which allows the optimisation of composition and heat treatment temperatures simultaneously. Although the predicted precipitate strengthening contributions is reduced due to the new austenisation criteria applied, the newly designed alloys are predicted to reach strength levels beyond those of existing commercial counterparts. A second round of prototype alloys will further evaluate the integrated design approach (see Chapter 6).

6

Experimental Validation: the Second Round of Prototype Alloys

6.1 Alloy Compositions

The second round of prototype alloys are designed employing the integrated model presented in Chapter 5 wherein the alloy composition is optimised simultaneously with solution and ageing temperatures. The desired precipitation strengthening effect achieves a maximum while undesirable phases throughout the entire heat treatment are suppressed according to thermodynamic predictions. The same strengthening precipitate scenarios are applied as in the first round of prototype alloys: alloy NiTi2 is strengthened by precipitation of Ni_3Ti , alloy CuNi2 contains a balance of Cu and NiAl/ Ni_3Ti intermetallics, alloy Car2 utilises MC carbides for strengthening and alloy CarCo2 follows the same principle but allowing higher Co concentration. The concentration ranges applied in the optimisation are listed in Table 6.1. The optimal alloy compositions with corresponding solution and ageing treatment temperatures, as well as their predicted M_s temperatures are shown in Table 6.2. In comparison with alloy compositions of the first round, the compositions of alloy NiTi2 and CuNi2 do not change much except that C takes the new lower limit and Ni, Co and V levels slightly increase. The concentrations of C, Ti and Nb in alloys Car2 and CarCo2 decrease significantly in order to avoid the formation of primary carbides. The other components also change the concentration accordingly so as to maximise the formation of strengthening precipitates and avoid the precipitation of other undesirable phases. The optimal ageing temperatures of all alloys remain in the range of experimental optima (723 - 823 K). The designed solution treatment temperatures of alloy NiTi2 and CuNi2 are around

the previous experimental value of 1423 K while alloy Car2 prefers higher temperature (1533 K) in order to dissolve all the carbide formers in the austenite matrix without forming primary carbides. Unlike alloy Car2, alloy CarCo2 prefers a lower designed solution treatment temperature because the high Co concentration suppresses the primary carbide formation from a thermodynamic viewpoint. The Ms temperatures of alloy NiTi2 and CuNi2 is about the critical value of 473 K but alloys utilising MC carbide have higher Ms temperatures well above 473 K and hence ensure the formation of lath martensite.

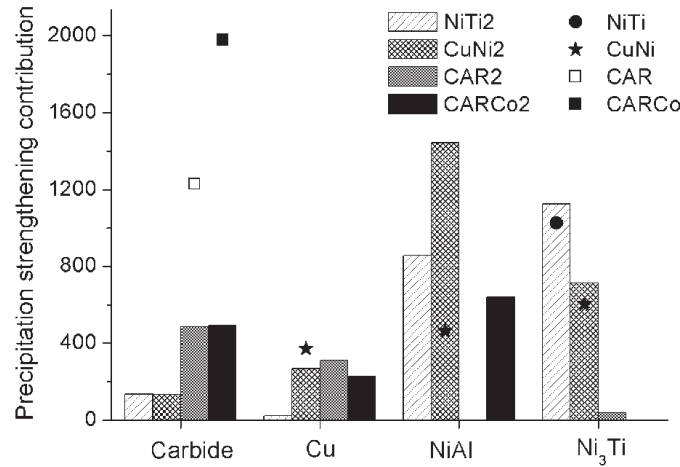


FIGURE 6.1. The precipitation strengthening configurations of alloys NiTi2, CuNi2, Car2 and CarCo2. The symbols indicate the corresponding values of the first round prototype alloys.

The precipitation strengthening contributions of all precipitates in different alloys are compared in Figure 6.1. As for the earlier results, all alloys possess multiple strengthening precipitates beyond the intended species and hence obtain an extra strengthening contribution. The precipitation strengthening contribution values for the alloys from the first round are also indicated by symbols in corresponding columns in Figure 6.1. It can be observed that, the strengthening contribution of Ni₃Ti in alloy NiTi2 is higher than in alloy NiTi. This results from the allowed higher Ti concentration and the variation of ageing temperature and not due to the newly implemented criteria. The same can be observed for alloy CuNi2. This is in agreement with observations in Figure 5.2 that the new criteria do not decrease the strengthening contribution much and can be compensated by the variation of heat treatment temperatures. However, the predicted strengthening contribution of MC carbide in alloys Car2 and CarCo2 decreases remarkably because C, Ti and Nb take much lower concentrations than in the first round. Nevertheless, in the first round of alloys Car and CarCo, the formation of primary carbide consumes

	C	Cr	Ni	Ti	Mo	Al	Cu	Co	Nb	N	V	Mn	Si	T _{Age}	T _{Aus}
Min	0.01	12.00	1.00	0.01	0.50	0.01	0.50	0.01	0.01	0.01	0.01	0.50	0.30	693	1223
Max	0.30	20.00	15.00	2.00	10.0	2.00	2.00	2.00 (15.00 ⁴)	1.00	0.01	1.00	0.50	1.00	848	1533

TABLE 6.1. Concentration ranges of all components employed in the second round of prototype alloy design (wt%). The design of alloy CarCo2 allows a higher Co limit up to 15 wt % as indicated by superscript 4 in the table.

Alloys	C	Cr	Ni	Ti	Mo	Al	Cu	Co	Nb	N	V	Mn	Si	T _{Age} (K)	T _{Aus} (K)	M _s (K)	
NiTi2	Design	0.010	12.00	13.19	2.00	0.50	1.42	0.50	1.55	0.01	0.01	0.49	0.50	0.30	758	1403	474
	Actual	0.005	11.96	13.30	2.07	0.51	1.40	0.54	1.72	0.06	–	0.50	0.60	0.32			473
CuNi2	Design	0.010	12.00	11.39	1.49	0.50	2.00	2.00	2.00	0.01	0.01	0.23	0.50	0.82	758	1463	476
	Actual	0.007	11.90	11.90	1.62	0.52	2.00	2.09	2.11	0.03	–	0.24	0.61	0.82			469
Car2	Design	0.075	12.00	4.16	0.46	0.50	0.01	2.00	2.00	0.11	0.01	0.01	0.50	0.55	738	1533	542
	Actual	0.089	11.98	4.14	0.53	0.51	0.03	2.22	2.09	0.11	–	0.005	0.61	0.57			534
CarCo2	Design	0.075	12.00	4.61	0.97	0.50	1.10	1.95	14.52	0.23	0.01	0.01	0.50	1.00	818	1253	625
	Actual	0.097	11.96	4.43	1.10	0.51	1.06	2.04	14.30	0.24	–	0.005	0.61	1.06			615

TABLE 6.2. The designed and actual alloy compositions and predicted Ms temperature of alloy NiTi2, CuNi2, Car2 and CarCo2. Concentrations are in weight percent.

most of the carbide formers and hence produce no significant strengthening effect from MC carbides. In the second round of alloys, if MC carbides form in the desirable form of finely distributed nanosized precipitates rather than primary carbides, they should provide a significant strengthening contribution to the alloy. At last, it should be noticed that the predicted contribution of Ni_3Ti in alloys Car2 and CarCo2 is not as high as that in Car and CarCo.

6.2 Experimental Procedures

The second round of prototype alloys, NiTi2, CuNi2, Car2 and CarCo2, were prepared in a vacuum induction melting furnace as ingots of approximately 25 Kg. The melting temperature was kept relatively low at about 1773 K and the chamber was protected by argon in order to minimise oxidation. The ingots were ground to smooth their surface, soaked at 1473 K for 2 hours and subsequently forged into a slab of $80 \times 80 \times 300$ mm at a finishing temperature above 1173 K. The slabs were reheated to 1473 K for 2 hours, and subsequently hot rolled into plates of 15 mm thickness by 6 consecutive passes in the temperature range of 1323-1073 K (Table 6.3), followed by natural air cooling. The chemical analysis of the experimental alloys is given in Table 6.2.

Temperature (K)	1423	1373	1273	1223	1173	1223	1073
Thickness reduction	80-60	60-45	45-34	34-27	27-20	20-15	15-12
Reduction ratio %	25	25	24	21	26	25	20

TABLE 6.3. Hot rolling processing parameters of second round of prototype alloys.

The as rolled materials were subjected to various solution treatment conditions and subsequently quenched to room temperature in order to achieve a lath martensite matrix before ageing. Alloys NiTi2 and CuNi2 were also subjected to cold rolling after solution treatment in order to stimulate the martensitic transformation. The details are discussed in the next section. The specimens at the optimal heat treatment condition were aged at 723, 773 and 823 K from 6 minutes up to one day, followed by air cooling. The tensile specimens were prepared along the longitudinal direction. Tensile tests were performed at room temperature and Vickers hardness was measured with a load of 1 Kg.

The microstructures were investigated by optical microscopy, scanning electron microscopy (SEM), transmission electron microscopy (TEM) in combination with energy dispersive spectroscopy (EDS). X-ray Diffraction (XRD) was also applied to identify phases. Optical microscopy and SEM were carried out on specimens etched with Villela's reagent. The TEM investigation was carried out with a Philips

CM30T microscope operated at 300 kV and a Jeol JEM-2200 FS at 200 kV. The TEM thin foils were firstly mechanically polished to approximately 50 μm in thickness and punched to the standard size of 3 mm diameter. Electro-polishing was performed with a solution of 10% perchloric acid + 90% methanol maintained at 233 K and 12 V.

Electrochemical measurements of open circuit potential (OCP) and, potentiodynamic polarisation (PP) were performed in order to characterise the corrosion resistance of the second round of prototype alloys. Corrosion resistance investigations were also performed on existing reference alloys: standard stainless steels 304 and 316, non-stainless UHS steels 300M and Aermet 100 and maraging stainless steel 1RK91. OCP and PP measurements were conducted in a 3.5% NaCl solution (pH 6, open to air) using a platinum counter electrode and a saturated calomel or Ag/AgCl/Cl⁻ (saturated KCl) reference electrode. After stabilisation of the OCP in the solution for 24 hours, the polarisation curves were obtained by scanning the potential from -0.5 V versus OCP to +1.0 V versus OCP for each sample.

6.3 Characterisation of As-hot-rolled Materials

The microstructures of the slabs after hot rolling were characterised using optical microscopy on the cross-section perpendicular to the rolling direction. All alloys display homogeneous microstructures as shown in Figure 6.2. Alloy NiTi2 (Figure 6.2(a)) possesses a mainly austenitic matrix after hot rolling and the undesirable δ -ferrite is successfully avoided. However, in alloy CuNi2, a significant amount of δ -ferrite in an austenite matrix can still be observed as shown in Figure 6.2(b). Figures 6.2(c,d) show that alloys Car2 and CarCo2 have similar microstructures of very fine martensite matrix without notable primary carbides as in alloy Car and CarCo. The characterisation of as-hot-rolled materials reveals that undesirable phases such as δ -ferrite in alloy NiTi and primary carbides in alloys Car and CarCo are basically successfully avoided in the second round of prototypes, except the alloy CuNi2, by taking into account the thermodynamic equilibrium at the homogenisation temperature.

6.4 Solution Treatment Optimisation

In order to dissolve occasional precipitates resulting from the casting and/or hot rolling processes, and achieve better homogeneity, the hot rolled slabs were cut into small pieces for solution treatment. Different solution treatment conditions were followed at temperatures of 1373, 1423 and 1473 K, for residence times of 15 and 60 minutes, respectively. Following the solution treatment the specimens were

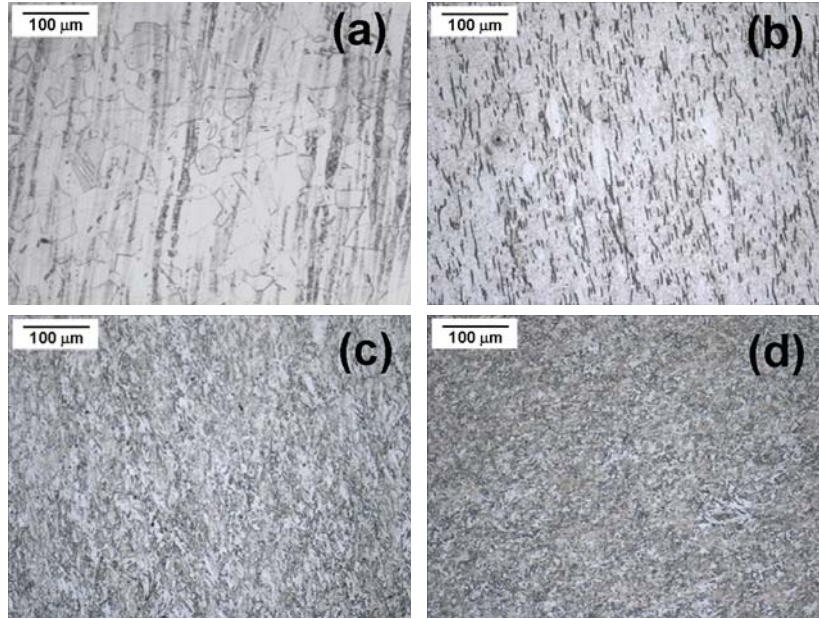


FIGURE 6.2. Optical micrographs after hot rolling on the cross-section perpendicular to the rolling direction of alloys (a) NiTi2 (b) CuNi2 (c) Car2 and (d) CarCo2.

oil quenched. The microstructures were characterised by optical microscopy and the hardness were measured on different solution treatment conditions.

Figure 6.3 shows the microstructure of alloy NiTi2 after solution treatment of (a) 1373 K for 15 minutes, (b) 1423 K for 60 minutes and (c) 1473K for 60 minutes, respectively. In all conditions, no δ -ferrite phase is observed resulting from the solution treatment or oil quench. The matrix is relatively homogeneous without notable precipitates, however, the matrix remains austenitic after quenching. The micrographs also suggest that the growth of austenite grains at 1373 and 1423 K is limited while in the case of 1473 K for 1 hour, their size increases significantly. The XRD pattern of the solution treatment condition of 1423 K for 60 minutes is presented in Figure 6.3(d) which confirms that austenite is the main matrix and there are no detectable precipitates. Furthermore, Figure 6.3(d) also reveals a small peak of martensite which suggests that the austenite in alloy NiTi2 is not very stable and hence the martensitic transformation might be promoted by means of an extra heat treatment or plastic deformation. The hardness after solution treatment is shown in Table 6.4. Despite the variations of solution treatment conditions, the hardness remains at the same level of austenite matrix which is in agreement with micrographs and XRD analysis.

In order to further trigger the martensitic transformation in alloy NiTi2, oil quenched specimens were subjected to an extra cryogenic treatment of (a) at 253

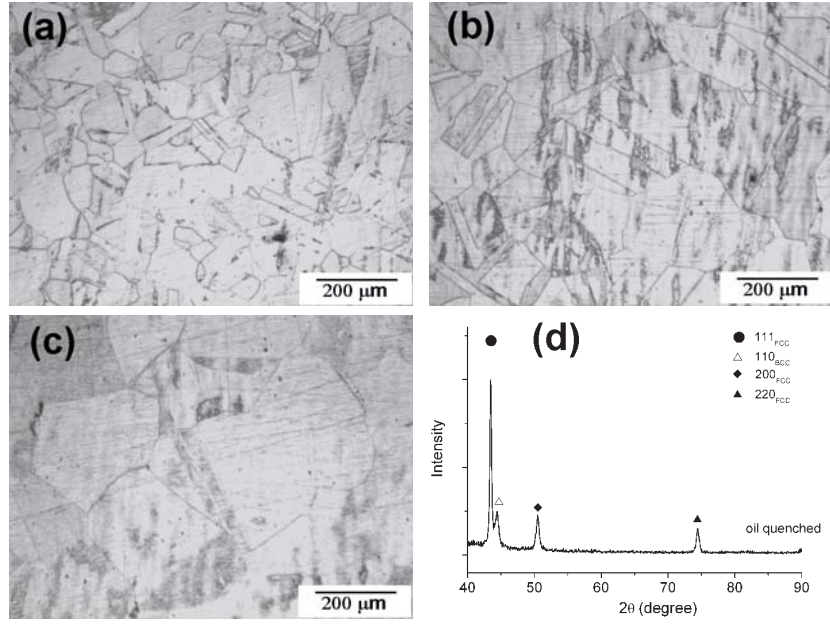


FIGURE 6.3. Optical micrographs of alloy NiTi2 after solution treatment at (a) 1373 K for 15 minutes, (b) 1423 K for 60 minutes and (c) 1473 K for 60 minutes, followed by oil quench. The XRD pattern of condition (b) is shown in (d).

	1373 K		1423 K		1473 K	
	15 mins	60 mins	15 mins	60 mins	15 mins	60 mins
NiTi2	150.6	153.2	154.6	134.8	146.8	146.3
CuNi2	165.2	175.3	160.3	164.7	164.1	154.9
Car2	333.4	324.6	327.1	335.8	338.5	321.7
CarCo2	297.4	304.6	297.4	308.6	331.7	329.5

TABLE 6.4. Vickers hardness of second round of prototype alloys after various solution treatment followed by oil quench.

K for one week or (b) liquid nitrogen immersion for 1 hour. The microstructure after liquid nitrogen quench is shown in Figure 6.4(a). Table 6.5 shows that the hardness after cryogenic treatment remains the same as that from the oil quenched condition, which implies that no extra martensite is promoted. In order to investigate the role of cooling rate on martensitic transformation in alloy NiTi2, the specimens were also quenched at a higher cooling rate employing a quench media of brine solution (10% NaCl) following the solution treatment of 1423 K for 1 hour. The microstructure as shown Figure 6.4(b), together with the hardness after brine quench (157.5 Hv) and XRD pattern in comparison with oil quench (Figure 6.4(c)), all suggest that a faster cooling rate does not result in more martensite formation. In summary, neither cryogenic treatment nor a faster cooling rate can foster the formation of martensite in alloy NiTi2. Nevertheless, as has been observed in alloy NiTi, deformation can stimulate the formation of martensite by means of TRIP effect. Therefore, cold rolling is suggested to create more martensite in the matrix (see section 6.5).

		1373 K		1423 K		1473 K	
		15 mins	60 mins	15 mins	60 mins	15 mins	60 mins
NiTi2	Oil Quench	150.6	153.2	154.6	134.8	146.8	146.3
	OQ + 253 K	144.8	149.5	156.5	153.7	146.3	143.9
	OQ + 77 K	146.7	162.8	142.3	136.7	149.5	140.6
CuNi2	Oil Quench	165.2	175.3	160.3	164.7	164.1	154.9
	OQ + 253 K	164.8	207.2	162.4	194.5	200.9	182.6
	OQ + 77 K	157.3	164.8	172.4	155.9	174.6	182.9

TABLE 6.5. Hardness of alloys NiTi2 and CuNi2 after oil quench (OQ) and extra cryogenic treatment at 253 K for one week and in liquid nitrogen for 1 hours.

In comparison to alloy CuNi, precipitation of primary carbides is successfully avoided in alloy CuNi2 while δ -ferrite remains present. As shown in 6.5(a-c), the amount of δ -ferrite increases with solution treatment temperature especially after treatment at 1473 K for 60 minutes (Figure 6.5(c)). The hardness at different conditions in Table 6.4 generally shows higher value than alloy NiTi2 possibly due to more martensite being present. The XRD results after solution treatment of 1423 K for 60 minutes (Figure 6.5(d)) also clearly indicate the BCC peak which is the contribution of both δ -ferrite and martensite. As discussed earlier in Chapter 4, the presence of δ -ferrite in the final microstructure deteriorates mechanical properties as well as influences the distribution of alloying elements and hence changes the martensitic transformation and ageing precipitation kinetics. Choosing a solution temperature lower than 1373 K might further reduce the amount of δ -ferrite at the cost of very slow dissolution kinetics.

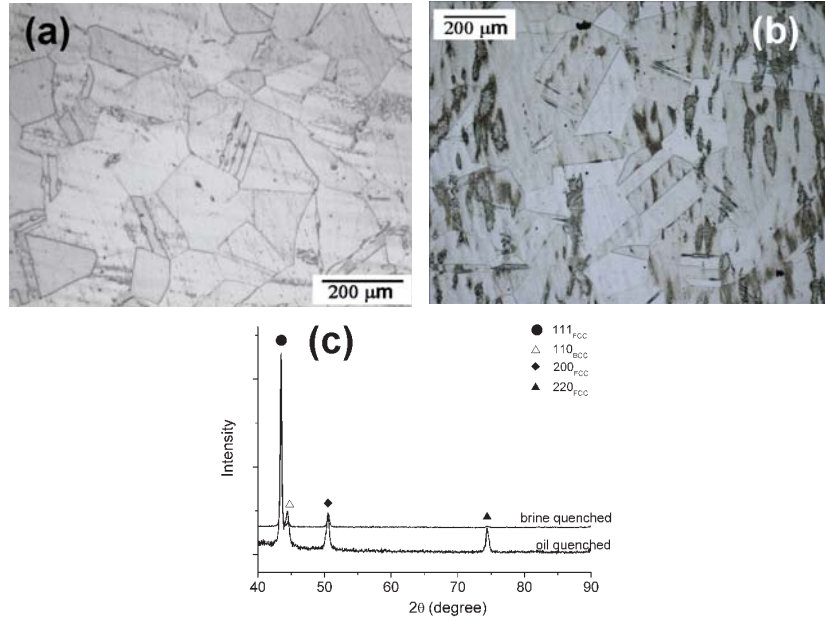


FIGURE 6.4. Optical micrographs of alloy NiTi2 after solution treatment at 1423 K for 60 minutes, followed by (a) oil quench and maintaining in liquid nitrogen for 1 hour and (b) brine quench. The XRD pattern of condition (b) is shown in (c).

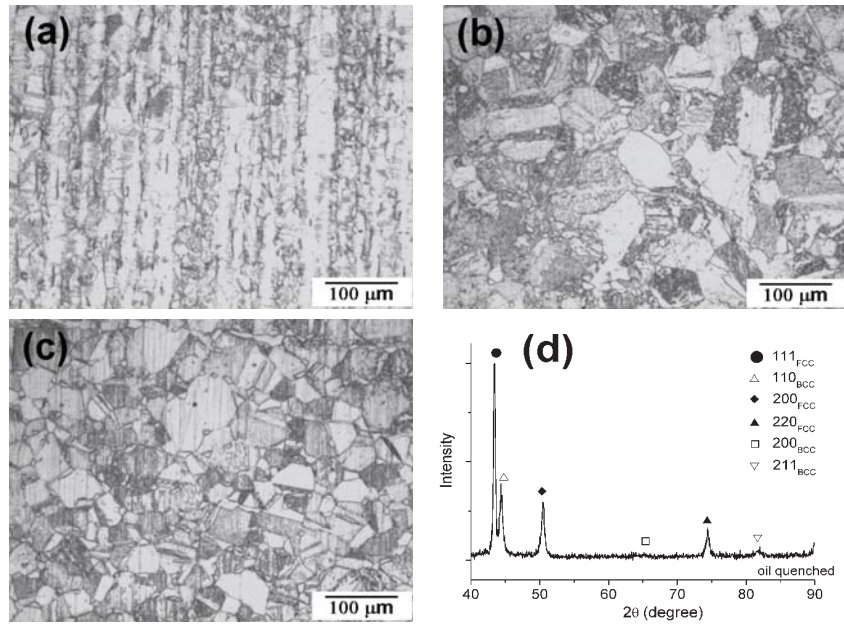


FIGURE 6.5. Optical micrographs of alloy CuNi2 after solution treatment at (a) 1373 K for 15 minutes, (b) 1423 K for 60 minutes and (c) 1473 K for 60 minutes, followed by oil quench. The XRD pattern of condition (b) is shown in (d).

After oil quenching, the austenitic matrix partially transforms to martensite and the rest remains as austenite. In order to promote the transformation into martensite, the specimens were cryogenically treated in the same way as alloy NiTi2. The hardness results shown in Table 6.5 indicate the cryogenic treatment at 253 K for 1 week slightly increases the amount of martensite while submerging specimens in liquid nitrogen does not show any notable effects. The cooling rate effect was investigated by changing the quench media from oil to brine after solution treatment. Same as alloy NiTi2, faster cooling rate does not seem to promote significantly the martensitic transformation, as indicated by the hardness in Table 6.6, typical microstructures in Figures 6.6(b-c) and the XRD comparison in Figure 6.6(d).

	1373 K	1423 K	1473 K
Oil Quench	175.3	164.7	154.9
Brine Quench	162.8	207.4	196.8

TABLE 6.6. Hardness of alloy CuNi2 after solution treatment at 1373, 1423 and 1473 K for 60 minutes followed by oil/brine quench.

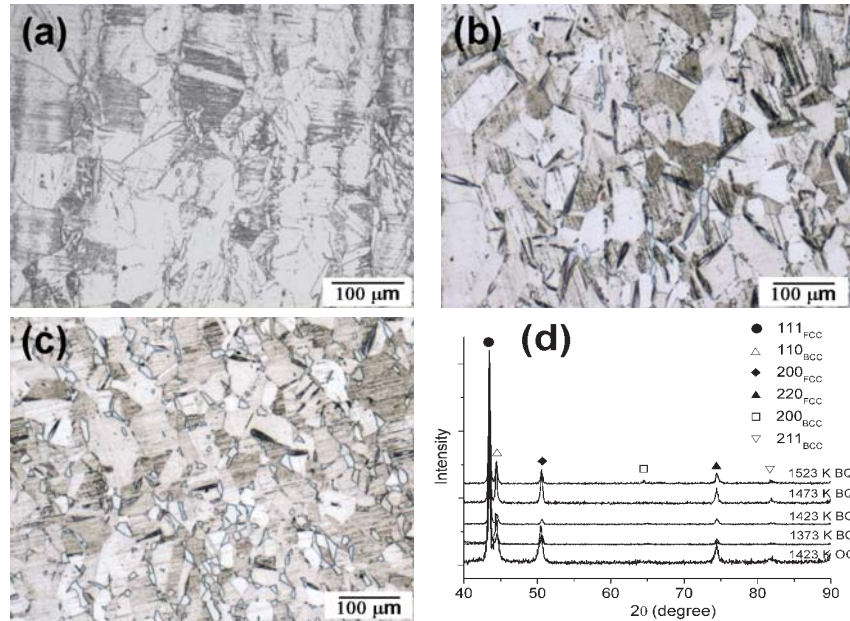


FIGURE 6.6. Optical micrographs of alloy CuNi2 after (a) solution treatment at 1423 K for 60 minutes, followed by oil quench and submerging in liquid nitrogen for 1 hour, (b) solution treatment at 1423 K for 60 minutes, followed by brine quench and (c) solution treatment at 1473 K for 60 minutes, followed by brine quench. The XRD patterns of different conditions are shown in (d).

Typical optical micrographs of alloy Car2 and CarCo2 after solution treatment at 1373 K for 15 minutes, 1423 K for 60 minutes and 1473 K for 60 minutes are shown in Figures 6.7(a-c) and Figures 6.8(a-c), respectively. The prior austenite grains grow significantly with increasing solution treatment temperature and/or longer time, and subsequently transform to lath martensite upon oil quench. The hardness of both alloys at different solution treatment conditions are at the same level above 300 Hv suggesting the grain size has a minor effect on the hardness. A very small amount of primary carbides can be identified by optical microscopy. The XRD patterns of alloy Car2 and CarCo after solution treatment at 1423 K for 60 minutes as shown in Figures 6.7(d) and 6.8(d) display only peaks of BCC martensite without notable signals of primary carbides or retained austenite. In comparison with first round alloys Car and CarCo, the deleterious precipitation of primary carbides is successfully avoided in the second round.

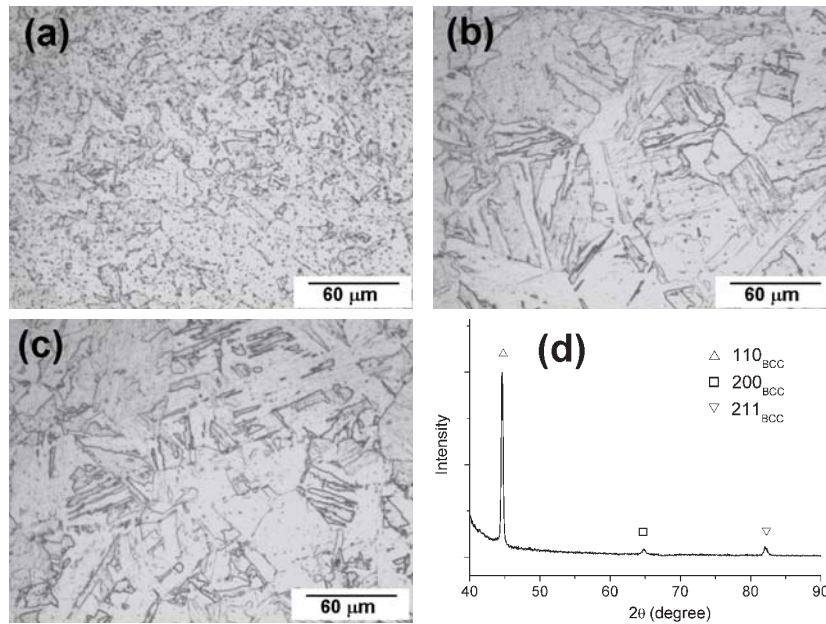


FIGURE 6.7. Optical micrographs of alloy Car2 after solution treatment at (a) 1373 K for 15 minutes, (b) 1423 K for 60 minutes and (c) 1473 K for 60 minutes, followed by oil quench. The XRD pattern of condition (b) is shown in (d).

Considering the martensitic transformation, the presence of undesirable phases and hardness of different solution treatment conditions, a best compromise was chosen, for all alloys, NiTi2, CuNi2, Car2 and CarCo2, a solution treatment temperature of 1423 K and a time of 60 minutes, followed by oil quench. It should be noticed that the selected ageing treatment temperature is based on an experimental investigation rather than those designed to be optimal and which were listed in Table 6.2. This will be addressed in the discussion.

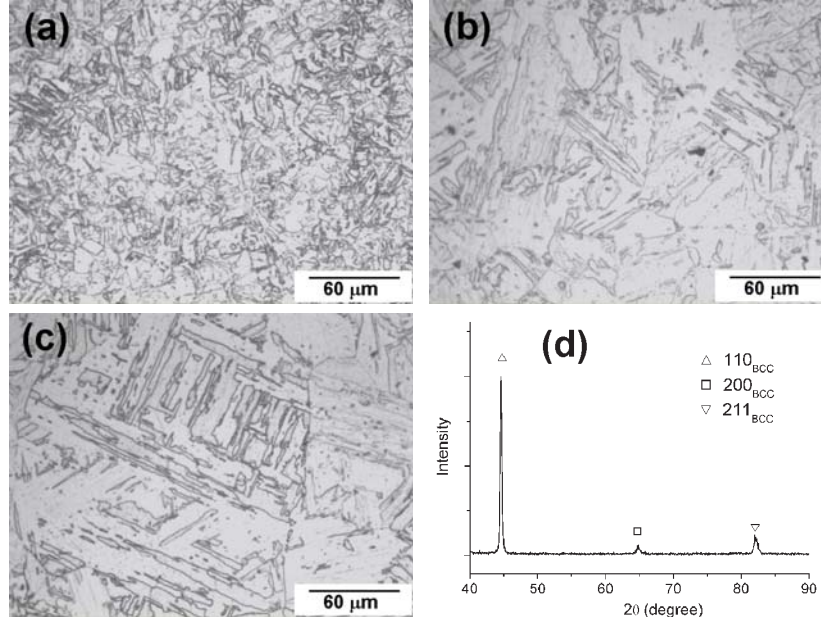


FIGURE 6.8. Optical micrographs of alloy CarCo2 after solution treatment at (a) 1373 K for 15 minutes, (b) 1423 K for 60 minutes and (c) 1473 K for 60 minutes, followed by oil quench. The XRD pattern of condition (b) is shown in (d).

6.5 Cold Rolling

Previous solution treatment experiments show that variations in temperature/time and cooling rate do not significantly influence the martensitic transformation in alloys NiTi2 and CuNi2. An other effective means to promote the martensitic transformation is cold rolling, as the austenite in alloy NiTi2 and CuNi2 are metastable and already partially transformed into martensite upon quenching. The deformation may provide enough energy so as to stimulate the plasticity induced martensitic transformation and hence increase the matrix strength before subjected to the next heat treatment step, precipitation ageing. Therefore, cold rolling was performed on alloys NiTi2 and CuNi2 after solution treatment and oil quench, following the cold rolling process parameter as shown in Tale 6.7.

Thickness measured after each step of cold rolling (mm)											
NiTi2	4.92	4.68	4.55	4.10	3.80	3.48	3.20	2.93	2.63	2.37	1.99
CuNi2	5.30	4.95	4.65	4.53	4.19	3.91	3.64	3.35	3.05	2.76	2.30

TABLE 6.7. Cold rolling processing parameters of the second round of prototype alloys.

Representative micrographs of alloys NiTi2 and CuNi2 after cold rolling are presented in Figures 6.9 and 6.10, respectively. The matrix of both alloys can

not be identified easily as being martensite, but X-ray diffractograms as shown in Figures 6.9(b) and 6.10(c) clearly indicate that the volume fraction of martensite increases dramatically after cold rolling. The hardness and tensile properties also confirm the occurrence of the martensitic transformation and they will be discussed later in this chapter.

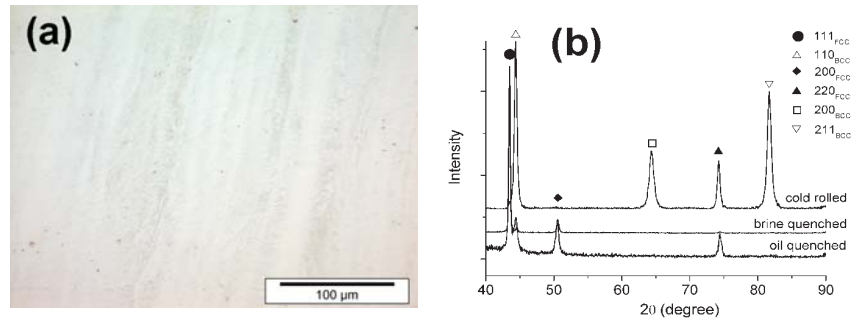


FIGURE 6.9. (a) Optical micrographs and (b) XRD pattern of alloy NiTi2 after cold rolling.

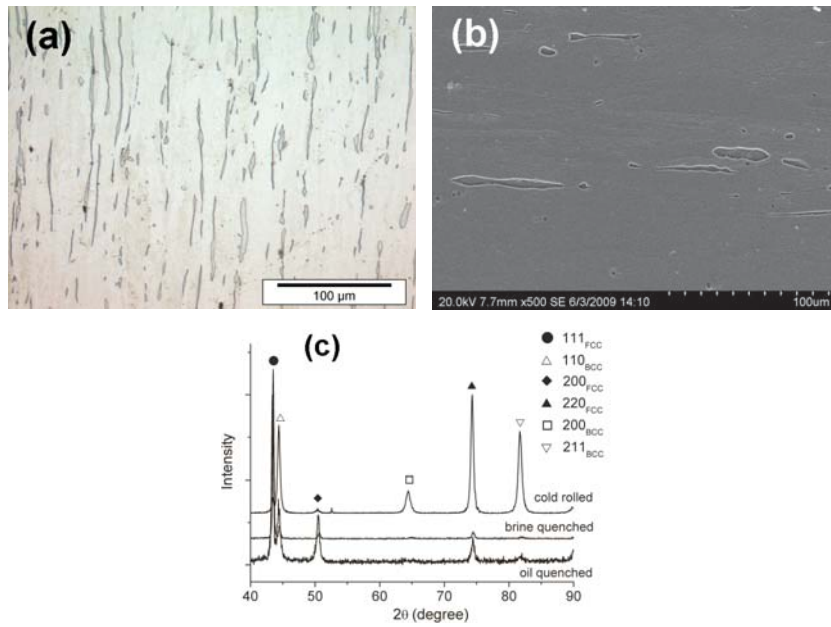


FIGURE 6.10. (a) Optical micrographs, (b) SEM micrograph and (c) XRD pattern of alloy CuNi2 after cold rolling.

6.6 Ageing Treatment

The specimens after solution treatment (alloys Car2 and CarCo2) and cold rolling (alloys NiTi2 and CuNi2) were subjected to ageing treatment in order to form strengthening precipitates. Given that the second round of prototype alloys were designed with an optimal ageing temperature in the range of 738 - 813 K, the ageing experiments were performed at 723, 773 and 823 K, for ageing times from 6 minutes up to 1 day at each temperature. The tensile tests were performed at room temperature. The microstructures and hardness were characterised at the cross section of the tensile specimen, which main axis is parallel to the rolling direction.

6.7 Results

6.7.1 *Mechanical Properties*

Variations in hardness, tensile strength and total elongation at fracture as a function of aging time at different temperatures are shown in Figures 6.11-6.14 for alloys NiTi2, CuNi2, Car2 and CarCo2, respectively. The strength levels of alloy NiTi2 after solution treatment, cold rolling and various ageing conditions are compared in Figure 6.11(a). It is found that the tensile strength of cold rolled specimens increase dramatically in comparison with the solution treated condition. The hardness shown in Figure 6.11(c) also reveals a hardness increase up to 50 % by cold rolling. The strength/hardness increase is because of the TRIP effect which transforms the matrix from retained austenite into martensite. This can be further confirmed by the XRD pattern shown in Figure 6.9(b). In addition to the significant strength increase resulting from the cold rolling, alloy NiTi2 also displays a significant ageing hardening capability. The strength increases about 30 % after a short time ageing treatment (6 minutes) at all three ageing temperatures. Prolonged ageing or variation of ageing temperatures do not lead to further increase in the tensile strength. However, ductility increases with ageing time, especially at higher ageing temperature, because the material was cold rolled prior to ageing treatment. The UTS of alloy NiTi2 approaches 1.5 GPa after ageing at 723 K for 24 hours, with total elongation about 5 %. Ageing at either 773 K or 823 K for 24 hours results in a UTS of about 1.4 GPa in combination with a good ductility of 15 % total elongation.

The mechanical properties of alloy CuNi2 are shown in Figure 6.12, in which the TRIP effect is also very prominent. The as solution treated specimen has a relatively low yield strength of about 600 MPa but a good elongation above 30 %. After cold rolling the yield strength value reaches 1070 MPa and ductility

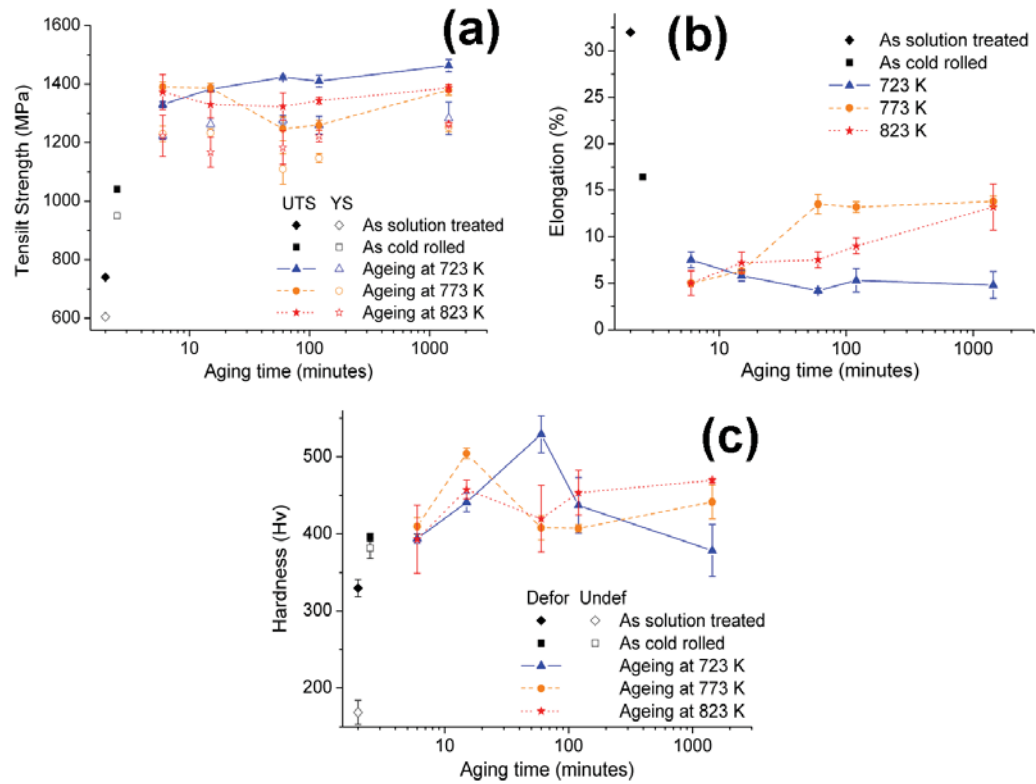


FIGURE 6.11. Variation of hardness, tensile strength and total elongation of alloy NiTi2 with ageing time. The ageing temperatures are 723, 773 and 823 K respectively.

decreases dramatically. A remarkable increase in hardness is also observed for the cold rolling condition. The enhancement of the mechanical properties due to TRIP effect is also in agreement with the XRD result in Figure 6.10(c). The ageing treatment also plays a prominent role in improving the tensile strength. In Figure 6.12(a), a very rapid increase in strength is observed indicating a fast precipitation kinetics. At ageing temperature of 773 K and 823 K, the tensile strength variation with time suggests slight overageing at 24 hours which is not consistent with hardness as shown in Figure 6.12(c). The best strength level is achieved for an ageing treatment of 15 minutes at 823 K, resulting an UTS close to 1.7 GPa but with low ductility. For a prolonged ageing treatment of 24 hours at 773 K or 823 K, a good combination of strength and ductility can be achieved of 1.55 GPa along with 10 % elongation.

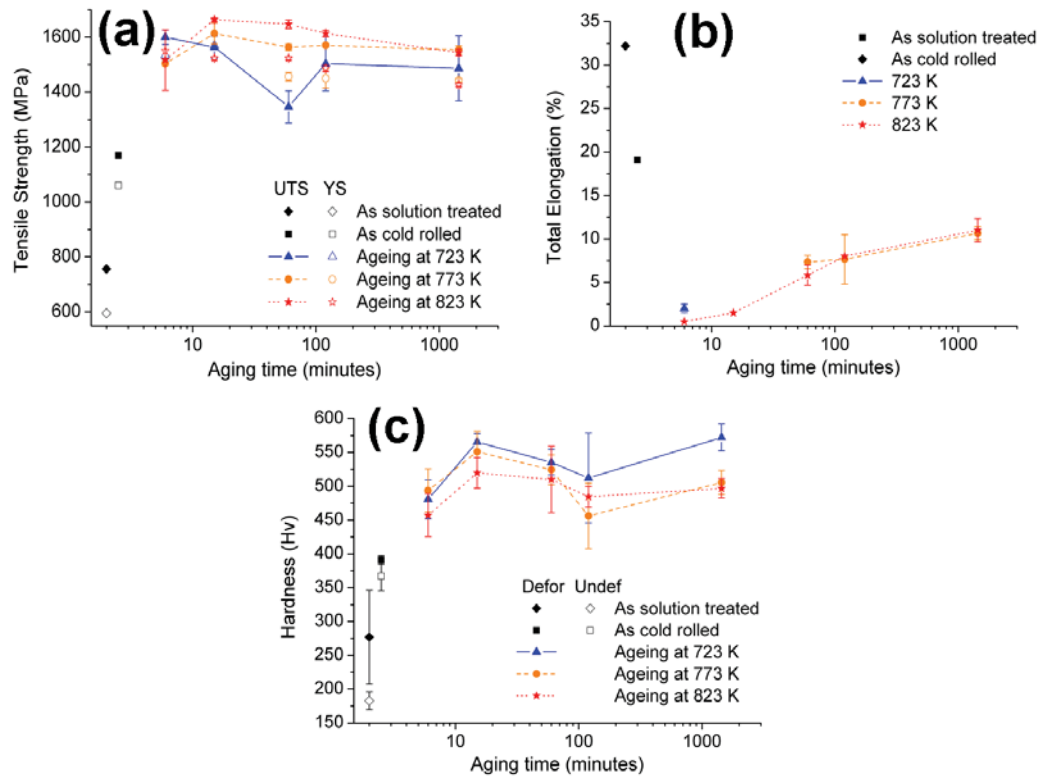


FIGURE 6.12. Variation of hardness, tensile strength and total elongation of alloy CuNi2 with aging time. The aging temperatures are 723, 773 and 823 K respectively.

Figure 6.13(a) shows the variation of strength as a function of aging time at different temperatures for alloy Car2. The strength of the solution treated specimens is about 1 GPa, which is in agreement with the XRD in Figures 6.7(d) indicating a martensitic matrix. A good ductility of 14.7 % is observed in the as solution treated

condition. With respect to ageing treatment, the strength increases but ductility decreases gradually with time at temperature of 723 K resulting in an optimum strength of 1.6 GPa at 24 hours within the ageing times considered. At an ageing temperature of 773 K, the optimal time is one hour and prolonged ageing leads to a slight decrease in strength and an increase in elongation. The strengthening effect for an ageing temperature of 823 K seems to be less effective and reaches a maximum at 15 minutes resulting in an UTS of 1.27 GPa in combination with 16 % elongation. The hardness evolution with ageing treatment as shown in Figure 6.13(b) does not display consistency with the strength results: hardness increases monotonically with ageing time at 723 and 823 K, while the hardness reaches optimum after 1 hours at 773 K. The highest hardness is observed after ageing at 823 K for 24 hours in which the hardness is above 500 Hv.

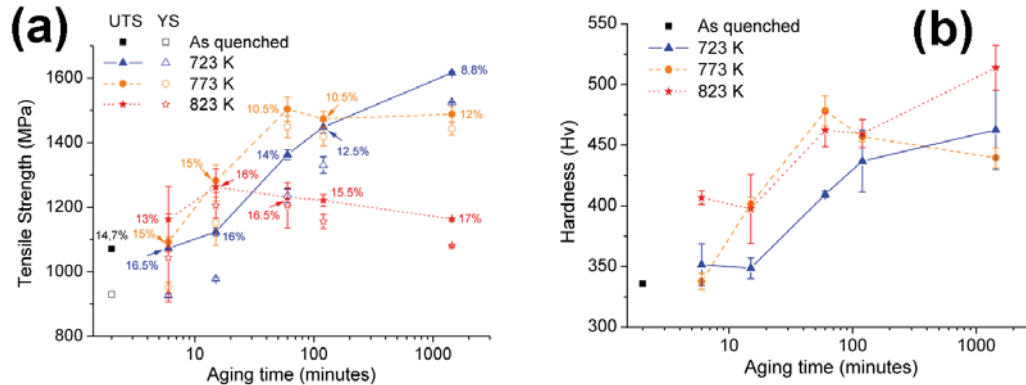


FIGURE 6.13. Variation of hardness, tensile strength and total elongation of alloy Car2 with ageing time. The ageing temperatures are 723, 773 and 823 K respectively. The total elongation is indicated by values in plot (a).

The hardness, tensile strength and total elongation values for alloy CarCo2 are plotted in Figure 6.14 as a function of ageing time. The hardness results indicate the ageing response is rapid so that the hardness increases from 300 to 450 Hv after 6 minutes at 723 and 773 K, and almost reaches 600 Hv after 6 minutes at 823 K. Further ageing at 723 and 773 K shows increases in hardness for times up to 2 hours, resulting in a maximum hardness of 500 and 550 Hv, respectively, and overageing occurs afterwards. However, the tensile tests suggest a very different effect as short ageing of 6 minutes leads to only a slight increase in strength while good ductility remains. Afterwards, the strength shows big deviations and some specimens suffered from brittle fracture except those aged 723 and 823 K for 24 hours in which a good ductility level can be obtained again. A good balance in strength and ductility can be achieved after ageing at 723 K for 24 hours in which an ultra high strength above 1.6 GPa is obtained together with ductility of 10 %. In these conditions for which the hardness achieve its peak value, ageing at 773 K for 2 hours, the strength is unexpected low. The inconsistency between

hardness and strength trends may be due to alloy inhomogeneity, inclusions and microcracks during alloy fabrication and defects introduced during the machining of tensile specimens.

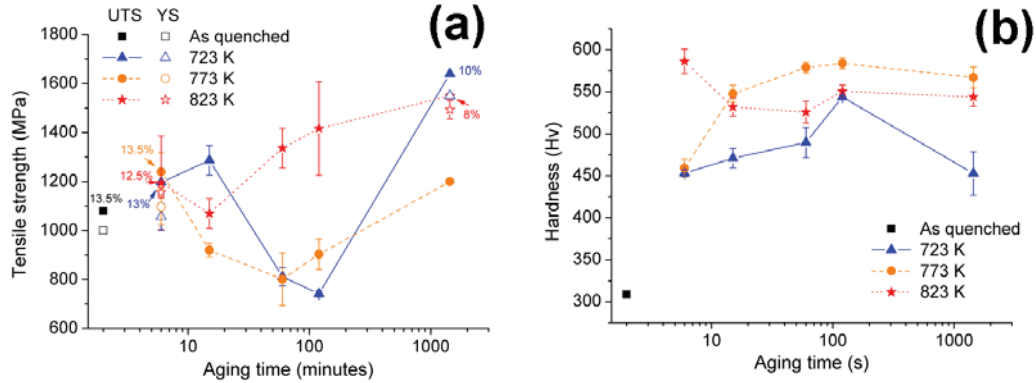


FIGURE 6.14. Variation of hardness, tensile strength and total elongation of alloy CarCo2 with ageing time. The aging temperatures are 723, 773 and 823 K respectively. The total elongation is indicated by values in plot (a).

6.7.2 Microstructures

Representative micrographs of selected conditions of alloys NiTi2, CuNi2, Car2 and CarCo2 are shown in Figures 6.15-6.20 respectively. As compared to the cold rolled condition shown in Figure 6.9(a), a banded martensite structure in alloy NiTi2 resulting from cold rolling is better revealed after ageing treatment at 773 K for 6 minutes, as shown Figure 6.15(a). After prolonged ageing (24 hours) at the higher temperature of 823 K, Figure 6.15(c) shows a better contrast. The different degrees of contrast may be due to the evolution of the precipitate population or different degrees of depletion of the alloying elements in the matrix. Although the matrix seems to consist of dark and white bands, they both are believed to be martensite as the austenite is identified as the weak peaks in the XRD pattern after ageing at 773 K for 24 hours (Figure 6.16). It should also be noticed that the austenite peak becomes stronger relative to the cold rolled condition which suggests the formation of some revert austenite, which is not distinguished in optical micrographs in Figure 6.15. The formation of reverse austenite can be responsible for the ductility improvement with ageing treatment as displayed in Figure 6.11(b). The SEM micrographs of specimens aged at 773 K for 60 minutes and 823 K for 24 hours are shown in Figures 6.15(b) and (d). Despite the significant precipitation strengthening effect observed in Figures 6.11, no precipitates can be clearly distinguished using optical microscopy. A detailed precipitate characterisation is presented in the discussion.

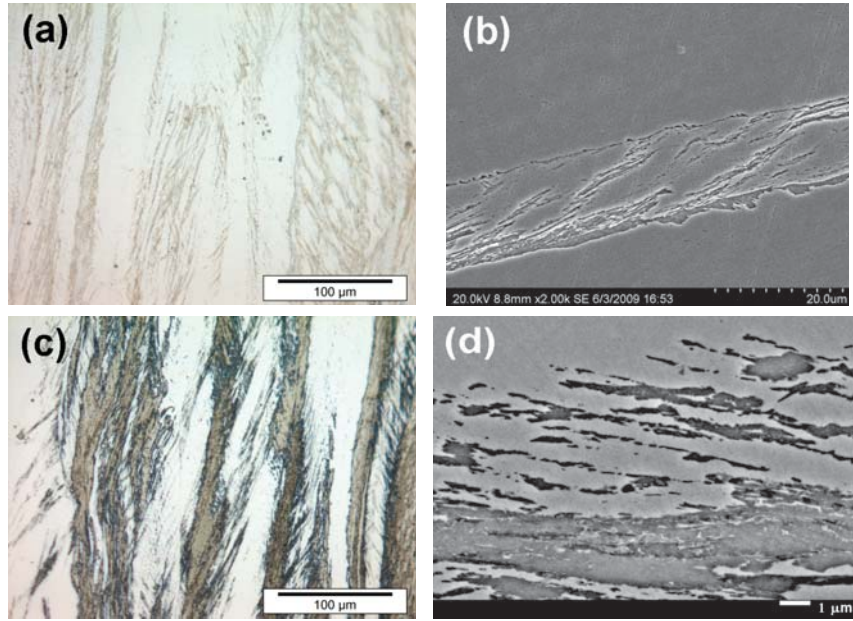


FIGURE 6.15. Micrographs of alloy NiTi2 on the cross section of tensile specimens after (a) ageing at 773 K for 6 minutes (OM), (b) ageing at 773 K for 60 minutes (SEM) and (c-d) ageing at 823 K for 24 hours (OM and SEM).

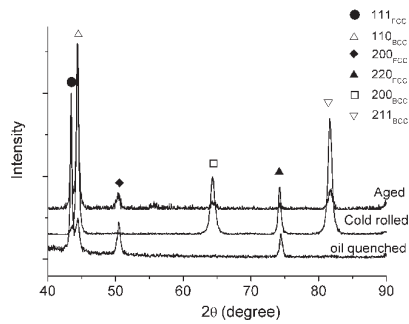


FIGURE 6.16. X-ray diffraction of alloy NiTi2 after ageing treatment of 773 K for 24 hours.

Figure 6.17 displays microstructures of alloy CuNi2 which are similar to those of alloy NiTi2 except now some δ -ferrite can be observed. In the ageing condition of 823 K for 24 hours, the dark region becomes very prominent, which indicates an intensive precipitation stage. Some precipitate features can be identified in Figure 6.17 but their details will be characterised by TEM and presented in the discussion. It should also be mentioned that in the δ -ferrite grains, a very dense network of nanosized precipitates can be observed as shown in Figure 6.17(d). The densely distributed ultra fine precipitates might be Cu rich particles, as they were reported to precipitate intragranularly within δ -ferrite grains [37][86]. The ageing treatment of alloy CuNi2 does not introduce reverse austenite as indicated by the XRD pattern in Figure 6.18.

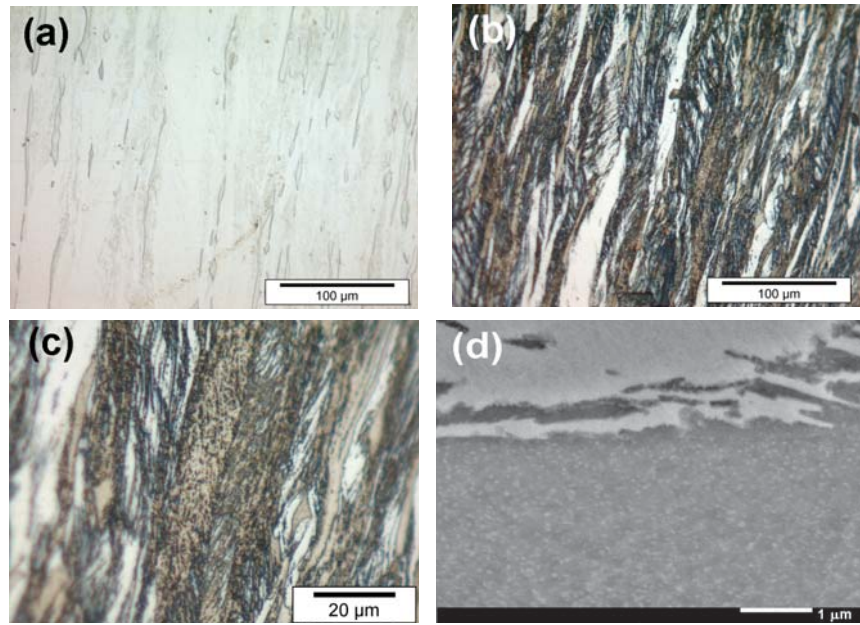


FIGURE 6.17. Micrographs of alloy CuNi2 on the cross section of tensile specimens after (a) ageing at 773 K for 6 minutes (OM), (b-c) ageing at 823 K for 24 hours (OM) and (d) ageing at 823 K for 24 hours (SEM).

In alloy Car2, a lath martensite matrix forms upon quenching prior to ageing treatment and therefore in all ageing conditions, only randomly oriented lath martensite can be identified as shown in Figures 6.19. At the early stages of ageing treatment, 15 minutes at 723 K (Figure 6.19(a)) and 6 minutes at 773 K (Figure 6.19(b)), a small fraction of primary carbides can be found, both along and within the prior austenite grains. The newly formed precipitates responsible for strengthening can be clearly identified, especially at higher temperatures and longer times, as displayed in 6.19(c,d). In comparison with the previous alloy Car, the amount of primary carbides decreases dramatically which may free the carbide formers in

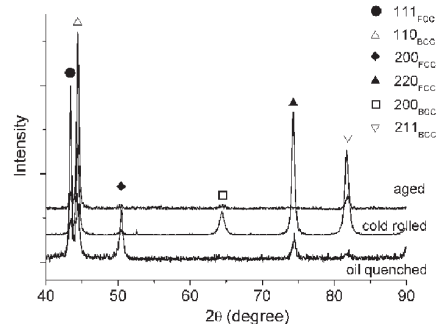


FIGURE 6.18. X-ray diffraction of alloy CuNi2 after ageing treatment of 773 K for 24 hours.

the matrix and hence allows the formation of the strengthening carbides in the desired form during ageing. The nature of the precipitates will be characterised in the next section.

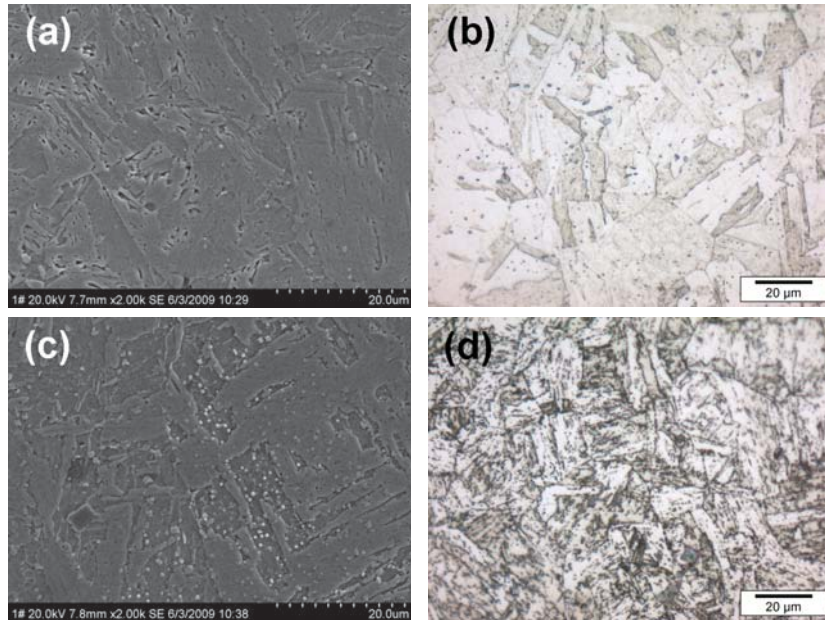


FIGURE 6.19. Micrographs of alloy Car2 on the cross section of tensile specimens after (a) ageing at 723 K for 15 minutes (SEM), (b) ageing at 773 K for 6 minutes (OM), (c) ageing at 823 K for 2 hours (SEM) and (d) ageing at 823 K for 24 hours (OM).

After the ageing treatment, alloy CarCo2 also shows a similar martensitic matrix with some micro-sized primary carbides distributed in the matrix (Figures 6.20). However, other smaller precipitates can be found throughout the martensite matrix, and their size and density increase with ageing temperature and/or

time, as shown in Figures 6.20. Further investigation is required to characterise the precipitation reaction and hence explain the strengthening effects.

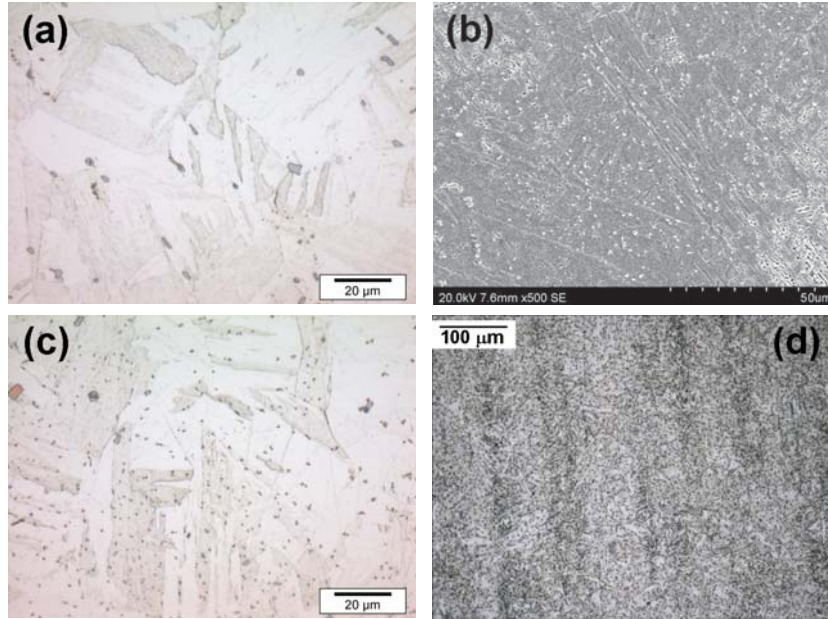


FIGURE 6.20. Micrographs of alloy CarCo2 on the cross section of tensile specimens after (a) ageing at 723 K for 6 minutes (OM), (b) ageing at 723 K for 24 hours (OM), (c) ageing at 773 K for 1 hour (OM) and (d) ageing at 773 K for 24 hours (SEM).

6.7.3 Fractography

The fracture surfaces of alloy NiTi2, CuNi2, Car2 and CarCo2 for selected aging treatment conditions were investigated by SEM. Figure 6.21(a) shows a typical fracture surface for alloy NiTi2 after aging at 723 K for 6 minutes in which both brittle and ductile areas can be found. After an ageing treatment at 773 K for 2 hours (Figure 6.21(b)), the dimples become bigger and deeper with a better homogeneous distribution, in agreement with elongation changes shown in Figure 6.11. The fracture surface of alloy CuNi2 shown in Figure 6.21(c) displays a typical brittle fracture and some ductility can be achieved after longer ageing as some small dimples can be observed in Figure 6.21(d). Alloy Car2 displays good ductility at its early precipitation stage as shown in Figure 6.21(e) while it becomes more brittle as it is subjected to longer ageing treatment which leads to more intensive precipitate distribution. Similarly to alloy Car2, alloy CarCo2 also shows dense, big and deep dimples in the ageing condition of 723 K for 6 minutes (Figure 6.21(g)), while ductility is completely lost after ageing at 773 K for 2 hours (Figure 6.21(h)). In

summary, the fractographs shown in Figure 6.21 correspond well to the elongation measured by tensile tests.

6.8 Discussion

6.8.1 The Effects of Composition and Heat Treatment Temperatures

The second round of prototype alloys were designed in an integrated manner so that the alloy composition is optimised simultaneously with solution treatment and ageing temperatures. The alloy strengthening contribution will reach an optimum value while satisfying all go/nogo criteria at the designed solution and ageing temperatures only if the alloy composition is exactly the same as the designed values. However, the alloy fabrication is not a simple process and there are always composition deviations at various extents. Deviations in the alloy composition may change the thermodynamics of alloy systems, and hence change the optimal heat treatment temperature accordingly. Table 6.8 shows the resulting equilibrium calculations from ThermoCalc at both designed and experimentally chosen temperatures of solution treatment and ageing treatment, with the actual alloy compositions. The thermodynamic equilibrium with the designed alloy compositions is also calculated, but only at designed optimal heat treatment temperatures and results are shown in Table 6.8.

Alloys	Comp	Solution treatment				Ageing treatment			
		$T_{Aus}(K)$	Aus	MC	δ -Fer	$T_{Age}(K)$	MC	Ni ₃ Ti	Cu
NiTi2	Actual	1403	99.89	0.11		758	0.10	9.07	0.27
		1423	99.89	0.11		773	0.10	9.01	0.25
	Design	1403	99.82	0.17		758	0.17	8.54	0.32
CuNi2	Actual	1463	97.16	0.15	2.69	758	0.15	6.69	1.77
		1423	98.03	0.15	1.81	773	0.15	6.57	1.75
	Design	1463	99.71	0.17	0.12	758	0.17	5.70	1.78
Car2	Actual	1533	99.25	0.75		738	0.96	0.36	1.94
		1423	99.13	0.87		773	0.96	0.21	1.91
	Design	1533	99.50	0.50		738	0.93	0.60	1.71
CarCo2	Actual	1253	99.04	0.96		818	0.98		1.86
		1423	99.13	0.87		773	0.97	0.21	1.91
	Design	1253	99.85	0.15		818	0.82	5.39	1.78

TABLE 6.8. Phase equilibrium fractions calculated by ThermoCalc on actual and designed compositions of the second round of prototype alloys at solution and ageing temperatures of both experiments (1423 and 773 K) and designed optimum as in Table 6.2. The amounts of phases are in molar percent.

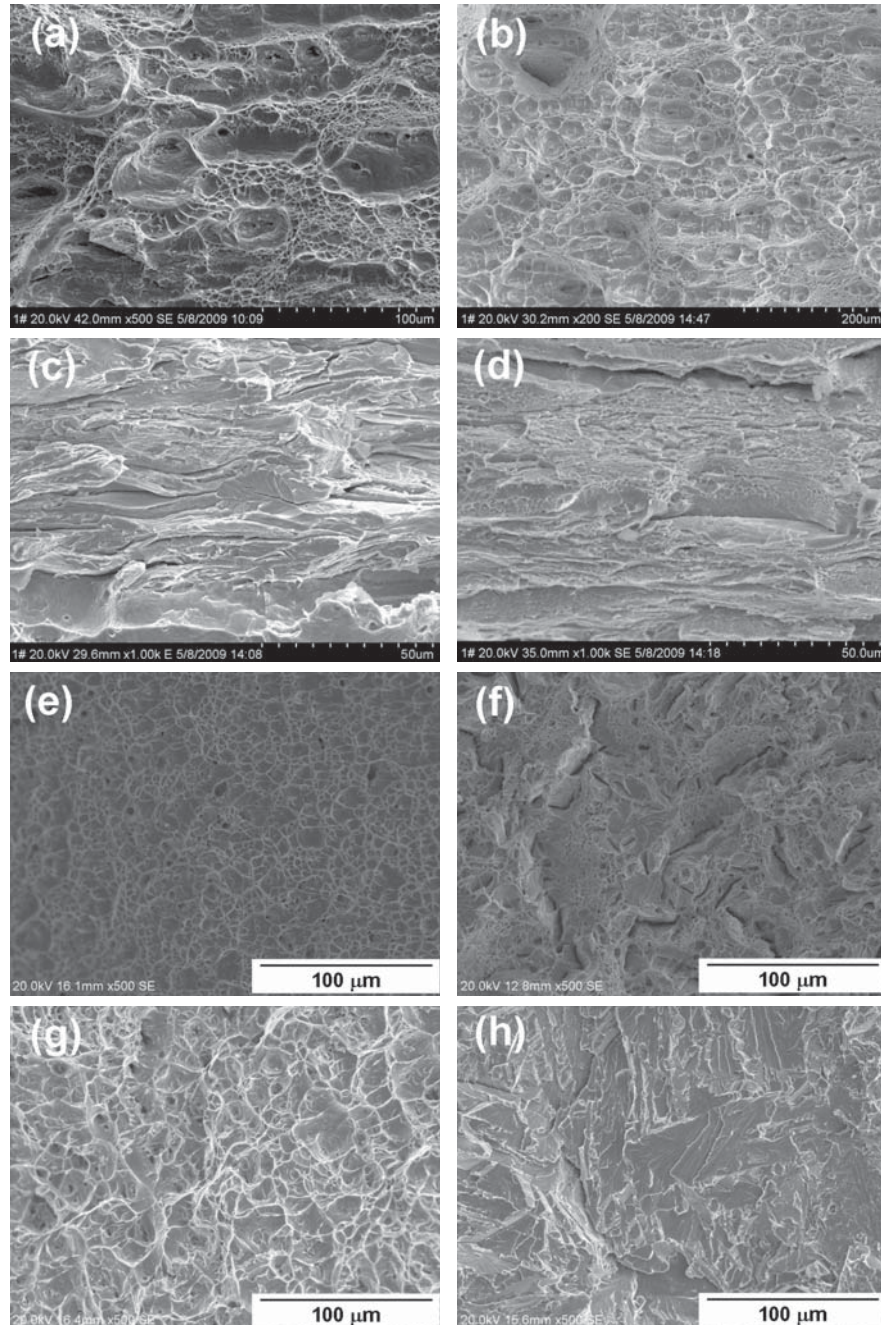


FIGURE 6.21. Fractographs of tensile specimens after ageing treatment of (a) alloy NiTi2 at 723 K for 6 mins, (b) alloy NiTi2 at 773 K for 2 hours, (c) alloy CuNi2 at 773 K for 6 mins, (d) alloy CuNi2 at 773 K for 24 hours, (e) alloy Car2 at 723 K for 6 mins, (f) alloy Car2 at 773 K for 24 hours, (g) alloy CarCo2 at 773 K for 6 mins and (h) alloy CarCo2 at 773 K for 2 hours.

For alloy NiTi2, with the actual alloy composition, the designed heat treatment temperature (1403 K for solution treatment and 758 K for ageing treatment) and experimental chosen ones (1423 K for solution and 773 K for ageing) do not make real differences in terms of phase fractions. The criteria for avoiding primary carbides and δ -ferrite at solution treatment remain fulfilled at the new solution temperature. Similar amounts of strengthening precipitates of Ni_3Ti are formed at both designed and actual ageing temperatures. In comparison to the designed composition, the deviations of composition do not produce significant changes. Due to the fact that actual C concentration is lower than the designed value, the primary carbide is therefore shown a smaller fraction in the actual alloy. In summary, the composition deviations of alloy NiTi2 do not lead to notable changes at designed temperatures and changing the designed temperatures to experimental values also does not result in big differences.

With respect to alloy CuNi2, the actual alloy shows a significant fraction of δ -ferrite (2.69 %) at the designed solution treatment temperature (1463 K) due to the composition deviations of Ni, Ti and Cu. The presence of δ -ferrite is in agreement with experimental observation. However, the predicted fraction of δ -ferrite decreases with lower solution treatment temperatures which was also observed by experiments. Therefore, an experimental adaption of solution temperature is necessary so as to reduce the amount of δ -ferrite, rather than keeping the designed optimum. The differences of alloy composition and ageing temperature show minor effects on phase fractions predicted for the ageing condition. In conclusion, deviations of alloy composition of alloy CuNi2 produce significant increase of δ -ferrite formation and changing to lower solution temperature is advised to minimise its fraction. These predictions are in good agreement with experimental observations.

ThermoCalc calculations show that alloy Car2 for its designed composition will yield 0.5 % of primary carbide at a temperature of 1533 K which amount is exactly at the limit of the design criterion. The C concentration of actual alloy is higher than the designed value hence it will contain higher fractions of primary carbide at designed temperature of 1533 K (0.75 %) and actual temperature of 1423 K (0.87 %). The effects of composition and temperature are less prominent regarding to carbide formation at the ageing treatment. However, it is important to note that, the difference of primary carbide fraction and carbide fraction at the ageing stage, which is the amount of carbide precipitates forming during ageing, decreases significantly from (0.93-0.50) to (0.96-0.75/0.87) which implies a smaller strengthening contribution from carbides. A reduced amount of Ni_3Ti precipitates is predicted with the real alloy composition in comparison to designed composition and its molar fraction decreases with higher ageing temperature. Alloy CarCo2 shows similar results as alloy Car2 which suggest the superfluous primary carbides can be partially dissolved at a higher solution temperature. The composition variations lead to a significant reduction of Ni_3Ti precipitates although in this alloy it is not designed to be the major strengthening precipitate species.

Another effect of deviations of alloy composition is on the Ms temperature and hence the martensitic transformation. As shown in Table 6.8, the Ms temperatures of alloy NiTi2 and CuNi2 with the desired composition are exactly at the design limit of 473 K. In the real alloys, because of the higher concentration of austenite stabiliser, Ni, the predicted Ms temperatures are lower than 473 K. This results in a metastable austenite matrix which is consistent with the fact that the matrix was only partially transformed to martensite upon quench, and only intensively transformed to martensite when subjected to cold rolling. The Ms temperatures of alloy Car2 and CarCo2 are also changed slightly because of concentration deviations but still well above the limit of 473 K. A fully martensitic matrix after quenching is expected according to the predicted Ms temperature and indeed, it has been observed experimentally.

Effects of alloy composition as well as heat treatment temperatures on equilibrium phase fractions have been analysed employing ThermoCalc. The results suggest that unavoidable deviations of alloy composition may produce significant changes of phase fractions at equilibrium. Adaptions of heat treatment temperatures rather than the designed optimum are advised to compensate negative effects introduced by composition deviations. Nevertheless, alloy design integrating composition and heat treatment temperature is a successful approach as it takes into account the cross effects of composition and temperature and provides good references of heat treatment temperatures which can be further improved experimentally or computationally, in response to changes of alloy composition. The methodology following subsequent optimisations of composition and heat treatment condition would not be sufficient to dissolve the undesirable phases introduced by composition deviations, by means of only varying heat treatment parameters. For instance, the δ -ferrite and primary carbides in the first round of prototype alloys, which were designed without considering temperature effects, could not be dissolved by a later heat treatment.

6.8.2 Identification of Strengthening Precipitates

In order to identify the precipitate characteristics of the second round of prototype alloys, a prolonged ageing condition of 24 hours at a modest temperature of 773 K was selected to determine the nature of precipitates employing SEM and TEM microscopy, in combination with EDS analysis. Figures 6.22 show very clear images of a dense network of precipitates found in alloy NiTi2. The precipitates display rod shape with a diameter of about 10 nm and length of hundreds of nanometres, following certain preferred orientations, and distributed homogeneously within lath martensite grains. The high resolution TEM image shown in Figure 6.22(c) clearly reveals the morphology of the rod shaped precipitate. Smaller precipitates of the same shape can also be identified as in Figure 6.22(b). The smaller size can be due to precipitates which are either at a relatively early precipitation stage or at an overaging stage in which dissolution occurs.

An EDS investigation was performed along the horizontal line crossing two of the precipitates as shown in Figure 6.23. The corresponding concentration profiles of Ni, Ti and Cu are plotted below the STEM image. The EDS results clearly show that precipitates are mainly composed of Ni and Ti, with some segregation of Cu. The concentration profiles together with the morphology of the precipitate and thermodynamic predictions as shown in Table 6.8 suggest that the precipitate nature is Ni_3Ti intermetallics. This kind of needle/rod shape Ni_3Ti precipitates has been observed in various maraging steels [43][49][48]. The precipitate characterisation confirms that the alloy NiTi2 successfully achieves the design goal of a microstructure of lath martensite matrix strengthened by densely dispersed nano size Ni_3Ti precipitates. Moreover, very few primary carbides could be identified along prior austenite grain boundaries which is also in agreement with predictions in Table 6.8. Apart from densely distributed Ni_3Ti and very small amount of primary carbides, no other precipitates were identified, suggesting that the formation of Ni_3Ti precipitates is responsible for the ageing strengthening effect, which is exactly the design strategy of alloy NiTi2.

Alloy CuNi2 was also investigated by TEM after ageing treated at 773 K for 24 hours. This alloy is designed to be strengthened by precipitates of Cu clusters in combination with NiAl and/or Ni_3Ti intermetallics, as shown in Table 6.8. However, only one kind of precipitate is identified by TEM as shown in Figures 6.24. The diffraction pattern at the corner in 6.24(b) indicates a precipitate of Ni_3Ti with HCP crystallography. The EDS concentration profiles, as shown in Figure 6.25, further confirm that precipitates are rich in Ni and Ti. Different to Ni_3Ti precipitates in alloy NiTi2, the Ni_3Ti precipitates display a spheroidal shape and are most likely already in a coarsened stage, although they still provide very strong strengthening effects as shown in Figure 6.12. The presence of spheroidal Ni_3Ti precipitates has been reported in maraging steels before [43]. It is very interesting to highlight that the EDS result also shows the precipitate is rich in Cu in comparison with the matrix. This is in agreement with the experimental observations of precipitation sequence in maraging steel 1RK91 nanoflex [39][40][41][42] in which Cu particles are the first to form after only a few minutes at 748 K and hence act as potential nuclei and encourage the precipitation of Ni_3Ti intermetallics. Moreover, this may also be the reason that Ni_3Ti shows different spheroid like morphology rather than the needle/rod shape as in the low Cu alloy NiTi2.

Alloy Car2 and CarCo2 are intended to be strengthened by TiNbC carbides with some amounts of other precipitates of Ni_3Ti and Cu particles. Due to the similarity of these two alloys, only alloy Car2 were carefully investigated for identifying precipitates. Figures 6.26 show the distribution of spheroidal intragranular precipitates with an average size of 100-300 nanometers in diameter, after an ageing treatment at 773 K for 24 hours. The SEM-EDS analysis shown in Figure 6.26(c) clearly indicates that the precipitate is TiNbC carbide. Therefore, the design target of utilising TiNbC carbides in alloy Car2 is successfully achieved, although they

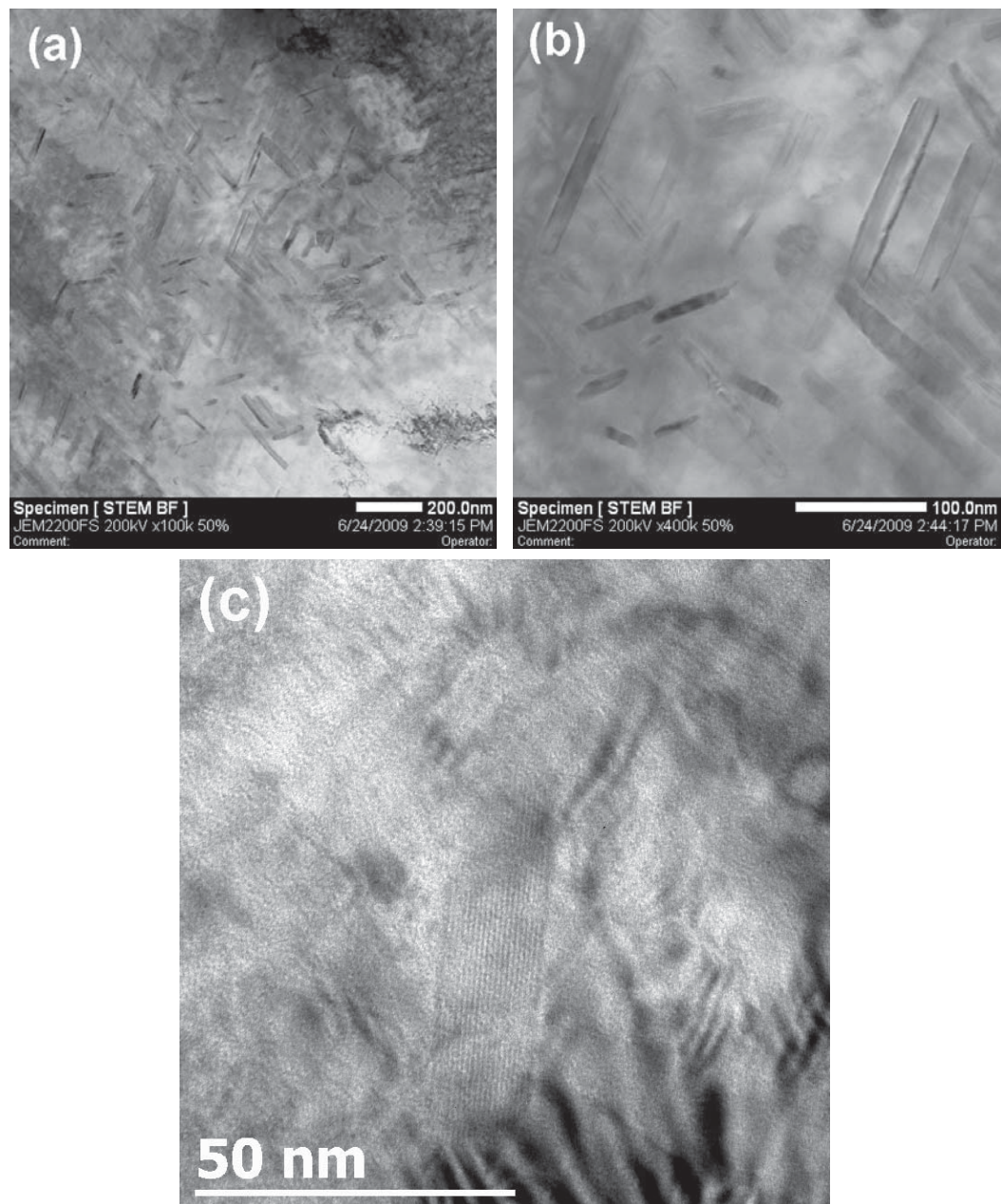


FIGURE 6.22. Micrographs of precipitates in alloy NiTi2 after ageing at 773 K for 24 hours. (a-b) STEM BF images and (c) HRTEM iamge.

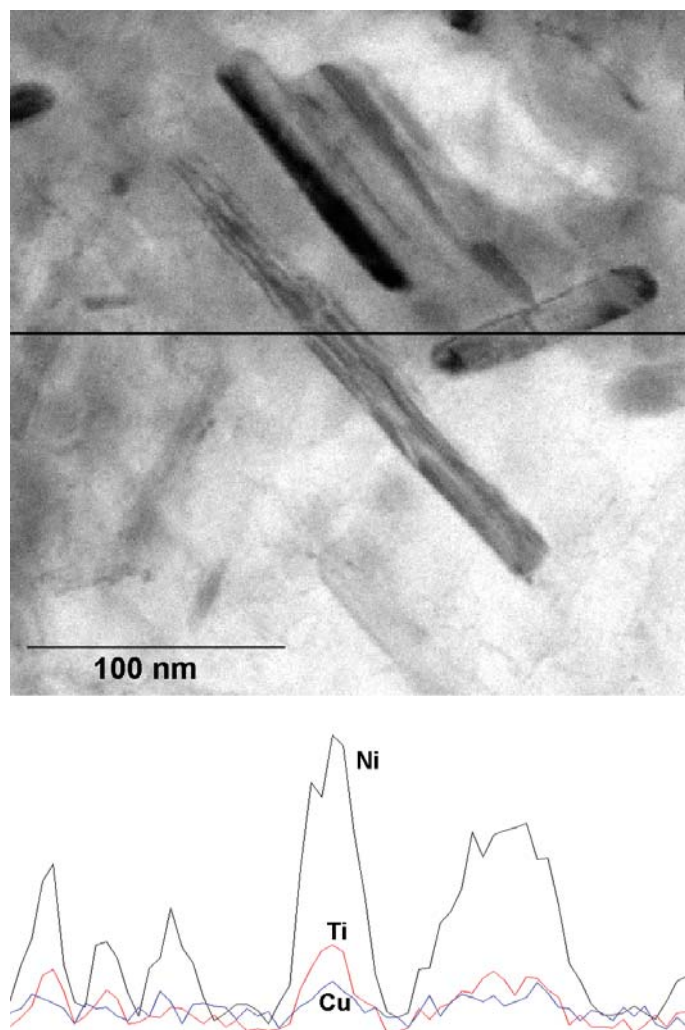


FIGURE 6.23. STEM micrograph of precipitates in alloy NiTi₂ after ageing at 773 K for 24 hours with EDS results of concentration profiles of Ni, Ti, and Cu, measured on the horizontal line as indicated.

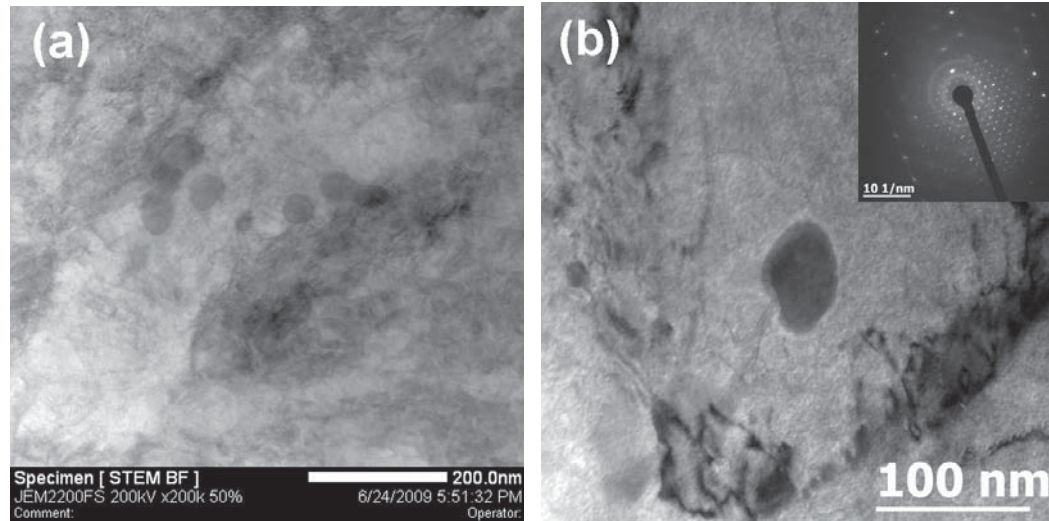


FIGURE 6.24. (a) STEM and (b) TEM images of precipitates in alloy CuNi2 after ageing treatment of 773 K for 24 hours. The diffraction pattern of precipitate in (b) is shown in the corner.

are of a bigger size than is desirable because the ageing condition investigated is sufficient for coarsening to take place. The precipitation strengthening contribution of carbide may be more prominent at lower ageing temperature or shorter times.

Other finely dispersed species than TiNbC precipitates was found in alloy Car2 and a STEM image is shown in Figure 6.27(a). This phase forms a very dense network of nano precipitates less than 10 nm and are homogeneously distributed in the lath martensite matrix. They are identified as Ni_3Ti by their diffraction pattern as shown in Figure 6.27(a). Figure 6.27(b) shows HRTEM image of ultra fine precipitates, in which some big Ni_3Ti precipitates are in an orientation close to zone axis and hence can be clearly distinguished from matrix by the larger lattice parameters. The other smaller precipitates which can not be clearly differentiated may be at other orientation, or a different nature of precipitate. The precipitates are found to be very resistant to coarsening since their sizes remain less than 10 nm after ageing at 773 K for 24 hours and therefore provide significant contribution to strength. This feature of Ni_3Ti precipitates is consistent with experimental observations by Raabe [53] and He [49][48].

The STEM-EDS analysis of ultra fine precipitates are shown in Figures 6.28. Figure 6.28(a) shows similar result to Figure 6.24 which suggests Ni_3Ti precipitates possibly form on former Cu clusters and hence are rich in Ni, Ti and Cu. However, some precipitates are found to be only rich in Cu, as shown in 6.28(b). The Cu particles show twinned structure fringes similarly as reported by Habibi-Bajguirani in PH15-5 maraging steels [34][95]. The precipitation characteristics in

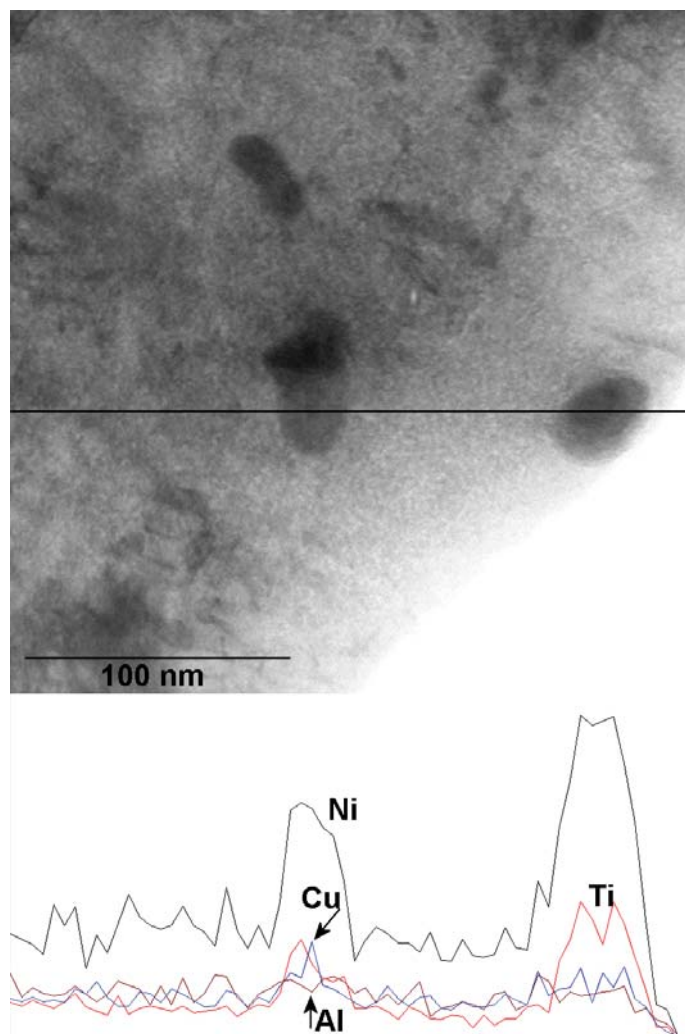


FIGURE 6.25. STEM micrograph of precipitates in alloy CuNi2 after ageing at 773 K for 24 hours with EDS results of concentration profiles of Ni, Ti, Al and Cu, measured on the horizontal line as indicated.

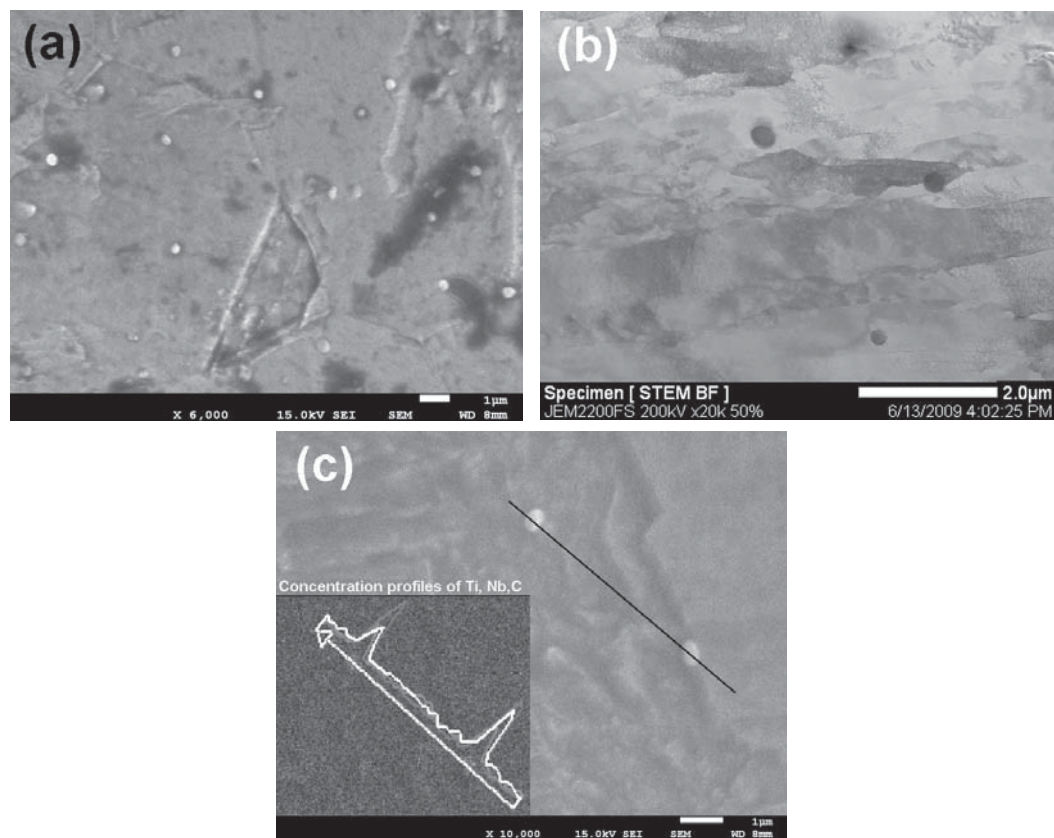


FIGURE 6.26. Micrographs of precipitates in alloy Car2 after ageing treatment at 773 K for 24 hours. (a) SEM image, (b) STEM image and (c) SEM image with EDS analysis of concentration profiles of Ti, Nb and C, on the line as indicated.

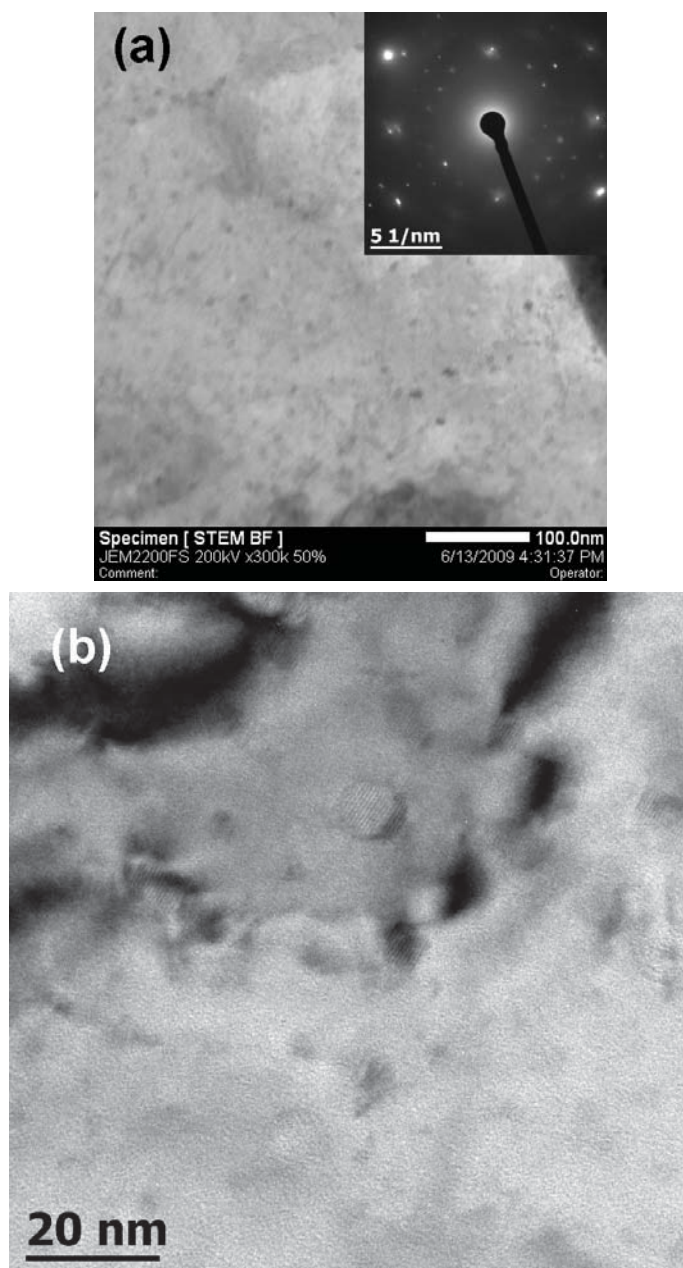


FIGURE 6.27. (a) STEM image of precipitates in alloy Car2 after ageing at 773 K for 24 hours with diffraction pattern of the selected area and (b) HRTEM image of the precipitates.

alloy Car2 are very complex as it possesses different precipitates of TiNbC carbide at size of 100-300 nanometres, Ni_3Ti precipitates with slight segregation of Cu about 10 nm and Cu precipitates with twinned structures less than 10 nm. It is important to highlight that all three species have been predicted by ThermoCalc as discussed earlier. The strengthening effect are believed to be due to contributions from mixture of multiple precipitates and further investigation is required to understand the details.

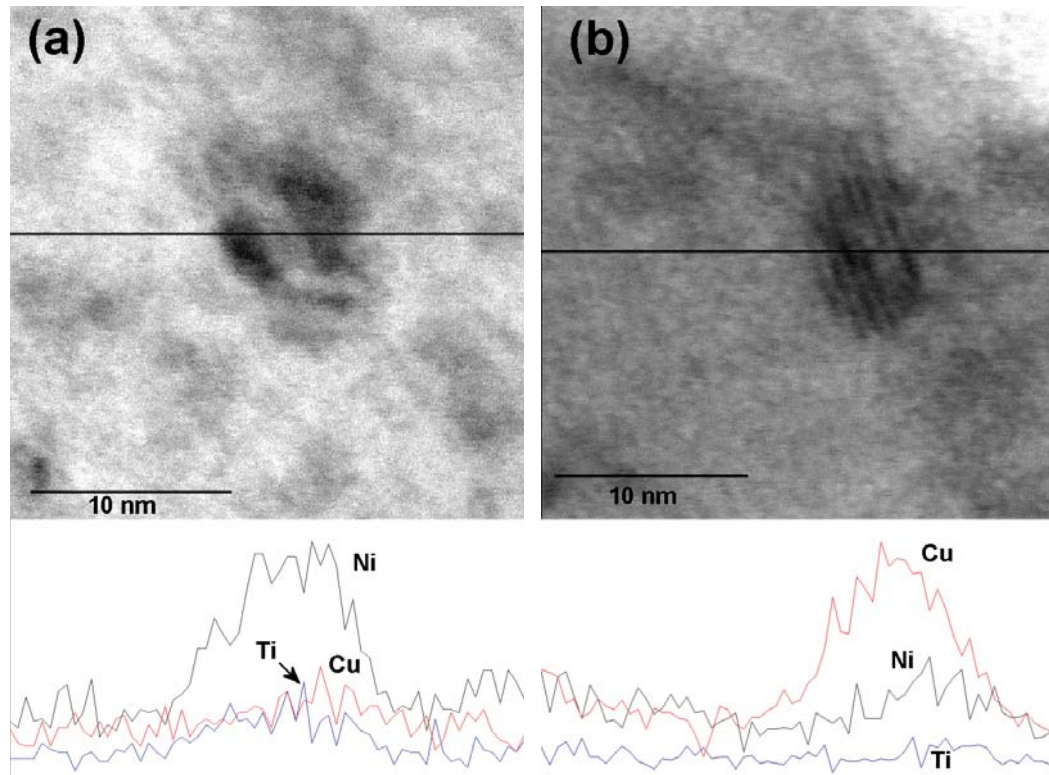


FIGURE 6.28. STEM micrographs of precipitates in alloy Car2 after ageing at 773 K for 24 hours with EDS results of concentration profiles of Ni, Ti and Cu, measured on the horizontal line as indicated.

6.8.3 Corrosion Resistance

As an essential part of design goals, the corrosion resistance of UHS stainless steels developed in this thesis should be sufficient so as to be applied in corresponding applications. Corrosion is an electrochemical process that is characterised by mass transport as well as the electrical and ionic charge. There are various forms of corrosion including uniform attack, crevice corrosion, pitting corrosion, galvanic corrosion, intergranular corrosion, selective leaching, erosion corrosion, stress corrosion, and hydrogen damage [149]. However, because of the nature of stainless

steels, the formation of passive Cr-oxyhydroxide film on the surface, pitting corrosion is the main issue associated with stainless steels corrosion [150].

Potentiodynamic polarisation measurements were performed on various alloys including UHS non-stainless steel 300M and Aermet100, standard austenitic stainless steels 304 and 316, UHS maraging stainless steel 1RK91 nanoflex and the second round of prototype alloys NiTi2, CuNi2, Car2 and CarCo2 after ageing treatment at 773 K for 6 minutes and 24 hours respectively. Figure 6.29 shows typical potentiodynamic polarisation curves in which different corrosion features can be observed. Alloy Aermet100 is a grade of non-stainless steels and therefore, the corrosion potential is very low indicating easy corrosion initiating while the corrosion current density is high suggesting a fast corrosion rate. The potentiodynamic polarisation curves of alloy Car2 and CarCo2 after ageing at 773 K for 24 hours display more noble corrosion potentials with lower current density implying better corrosion resistance comparing to alloy NiTi2 and Aermet100. Moreover, clear breakdown/pitting potentials can be observed for alloy Car2 and CarCo2 which indicate they undergo pitting corrosion and alloy Car2 is more resistant to pitting corrosion.

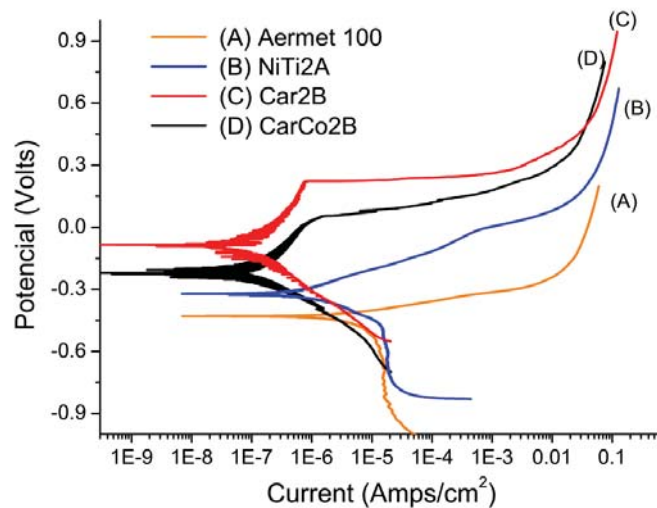


FIGURE 6.29. Typical potentiodynamic polarization curves for alloy Aermet100 (A), alloy NiTi2 after ageing at 773 K for 6 minutes (B), alloy Car2 after ageing at 773 K for 24 hours (C) and alloy CarCo2 after ageing at 773 K for 24 hours (D).

Corrosion potential - current density profiles obtained from potentiodynamic polarisation curves are summarised in Figure 6.30. The pitting potential and current density are also indicated for the stainless grades. The comparison of corrosion potential and current density shows that alloy 300M and Aermet100 have very

negative potential and high current because of their non-stainless nature. Alloy Car2 possesses the best corrosion resistance clearly superior to its existing counterparts of alloy 1RK91 nanoflex and standard stainless steels 304 and 316. Corrosion resistance of all prototype alloys decreases with longer ageing time corresponding to precipitation kinetics and depletion of the matrix. Alloys CarCo2, NiTi2 and CuNi2 display a similar level of corrosion resistance as the reference alloys (304, 316 and 1RK91). However, alloys CarCo2 and CuNi2 show inferior corrosion resistance at prolonged ageing conditions. The pitting resistance of designed alloys follow the same order of alloy Car2, CarCo2 and NiTi2/CuNi2. Alloys Car2 and CarCo2 are clearly better than reference alloys after short time ageing in terms of pitting resistance. However, the pitting potentials of all alloys decrease with long ageing time. Particularly, alloy CarCo2 displays good pitting resistance at 6 minute of ageing but shows surprising low resistance after 24 hour ageing.

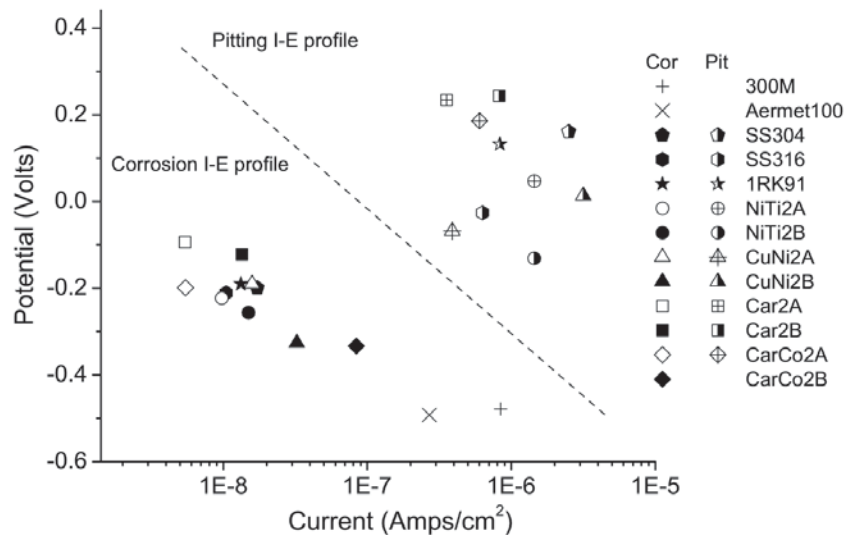


FIGURE 6.30. General corrosion potential-current density profiles and pitting corrosion potential - current density profiles of various alloys. For the second round of prototype alloys, the corrosion test were performed after ageing at 773 K for 6 minutes (A) and 24 hours (B).

Optical micrographs of exposed surfaces after corrosion tests are shown in Figure 6.31(a), for selected conditions. Figure 6.31(a) clearly shows that the corrosion resistance of alloy 300M is inferior to that of the stainless grades. Figure 6.31(c) reveals a much denser network of pits in comparison to Figure 6.31(b) suggesting the corrosion resistance of alloy 316 is superior to alloy NiTi2 after ageing for 24 hours, which is in agreement with data in Figure 6.30. Alloy Car2 aged for 24 hour displays a few, but deep pits (Figure 6.31(d)) indicating that the alloy is resistant to pitting corrosion, while once initiated, the pitting corrosion can proceed fast.

This is consistent with alloy Car2 after ageing of 24 hours displaying a relative high pitting potential but high current density as well (Figure 6.30). The high pitting resistance of alloy CarCo2 after short ageing as observed in Figure 6.30 results in very few pits after the corrosion tests, as shown in Figure 6.31(e). However, after long time ageing, the corrosion resistance becomes very weak as suggested by Figure 6.31(f).

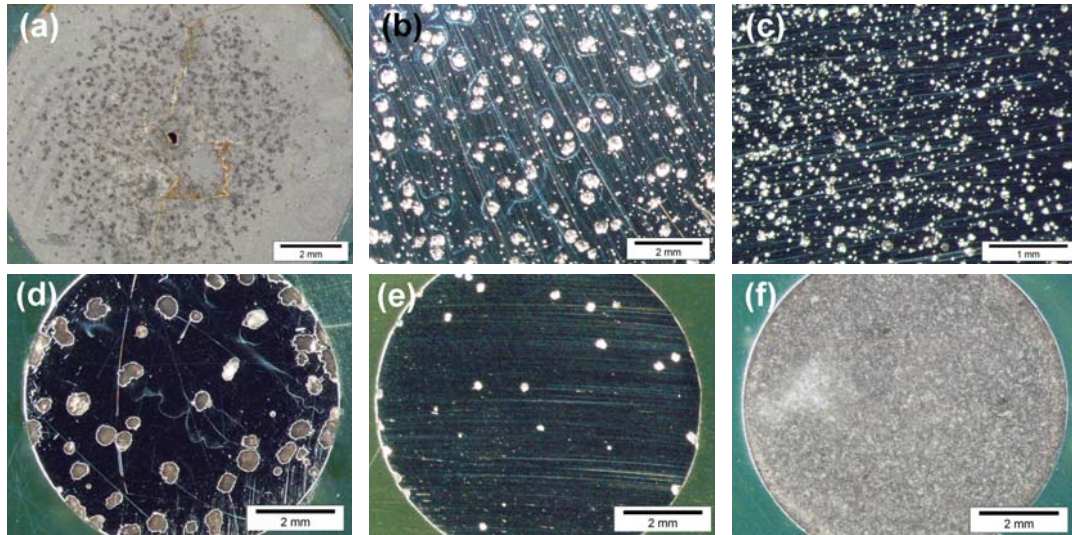


FIGURE 6.31. Optical micrographs after corrosion test of (a) UHS steel 300M, (b) stainless steel 316, (c) alloy NiTi2 after ageing at 773 K for 24 hours, (d) alloy Car2 after ageing at 773 K for 24 hours and (e-f) alloy CarCo2 after ageing of 773 K for 6 minutes and 24 hours, respectively.

6.8.4 Comparison to Existing Counterparts

After two rounds of prototype alloys, the best properties of all newly designed alloys are compared to various existing high-end maraging steels in Figure 6.32. The locations of our prototype alloys indicate that their properties are generally at the state of the art of ultra high strength steels, and in some cases, achieve a better combination of strength and ductility than any of the existing alloys. Alloys NiTi and CuNi are in the category of maraging trip steels possessing very good balance of strength and ductility. Alloy CuNi achieves the best combination of 1.2 GPa UTS along with 40 % elongation. Alloys NiTi2 and CuNi2 follow the same principle but they are cold rolled in order to further stimulate the martensitic transformation prior to ageing treatment. Therefore, the strength levels of these two grades increase significantly at the cost of ductility. Alloys from the first round of experiments utilising carbides for strengthening are not very successful because of the formation of undesirable primary carbides consuming all carbide formers,

and their decreased formation of nanosized strengthening precipitates during ageing as well as resulting in a low ductility. However, the properties of alloy CarCo are close PH13-8. The second round of carbide strengthening alloy Car2 and CarCo2 achieve better properties than the first round and reach the state of the art of ultra high strength steels. Given the fact that all alloys were produced on a small experimental scale, it is safe to assume that if the alloys were produced on an industrial scale with better control, and the heat treatment conditions were further optimised, it is believed that the alloys properties would be further enhanced.

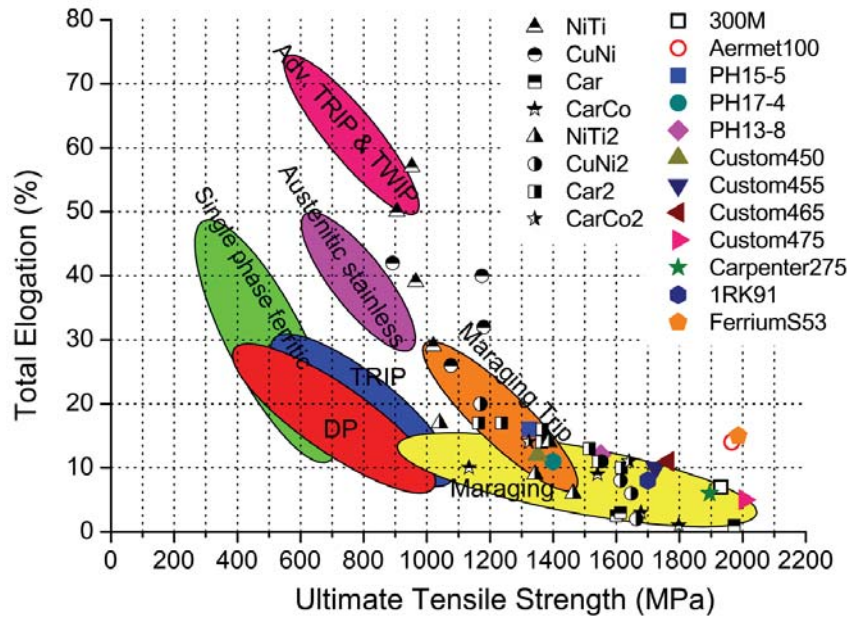


FIGURE 6.32. The strength-ductility profile of various existing high-end maraging steel grades and newly designed alloys presented in this thesis.

6.9 Conclusion

The second round of prototype alloys following the same design scenarios as in the first round are redesigned employing an integrated model. This allows for the simultaneous optimisation of alloy composition and high and low temperature treatments, which leads to achieving desired microstructures while avoiding undesirable phases throughout the heat treatment. The results show that, the undesirable δ -ferrite in alloy NiTi is completely avoided in the second round of NiTi2, while in alloy CuNi2 it remains present, with a smaller amount, due to small deviations of alloy composition from the target composition. In alloys Car2 and CarCo2, the

formation of micro size primary carbides is successfully suppressed and hence promote the strengthening precipitation of fine TiNbC during ageing. The austenitic matrix of alloys NiTi2 and CuNi2 are partially transformed to martensite upon quenching and the martensitic transformation can not be promoted by employing cryogenic treatment or fast cooling rate, but by cold rolling. As quenched alloys Car2 and CarCo2 display the desired martensite matrix as desired because of their relatively higher Ms temperature.

Despite the dramatic strength/hardness increase of alloys NiTi2 and CuNi2 upon cold rolling and the accompanying martensitic transformation, the strength/hardness of these two alloys can be significantly further increased by ageing strengthening. The precipitation shows a very fast kinetics and strength/hardness remain the same level upon prolonged ageing. The ductility increases with ageing time and therefore, a good combination of strength and ductility can be achieved after 24 hours ageing. Alloys Car2 and CarCo2 also display strong precipitation effects with relative slow kinetics, and an attractive combination of 1.6 GPa UTS with elongation of 10 % can be achieved for both alloys, after ageing at 773 K for 24 hours.

The precipitation characterisation shows that in alloy NiTi2, exactly as desired, a very dense network of nanosized Ni_3Ti precipitates is present and Ni_3Ti precipitates display a needle/rod morphology. In alloy CuNi2, only one kind of precipitate, Ni_3Ti can be identified, which is spheroidal in shape and contains Cu. Alloy Car2 displays complex precipitation characteristics: homogeneous distributed TiNbC carbides at size of 100-300 nm, very finely dispersed spheroid Ni_3Ti around 10 nm and some Cu particle less than 10 nm with twinned structure. In all alloys, the experimentally found precipitates are identical to the designed species according to ThermoCalc predictions, which provides a solid proof of the computational alloy design approach presented in this thesis.

The designed alloys achieve mechanical properties comparable to those of state of art of UHS stainless steels while having a superior corrosion resistance. Although the optimal heat treatment temperatures are designed with corresponding composition employing the integrated model, due to the to unavoidable deviations of composition, the heat treatment temperatures may need further optimisation experimentally and computationally.

7

Summary

New alloys are conventionally designed following the trial and error approach, which requires the systematic production of various compositions and a large number of experiments in order to optimise the alloy composition with corresponding heat treatment parameters. This semi-empirical approach is recognised to display a low successful rate, high time consumption and cost. Therefore, there is a clear trend of shifting to theory-guided computational alloy design approaches following the goal/means oriented strategy. This thesis pursues not only a general theory-guided computational alloy design framework based on fundamental thermodynamical, mechanical and physical metallurgy principles, but also to define and provide prototype alloys of novel grades of ultra high strength stainless steels, with mechanical and corrosion resistant properties equivalent or superior to existing counterparts. Typical applications of the steel grades selected are landing gear and other heavy duty structures in passenger and military aircrafts. The characterisation of prototype alloys validates the alloy design methodology presented in the thesis.

The state of the art of existing ultra high strength steels, both stainless and non-stainless grades, is reviewed in Chapter 1. Despite of the large variety of steel grades developed in last decades, demands for further improvement in strength and ductility, and sometimes also in combination with superior corrosion resistance, are persistent. Considering the complexity of modern UHS steels involving various alloying elements in wide concentration ranges, the traditional trial and error approach is shown to be no longer sufficient.

In Chapter 2, following the goal/mean oriented design strategy, desirable microstructures of UHS stainless steel, a lath martensite matrix strengthened by a dense dispersion of nanosized precipitates of selected species along with a Cr rich protective film on the surface, have been identified as being crucial to obtain mechanical and corrosion resistant properties required for its application. The different components of desirable microstructures are translated into multiple quantifiable criteria based on thermodynamic and physical metallurgy principles. Specifically, the total number of precipitate particles (*NPP*) is maximised so as to optimise strength while Ms temperature is above 473 K for ensuring the lath martensite formation, undesirable phases are suppressed with a total volume amount less than 1 % and there is enough Cr (>12 wt%) in the matrix upon the completion of the precipitation reaction in order to form the protective Cr oxide layer. The multiple criteria are classified as optimisation criterion (*NPP*) and go/nogo criteria (the others) and are embedded in a genetic optimisation algorithm so as to compromise the conflicting criteria and find the optimal alloy composition in a huge compositional domain containing 13 alloying elements at 32 levels each. Four scenarios of UHS stainless steels employing different strengthening precipitates, MC carbide, Cu cluster, Ni₃Ti intermetallics and all together, are successfully designed consisting of 13 alloying elements. The computational comparison of newly designed alloys with the existing commercial counterparts shows that designed alloys possess significant increases of total number of precipitate particles (*NPP*) assuming they keep the critical nuclei size. The new alloy compositions partially resemble the success of existing alloys while other components lead to novel formulations not resembling existing grades.

In Chapter 3, the optimisation criterion is further developed to evaluate the precipitation strengthening contribution assuming a mixture of bypassed and sheared strengthening mechanisms, rather than the number density of precipitate particles as in Chapter 2. The exercise alloys are redesigned and display significant precipitation strengthening improvements with respect to commercial alloys. Moreover, the contributions of various alloying elements combined in pairs are disentangled and pseudo binary elements contour plots have been constructed as an aid for the alloy manufacturer to identify elements on which compositional variations are allowed, without compromising aimed properties such as strength. The other major improvement of the model in Chapter 3 is to add a new ageing temperature gene to allow the simultaneous optimisation of the alloy composition and ageing temperature. Effects of ageing temperature are studied and the results present a quantitative justification of the precipitation temperature of existing commercial UHS stainless steels. The predicted ageing temperature windows show excellent agreement with the experimental optima.

The first round of prototype alloys employing Ni₃Ti (alloy NiTi), Cu and NiAl/Ni₃Ti (alloy CuNi), MC carbides (alloy Car) and MC carbides with high Co content (alloy CarCo) are described and characterised in Chapter 4. Alloy NiTi and CuNi

display austenitic matrix upon quench with distributions of significant amounts of δ -ferrite and TiNbC primary carbides which could not be dissolved by solution treatment. The results of mechanical tests did not show notable ageing precipitate strengthening, while a good combination of high strength and ductility was achieved because of the TRIP effect. The alloys Car and CarCo show fully lath martensite matrix as designed, but with significant amount of primary carbides formed during casting. The primary carbides remain stable at solution treatment and therefore can not release solutes to form strengthening precipitates of finer TiNbC carbides and limit fracture strength levels due to their crack initiating effect. Nevertheless, obvious ageing strengthening effects have been observed in alloys Car and CarCo leading to strength levels above 1.6 GPa as well as some ductility. The strengthening precipitate in alloy CarCo is found to be a finely dispersed population of nanosized Ni_3Ti . The presence of undissolved phases, *i.e.* TiNbC primary carbides and δ -ferrite, influences the austenite matrix composition and hence the martensitic transformation upon quenching. Moreover, it also jeopardises the formation of desirable strengthening precipitates. The results clearly suggest that simply assuming that the matrix is fully in the austenitic state during solution treatment, and hence transforms to martensite upon quenching, is not sufficient. However, the ThermoCalc calculations on prototype alloys can well predict presences of δ -ferrite, TiNbC primary carbides, as well as strengthening precipitates observed during ageing. Therefore, based on the first set of experimental alloys, it is concluded that also the microstructure prior to the ageing treatment should be taken into account in an extension of the model.

The extended integrated model is presented in Chapter 5 which allows the simultaneous optimisation of alloy compositions as well as heat treatment temperatures so as to achieve desired microstructures while avoiding undesirable phases throughout the entire heat treatment. The exercise alloys following same scenarios as in Chapter 2 and 3 are redesigned. Compared to previous design models considering only the aging stage, the consideration of undesirable phases during the austenisation treatment leads to significant compositional changes in alloys strengthened by MC carbides and Cu particles, but minor changes in the system utilising NiAl/ Ni_3Ti . The optimal strengthening contributions in all systems decrease notably by incorporating new criteria, but through increasing austenisation temperature and decreasing ageing temperature, they can be well compensated. Therefore, they become comparable to those without considering austenisation and remain beyond those of existing commercial counterparts. The effects of simultaneous optimisation of composition and heat treatment temperatures in an integrated manner is superior to subsequent optimisations.

Applying the model presented in Chapter 5, the second round of prototype alloys are designed corresponding to the same strengthening precipitates as in the first round prototypes. As a result of this, the undesirable δ -ferrite in alloy NiTi is completely avoided in the second round of NiTi2, while in alloy CuNi2 it re-

mains present, with a smaller amount, due to deviations in alloy composition. The austenitic matrix of alloys NiTi2 and CuNi2 is partially transformed to martensite upon quenching and the martensitic transformation can not be promoted by employing cryogenic treatment or fast cooling rate. However, the cold rolling significantly promotes the martensitic transformation because of the TRIP effect and hence increases the strength and hardness dramatically. Moreover, alloys NiTi2 and CuNi2 display remarkable precipitation strengthening effect during ageing with a fast kinetics. With the help of integrated model, the formation of micro size primary carbides is also successfully suppressed in alloys Car2 and CarCo2 and hence allow the strengthening precipitation of fine TiNbC particles during ageing. Alloy Car2 and CarCo2 form martensite matrix naturally upon oil quenching, display strong precipitation strengthening effects with relative slow kinetics and both alloys achieve good combination of 1.6 GPa UTS with elongation of 10 % after ageing at 773 K for 24 hours. The precipitation characterisation of alloy NiTi2 confirms the presence of anticipated precipitates, a very dense network of nano-sized Ni_3Ti intermetallics in needle/rod shape distributed homogeneously in the lath martensite matrix. In alloy CuNi2, Ni_3Ti precipitates are identified as well, but were found to have a spheroid like shape and to be rich in Cu. Alloy Car2 displays multiple precipitate distributions: homogeneously distributed TiNbC carbides at size of 100-300 nm, very finely dispersed spheroidal Ni_3Ti around 10 nm and some Cu particle less than 10 nm with twinned structure. In all alloys, the desired microstructure of lath martensite strengthened by intended precipitates are found. This strongly validates the alloy design approach presented in this thesis. The corrosion resistant property is also characterised for the second round of alloys which show equivalent or superior corrosion resistance in comparison with existing counterparts.

In conclusion, the thesis presents a general theory-guided computation alloy design methodology. This allows for the simultaneous optimisation of alloy composition and heat treatment parameters in order to achieve desirable microstructures, and to avoid undesirable phases throughout the heat treatment. The design approach employing genetic optimisation algorithm is successfully applied in the design of ultra high strength stainless steels. The prototype alloys generally obtain designed microstructures and hence achieve mechanical properties approaching the state of the art of existing UHS stainless steels, together with equivalent or superior corrosion resistance. The model is therefore validated by the prototype alloys. Based on steel makers experiences, it is foreseen that production of these new steel grades on an industrial scale will lead to a substantial further increase in mechanical properties.

The design methodology presented here is of a general nature. Properties can be translated into quantifiable microstructures, and physical metallurgy concepts and models can be added to, the model can be added to extend for the design of other alloys or other kinds of steels, for instance, TRIP steels and creep resistant steels.

Properties other than strength can also be tackled, such as fracture toughness, given that the fracture toughness can be modelled as a function of composition and heat treatment. Moreover, the precipitation kinetics plays a paramount role in determining mechanical properties. A better evaluation of strength and/or toughness can be obtained by taking the precipitation kinetics into account. A KWN based precipitation kinetics model is presented in the appendix which is capable to describe the precipitation evolution with particle size distributions. The kinetics model can also be implemented into the alloy design framework and to further control the precipitate size and distributions, at the cost of computational time and increasing the complexity of the model. At last, it is interesting to mention that, with the capability of simultaneous optimisation of alloy composition as well as heat treatment parameters, alloy design utilising multiple precipitate species, but forming or dissolving at different ageing temperatures are also possible. This will allow further tailoring of precipitates: the alloy can be subjected to multiple steps of ageing treatment at designed temperature so as to promote or suppress the precipitation of corresponding species, and hence optimise mechanical properties to levels of control beyond those currently in use in the industry. This should lead to new and improved high performance alloys with applications in the field of aerospace engineering and elsewhere.

Samenvatting

Nog steeds worden nieuwe legeringen meestal ontwikkeld op basis van een stapsgewijze methode waarbij de samenstelling en warmtebehandeling systematisch gevarieerd wordt. Bij deze methode is een groot aantal experimenten nodig om te komen tot een optimalisatie van de samenstelling en de bijbehorende warmtebehandelingen. Deze half-empirische methode heeft een lage kans op succes en vergt veel tijd en financiële middelen. Er is daarom een duidelijke trend waarneembaar om over te gaan naar modelgestuurde benadering op basis van metaalfysische modellen, daarbij uitgaande van de zogenaamde ‘doel-route’ benadering. In dit proefschrift wordt deze benadering gevolgd voor de ontwikkeling van nieuwe roestvaste staalsoorten met ultra hoge sterktes (UHS-RVS staalkwaliteiten). In deze modelmatige benadering worden diverse thermodynamische, metaalfysische en mechanische eigenschappen modellen gecombineerd. De nieuw te formuleren legeringen moeten betere mechanische en corrosieve eigenschappen hebben dan de bestaande legeringen. Dergelijke legeringen vinden hun toepassing in onderstellen en andere zwaarbelaste constructies in militaire en civiele vliegtuigen. De karakterisering van de structuur en eigenschappen van de nieuwe legeringen wordt gebruikt om het model te valideren en zo nodig aan te passen.

In hoofdstuk 1 wordt een overzicht gegeven van de structuur en eigenschappen van bestaande corrosievaste en andere staalkwaliteiten met ultra hoge mechanische eigenschappen. Niettegenstaande het reeds bereikte hoge nivo van eigenschappen is er een duidelijke behoefte aan nog betere materialen. Gezien de complexiteit van de bestaande hoge sterkte legeringen lijkt een verdere ontwikkeling op basis van de klassieke stapsgewijze benadering niet de meest geëgende methode.

In hoofdstuk 2 wordt de ‘doel-route’ methode uitgelegd en toegepast op ultra hoge sterkte roestvaste staalsoorten. Hieruit blijkt dat een microstructuur bestaande uit een fijne plaat-martensiet versterkt met een hoge dichtheid van precipitaten van het juiste soort en van de juiste dimensies en een chroomrijke matrix essentieel zijn om de gewenste eigenschappen te bereiken. Deze microstructurele en samenstellingseisen worden, gebruikmakend van thermodynamische en metaalfysische principes, vertaald in diverse kwantificeerbare criteria. Deze criteria zijn: i) het totaal aantal precipitaten (NPP) om een zo hoog mogelijke sterkte te verkrijgen, ii) een martensiet starttemperatuur van tenminste 473 K om een volledig martensietische uitgangsstruktuur te krijgen, iii) een maximaal volumegehalte van 1% van ongewenste structuurbestanddelen om breukinitiatie te voorkomen en iv) een resterend chroomgehalte in de matrix aan het einde van de precipitatiebehandeling groter dan 12% om de vorming van een gesloten chroomoxide laag mogelijk te maken. Het eerste criterium dient als optimalisatiecriterium terwijl de andere criteria als go/no go criteria worden toegepast in het ontwikkelde genetisch algoritme. Via deze aanpak kan een zeer uitgestrekt samenstellingsdomein van 13 legeringselementen, op 32 niveaus elk, onderzocht worden op haar optima.

Op basis van het type gewenste precipitaten zijn er vier scenario’s gedefinieerd: MC cabides, Cu precipitaten, Ni_3Ti intermetallische deeltjes en een maximum totaal aantal precipitaten. De vergelijking van de precipitaatdichtheid in de vier nieuwe legeringen met de berekende dichtheden voor bestaande UHS-RVS samenstellingen laat een duidelijke verhoging zien. De samenstellingen van de nieuwe legeringen lijken gedeeltelijk op die van de bestaande legeringen, maar voor sommige elementen worden andere optimale niveaus berekend.

In hoofdstuk 3 wordt het optimalisatie criterium NPP verder ontwikkeld waarbij rekening gehouden wordt met een combinatie van versteviging door precipitaatdoorsnijding en dislocatie multiplicatie door ondoordringbare precipitaten. Dit nieuwe optimalisatie criterium vervangt het totaal aantal precipitaten criterium van hoofdstuk 2. Gebruikmakend van het nieuwe criterium zijn de vier nieuwe legeringen opnieuw berekend en opnieuw wordt een sterktoename ten opzichte van bestaande legeringen voorspeld. De invloed van de diverse legeringselementen op sterkte zijn zichtbaar gemaakt in illustratieve pseudo-binaire plots, waarin ook de verboden gebieden als gevolg van de criteria voor martensietvorming, ongewenste bestanddelen en corrosievastheid afgebeeld kunnen worden. Een andere verbetering ten opzichte van het model in hoofdstuk 2 is het loslaten van een vaste precipitatie temperatuur. Hierdoor kunnen de samenstelling en de precipitatie temperatuur gezamenlijk en gelijktijdig geoptimaliseerd worden. De resultaten van de simulaties geven een kwantificering van het precipitatie temperatuurs-gebied van bestaande legeringen. Een uitstekende overeenkomst met industrieel bepaalde optima wordt verkregen.

De vier, op basis van het model berekende staalsoorten op basis van Ni_3Ti (legering NiTi), Cu precipitaten in combinatie met Ni_3Ti (legering CuNi), MC carbides (legering Car) en MC carbides in combinatie met een verhoogd Co (legering CarCo), zijn vervolgens vervaardigd en gekarakteriseerd. De resultaten zijn beschreven in hoofdstuk 4. De legeringen NiTi en CuNi vertonen na afschrikken een austeniet matrix met daarin aanzienlijke hoeveelheden delta-ferriet *alsmede* grote primaire TiNbC carbides, die door verdere thermische nabehandeling niet in oplossing gebracht konden worden. In de mechanische testen wordt een gering effect van de precipitatiebehandeling waargenomen. De mechanische eigenschappen zijn desondanks van een hoog nivo door het optreden van het zogenaamde TRIP effect. De legeringen Car en CarCo vertonen wel de beoogde volledige martensietstructuur, maar opnieuw worden grote primaire carbides waargenomen. Deze primaire carbides onttrekken de voor de vorming van de gewenste versterkende precipitaten benodigde legeringselementen aan de matrix en leiden tot versnelde breukinitiatie. Desondanks worden sterkteniveaus boven de 1.6 GPa met een redelijke ductiliteit verkregen. De versterkende precipitaten in de CarCo legering blijken Ni_3Ti precipitaten te zijn. De aanwezigheid van de ongewenste primaire carbides en delta-ferriet beïnvloedt de samenstelling van de austenietmatrix en daarmee de martensietvorming. De waarnemingen aan de experimentele legering laten zien dat de in de berekeningen gemaakte aanname van een volledige austenietstructuur met de nominale samenstelling aan het begin van de afschrikbehandeling, onvoldoende precies is. Thermocalc biedt echter de mogelijkheid ook de vorming van delta-ferriet en primaire carbides bij hoge temperaturen te berekenen. Het model is daarom aangepast met een module waarbij de microstructuur na de austeniteerbehandeling in rekening gebracht wordt.

Het aangepaste model wordt beschreven in hoofdstuk 5. Dit uitgebreidere model biedt de mogelijkheid zowel de samenstelling als de temperaturen tijdens de totale warmtebehandeling te optimaliseren *met als* doel de gewenste structuurbestanddelen te optimaliseren terwijl ongewenste structuurbestanddelen voorkomen worden. Opnieuw zijn nieuwe legeringen berekend voor de vier precipitatenfamilies. Het willen voorkomen van ongewenste fases tijdens de austeniseerbehandeling leidt tot grote veranderingen in de optimale samenstellingen voor de legeringen op basis van MC carbides en Cu precipitaten maar kleine verschuivingen voor de systemen gebaseerd op $\text{NiAl}/\text{Ni}_3\text{Ti}$ intermetallische deeltjes. De berekende maximaal te bereiken versterking door de aanwezigheid van precipitaten neemt volgens het nieuwe model aanzienlijk af, maar de sterkteafname kan gedeeltelijk gecompenseerd worden door aanpassing van de austeniteer- en precipitatie temperaturen. De berekende te behalen sterktes van de nieuwe legeringen blijven echter boven die berekend voor de bestaande kwaliteiten. Uit de simulaties blijkt dat gelijktijdige optimalisatie van samenstelling en warmtebehandelings-temperaturen leidt tot betere resultaten dan een stapsgewijze optimalisatie van beide parameters afzonderlijk.

Gebruikmakend van het model van hoofdstuk 5 zijn nieuwe legeringen berekend, vervaardigd en geëvalueerd. De ongewenste delta-ferriet in de NiTi legering uit de 2e ronde blijkt inderdaad volledig afwezig te zijn maar enige delta-ferriet wordt aangetroffen in de CuNi2 legering. Dit wordt toegeschreven aan een iets afwijkende samenstelling t.o.v. de gespecificeerde samenstelling. De austeniet matrix in de NiTi2 en de CuNi2 legering transformeert slechts gedeeltelijk tot martensiet en de fractie martensiet kan niet verder verhoogd worden door een cryogene behandeling. Koud walsen van deze legering leidde tot versterkte martensietvorming en een hogere sterkte als gevolg van het TRIP effect. De legeringen NiTi2 en CuNi2 vertonen een opmerkelijke en snelle precipitatieharding. Door aanpassing van het model kan de vorming van ongewenste primaire carbides in de Car2 en CarCo2 legeringen voorkomen worden. Hierdoor zijn meer legeringselementen beschikbaar voor de vorming van de versterkende TiNbC precipitaten. Legeringen Ca2 en CarCo2 laten, na afschrikken in olie, een homogene martensietstructuur zien en vertonen een uitstekende, maar traag verlopende, precipitatieharding. Na een precipitatiebehandeling bij 773 K gedurende 24 uur wordt een sterkte van 1.6 GPa en een breukrek van 10% verkregen. Karakterisering van de behandelde NiTi2 legering met behulp van TEM technieken laat een homogene verdeling van naald- of staafvormige Ni₃Ti precipitaten van de gewenste afmetingen zien. In de CuNi2 legering worden ook Ni₃Ti precipitaten aangetoond, maar deze zijn bolvormig en rijk aan Cu. Legering Car2 bevat verschillende precipitaat populaties: homogeen verdeelde TiNbC carbides met afmetingen van 100-300 nm, fijn verdeelde bolvormige Ni₃Ti precipitaten van 10 nm en Cu deeltjes kleiner dan 10 nm met inwendige tweelingen. In alle onderzochte legeringen wordt de beoogde martensietische microstructuur met daarin verstevigende precipitaten waargenomen. De corrosieweerstand van de legeringen uit de 2e serie is ook gemeten. Het blijkt dat deze gelijk aan of zelfs beter is dan die van de commerciële referentiematerialen.

Samenvattend: dit proefschrift beschrijft een algemene, modelgestuurde methodologie voor de ontwikkeling van nieuwe hoogwaardige legeringen, waarbij de chemische samenstelling en de warmtebehandelingstemperaturen simultaan geoptimaliseerd worden om een maximale precipitatieharding te verkrijgen terwijl ongewenste structuurbestanddelen tijdens alle stappen van de warmtebehandeling afwezig zijn. De methode van het genetisch algoritme is met succes toegepast op het ontwerpen van nieuwe UHS roestvast staal kwaliteiten. De demonstratielegeringen hebben grosso-modo de beoogde microstructuur en hebben mechanische en corrosieve eigenschappen die die van de bestaande UHS-RVS kwaliteiten overstijgen. De vervaardigde testlegeringen bevestigen de juistheid van het model. Gebaseerd op de ervaring uit de staalindustrie is te verwachten dat vervaardiging van de nieuwe legeringen op industriële schaal zal leiden tot een substantiële verdere verbetering van de mechanische eigenschappen boven die van de huidige experimentele onder laboratorium condities vervaardigde legeringen.

De ontwerpmethodologie zoals hier gepresenteerd, is breder inzetbaar dan voor dit specifieke doel. Het model kan gemakkelijk geschikt gemaakt worden voor de ontwikkeling van andere staalkwaliteiten, zoals TRIP en kruip-staalsoorten, mits de gewenste eigenschappen vertaald kunnen worden in kwantificeerbare microstructuren en fysisch metallurgische modellen en concepten. Ook andere eigenschappen dan sterkte, zoals breuktaaiheid, kunnen geoptimaliseerd worden, mits de nieuwe eigenschap beschreven kan worden als een functie van samenstelling en warmtebehandeling. Aangezien precipitatie een belangrijke rol speelt voor beide eigenschappen, zou een nog betere optimalisatie verkregen kunnen worden door ook de kinetiek van de precipitaatvorming in rekening te brengen. In de appendix van dit proefschrift wordt een nieuw KWN precipitatiemodel beschreven dat de ontwikkeling van de grootteverdeling van de precipitaten beschrijft. Dit model kan in beginsel in het totale model opgenomen worden, maar hierdoor neemt de complexiteit en de benodigde computertijd verder toe.

Tot slot dient opgemerkt te worden dat het huidige model ook verdere optimalisatie van eigenschappen op basis van de aanwezigheid van diverse typen precipitaten via een getrapte precipitatieharding bij diverse temperaturen, mogelijk maakt.

De hier gepresenteerde aanpak biedt dus diverse mogelijkheden om op een efficiënte wijze te komen tot nieuwe legeringen met uitzonderlijke eigenschappen welke hun toepassing zullen vinden in de luchtvaartindustrie en elders.

Appendix A

A KWN Based Precipitation Kinetics Model

A.1 Introduction

The alloy design approach described in this thesis is mainly based on thermodynamics, although some kinetic principles have been taken into account by assuming the precipitates form very fast, and with a dispersion of dense and tiny particles which keep their original critical nuclei size. However, this hypothesis does not hold true, especially for conditions of higher ageing temperature and/or longer time. In order to quantify the precipitation strengthening contribution in a precise manner, the precipitate population (particle size and distribution) is of great importance [100]. This chapter presents precipitation kinetics model built in a Kampmann Wagner numerical (KWN) framework, which simultaneously deals with the precipitation kinetics of nucleation, growth and coarsening. The model takes the natural advantages of the KWN model to describe the precipitate particle size distribution, and is coupled with thermodynamic calculations Via ThermoCalc. The model is applied to Chi phase precipitation in an existing maraging steel (Sandvik Nanoflex lRK91) and the predictions are compared to experimental observations.

The decomposition of a supersaturated solid solution by precipitation of a new phase is often considered in terms of three distinct steps [127]: nucleation of the new phase through the random formation of supercritical clusters of atoms; growth of these clusters by the diffusional transportation of atoms; and finally coarsening, which involves the dissolution of small particles at the expense of large ones. Because the former processes are driven by a decrease in the volume free en-

ergy, they are completed when the equilibrium volume fraction of the new phase is reached at the holding temperature. In contrast, particle coarsening, which is driven by the reduction in interfacial energy, may continue until just one single particle exists within the system. There are various of models for describing each stage and the overall kinetics are commonly modelled separately in a sequential manner [151][152].

In order to predict the precipitation kinetics without drawing artificial boundaries between nucleation, growth and coarsening regimes, Langer and Schwartz first embedded the three processes within a model referred to as MLS [153] which could predict the evolution of the mean particle size for an assumed distribution. More recently, Kampmann and Wagner modified MLS approach and produced a numerical KWN model [154][155] capable to describe the particle size distribution (PSD) in the time domain, which deals with nucleation-growth-coarsening phenomena within the same formulation and does not rely on any prior distribution assumption. A few models based on this framework have been applied to a number of systems [156][157][158][159]. An important limitation in those approaches is that the overall kinetics is computed by imposing a constant concentration at the precipitate/matrix interface, and by employing a driving force obtained from the binary dilute solution approximation. Because of the decrease of solute supersaturation in the matrix during precipitation, the local equilibrium concentration at the precipitate/matrix interface may change significantly. Moreover, the chemical free energy change during nucleation based on the dilute solution approximation in high-alloy systems is also not precise, especially for ternary or higher order systems. The model presented here intends to overcome this problem via computing multicomponent thermodynamic equilibrium in the time domain, to obtain the instantaneous local equilibrium condition at the matrix/precipitate interface during precipitation. The instantaneous driving force for nucleation is calculated from ThermoCalc [126] employing the TCFe3 [129] thermodynamic database and the MOB2 [160] mobility database. A master-slave computation of KWN kinetics combined with ThermoCalc thermodynamic computation is therefore performed at every time step. A further improvement in the present computation is the incorporation of capillarity effects at early growth stages via employing a modified version of Zener's theory of precipitate growth [161].

A.2 Model development

Based on the KWN approach, the time evolution of the precipitate particles is computed in discrete time steps. The particle size distribution is divided into a series of discrete size classes, each represented by a control volume. In every time step, the following computations are performed:

1. An instantaneous value of the matrix supersaturation is obtained from ThermoCalc following a phase equilibrium computation.
2. Nucleation is modelled by determining the number of new nuclei appearing in the class and characterised by a critical radius r^* and composition c^{pm} . The number of particles is then updated.
3. The growth rate of the existing particles within the spatial boundary of the control volume is obtained accounting for capillarity effects;.
4. The transport of particles between every control volume is calculated via a discretisation of the continuity equation for the particle number, updating the volume fraction of the precipitates.
5. Mass balance is imposed assuming the matrix composition to be homogeneous. Each of these computations is outlined next.

A.2.1 Phase equilibrium

Thermodynamic computations are performed to obtain the instantaneous local equilibrium composition of the precipitate/matrix interface using ThermoCalc with the TCFe3 database. This produces the solute concentration in the matrix (m) in equilibrium with the precipitate (p), c^{mp} , and the solute concentration of precipitates (p) in equilibrium with the matrix (m), c^{pm} . In addition, the chemical potentials of all the components are obtained and employed to determine the chemical driving force for the nucleation of the precipitates. The diffusivity pre-exponential factor D_0 and the activation energy Q for diffusion are obtained from the mobility database MOB2.

A.2.2 Nucleation

The steady state nucleation rate is obtained from [127],

$$I = \frac{dN}{dt} = N_0 \frac{kT}{h} \exp\left[\frac{-(\lambda_1 G^* + Q^*)}{kT}\right] \quad (\text{A.1})$$

where N_0 is the initial density of nucleation sites, Q^* is the activation energy for the transfer of atoms across the interface (taken to be equal to the activation energy for diffusion control species) [151][162][163][164], k is the Boltzmann constant, h is the Planck's constant, G^* is the free energy required to overcome the barrier for nucleation and λ_1 is a scaling factor used for compensating the overestimated value for G^* [33-35]. The activation energy G^* [165][166][167] for a spherical nucleus is given by

$$G^* = \frac{16\pi}{3} \frac{\sigma^3}{\Delta G_v^2} \quad (\text{A.2})$$

where σ is the precipitate/matrix interfacial energy per unit area and ΔG_V is the chemical free energy change per unit volume.

By denoting μ_k^m as the k component chemical potential of pure metastable austenite, μ_k as the equilibrium chemical potential of the k component in precipitate and c_k^{pm} as the equilibrium composition of the precipitate, the molar driving force for nucleation, ΔG_m , can be obtained from the dot product,

$$\Delta G_m = c_k^{pm} \cdot \mu_k^m - c_k^{pm} \cdot \mu_k = c_k^{pm} \cdot (\mu_k^m - \mu_k) \quad (\text{A.3})$$

ΔG_v is thus approximated by dividing ΔG_m by the precipitate molar volume.

The critical radius of the nucleus accounting for capillarity effects is obtained from [161]

$$\rho_c = \frac{2c^{mp}\Gamma}{\bar{c} - c^{mp}} \quad (\text{A.4})$$

where Γ is the capillarity constant given by the regular solution approximation,

$$\Gamma = \left(\frac{\sigma\nu^p}{kT}\right)\left(\frac{1 - c_k^{mp}}{c_k^{pm} - c_k^{mp}}\right) \quad (\text{A.5})$$

where σ is the interfacial energy per unit area and ν^p is the volume per atom in the precipitate phase.

A.2.3 Particle growth rate

The modelling of precipitate growth with local equilibrium at the interface is based on the theory for spherical precipitates by Zener [168], and later extended by Rivera and Bhadeshia [161] to approximately account for capillarity effects. The development of the radius of the spherical precipitate is assumed to follow the parabolic equation

$$\rho = \alpha \cdot (Dt)^{1/2} \quad (\text{A.6})$$

where α is a dimensionless growth parameter and D is the diffusion coefficient of the dominant species.

At a radius r , which origin is located at the centre of the particle, the concentration field can be described as

$$c\{t, r\} = \bar{c} + \left[(c^{mp} + \frac{2c^{mp}\Gamma}{\rho}) - \bar{c}\right]\phi\left\{\frac{r}{(Dt)^{1/2}}\right\}/\phi\{\alpha\} \quad (\text{A.7})$$

where \bar{c} is the average solute concentration in the matrix and

$$\phi\{\alpha\} = \frac{1}{\alpha} \exp\left(-\frac{\alpha^2}{4}\right) - \frac{\pi^{1/2}}{2} \left[1 - \operatorname{erf}\left(\frac{\alpha}{2}\right)\right] \quad (\text{A.8})$$

The rate at which solute is incorporated into the growing precipitate must be equal to that arriving by diffusion to the interface, therefore

$$v\left[c^{pm} - \left(c^{mp} + \frac{2c^{mp}\Gamma}{\rho}\right)\right] = D \frac{\partial c}{\partial r}\bigg|_{r=\rho} \quad (\text{A.9})$$

The expression for the particle growth rate v can be obtained from

$$\begin{aligned} v\{r, t\} &= \frac{\partial \rho}{\partial t} \\ &= - \frac{2D\sqrt{Dt}(2c^{mp}\Gamma - \bar{c}r + c^{mp}r)}{r(2c^{mp}\Gamma + c^{mp}r - c^{pm}r)\{-2\sqrt{Dt} + \sqrt{\pi}re^{r^2/4Dt}[1 - \operatorname{erf}(r/2\sqrt{Dt})]\}} \end{aligned} \quad (\text{A.10})$$

The diffusion coefficient D is calculated from $D = D_0 \exp(-\lambda_2 Q/RT)$, where D_0 and Q are obtained from the ThermoCalc mobility database MOB2. Due to the fact that precipitation occurs at the grain boundaries, the growth is not controlled only by bulk diffusion. The parameter λ_2 ($0.6 < \lambda_2 < 1$) reflects the contribution of the faster grain boundary diffusivity on the growth kinetics of the precipitates. A value of $\lambda_2 = 0.4$ - 0.8 is commonly taken for grain boundary diffusion [169][170][171].

When computing multicomponent growth, the lengthening of the precipitates has to be calculated from

$$(c_i^{mp} - c_i^{pm})v = -D_i \nabla c_i \quad (\text{A.11})$$

where i stands for the components diffusing across the interface boundary leading to multiple equations that have to be simultaneously solved. The concentrations at the interface (c_i^{mp} and c_i^{pm}) have to be obtained from the phase diagram. This is a non-trivial process that requires enormous computational efforts when combined differences in interfacial compositions and diffusion coefficients require a non-equilibrium tie line selection. The authors have developed a mathematical approach for tackling this problem[172][173] which was applied to this case.

A.2.4 Transport of particles

Analogous to the diffusion problem, the growth or dissolution of particles that occur during a time increment Δt can be regarded as a flux of matter in or out of the control volume. The mass balance hence gives

$$\frac{\partial N_i}{\partial t} = -\frac{\partial N_i v_i}{\partial r} + S \quad (\text{A.12})$$

where N_i is the number density of particles of the i^{th} particle size group, v_i is the particle growth rate within i and S is the nucleation rate.

The volume fraction of the precipitate phase can now be calculated as

$$f_p = \sum N_i \frac{4}{3} \pi r_i^3 \quad (\text{A.13})$$

where r_i is the radius of the particles in the i^{th} group.

A.2.5 Mass balance

Once the volume fraction is computed, the mean solute concentration of all the components in the matrix are updated following the relationship

$$\bar{c} = c_0 - (c_p - \bar{c}) \int_0^\infty \frac{4}{3} \pi r^3 \phi dr \quad (\text{A.14})$$

where ϕ is the size distribution function. The newly obtained multicomponent matrix composition is employed as an input for the thermodynamic computations in the next time step.

A.3 Experimental procedures

A.3.1 Alloy composition

The composition of the steel was determined by X-ray fluorescence and is given in Table A.1. The as-received material was delivered as strips of 31x0.5 mm in thickness. The initial microstructure consists of austenite and Chi phase. The presence of Chi phase has been verified by X-ray diffraction and SEM-EDX experiments [174].

A.3.2 Heat treatment

The heat treatments were performed using an Adamel Lhomargy DT1000 high-resolution dilatometer [175]. Specimens were heated to 1373 K and held for 300 and 1800 s in order to dissolve all precipitates, then cooled down at 50 K/s to

Cr	Ni	Mo	Ti	Al	Cu	Mn	Co
11.4	8.7	3.4	1.1	0.7	2.5	0.3	0.08
V	S	P	C	N	Si	Fe	
0.06	0.04	0.03	0.008	0.006	0.3	balance	

TABLE A.1. Chemical composition of the studied steel in weight percent.

1173 K and held for different times (120, 300, 900, 1800 and 3600 s) to study the precipitation kinetics, and were then cooled down to room temperature at 50 K/s. Samples of 5 mm in width and 12 mm in length were used. To study the late stage of coarsening, a section of the sample treated for 1800 s at 1373 K, aged at 1173 K for 3600 s and cooled down to room temperature, was reheated to 1173 K for another 13 hours and subsequently water quenched.

A.3.3 Microstructure examination

For the metallographic characterisation, the specimens were mounted in bakelite, ground and polished in different lap clothes (finishing with 1 μm diamond paste). A variation of Villela's mixed-acid etch [176][174] (3 parts HCl, 2 parts HNO_3 and 1 part H_2O) was used to disclose the Chi phase by optical microscopy. The SEM analysis was carried on a JEOL JSM-840A microscope with the same etching solution. The two-dimensional quantitative measurement of the radius of the Chi phase was performed using an image analyser. An estimation of the three-dimensional radius of the Chi phase was done following the method of Hull and Houk [177]. XRD and SEM-EDX experiments were also conducted to verify that chi was the observed phase.

A.3.4 Experimental Results

Figures A.1 (a) and (b) show representative optical micrographs of the specimen solution treated at 1373 K for 300 and 1800 s, respectively. After solution treatment, samples were aged to induce enough precipitation at grain boundaries so as to be revealed by chemical etching using Villela's mixed acid. It should be mentioned that austenite grain growth at 1173 K for periods up to 3600 s is almost negligible. Thus the grain size can be considered to be constant during aging. From the micrographs it is clear that the average size of the grain after 1800 s solution treatment is bigger than the sample subjected to 300 seconds treatment: 107 μm and 43 μm , respectively.

Figures A.2 a-c show the microstructure of the specimen aged at 1173 K for 300, 1800 and 3600 s after solution treatment. They show that Chi precipitates are mostly present at the austenite grain boundaries. The growth rate is appreciated from comparing these figures. Figure A.2d is an SEM image of the specimen after 14 hours aging. It shows that the Chi precipitate appears both at the grain boundaries and within the grains. The precipitates located at the grain boundaries

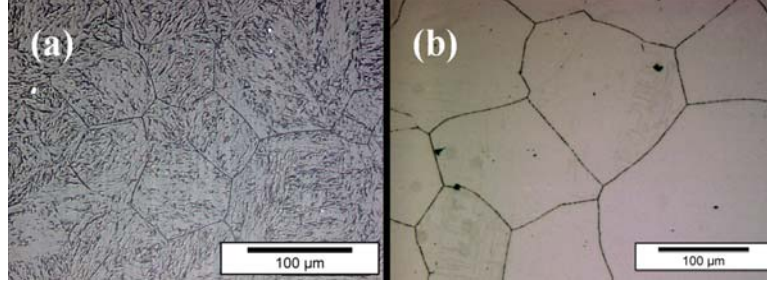


FIGURE A.1. Optical micrographs of specimen after solution treatment at 1373 K for a) 300 s and b) 1800 s.

are much bigger than those inside the grains. In the vicinity of the grain boundaries, precipitate free zones are appreciated in Figure A.2d. Moreover, the particles appearing there have an increased size and become more spherical, suggesting that the interfacial energy minimisation accompanying coarsening is taking place. The average size of the grain boundary particles for different aging times was estimated using an image analyser (Table A.2).

Time (s)	120	300	900	1800	3600
A (μm)	0.20 ± 0.05	0.21 ± 0.04	0.24 ± 0.02	0.26 ± 0.02	0.31 ± 0.02
B (μm)	0.14 ± 0.03	0.16 ± 0.03	0.21 ± 0.04	0.22 ± 0.03	0.27 ± 0.04

TABLE A.2. Chi average particle size for different aging times. A and B refer to the specimen solution treated at 1373 K for 1800 and 300 s, respectively

The microstructures of the specimens solution treated for 300 s at 1373 K and further aged for different times are shown in Figure A.3. As the average grain size is small, more grain boundaries stimulate precipitate nucleation, leading to a higher number density of particles. Moreover, the average precipitate size is smaller as compared to the 1800 s solution treatment shown in Table A.2.

A.4 Model Application

The model is applied to simulate the Chi (χ , $\text{Fe}_{36}\text{Cr}_{12}\text{Mo}_{10}$) precipitate evolution in a multicomponent alloy system which nominal composition is simplified to 12Cr-9Ni-4Mo wt.% with Fe to balance. The initial equilibrium interface condition at 1173 K is obtained from ThermoCalc and shown in Table A.3. Being that the diffusivities of Cr, Mo and Ni in austenite are approximately equal, and that Mo possesses the biggest compositional gradient at the interface, this element is chosen as rate controlling for Chi nucleation (Equation A.1) and growth rate (Equation A.10). The Chi precipitate particles are considered to be distributed in the range of 2 nm to 2 μm , and this range is discretised to 500 size groups.

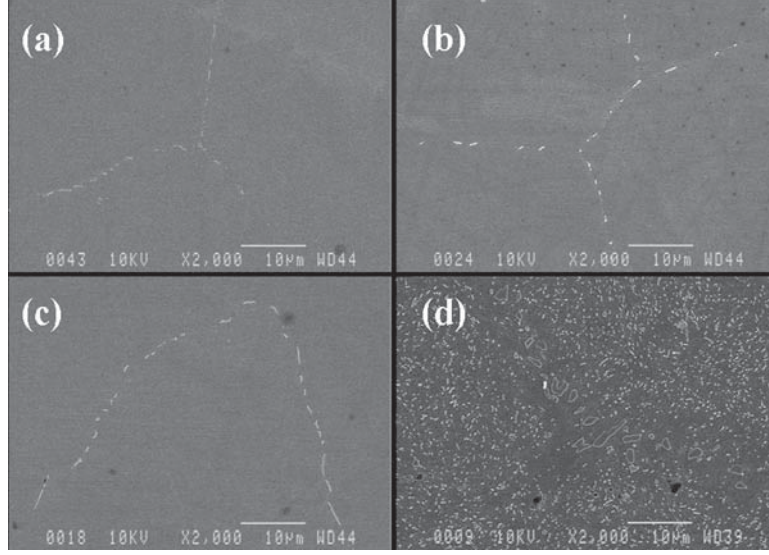


FIGURE A.2. Scanning electron micrographs of specimens solution treated at 1373 K for 1800 s and aged at 1173 K for (a) 300 s, (b) 1800 s, (c) 3600 s and (d) 50400 s.

Equation A.12 is discretised with a forward Euler scheme for time and first order upwind schemes in space. Therefore, the time step for the n^{th} calculation is chosen from the stabilisation condition,

$$\Delta t^n \leq \Delta t_{CFL} = \frac{CFL \cdot \Delta x}{|\max v(x, t^n)|} \quad (\text{A.15})$$

where CFL number is chosen as 0.9 and Δx denotes the mesh width, given by $\Delta x = l/N = (2000 - 2)/500 = 3.996$ nm. The parameter ‘ $\max v(x, t^n)$ ’ is the maximum value for all the growth rates in different control volumes at a time t^n . In order to prevent excessively large time steps, if $\Delta t \geq 1$ as provided by equation A.15, a value of $\Delta t = 1$ is taken. For the sake of reducing computation time, the ThermoCalc equilibrium calculations are performed for every time in the first 1000 steps and then every 100 steps; but if $\Delta t^n \geq 0.01$ s, they are performed every step.

Weight fraction	Cr	Mo	Ni	Fe
Alloy	0.1200	0.0400	0.0900	Balance
Austenite	0.1185	0.0356	0.0915	Balance
Chi precipitate	0.1800	0.2114	0.0294	Balance

TABLE A.3. The initial interface equilibrium composition at 1173 K

The interfacial energy of precipitates in steel is usually within the range of 0.1-0.5 Jm⁻², but no value for the Chi phase was found in the literature. An interfacial

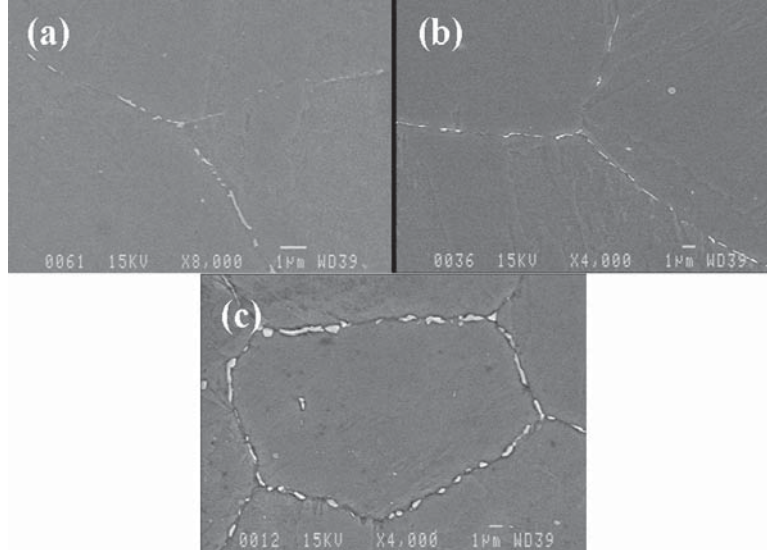


FIGURE A.3. Scanning electron micrographs of specimens solution treated at 1373 K for 300 s and aged at 1173 K for (a) 300 s, (b) 1800 s and (c) 3600 s.

energy of 0.1 Jm^{-2} was chosen here as it fitted the experimental results best. The factor λ_1 is taken as 0.0015 [167][166]. Given that the Chi precipitates are mostly found at the grain boundaries, the initial density of nucleation sites should reflect the overall grain boundary surface per unit volume and hence the grain size. The initial density of nucleation sites is chosen as $0.4 \cdot 10^{18}$ and 10^{18} m^{-3} respectively (hereafter referred as Case A and B) This values are inversely proportional to the average grain sizes of $107 \mu\text{m}$ and $43 \mu\text{m}$ found by experiments after 1800 and 300 s solution treatment, respectively. The factor λ_2 is chosen the value of 0.75 and employed for both cases. N_0 and λ_2 are parameters fitting the experimental measurements.

Figure A.4 shows the particle size evolution of Chi precipitate during aging at 1173 K for up to 7200 seconds. The empty squares and circles show the calculated progress of average particle radius. The dashed curves show the critical radius of the new nuclei formed in each time step, as obtained from Equation A.4; this also defines the critical size separating particles under growth or dissolution. Figure A.4 shows that at the early aging stage, the critical particle size increases very slowly because the volume fraction of the Chi precipitate is small and the matrix supersaturation is high enough to have insignificant effects on the nuclei size. Meanwhile, for the existing particles, the solution supersaturation and limited amount of the particles also lead to the ‘free’ growth of the particles in the absence of soft-impingement effects. Therefore, the average radius of Chi particles has a fast increase at this stage. The predicted evolution of particle number density as a function of time is plotted in Figure A.5. It shows that the number density of

particles increases rapidly from the beginning because of the high nucleation rate, the very slow dissolution kinetics and the accumulation of the particles. Because of both the fast increase of the particle size and the high number density of particles, the volume fraction increases abruptly in this stage, as shown in Figure A.6.

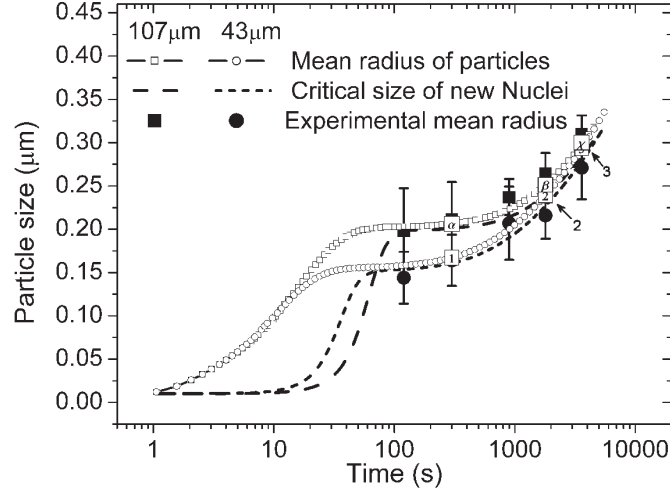


FIGURE A.4. Predicted and experimental evolution of Chi precipitate average and critical radius as a function of time at 1173 K for the average austenite grain size $107 \mu\text{m}$ (square) and $43 \mu\text{m}$ (circle), pre-solution treatment at 1373 K for 1800 s and 300 s, respectively. The bullets labelled 1-3 and α, β, γ are points of which the particle size distributions will be given.

As result of the fast solute depletion, after about 20 seconds, the solid solution concentration in the matrix decreases significantly and therefore the critical radius of new nuclei starts to increase faster; the nucleation rate decreases to a very low value; and the total number of particles remains at a certain level (Figure A.4 and Figure A.5). As the volume fraction gets close to the equilibrium condition at this stage, the limited solid solution supersaturation suppresses the growth and consequently the growth rate of average particle radius decreases.

In the next stage, the coarsening mechanism starts to dominate the process in terms of big precipitates growing at the expense of smaller ones. The critical radius for nucleation approaches the mean particle radius, and they increase together with time (Figure A.4). The total number of particles decreases while the volume fraction keeps close to the equilibrium level (Figure A.5 and Figure A.6). The computations show that the overall precipitation kinetics switches smoothly from the nucleation-growth dominated regime to growth-coarsening dominated regime without artificial separation of these three processes, this is a feature of the KWN model.

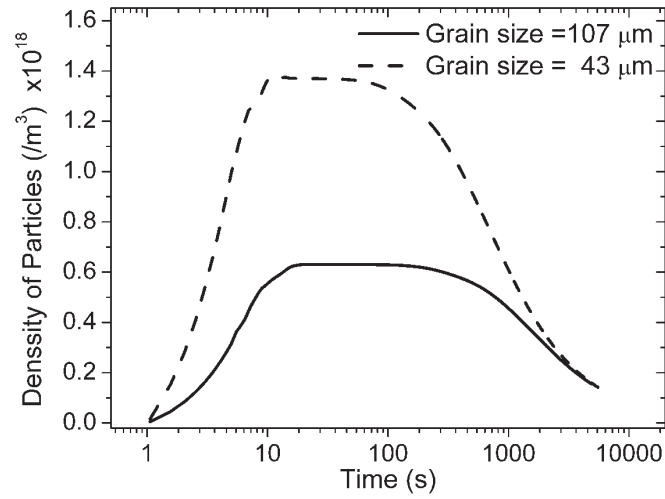


FIGURE A.5. Predicted evolution of density of Chi precipitate particles as a function of time at 1173 K, for two average austenite grain size 107 μm and 43 μm .

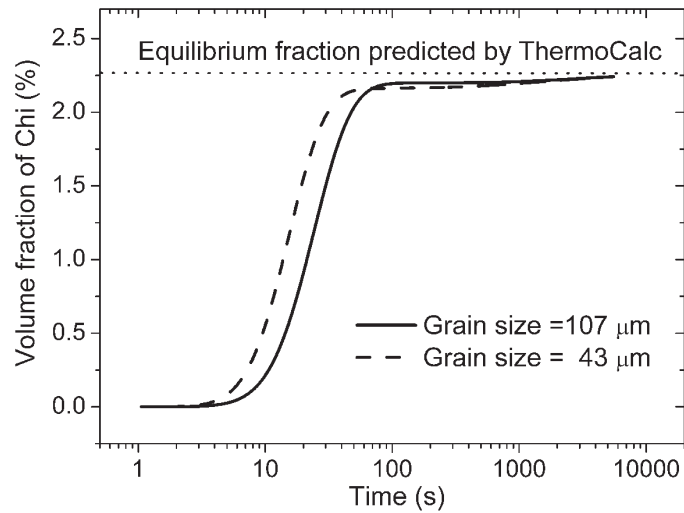


FIGURE A.6. Predicted evolution of volume fraction of Chi precipitate as a function of time at 1173 K, for two average austenite grain size 107 μm and 43 μm .

The model is applied to two initial austenite grain sizes (A and B) by means of assuming a different initial density of nucleation sites N_0 . Figure A.4 shows that there is not much difference in the average and critical particle size between the two cases at the beginning of the precipitation process, in the meantime, the number density of the particles is much higher in case B because of the higher nucleation rate, as shown in Figure A.5. Consequently, the volume fraction of Chi phase also increases faster in case B (Figure A.6) and the volume fraction of Chi phase also gets close to equilibrium fraction at an earlier time, but with smaller average particle size. This is also the reason why the critical radius starts to increase also at an earlier time in case B. Eventually, at later stages (>2000 s), and due to the faster coarsening process in case B, the number density of particles and the average size of particles reach a similar value in both cases (A and B), as indicated in Figure A.4 and Figure A.5.

The model allows tracing the particle size distribution throughout the whole evolution process. The predicted particle size distributions of both cases A and B are plotted in Figure A.7 a and b, after 300, 1800 and 3600 seconds aging corresponding, respectively, to the points marked 1-3 and character α, β, χ in mean particle radius curve in Figure A.4. The statistical results of the experimental observation are also plotted in Figure A.7 as a histogram for comparison with the simulation. At 120 s, the particle size distribution is characterised by a sharp peak around the average particle radius. For longer aging times, the position of this peak switches to the right reflecting the increase in the mean particle size. The width of the peak increases and its height decreases due to both the lower values in total particle number and the growth/dissolution kinetics. It is worth noting that the distribution is the natural output of the KWN model and is not the result of an assumption.

The experimental results of the average particle radius shown in Table A.2 are plotted as solid squares and circles with error bars in Figure A.4, showing that the simulation results are in good agreement with the available experimental observations. The model validation (Figures A.4 and A.2) results from comparing the model predictions to the experimental data at late precipitation stages. Due to the high temperature at which precipitation takes place (1173 K), the reaction occurs at a very large pace, and the first experimental measurements were made at 120 s after the onset of ageing. The validation is therefore not complete as no information was available on the critical early stages at which the formative process starts and further work is required in this respect. The fitting of the results to the limited available experimental information on particle size and size distribution was, however, essential for obtaining the unknown values for the interfacial energy per unit area and the initial density of nucleation sites. It should be noticed that only the precipitates at grain boundaries have been taken into account in estimating the experimental average particle size. This is because, although the intragranular precipitate may be formed at the very beginning of ageing, the growth of

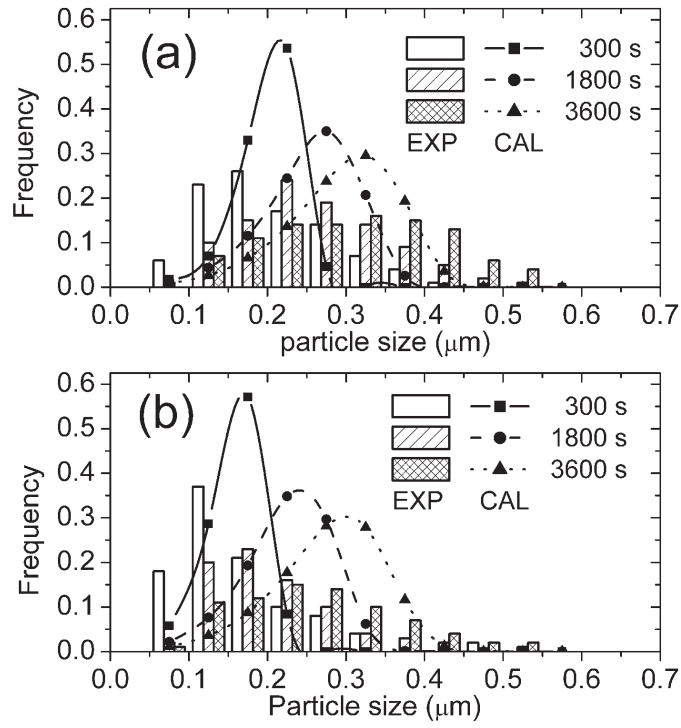


FIGURE A.7. Predicted and experimental results of particle size distribution of Chi precipitate for 300 s, 1800 s and 3600 s ageing at 1173 K, for two average austenite grain size (a) 107 μm and (b) 43 μm , pre solution treatment at 1373 K for 1800 s and 300 s, respectively.

intragranular precipitate is very slow compared to intergranular ones due to slow bulk diffusivities. Therefore, the intragranular precipitates are too small to be distinguished by SEM at the aging time we investigated. However, the existence of the precipitation within the matrix can be proven by Figure A.2d in which Chi precipitate has reached a significant size due to long time aging. The region with the larger Chi precipitates, which includes both grain boundaries and precipitate free zones next to them, as shown in Figure A.2d, can be treated as an independent system. In this area, the diffusivity is much faster than the bulk diffusion and intergranular precipitates consume most of the solute in solid solutions in the matrix. For the short aging times to which the model is applied, the slow bulk diffusion has not significantly affected the fast grain boundary precipitation kinetics. But for very long time aging or precipitate evolution in the service period, the model should be modified to consider the cross effects of the intergranular and intragranular precipitates to obtain the overall precipitation kinetics.

A.5 Conclusion

A model describing the precipitation kinetics is developed. The model is based on a KWN framework with a growth rate computation incorporating capillarity effects. The model is coupled with thermodynamic calculations via ThermoCalc for obtaining the instantaneous equilibrium condition at interface, the driving force for nucleation and the solute diffusion coefficients. The model successfully predicts the overlapped nucleation-growth-coarsening kinetics in a natural way and trace the particle size distribution throughout the process. The model was applied to describe Chi precipitation kinetics at the grain boundary depletion zones, showing that they can be treated as an independent system. The predicted evolution of Chi precipitates (average particle size and distribution) for different heat treatments is in good agreement with experimental observations at late precipitation stages.

Bibliography

- [1] R. G. Davies. Influence of martensite composition and content on the properties of dual phase steels. *Metallurgical Transactions A*, 9(5):671–679, 1978.
- [2] R. G. Davies. The deformation behavior of a vanadium-strengthened dual phase steel. *Metallurgical Transactions A*, 9(1):41–52, 1978.
- [3] N. K. Balliger and T. Gladman. Work hardening of dual-phase steels. *Metal science*, 15(3):95–108, 1981.
- [4] N. J. Kim and G. Thomas. Effects of morphology on the mechanical behavior of a dual phase Fe/2Si/0.1C steel. *Metallurgical transactions. A, Physical metallurgy and materials science*, 12 A(3):483–489, 1981.
- [5] G. R. Speich, V. A. Demarest, and R. L. Miller. Formation of austenite during intercritical annealing of dual-phase steels. *Metallurgical transactions. A, Physical metallurgy and materials science*, 12 A(8):1419–1428, 1981.
- [6] G. J. Weng. The overall elastoplastic stress-strain relations of dual-phase metals. *Journal of the Mechanics and Physics of Solids*, 38(3):419–441, 1990.
- [7] D. T. Llewellyn and D. J. Hillis. Dual phase steels. *Ironmaking and Steel-making*, 23(6):471–478, 1996.
- [8] M. Sarwar and R. Priestner. Influence of ferrite-martensite microstructural morphology on tensile properties of dual-phase steel. *Journal of Materials Science*, 31(8):2091–2095, 1996.

- [9] F. Lecroisey and A. Pineau. Martensitic transformations induced by plastic deformation in the Fe-Ni-Cr-C system. *Met Trans*, 3(2):387–396, 1972.
- [10] P. C. Maxwell, A. Goldberg, and J. C. Shyne. Stress-assisted and strain-induced martensites in Fe-Ni-C alloys. *Metallurgical Transactions*, 5(6):1305–1318, 1974.
- [11] G. B. Olson and Morris Cohen. Kinetics of strain-induced martensitic nucleation. *Metall Trans A*, 6 A(4):791–795, 1975.
- [12] G. B. Olson and M. Azrin. Transformation behavior of TRIP steels. *Metallurgical Transactions A*, 9(5):713–721, 1978.
- [13] G. B. Olson and M. Cohen. Stress-assisted isothermal martensitic transformation: application to TRIP steels. *Metallurgical Transactions A*, 13(11):1907–1914, 1982.
- [14] I. Tamura. Deformation-induced martensitic transformation and transformation-induced plasticity in steels. *Metal science*, 16(5):245–253, 1982.
- [15] Kohichi Sugimoto, Masahiro Misu, Mitsuyuki Kobayashi, and Hidenori Shirasawa. Effects of second phase morphology on retained austenite morphology and tensile properties in a TRIP-aided dual-phase steel sheet. *ISIJ International*, 33(7):775–782, 1993.
- [16] P. Jacques, E. Girault, T. Catlin, N. Geerlofs, T. Kop, S. Van Der Zwaag, and F. Delannay. Bainite transformation of low carbon Mn-Si TRIP-assisted multiphase steels: influence of silicon content on cementite precipitation and austenite retention. *Materials Science and Engineering A*, 273-275:475–479, 1999.
- [17] F. D. Fischer, G. Reisner, E. Werner, K. Tanaka, G. Cailletaud, and T. Antretter. New view on transformation induced plasticity (TRIP). *International journal of plasticity*, 16(7):723–748, 2000.
- [18] J. Wang and S. Van der Zwaag. Stabilization mechanisms of retained austenite in transformation-induced plasticity steel. *Metallurgical and Materials Transactions A: Physical Metallurgy and Materials Science*, 32(6):1527–1539, 2001.
- [19] E. Jimenez-Melero, N. H. van Dijk, L. Zhao, J. Sietsma, S. E. Offerman, J. P. Wright, and S. van der Zwaag. Martensitic transformation of individual grains in low-alloyed TRIP steels. *Scripta Materialia*, 56(5):421–424, 2007.
- [20] O. Grassel and G. Frommeyer. Effect of martensitic phase transformation and deformation twinning on mechanical properties of Fe-Mn-Si-Al steels. *Materials Science and Technology*, 14(12):1213–1217, 1998.

- [21] O. Grassel, L. Kruger, G. Frommeyer, and L. W. Meyer. High strength Fe-Mn-(Al,Si) TRIP/TWIP steels development - properties - application. *International journal of plasticity*, 16(10):1391–1409, 2000.
- [22] S. Allain, J. P. Chateau, and O. Bouaziz. A physical model of the twinning-induced plasticity effect in a high manganese austenitic steel. *Materials Science and Engineering A*, 387-389(1-2 SPEC. ISS.):143–147, 2004.
- [23] S. Vercammen, B. Blanpain, B. C. De Cooman, and P. Wollants. Cold rolling behaviour of an austenitic Fe-30Mn-3Al-3Si TWIP-steel: The importance of deformation twinning. *Acta Materialia*, 52(7):2005–2012, 2004.
- [24] D. Barbier, N. Gey, A. Sébastien, and M. Humbert. Grain size effect on the tensile behavior of a FeMnC TWIP steel in relation with the microstructure and texture evolutions. *Ceramic Transactions*, 200:79–86, 2008.
- [25] B. Dong, X. L. Ma, H. F. Peng, and C. X. Chen. SME, TRIP and TWIP effects of high manganese steels. *Journal of Iron and Steel Research*, 21(3):1–7, 2009.
- [26] V. G. Gavriljuk and H. Berns. Precipitates in tempered stainless martensitic steels alloyed with nitrogen, carbon or both. *Materials Science Forum*, 318:71–80, 1999.
- [27] A. Ghosh, S. Das, and S. Chatterjee. Ultrahigh strength hot rolled microalloyed steel: Microstructure and properties. *Materials Science and Technology*, 21(3):325–333, 2005.
- [28] R. L. Klueh, N. Hashimoto, and P. J. Maziasz. Development of new nanoparticle-strengthened martensitic steels. *Scripta Materialia*, 53(3):275–280, 2005.
- [29] P. Michaud, D. Delagnes, P. Lamesle, M. H. Mathon, and C. Levillant. The effect of the addition of alloying elements on carbide precipitation and mechanical properties in 5 % chromium martensitic steels. *Acta Materialia*, 55(14):4877–4889, 2007.
- [30] K. Miyata and Y. Sawaragi. Effect of Mo and W on the phase stability of precipitates in low Cr heat resistant steels. *ISIJ International*, 41(3):281–289, 2001.
- [31] K. Miyata, T. Omura, T. Kushida, and Y. Komizo. Coarsening kinetics of multicomponent MC-type carbides in high-strength low-alloy steels. *Metallurgical and Materials Transactions A: Physical Metallurgy and Materials Science*, 34 A(8):1565–1573, 2003.

- [32] E. V. Pereloma, I. B. Timokhina, K. F. Russell, and M. K. Miller. Characterization of clusters and ultrafine precipitates in Nb-containing C-Mn-Si steels. *Scripta Materialia*, 54(3):471–476, 2006.
- [33] C. Servant, E. H. Gherbi, and G. Cizeron. TEM investigation of the tempering behaviour of the maraging PH 17.4 Mo stainless steel. *Journal of Materials Science*, 22(7):2297–2304, 1987.
- [34] H. R. Habibi-Bajguirani and M. L. Jenkins. High-resolution electron microscopy analysis of the structure of copper precipitates in a martensitic stainless steel of type PH 15-5. *Philosophical Magazine Letters*, 73(4):155–162, 1996.
- [35] H. R. Habibi-Bajguirani, C. Servant, and G. Cizeron. TEM investigation of precipitation phenomena occurring in PH 15-5 alloy. *Acta Metallurgica et Materialia*, 41(5):1613–1623, 1993.
- [36] D. Isheim, M. S. Gagliano, M. E. Fine, and D. N. Seidman. Interfacial segregation at Cu-rich precipitates in a high-strength low-carbon steel studied on a sub-nanometer scale. *Acta Materialia*, 54(3):841–849, 2006.
- [37] W. D. Yoo, J. H. Lee, K. T. Youn, and Y. M. Rhyim. Study on the microstructure and mechanical properties of 17-4 PH stainless steel depending on heat treatment and aging time. *Solid State Phenomena*, 118:15–20, 2006.
- [38] K. Stiller, F. Danoix, and A. Bostel. Investigation of precipitation in a new maraging stainless steel. *Applied Surface Science*, 94-95:326–333, 1996.
- [39] K. Stiller, F. Danoix, and M. Hättstrand. Mo precipitation in a 12Cr-9Ni-4Mo-2Cu maraging steel. *Materials Science and Engineering A*, 250(1):22–26, 1998.
- [40] K. Stiller, M. Hättstrand, and F. Danoix. Precipitation in 9Ni-12Cr-2Cu maraging steels. *Acta Materialia*, 46(17):6063–6073, 1998.
- [41] M. Andersson, K. Stiller, and M. Hättstrand. Comparison of early stages of precipitation in Mo-rich and Mo-poor maraging stainless steels. *Surface and Interface Analysis*, 39(2-3):195–200, 2007.
- [42] M. Hättstrand, J. O. Nilsson, K. Stiller, P. Liu, and M. Andersson. Precipitation hardening in a 12Cr-9Ni-4Mo-2Cu stainless steel. *Acta Materialia*, 52(4):1023–1037, 2004.
- [43] D. M. van der Walker. Precipitation sequence of Ni_3Ti in Co-free maraging steel. *Metallurgical transactions. A, Physical metallurgy and materials science*, 18 A(7):1191–1194, 1987.

- [44] D. H. Ping, M. Ohnuma, Y. Hirakawa, Y. Kadoya, and K. Hono. Microstructural evolution in 13Cr-8Ni-2.5Mo-2Al martensitic precipitation-hardened stainless steel. *Materials Science and Engineering A*, 394(1-2):285–295, 2005.
- [45] S. Erlach, F. Danoix, H. Leitner, P. Auger, I. Siller, and H. Clemens. Precipitation reactions during the early stages of aging in a Ni and Al alloyed martensitic medium carbon steel. *Surface and Interface Analysis*, 39(2-3):213–220, 2007.
- [46] S. D. Erlach, H. Leitner, M. Bischof, H. Clemens, F. Danoix, D. Lemarchand, and I. Siller. Comparison of NiAl precipitation in a medium carbon secondary hardening steel and C-free PH13-8 maraging steel. *Materials Science and Engineering A*, 429(1-2):96–106, 2006.
- [47] Z. Guo, W. Sha, and D. Vaumousse. Microstructural evolution in a PH13-8 stainless steel after ageing. *Acta Materialia*, 51(1):101–116, 2003.
- [48] Y. He, K. Yang, and W. Sha. Microstructure and mechanical properties of a 2000 MPa grade Co-free maraging steel. *Metallurgical and Materials Transactions A: Physical Metallurgy and Materials Science*, 36(9):2273–2287, 2005.
- [49] Y. He, K. Yang, W. Sha, and D. J. Cleland. Microstructure and mechanical properties of a 2000 MPa Co-free maraging steel after aging at 753 K. *Metallurgical and Materials Transactions A: Physical Metallurgy and Materials Science*, 35(9):2747–2755, 2004.
- [50] Y. He, K. Yang, W. Sha, Z. Guo, and K. Liu. Age hardening and mechanical properties of a 2400 MPa grade cobalt-free maraging steel. *Metallurgical and Materials Transactions A: Physical Metallurgy and Materials Science*, 37(4):1107–1116, 2006.
- [51] J. R. Davis. *Alloy Digest Sourcebook: Stainless Steels*. ASM International, 2000.
- [52] *The ASM Alloy Center*. ASM International, 2009.
- [53] D. Raabe, D. Ponge, O. Dmitrieva, and B. Sander. Nanoprecipitate-hardened 1.5 GPa steels with unexpected high ductility. *Scripta Materialia*, 60(12):1141–1144, 2009.
- [54] G. B. Olson. Computational design of hierarchically structured materials. *Science*, 277(5330):1237–1242, 1997.
- [55] B. Sundman and J. Ågren. Computer applications in the development of steels. *MRS Bulletin*, 24(4):32–36, 1999.

- [56] A. A. Howe and D. C. J. Farrugia. Alloy design: From composition to through process models. *Materials Science and Technology*, 15(1):15–21, 1999.
- [57] J. Ågren. Thermodynamics and heat treatment. *Materials Science Forum*, 163(1):3–14, 1994.
- [58] G. N. Haidemenopoulos, M. Grujicic, G. B. Olson, and M. Cohen. Thermodynamics-based alloy design criteria for austenite stabilization and transformation toughening in the Fe-Ni-Co system. *Journal of Alloys and Compounds*, 220(1-2):142–147, 1995.
- [59] S. I. Park, S. Z. Han, Z. H. Lee, and H. M. Lee. A correction to optimum alloy composition for design of high-temperature high-strength Al-Ti-V-Zr alloys through thermodynamic calculations. *Scripta Materialia*, 37(1):93–97, 1997.
- [60] S. W. Yoon, J. R. Soh, H. M. Lee, and B. J. Lee. Thermodynamics-aided alloy design and evaluation of Pb-free solder, Sn-Bi-In-Zn system. *Acta Materialia*, 45(3):951–960, 1997.
- [61] H. Zhong, L. Feng, P. Liu, and T. Zhou. Design of a Mg-Li-Al-Zn alloy by means of CALPHAD approach. *Journal of Computer-Aided Materials Design*, 10(3):191–199, 2003.
- [62] Y. B. Kang, A. D. Pelton, P. Chartrand, P. Spencer, and C. D. Fuerst. Thermodynamic database development of the Mg-Ce-Mn-Y system for Mg alloy design. *Metallurgical and Materials Transactions A: Physical Metallurgy and Materials Science*, 38(6):1231–1243, 2007.
- [63] V. Trabadelo, S. Giménez, T. Gómez-Acebo, and I. Iturriza. Critical assessment of computational thermodynamics in the alloy design of PM high speed steels. *Scripta Materialia*, 53(3):287–292, 2005.
- [64] S. Mandal, P. V. Sivaprasad, P. Barat, and B. Raj. An overview of neural network based modeling in alloy design and thermomechanical processing of austenitic stainless steels. *Materials and Manufacturing Processes*, 24(2):219–224, 2009.
- [65] C. E. Campbell and G. B. Olson. Systems design of high performance stainless steels I. conceptual and computational design. *Journal of Computer-Aided Materials Design*, 7(3):145–170, 2000.
- [66] H. K. D. H. Bhadeshia. Neural networks in materials science. *ISIJ International*, 39(10):966–979, 1999.

- [67] J. Wang, P. J. Van Der Wolk, and S. Van Der Zwaag. Effects of carbon concentration and cooling rate on continuous cooling transformations predicted by artificial neural network. *ISIJ International*, 39(10):1038–1046, 1999.
- [68] P. J. Van Der Wolk, J. Wang, J. Sietsma, and S. Van Der Zwaag. Modelling the continuous cooling transformation diagram of engineering steels using neural networks part I: Phase regions. *Zeitschrift fuer Metallkunde/Materials Research and Advanced Techniques*, 93(12):1199–1207, 2002.
- [69] P. J. Van Der Wolk, J. Wang, J. Sietsma, and S. Van Der Zwaag. Modelling the continuous cooling transformation diagram of engineering steels using neural networks part II: Microstructure and hardness. *Zeitschrift fuer Metallkunde/Materials Research and Advanced Techniques*, 93(12):1208–1216, 2002.
- [70] M. Mahfouf, M. Jamei, and D. A. Linkens. Optimal design of alloy steels using multiobjective genetic algorithms. *Materials and Manufacturing Processes*, 20(3):553–567, 2005.
- [71] S. H. M. Anijdan, A. Bahrami, H. R. M. Hosseini, and A. Shafyei. Using genetic algorithm and artificial neural network analyses to design an Al-Si casting alloy of minimum porosity. *Materials and Design*, 27(7):605–609, 2006.
- [72] S. Datta, F. Pettersson, S. Ganguly, H. Saxén, and N. Chakraborti. Designing high strength multi-phase steel for improved strength-ductility balance using neural networks and multi-objective genetic algorithms. *ISIJ International*, 47(8):1195–1203, 2007.
- [73] D. Raabe, B. Sander, M. Friák, D. Ma, and J. Neugebauer. Theory-guided bottom-up design of beta-titanium alloys as biomaterials based on first principles calculations: Theory and experiments. *Acta Materialia*, 55(13):4475–4487, 2007.
- [74] L. Vitos, P. A. Korzhavyi, and B. Johansson. Stainless steel optimization from quantum mechanical calculations. *Nature Materials*, 2(1):25–28, 2003.
- [75] S. Hao, W. K. Liu, B. Moran, F. Vernerey, and G. B. Olson. Multi-scale constitutive model and computational framework for the design of ultra-high strength, high toughness steels. *Computer Methods in Applied Mechanics and Engineering*, 193(17-20):1865–1908, 2004.
- [76] U. E. Klotz, C. Solenthaler, and P. J. Uggowitzer. Martensitic-austenitic 9-12 Cr steels - alloy design, microstructural stability and mechanical properties. *Materials Science and Engineering A*, 476(1-2):186–194, 2008.

- [77] B. J. Lee, H. D. Kim, and J. H. Hong. Calculation of equilibria in SA508 grade 3 steels for intercritical heat treatment. *Metallurgical and Materials Transactions A: Physical Metallurgy and Materials Science*, 29(5):1441–1447, 1998.
- [78] S. Mandal, P. V. Sivaprasad, S. Venugopal, K. P. N. Murthy, and B. Raj. Artificial neural network modeling of composition-process-property correlations in austenitic stainless steels. *Materials Science and Engineering A*, 485(1-2):571–580, 2008.
- [79] Z. Guo and W. Sha. Modelling the correlation between processing parameters and properties of maraging steels using artificial neural network. *Computational Materials Science*, 29(1):12–28, 2004.
- [80] S. H. Hsiang, J. L. Kuo, and F. Y. Yang. Using artificial neural networks to investigate the influence of temperature on hot extrusion of AZ61 magnesium alloy. *Journal of Intelligent Manufacturing*, 17(2):191–201, 2006.
- [81] R. Ravi, Y. V. R. K. Prasad, V. V. S. Sarma, and R. S. Raidu. Artificial neural network model for predicting stable and unstable regions in Cu-Zn alloys. *Materials and Manufacturing Processes*, 21(8):756–760, 2006.
- [82] R. Honeycombe and H. K. D. H. Bhadeshia. *Steels: Microstructure and Properties*. Butterworth-Heinemann, third edition edition, 2006.
- [83] D. T. Llewellyn and R. C. Hudd. *Steels: Metallurgy and Applications*. Butterworth-Heinemann, third edition edition, 1998.
- [84] G. E. Totten and M. A. H. Howes. *Steel Heat Treatment Handbook*. CRC, 1997.
- [85] A. J. Ardell. Precipitation hardening. *Metallurgical Transactions A*, 16(12):2131–2165, 1985.
- [86] M. Murayama, Y. Katayama, and K. Hono. Microstructural evolution in a 17-4 PH stainless steel after aging at 400 C. *Metallurgical and Materials Transactions A: Physical Metallurgy and Materials Science*, 30(2):345–353, 1999.
- [87] C. N. Hsiao, C. S. Chiou, and J. R. Yang. Aging reactions in a 17-4 PH stainless steel. *Materials Chemistry and Physics*, 74(2):134–142, 2002.
- [88] U. K. Viswanathan, S. Banerjee, and R. Krishnan. Effects of aging on the microstructure of 17-4 PH stainless steel. *Materials Science and Engineering*, 104(C):181–189, 1988.
- [89] U. K. Viswanathan, P. K. K. Nayar, and R. Krishnan. Kinetics of precipitation in 17-4 PH stainless steel. *Materials Science and Technology*, 5(4):346–349, 1989.

- [90] P. W. Hochanadel, C. V. Robino, G. R. Edwards, and M. J. Cieslak. Heat treatment of investment cast PH 13-8 Mo stainless steel: Part I. mechanical properties and microstructure. *Metallurgical transactions. A, Physical metallurgy and materials science*, 25 A(4):789–798, 1994.
- [91] C. V. Robino, P. W. Hochanadel, G. R. Edwards, and M. J. Cieslak. Heat treatment of investment cast PH 13-8 Mo stainless steel: Part II. isothermal aging kinetics. *Metallurgical transactions. A, Physical metallurgy and materials science*, 25 A(4):697–704, 1994.
- [92] V. Seetharaman, M. Sundararaman, and R. Krishnan. Precipitation hardening in a PH 13-8 Mo stainless steel. *Materials Science and Engineering*, 47(1):1–11, 1981.
- [93] Z. Guo, W. Sha, E. A. Wilson, and R. W. Grey. Improving toughness of PH13-8 stainless steel through intercritical annealing. *ISIJ International*, 43(10):1622–1629, 2003.
- [94] D. Sen, A. K. Patra, S. Mazumder, J. Mittra, G. K. Dey, and P. K. De. Morphology of carbide precipitates in solution quenched PH13-8 Mo stainless steel: A small-angle neutron scattering investigation. *Materials Science and Engineering A*, 397(1-2):370–375, 2005.
- [95] H. R. Habibi Bajguirani. The effect of ageing upon the microstructure and mechanical properties of type 15-5 PH stainless steel. *Materials Science and Engineering A*, 338(1-2):142–159, 2002.
- [96] K. Ozbaysal and O. T. Inal. Age-hardening kinetics and microstructure of PH 15-5 stainless steel after laser melting and solution treating. *Journal of Materials Science*, 29(6):1471–1480, 1994.
- [97] W Pitsch and A Schrader. *Arch. Eisenhüttenw*, 29:715–721, 1958.
- [98] F. Abe. Bainitic and martensitic creep-resistant steels. *Current Opinion in Solid State and Materials Science*, 8(3-4):305–311, 2004.
- [99] A. J. Allen, D. Gavillet, and J. R. Weertman. SANS and TEM studies of isothermal M_2C carbide precipitation in ultrahigh strength AF1410 steels. *Acta Metallurgica et Materialia*, 41(6):1869–1884, 1993.
- [100] M. Al Dawood, I. S. El Mahallawi, M. E. Abd El Azim, and M. R. El Koussy. Thermal aging of 16Cr-5Ni-1Mo stainless steel Part 1 - microstructural analysis. *Materials Science and Technology*, 20(3):363–369, 2004.
- [101] M. Al Dawood, I. S. El Mahallawi, M. E. Abd El Azim, and M. R. El Koussy. Thermal aging of 16Cr-5Ni-1Mo stainless steel Part 2 - mechanical property characterisation. *Materials Science and Technology*, 20(3):370–374, 2004.

- [102] C. E. Campbell and G. B. Olson. Systems design of high performance stainless steels II. prototype characterization. *Journal of Computer-Aided Materials Design*, 7(3):171–194, 2000.
- [103] M. Grujicic. Implication of elastic coherency in secondary hardening of high Co-Ni martensitic steels. *Journal of Materials Science*, 26(5):1357–1362, 1991.
- [104] R. G. Baker and J. Nutting. *SI Special Report*, 64(1):1–10, 1959.
- [105] James M. Leitnaker and James Bentley. Precipitate phases in type 321 stainless steel after aging 17 years at similar 600 degree C. *Metall Trans A*, 8 A(10):1605–1613, 1977.
- [106] A. F. Padilha, G. Schanz, and K. Anderko. Ausscheidungsverhalten des titanstabilisierten austenitischen stahls 15Cr-15Ni-1Mo-Ti-B. *Journal of Nuclear Materials*, 105(1):77–92, 1982.
- [107] A. R. Jones, P. R. Howell, and B. Ralph. The precipitation of niobium carbide at grain boundaries in an austenitic stainless steel. *Journal of Materials Science*, 11(9):1593–1599, 1976.
- [108] A. R. Jones, P. R. Howell, and B. Ralph. Quantitative aspects of precipitation at grain boundaries in an austenitic stainless steel. *Journal of Materials Science*, 11(9):1600–1606, 1976.
- [109] A. N. Bhagat, S. K. Pabi, S. Ranganathan, and O. N. Mohanty. Aging behaviour in copper bearing high strength low alloy steels. *ISIJ International*, 44(1):115–122, 2004.
- [110] C. S. Pande and M. A. Imam. Nucleation and growth kinetics in high strength low carbon ferrous alloys. *Materials Science and Engineering A*, 457(1-2):69–76, 2007.
- [111] E. Orowan. Theory of dislocation bowing. *Institute of Metals Symposium on Internal Stresses in Metals and Alloys*, page 451, 1948.
- [112] Peter Haasen. *Physical Metallurgy*. Cambridge University Press, Cambridge, UK, 1996.
- [113] R. Kirchhem. Growth kinetics of passive films. *Electrochimica Acta*, 32(11):1619–1629, 1987.
- [114] R. D. Joseph. *ASM Specialty Handbook: Stainless Steels*. ASM, 1994.
- [115] *ASM Handbook*, volume Metallography and Microstructure. ASM International, 1998.

- [116] K. W. Andrews. Empirical formulae for the calculation of some transformation temperatures. *Journal Iron Steel Institute*, 203(7):721, 1965.
- [117] R. A. Grange and H. M. Stewart. *Trans. AIME*, 167:467, 1946.
- [118] A. E. Nehrenberg. *Trans. AIME*, 167:494, 1946.
- [119] E. S. Rowland and S. R. Lyle. *Met. Progr.*, 47:907, 1946.
- [120] W. Steven and A. G. Haynes. The temperature of formation of martensite and bainite in low-alloy steels. *Journal Iron Steel Institute*, 183(8):349, 1956.
- [121] M. Hillert, T. Wada, and Wada. H. *Journal Iron Steel Institute*, 205:539, 1967.
- [122] Kiyohito Ishida and Taiji Nishizawa. Ferrite/austenite stabilizing parameter of alloying elements in steel at 200 to 500 degree C. *Trans Jap Inst Met*, 15(3):217–224, 1974.
- [123] C. Zener. *Journal of Metals*, 7:619, 1955.
- [124] K. Ishida. Calculation of the effect of alloying elements on the Ms temperature in steels. *Journal of Alloys and Compounds*, 220(1-2):126–131, 1995.
- [125] G. Ghosh and G. B. Olson. Kinetics of F.C.C. \rightarrow B.C.C. heterogeneous martensitic nucleation - I. the critical driving force for athermal nucleation. *Acta Metallurgica et Materialia*, 42(10):3361–3370, 1994.
- [126] J. O. Andersson, T. Helander, L. Hoglound, P. Shi, and B. Sundman. ThermoCalc and DICTRA, computational tools for materials science. *Calphad*, 26(2):273–312, 2002.
- [127] J. W. Christian. *Theory of transformation in metals and alloys, Part I*. Pergamon, Oxford, England, 2nd end edition, 1975.
- [128] G. E. Dieter. *Mechanical Metallurgy*. McGraw-Hill series in materials science and engineering. McGraw-Hill, New York, 1986.
- [129] *TCFE3 Thermo-Calc Steels/Fe-Alloys Database*. Royal Institute of Technology, Foundation of Computational Thermo-dynamics, Stockholm, Sweden, 3.0 edition, 2002.
- [130] I. A. Borisov. The influence of vanadium and other carbide forming elements on the properties of rotor steel. *Metallovedenie i Termicheskaya Obrabotka Metallov*, 10:33, 1994.
- [131] H. Kwon, C. M. Kim, K. B. Lee, H. R. Yang, and J. H. Lee. Effect of alloying additions on secondary hardening behavior of Mo-containing steels. *Metallurgical and Materials Transactions A: Physical Metallurgy and Materials Science*, 28 A(3):621–627, 1997.

- [132] A. F. Padilha and P. R. Rios. Decomposition of austenite in austenitic stainless steels. *ISIJ International*, 42(4):325–337, 2002.
- [133] T. Sourmail. Precipitation in creep resistant austenitic stainless steels. *Materials Science and Technology*, 17:1, 2001.
- [134] P. Zhong, B. Ling, and B. Z. Gu. Solution treatment effects in cobalt-nickel secondary hardening steel. *Acta Metallurgica Sinica Series A, Physical Metallurgy and Materials Science*, 9(6):613–618, 1996.
- [135] D. E. Goldberg. *Genetic Algorithms in Search, Optimization and Machine Learning*. Addison-Wesley, MA, 1989.
- [136] K. Krishnakumar. Micro-genetic algorithms for stationary and non-stationary function optimization. *Intelligent Control and Adaptive Systems*, SPIE 1196, 1989.
- [137] G. Syswerda. Uniform crossover in genetic algorithms. In *the 3rd International Conference on Genetic Algorithms*, pages 2–9, CA, 1989. Morgan Kaufmann Publishers.
- [138] J. Friedel. *Dislocations*. Pergamon Press, Oxford, 1964.
- [139] A. Deschamps and Y. Brechet. Influence of predeformation and ageing of an Al-Zn-Mg alloy - II. modeling of precipitation kinetics and yield stress. *Acta Materialia*, 47(1):293–305, 1998.
- [140] H. Fredriksson, M. Hillert, and M. Nica. Decomposition of the M_2C carbide in high speed steel. *Scandinavian Journal of Metallurgy*, 8(3):115–122, 1979.
- [141] H. Mitsuo, O. Seizi, Y. Kouichiro, K. Kazuo, K. Ryurou, K. Tamotsu, and K. Takahoko. Development of high-performance roll by continuous pouring process for cladding. *ISIJ International*, 32:1202, 1992.
- [142] A. Iqbal and J. E. King. The role of primary carbides in fatigue crack propagation in aeroengine bearing steels. *International Journal of Fatigue*, 12(4):234–244, 1990.
- [143] S. Lee, K. S. Sohn, C. Lee Gil, and B. I. L. Jung. Correlation of microstructure and fracture toughness in three high-speed steel rolls. *Metallurgical and Materials Transactions A: Physical Metallurgy and Materials Science*, 28(1):123–134, 1997.
- [144] S. Lee, D. O. Hyung Kim, J. H. Ryu, and K. Shin. Correlation of microstructure and thermal fatigue property of three work rolls. *Metallurgical and Materials Transactions A: Physical Metallurgy and Materials Science*, 28(12):2595–2608, 1997.

- [145] H. Shaikh, H. S. Khatak, S. K. Seshadri, J. B. Gnanamoorthy, and P. Rodriguez. Effect of ferrite transformation on the tensile and stress corrosion properties of type 316 L stainless steel weld metal thermally aged at 873 K. *Metallurgical and Materials Transactions A*, 26(7):1859–1868, 1995.
- [146] M. G. Pujar, R. K. Dayal, S. N. Malhotra, and T. P. S. Gill. Evaluation of microstructure and electrochemical corrosion behavior of austenitic 316 stainless steel weld metals with varying chemical compositions. *Journal of Materials Engineering and Performance*, 14(3):327–342, 2005.
- [147] J. Ooro. Martensite microstructure of 9-12Cr steels weld metals. *Journal of Materials Processing Technology*, 180(1-3):137–142, 2006.
- [148] Vijay K. Vasudevan, Sung J. Kim, and C. Marvin Wayman. Precipitation reactions and strengthening behavior in 18 wt pct nickel maraging steels. *Metallurgical transactions. A, Physical metallurgy and materials science*, 21 A(10):2655–2668, 1990.
- [149] P. A. Schweitzer. *Fundamentals of metallic corrosion : atmospheric and media corrosion of metals*. CRC Press, second edition edition, 2007.
- [150] Y. Waseda. *Characterization of corrosion products on steel surfaces*. Springer, 2006.
- [151] J. D. Robson and H. K. D. H. Bhadeshia. Modelling precipitation sequences in power plant steels part 1 - kinetic theory. *Materials Science and Technology*, 13(8):631–639, 1997.
- [152] J. D. Robson and H. K. D. H. Bhadeshia. Modelling precipitation sequences in power plant steels part 2 - application of kinetic theory. *Materials Science and Technology*, 13(8):640–644, 1997.
- [153] J. S. Langer and A. J. Schwartz. Kinetics of nucleation in near-critical fluids. *Physical Review A*, 21(3):948–958, 1980.
- [154] R. Kampmann and R. Wagner. *Decomposition of Alloys: The Early Stages*. Pergamon Press, Oxford, 1984.
- [155] R. Kampmann and R. Wagner. *Materials Science and Technology - A Comprehensive Treatment*. VCH, Weinheim, 1991.
- [156] J. D. Robson, M. J. Jones, and P. B. Prangnell. Extension of the N-model to predict competing homogeneous and heterogeneous precipitation in Al-Sc alloys. *Acta Materialia*, 51(5):1453–1468, 2003.
- [157] J. D. Robson. Modelling the overlap of nucleation, growth and coarsening during precipitation. *Acta Materialia*, 52(15):4669–4676, 2004.

- [158] J. D. Robson. Modelling the evolution of particle size distribution during nucleation, growth and coarsening. *Materials Science and Technology*, 20(4):441–448, 2004.
- [159] O. R. Myhr and O. Grong. Modelling of non-isothermal transformations in alloys containing a particle distribution. *Acta Materialia*, 48(7):1605–1615, 2000.
- [160] *MOB2, Mobility database*. Royal Institute of Technology, Foundation of Computational Thermo-dynamics, Stockholm, Sweden, 2.0 edition, 1999.
- [161] P. E. J. Rivera Diaz del Castillo and H. K. D. H. Bhadeshia. Theory for growth of spherical precipitates with capillarity effects. *Materials Science and Technology*, 17(1):30–32, 2001.
- [162] N. Fujita and H. K. D. H. Bhadeshia. Precipitation of molybdenum carbide in steel: Multicomponent diffusion and multicomponent capillary effects. *Materials Science and Technology*, 15(6):627–634, 1999.
- [163] S. Yamasaki and H. K. D. H. Bhadeshia. Modelling and characterisation of V_4C_3 precipitation and cementite dissolution during tempering of Fe-C-V martensitic steel. *Materials Science and Technology*, 19(10):1335–1343, 2003.
- [164] S. Yamasaki and H. K. D. H. Bhadeshia. Modelling and characterisation of Mo_2C precipitation and cementite dissolution during tempering of Fe-C-Mo martensitic steel. *Materials Science and Technology*, 19(6):723–731, 2003.
- [165] S. E. Offerman, N. H. Van Dijk, J. Sietsma, S. Grigull, E. M. Lauridsen, L. Margulies, H. F. Poulsen, M. Th. Rekvelde, and S. Van der Zwaag. Grain nucleation and growth during phase transformations. *Science*, 298(5595):1003–1005, 2002.
- [166] W. Xu, P. E. J. Rivera-Diaz-Del-Castillo, and S. Van Der Zwaag. Ferrite/pearlite band prevention in dual phase and TRIP steels: Model development. *ISIJ International*, 45(3):380–387, 2005.
- [167] P. E. J. Rivera Diaz del Castillo and S. van der Zwaag. A model for ferrite/pearlite band formation and prevention in steels. *Metallurgical and Materials Transactions A: Physical Metallurgy and Materials Science*, 35 A:425, 2004.
- [168] C. Zener. Theory of growth of spherical precipitates from solid solution. *Journal of Applied Physics*, 20(10):950–953, 1949.
- [169] Y. Mishin and C. Herzig. Grain boundary diffusion: Recent progress and future research. *Materials Science and Engineering A*, 260(1-2):55–71, 1999.

- [170] A. M. Brown and M. F. Ashby. Correlations for diffusion constants. *Acta Metallurgica*, 28(8):1085–1101, 1980.
- [171] J. Fridberg, L. E. Torndahl, and M. Hillert. Diffusion in iron. *Jernkontorets Ann*, 153(6):263–276, 1969.
- [172] P. E. J. Rivera Diaz del Castillo, W. Xu, and S. van der Zwaag. Theory for multicomponent diffusional kinetics and its application to the reaustenitisation of dual phase and TRIP steels. In *International Conference on Solid-Solid Phase Transformations in Inorganic Materials 2005*, vol. 2, pages 801–810, Arizona, 2005.
- [173] P. E. J. Rivera Diaz Del Castillo, P. Reischig, W. Xu, and S. Van Der Zwaag. Theory for diffusional transformation kinetics: Multicomponent and multi-phase systems. *Scripta Materialia*, 53(9):1089–1094, 2005.
- [174] D. San Martin, P. E. J. Rivera Diaz del Castillo, E. Peekstok, and S. van der Zwaag. A new etching route for revealing the austenite grain boundaries in an 11.4 % Cr precipitation hardening semi-austenitic stainless steel. *Materials Characterization*, 58(5):455–460, 2007.
- [175] F. G. Caballero, C. Capdevila, and C. García De Andrés. Influence of pearlite morphology and heating rate on the kinetics of continuously heated austenite formation in a eutectoid steel. *Metallurgical and Materials Transactions A: Physical Metallurgy and Materials Science*, 32(6):1283–1291, 2001.
- [176] G. F. Vander Voort. *Metallography: Principles and Practice*. Asm International, 1984.
- [177] F. C. Hull and W. J. Howk. Statistical grain structure studies: Plane distribution curves of regular polyhedron. *J. Met.*, 5:565–572, 1953.

Acknowledgements

This thesis would not have been made a reality without the support and help of many people, who I would like to thank.

First and foremost, I would like to express my deepest gratitude to my promoter Prof.dr.ir. Sybrand van der Zwaag and daily supervisor Dr. Pedro E.J. Rivera Díaz del Castillo who both played a central role in their own ways. Professor van der Zwaag has always been helpful, enthusiastic and inspiring to me, kept the research on the right track while providing broad vision and enough freedom. Dr. Pedro Rivera's detailed knowledge of phase transformation and general materials science were invaluable during the course of my time in Delft and he has been much more than a daily supervisor, at times a friend and at times a mentor. I also greatly appreciate the support of Corus RD&T for this project and special thanks to Dr. Peter Morris from Corus UK, who provided very important inputs for the project.

Another important partner of this project is Prof. Ke Yang and his group in the Institute of Metals Research, Chinese Academy of Science. Prof. Yang was always very kind and provided all necessary supports. Special thanks also go to Dr. Wei Yan and Wei Wang for their excellent experimental work on preparing and characterization of some of prototype alloys. Without their help, the thesis would not have been made this far.

The use of TEM was extremely necessary for this thesis work. At TU Delft, Frans Tichelaar and Qiang Xu (Kavli Institute of Nanoscience) are greatly appreciated for giving me the TEM operation training. A lot of supports also came

from Leo Kestens and Vitaliy Bliznuk at Gent University, Belgium, particularly the precipitation characterization using their high-end TEM facilities. My former colleague, David San Martin who is at CENIM Spain now, is another name I have to mention and would like to thank. He taught me a lot concerning the metallurgical characterization and also performed part of the experimental work presented in this thesis.

Our research group has been the most international group and I was always proud to be a part of this group where one could learn a lot in addition to science. Here I would like to thank all the (ex-) members of the group for providing such a great atmosphere. Suresh Neelakantan has been really a wonderful officemate, always willing to help. Thanks Mingxin Huang, for all kinds of discussions we had. Thanks Laura, Theo, Alwin, Steven, Arek, Santiago, Jie, Yanmin, GuiMing, Doty, Geeta, Maruti, Mazhar, Rahul, Sanna, Chris, Pim, Hartmut, Natalia, Bui, Meijie, Sangwoo and all former FAM members for all discussions, coffees, lunches, outings and whatever more.

Concerning the non-academic side of my time here, I have to thank a great number of people for their friendship. After all, life and friendship do not stop with a PhD. Thanks for the fun, helps, dinners, playing mah-jong, badminton and travelling together.

I would like to thank my family in China for their love, encouragement and support. Last, but furthest from the least, a very special thank goes to Xi, my wife. During the last four years we've both gone through a lot and it wouldn't have been possible without anyone else. 'Thanks' isn't a big enough word, but it'll have to do for here.

Curriculum Vitae

Wei XU

born on 20 October 1979
in Dandong, Liaoning Province, China

Sept. 1998 - Jul. 2002

Bachelor of Science in Mechanical Engineering, in Department of Mechanics and Mechanical Engineering, University of Science and Technology of China, Hefei, China.

Sept. 1999 - Jul. 2001

Bachelor of International Business Administration, in Management School, University of Science and Technology of China, Hefei, China.

Sept. 2002 - Jul. 2005

Master of Science in Materials and Solid Mechanics, in Department of Mechanics and Mechanical Engineering, University of Science and Technology of China, Hefei, China.

Mar. 2004 - Jan. 2005

Exchange Student in the Faculty of Aerospace Engineering, Delft University of Technology, Delft, the Netherlands, supported by CSC (China Scholarship Council) and NUFFIC (the Netherlands Organization for International Cooperation in Higher Education).

Jul. 2005 - Oct. 2009

Ph.D. candidate in the group of Fundamentals of Advanced Materials, Faculty of Aerospace Engineering, Delft University of Technology, Delft, The Netherlands, under supervision of Prof.dr.ir. Sybrand van der Zwaag and Dr. Pedro E.J. Rivera Díaz del Castillo.

List of Publications

Journal

- **W. Xu**, P.E.J. Rivera Díaz del Castillo and S. van der Zwaag, Design and Characterization of Novel Ultra High Strength Maraging TRIP stainless steels strengthened by nano precipitates of Ni₃Ti intermetallics. In preparation. *Acta Materialia*, to be submitted.
- **W. Xu**, P.E.J. Rivera Díaz del Castillo and S. van der Zwaag, Design and Characterization of Ultra High Strength Maraging Stainless Steels Utilizing Multiple Precipitates of Carbide and Intermetallics. *ISIJ International*, to be submitted.
- **W. Xu**, P.E.J. Rivera Díaz del Castillo and S. van der Zwaag, A Computational Design of UHS Maraging Stainless Steels Incorporating Composition as well as Austenitisation and Ageing Temperatures as Optimisation Parameters, *Philosophical Magazine*, 2009, 89 (20), pp 1647-1662.
- **W. Xu**, P.E.J. Rivera Díaz del Castillo and S. van der Zwaag, A combined optimization of alloy composition and aging temperature in designing new UHS precipitation hardenable stainless steels, *Computational Materials Science*, 2009, 45 (2), pp 467-473.
- **W. Xu**, P.E.J. Rivera Díaz del Castillo and S. van der Zwaag, The composition and temperature effects on the ultra high strength stainless steel design, *International Journal of Modern Physics B*, 2009, 23 (6-7), pp 1060-1065.
- **W. Xu**, P.E.J. Rivera Díaz del Castillo and S. van der Zwaag, Genetic alloy design based on thermodynamics and kinetics, *Philosophical Magazine*, 2008, 88 (12), pp 1825-1833.
- **W. Xu**, P.E.J. Rivera Díaz del Castillo and S. van der Zwaag, Designing nanoprecipitation strengthened UHS stainless steels combining genetic algorithms and thermodynamics, *Computational Materials Science*, 2008, 44 (2), pp 678-689.
- **W. Xu**, D. San Martin, P.E.J. Rivera Díaz del Castillo and S. van der Zwaag, Modelling and characterization of chi-phase grain boundary precipitation during aging of Fe-Cr-Ni-Mo stainless steel, *Materials Science and Engineering A*, 2007, 467 (1-2), pp 24-32.
- **W. Xu**, D. San Martin, P.E.J. Rivera Diaz del Castillo, S. van der Zwaag, Modelling Chi-Phase Precipitation in High Molybdenum Stainless Steels. *Advanced Materials Research*, 2007, 15-17, pp 531-536.

- **W. Xu**, P. E. J. Rivera-Daz-del-Castillo, S. van der Zwaag, Ferrite/Pearlite Band Prevention in Dual Phase and TRIP Steels PART I - Model Development, *ISIJ international*, 2005, 45 (3), pp 380.
- P.E.J. Rivera-Daz-del-Castillo, P. Reischig, **W. Xu**, S. van der Zwaag, Theory for Diffusional Transformation Kinetics: Multicomponent and Multiphase Systems, *Scripta Materialia*, 2005, 53, pp 1089.
- Wen Huang, **Wei Xu**, Yuanming Xia, Effect of Strain Rate on the Mechanical Properties of SiC Fiber, *Journal of Material Science*, 2005, 40 (2), pp 465.

Conference

- P.E.J. Rivera Díaz del Castillo, **W. Xu**, and S. van der Zwaag, Genetic Alloy Design Of Ultra High Strength Stainless Steels: From Thermodynamics To Quantum Design, Proceedings of THERMEC '09, Berlin, Germany, 25-29 August, 2009.
- **W. Xu**, P.E.J. Rivera Díaz del Castillo and S. van der Zwaag, Genetic computational design of novel ultra high strength stainless steels: model description and first experimental validation, Proceedings of TMS 2009 Annual Meeting and Exhibition: Synergies of Computational and Experimental Materials Science, San Fransisco, USA, 15-19 February, 2009
- **W. Xu**, P.E.J. Rivera Díaz del Castillo and S. van der Zwaag, Computational design of UHS stainless steel strengthened by multi-species nanoprecipitates combining genetic algorithms and Thermokinetics, proceedings of New Development on Metallurgy and Applications of High Strength Steels, Buenos Aires, Argentina, 26-28 May, 2008.
- **W. Xu**, P.E.J. Rivera Díaz del Castillo and S. van der Zwaag, Using genetic algorithm to design new ultra-high strength stainless steels reinforced by separate precipitate families, Proceedings of 6th European Stainless Steels Conference, Helsinki, Finland, 10-13 June, 2008.
- P. E. J. Rivera-Daz-del-Castill, **W. Xu**, S. van der Zwaag, Theory for Multicomponent Diffusional Kinetics and its Application to the Reaustenitisation of Dual Phase and TRIP Steels, Proceedings of an International Conference on Solid-Solid Phase Transformations in Inorganic Materials 2005, TMS 2005, San Fransisco, USA, 29 May-3 June, 2005.